



**HAL**  
open science

# Study of the production mechanisms of hydrogen (H-) and deuterium (D-) negative ions in continuous and pulsed microwave plasmas through complementary diagnostic techniques

Maria Mitrou

► **To cite this version:**

Maria Mitrou. Study of the production mechanisms of hydrogen (H-) and deuterium (D-) negative ions in continuous and pulsed microwave plasmas through complementary diagnostic techniques. Physics [physics]. Université Grenoble Alpes [2020-..]; Panepistīmio Patrón, 2024. English. NNT : 2024GRALI035 . tel-04812766

**HAL Id: tel-04812766**

**<https://theses.hal.science/tel-04812766v1>**

Submitted on 1 Dec 2024

**HAL** is a multi-disciplinary open access archive for the deposit and dissemination of scientific research documents, whether they are published or not. The documents may come from teaching and research institutions in France or abroad, or from public or private research centers.

L'archive ouverte pluridisciplinaire **HAL**, est destinée au dépôt et à la diffusion de documents scientifiques de niveau recherche, publiés ou non, émanant des établissements d'enseignement et de recherche français ou étrangers, des laboratoires publics ou privés.



## THÈSE

Pour obtenir le grade de

### DOCTEUR DE L'UNIVERSITÉ GRENOBLE ALPES et de l'UNIVERSITÉ DE PATRAS

École doctorale: Ingénierie – Matériaux, mécanique, environnement, énergétique, procédés, production (I-MEP<sup>2</sup>)

Spécialité : Mécanique des fluides, énergétique, procédés

Unité de recherche : Laboratoire de Physique Subatomique et Cosmologie (LPSC–CNRS), et le High Voltage Laboratory (University of Patras)

### Étude des mécanismes de production d'ions négatifs d'hydrogène ( $H^-$ ) et de deutérium ( $D^-$ ) en plasmas micro-onde continu et pulsé par des diagnostics complémentaires

### Study of the production mechanisms of hydrogen ( $H^-$ ) and deuterium ( $D^-$ ) negative ions in continuous and pulsed microwave plasmas with complementary diagnostic techniques

Présentée par :

**Maria MITROU**

#### Direction de thèse:

**Stéphane BECHU**

Research Director, Laboratory of Subatomic Physics and Cosmology (LPSC-CNRS)

Directeur

**Panagiotis SVARNAS**

Professor, Dept. of Electrical and Computer Engineering, University of Patras

Co-Directeur

#### Rapporteurs:

**Ivo FURNO**

Professor, Swiss Federal Institute of Technology (EPFL)

**Claudia LAZZARONI**

Assistant Professor, Process and Materials Sciences Laboratory (LSPM (UPR3407) - CNRS)

#### Thèse soutenue publiquement le 31/05/2024 devant le jury composé de:

**Roberto PASQUALOTTO**

Research Director, Consorzio RFX

Président

**Alexandros GERAKIS**

Senior Research & Technology Associate, Luxembourg Institute of Science and Technology

Examineur

**Martin KOGELSCHATZ**

Associate Professor, University Grenoble Alpes

Examineur

**Eleftherios AMANATIDES**

Associate Professor, Dept. of Chemical Engineering, University of Patras

Examineur

**Ivo FURNO**

Professor, Swiss Federal Institute of Technology (EPFL)

Rapporteur

**Claudia LAZZARONI**

Assistant Professor, Process and Materials Sciences Laboratory (LSPM (UPR3407) - CNRS)

Rapporteuse

**Stéphane BECHU**

Research Director, Laboratory of Subatomic Physics and Cosmology (LPSC- CNRS)

Directeur

**Panagiotis SVARNAS**

Professor, Dept. of Electrical and Computer Engineering, University of Patras

Co-directeur





*To my driving source, my parents,  
Tassos and Valentina.*



# ABSTRACT

---

Hydrogen negative ion sources are integral components in modern accelerator facilities and in the Neutral Beam Injection (NBI) systems of future fusion reactors. The latter application necessitates the development of such very powerful sources and the extension of their operation to deuterium. Numerous research activities on laboratory-scale experiments have been devoted to this subject aiming at understanding the fundamental processes that govern negative ion production. The gained knowledge has contributed essentially to the development of the prototype sources that will be employed in the NBI system of ITER, the largest Tokamak reactor under construction which is foreseen to demonstrate the potential of exploitation of thermonuclear fusion as an alternative source of energy. Nonetheless, there are important technological issues arising from the fundamental physics underlying these sources which need to be overcome in order for them to be able to deliver neutral beams with characteristics satisfying the baseline requirements.

In the present thesis, the production of hydrogen ( $\text{H}^-$ ) and deuterium ( $\text{D}^-$ ) negative ions is studied in Electron Cyclotron Resonance (ECR) driven plasmas. In particular, experimental studies have been carried out in two reactors of similar characteristics, namely “Prometheus I” and “SCHEME-II+”, by means of conventional and state-of-the-art diagnostic techniques tailored to investigate the macroscopic and atomic properties of the plasmas of the two isotopes. In these reactors, negative ion production is based on the so-called *volume production mechanism*. In this case, the Dissociative Electron Attachment (DEA) reaction is identified as the predominant one. Understanding those factors which influence this reaction may lead to its control and thus an even better control of the negative ion production.

In the “Prometheus I” reactor, extensive parametric studies in hydrogen and deuterium plasmas as a function of the supplied microwave power and working gas pressure reveal the existence of optima for negative ion production and allow the identification of isotopic differences. The negative ion yield reaches a value of  $0.57 \times 10^{16} \text{ m}^{-3}$  in both plasmas, although in the hydrogen case the ratio of the negative ions to the plasma density is consistently higher than in the case of deuterium. Indicatively, a ratio of 0.225 in  $\text{H}_2$  versus 0.125 in  $\text{D}_2$  is observed in representative operating conditions. Measurements, moreover, of the negative ion energies disclose the existence of two ionic populations of different energies. This has been attributed to the two main mechanisms leading to the excitation of molecules in high vibrational/rotational states, which in turn participate in the formation of negative ions via the DEA reaction.

On the other hand, the “SCHEME-II+” reactor is intended for studies of the influence of various materials exposed to the produced plasma on the production of the highly ro-vibrationally excited molecules. An advanced spectroscopic diagnostic technique, Vacuum Ultraviolet Fourier Transform (VUV-FT) absorption spectroscopy using synchrotron radiation, is utilized in order to directly probe these species under different plasma operating conditions. The significant positive

effect of metallic surfaces on the creation of these species is demonstrated, since a nearly fourfold increase of deuterium molecules in high vibrational states ( $v'' = 4-8$ ) is observed when the plasma faces a tantalum surface as opposed to a Quartz surface.

Finally, deuterium plasmas sustained in the pulsed mode of operation are investigated. Time-resolved measurements of the basic plasma parameters, performed in plasma pulses lying in the kHz range, reveal important post-plasma effects. In particular, a higher negative ion yield with respect to that measured in a plasma sustained in the continuous mode of operation has been observed.

**KEYWORDS:** Negative ions, Hydrogen, Deuterium, Electron Cyclotron Resonance plasma, Langmuir probes, Laser-induced photodetachment, VUV absorption spectroscopy with the use of synchrotron radiation.

## RESUMÉ

---

Les sources d'ions négatifs d'hydrogène font partie intégrante des accélérateurs modernes et des systèmes d'injection de neutres (NBI) dans les futurs réacteurs de fusion. Cette dernière application nécessite le développement de sources très puissantes et l'extension de leur fonctionnement au deutérium. De nombreuses activités de recherche sur des expériences à l'échelle du laboratoire ont été dédiées à ce sujet dans le but de comprendre les processus fondamentaux qui régissent la production d'ions négatifs. Les connaissances acquises ont essentiellement contribué au développement des sources prototypes qui seront employées dans le système NBI d'ITER, le plus grand réacteur Tokamak en construction destiné à démontrer le potentiel d'exploitation de la fusion en tant que source d'énergie alternative. Toutefois, d'importantes contraintes technologiques liées à la physique fondamentale gouvernant le fonctionnement de ces sources doivent être surmontées pour qu'elles puissent délivrer des faisceaux de neutres dont les caractéristiques satisfassent les exigences initiales.

Dans cette thèse, la production d'ions négatifs d'hydrogène ( $H^-$ ) et de deutérium ( $D^-$ ) est étudiée dans des plasmas entretenus à la résonance cyclotron électronique. En particulier, des études expérimentales ont été réalisées dans deux réacteurs présentant des caractéristiques similaires, "Prometheus I" et "SCHEME-II+", en utilisant des diagnostics conventionnels et avancés adaptés à l'étude des propriétés macroscopiques et atomiques des plasmas de ces deux isotopes. Dans ces réacteurs, la production d'ions négatifs est basée sur le mécanisme dit de *production en volume*. Dans ce cas, la réaction d'attachement dissociative des électrons (ADE) est identifiée comme la réaction prédominante. La compréhension des facteurs influençant cette réaction peut donc conduire à un meilleur contrôle de la production d'ions négatifs.

Dans le réacteur "Prometheus I", des études paramétriques dans des plasmas d'hydrogène et de deutérium, en fonction de la puissance micro-onde et de la pression du gaz, révèlent des optima pour la production d'ions négatifs et permettent de mettre en évidence des particularités isotopiques. Le rendement en ions négatifs atteint  $0.57 \times 10^{16} \text{ m}^{-3}$  dans les deux plasmas, mais le rapport entre les ions négatifs et la densité du plasma est systématiquement plus élevée pour  $H_2$  que pour  $D_2$ . Par exemple, un rapport de 0.225 pour  $H_2$  contre 0.125 pour  $D_2$  est obtenu dans des conditions représentatives de fonctionnement. En outre, la mesure de l'énergie des ions négatifs révèle l'existence de deux populations ioniques d'énergies différentes. Ceci a été attribué principalement à deux mécanismes responsables de l'excitation des molécules à des niveaux vibrationnels/rotationnels élevés participant à la formation d'ions négatifs via la réaction ADE.

En revanche, le réacteur "SCHEME-II+" est destiné à l'étude de l'influence de divers matériaux exposés au plasma pour la production de molécules ro-vibrationnellement excitées. Un diagnostic spectroscopique complexe, la spectroscopie d'absorption dans l'ultraviolet du vide à transformée de Fourier (VUV-FT) utilisant le rayonnement synchrotron, est utilisée pour les

sonder directement différentes conditions de fonctionnement du plasma. L'effet significatif des surfaces métalliques sur la création de ces espèces ro-vibrationnellement excitées a pu être démontré. Une augmentation de près d'un facteur quatre pour les molécules D<sub>2</sub> dans les états vibrationnels élevés ( $v'' = 4-8$ ) est observée lorsqu'une surface de tantale remplace une surface de quartz face au plasma.

Enfin, des plasmas de deutérium fonctionnant en mode pulsé sont examinés. Des mesures résolues en temps des paramètres plasma, effectuées dans des impulsions de plasma de l'ordre du kHz, révèlent d'importants effets post-plasma. Notamment, un rendement en ions négatifs plus élevé que celui mesuré dans un plasma fonctionnant en mode continu a été observé.

**MOTS CLÉS:** Ions Négatifs, Hydrogène, Deutérium, Plasma à la Résonance Cyclotron Électronique (ECR), Sondes Langmuir, Photodétachement laser, Spectroscopie d'absorption dans l'ultraviolet du vide en utilisant le rayonnement synchrotron.

## ΠΕΡΙΛΗΨΗ

---

Οι πηγές αρνητικών ιόντων υδρογόνου αποτελούν αναπόσπαστο τμήμα των σύγχρονων εγκαταστάσεων επιταχυντών αλλά και των διατάξεων έγχυσης δεσμών ουδέτερων σωματιδίων υψηλής ενέργειας των μελλοντικών αντιδραστήρων θερμοπυρηνικής σύντηξης. Η τελευταία εφαρμογή καθιστά αναγκαία την ανάπτυξη τέτοιων ισχυρών πηγών καθώς και την επέκταση της λειτουργίας τους στο δευτέριο. Πλήθος ερευνητικών δραστηριοτήτων σε διατάξεις εργαστηριακής κλίμακας έχουν επικεντρωθεί στο θέμα αυτό αποσκοπώντας στην κατανόηση των θεμελιωδών διεργασιών που διέπουν την παραγωγή αρνητικών ιόντων. Η αποκτηθείσα γνώση έχει συμβάλει καθοριστικά στην ανάπτυξη των πρότυπων πηγών που πρόκειται να χρησιμοποιηθούν στις διατάξεις έγχυσης δεσμών ουδέτερων σωματιδίων υψηλής ενέργειας του ITER, του υπό κατασκευή μεγαλύτερου αντιδραστήρα Tokamak που θα καταδείξει τη δυνατότητα εκμετάλλευσης της θερμοπυρηνικής σύντηξης ως εναλλακτική πηγή ενέργειας. Ωστόσο, υπάρχουν σημαντικά τεχνολογικά προβλήματα που σχετίζονται με τη θεμελιώδη φυσική που διέπει τις πηγές αυτές τα οποία είναι απαραίτητο να επιλυθούν προκειμένου να παραχθούν δέσμες με χαρακτηριστικά που ικανοποιούν τις πρότυπες προδιαγραφές.

Στην παρούσα διατριβή, μελετάται η παραγωγή αρνητικών ιόντων υδρογόνου ( $H^-$ ) και δευτερίου ( $D^-$ ) σε πλάσμα κυκλοτρονικού συντονισμού ηλεκτρονίων. Πιο συγκεκριμένα, πειραματικές μελέτες έχουν διεξαχθεί σε δύο αντιδραστήρες παρόμοιων χαρακτηριστικών, ήτοι τον αντιδραστήρα “Προμηθέας Γ” και τον αντιδραστήρα “SCHEME-II+”, μέσω συμβατικών και τεχνολογίας αιχμής διαγνωστικών τεχνικών προσαρμοσμένων στη διερεύνηση μακροσκοπικών και ατομικών παραμέτρων του πλάσματος των δύο ισοτόπων. Σε αυτούς τους αντιδραστήρες, ο σχηματισμός αρνητικών ιόντων στηρίζεται σε ένα μηχανισμό ο οποίος αφορά στην παραγωγή στον κύριο όγκο του πλάσματος. Σε αυτή την περίπτωση, η αντίδραση της διαχωρίζουσας προσάρτησης ηλεκτρονίων ταυτοποιείται ως η κυρίαρχη. Η κατανόηση των παραγόντων εκείνων που επηρεάζουν την αντίδραση αυτή δύναται να οδηγήσει στον έλεγχο της και συνεπώς στον ακόμη καλύτερο έλεγχο της παραγωγής των αρνητικών ιόντων.

Στον αντιδραστήρα “Προμηθέας Γ”, παραμετρικές μελέτες συναρτήσεως της παρεχόμενης μικροκυματικής ισχύος και της πίεσης των δύο αερίων λειτουργίας φανερώνουν την ύπαρξη βέλτιστων παράθυρων λειτουργίας για την παραγωγή αρνητικών ιόντων και επιτρέπουν την ταυτοποίηση ισοτοπικών διαφορών. Η πυκνότητα των αρνητικών ιόντων φτάνει στα περίπου  $0.6 \times 10^{16} \text{ m}^{-3}$  και στα δύο αέρια λειτουργίας. Παρα ταύτα, στην περίπτωση του υδρογόνου ο λόγος της πυκνότητας των αρνητικών ιόντων προς την πυκνότητα πλάσματος είναι μονίμως υψηλότερος σε σχέση με αυτόν στο δευτέριο. Ενδεικτικά, παρατηρείται τιμή του λόγου αυτού ίση με 0.225 στο  $H_2$  έναντι 0.125 στο  $D_2$  σε τυπικές συνθήκες λειτουργίας. Μετρήσεις, επιπλέον, των ενεργειών των αρνητικών ιόντων αποκαλύπτουν την ύπαρξη δύο πληθυσμών αρνητικών ιόντων χαρακτηριζόμενων από διαφορετικές ενέργειες. Αυτό έχει αποδοθεί στους δύο κύριους μηχανισμούς που οδηγούν στη διέγερση των μορίων

σε υψηλές δονητικές/περιστροφικές στάθμες, τα οποία με τη σειρά τους συμμετέχουν στο σχηματισμό αρνητικών ιόντων μέσω της αντίδρασης της διαχωρίζουσας προσάρτησης ηλεκτρονίων.

Από την άλλη πλευρά, ο αντιδραστήρας “SCHEME-II+” προορίζεται για μελέτες του ρόλου των διαφόρων υλικών των εκτιθέμενων στο πλάσμα στην παραγωγή δονητικά/περιστροφικά διεγερμένων μορίων. Μια προηγμένη διαγνωστική τεχνική φασματοσκοπίας, αυτή της φασματοσκοπίας απορρόφησης υπεριώδους κενού με χρήση ακτινοβολίας σύγχροτρον και φασματογράφου μετασχηματισμού Fourier, χρησιμοποιείται για την απευθείας ανίχνευση των σωματιδίων αυτών υπό διαφορετικές συνθήκες λειτουργίας του πλάσματος. Καταδεικνύεται η σημαντική θετική επίδραση συγκεκριμένων μεταλλικών επιφανειών στη δημιουργία αυτών των μορίων. Ενδεικτικά αναφέρεται η περίπτωση τέσσερις φορές αύξηση της συγκέντρωσης μορίων δευτερίου σε υψηλές δονητικές στάθμες ( $v'' = 4-8$ ) όταν το πλάσμα γειτνιάζει με επιφάνειες τανταλίου σε σχέση με την γειτνίαση με επιφάνειες χαλαζία.

Τέλος, γίνεται μελέτη πλάσματος δευτερίου υπό καθεστώς παλμικής μικροκυματικής οδήγησης. Χρονικά αναλυμένες μετρήσεις των βασικών παραμέτρων του πλάσματος, οι οποίες πραγματοποιούνται σε παλμούς οδήγησης συχνότητας kHz, αποκαλύπτουν ιδιαίτερα χαρακτηριστικά στο πέρας κάθε παλμού οδήγησης. Μεταξύ άλλων, παρατηρείται υψηλότερη παραγωγή αρνητικών ιόντων σε σχέση με κατά τη συνεχή μικροκυματική οδήγηση του πλάσματος.

**ΛΕΞΕΙΣ ΚΛΕΙΔΙΑ:** Αρνητικά ιόντα, Υδρογόνο, Δευτέριο, Πλάσμα Κυκλοτρονικού Συντονισμού Ηλεκτρονίων, Ηλεκτροστατικοί καθετήρες τύπου Langmuir, Φωτοαπόσπαση laser, Φασματοσκοπία απορρόφησης υπεριώδους κενού με χρήση ακτινοβολίας σύγχροτρον.

## ACKNOWLEDGMENTS

---

The present doctoral thesis was conducted on the basis of a joint PhD program within the framework of an established bi-lateral agreement between the University of Patras (Greece) and the University of Grenoble Alpes (France). I had thus the great chance to work in two laboratories, the High Voltage Laboratory in Greece and the Laboratory of Subatomic Physics and Cosmology in France. Now, as this four-year journey comes to an end, I wish to address several words of appreciation to those who have been an integral part of it.

First and foremost, I would like to express my immense gratitude to Prof. Dr. Panagiotis Svarnas and Dr. Stéphane Béchu who supervised the present work from start to finish, and without whom I would undoubtedly not have been able to see this project through. I am greatly appreciative for their trust in me, their patience, and their willingness to help me the many times it was needed. Most importantly though I will be forever indebted to them for the knowledge they have so generously passed down to me. I will always look up to their intelligence, passion for their work, and ethic. They are my mentors in every sense of the word.

From this position I must also recognize the essential financial contribution of the “Andreas Mentzelopoulos” scholarship foundation of the University of Patras, which awarded me with a three-year full-time scholarship in order to carry out my doctoral studies.

Furthermore, during this thesis I had the incredible opportunity to participate in three experimental campaigns that were carried out at the SOLEIL synchrotron facility (Saint-Aubin, France). A part of the results obtained in these experiments was pivotal for the completeness of this work. Thus, firstly, I am due many thanks to Dr. Nelson de Oliveira (Scientist on the DESIRS beamline) for his eagerness and availability to explain the details on the operation of the beamline and the installed instrumentation, and secondly, to Prof. Emer. Dr. Jean-Louis Lemaire for our collaboration and our enlightening discussions during the experimental runs. His expertise was invaluable for the correct interpretation of our results.

I would also like to extend my appreciation to Prof. Dr. Ivo Furno and Asst. Prof. Dr. Claudia Lazzaroni for accepting to review my manuscript and for providing me with excellent feedback. Additionally, it is truly an honor for me that Prof. Dr. Roberto Pasqualotto, Dr. Alexandros Gerakis, Assoc. Prof. Dr. Martin Kogelschatz, and Assoc. Prof. Dr. Eleftherios Amanatides all very kindly accepted to participate in the jury for the evaluation of my thesis.

From the High Voltage Lab. of which I have been a member even since my undergraduate studies, I must thank Prof. Eleftheria Pyrgioti for all the fond memories and our excellent collaboration throughout the years. I also owe great thanks to Mr. Konstantinos Petrou and Mr. Gerasimos Diamantis for their exceptional technical support the entire time.

To all the members of the Plasma Group at the LPSC, I will always be grateful to them for graciously greeting me into their team and making me instantly feel one of them. Especially though to Dr. Alexandre Bès I owe a lot, since he would always help me anytime I would ask and since through our daily – scientific but also oftentimes random – discussions I was able to learn the French language.

To top all this, during these years I had the extreme luck to work amongst exceptional colleagues also in the pursuit of their PhDs, and equally curious minds, who became dearest friends along the way. Each one of them hold a special position in my heart: Konstantinos Giotis, Quentin Gutierrez, Evaggelia Zavvou, Aimilia Barmdaki and Konstantinos Koutras. I will always cherish the countless hours we spent together in moments filled with laughter, and in discussions on our anxieties and ambitions for the future. I am also sincerely thankful to my long-time friends that have stood by my side ever since the first years of our undergraduate studies and as we grow together, in particular: Katerina Maragkou, Katerina Georgiou and Eleni Tzela, no matter how far apart life may take us.

My greatest affection though goes to my younger (... and perhaps smarter) sister whose determination and fearlessness have always been an inspiration to me.

Finally, as I close this personal note, I express my deepest love to my parents Tassos and Valentina to whom I dedicate my work as the smallest token of appreciation for their endless support through every step and every decision in my life. Their encouragement to always dare to dream big is my greatest driving source, for they are the biggest dreamers of all.

# TABLE OF CONTENTS

---

<b>ABSTRACT</b> .....	I
<b>RESUMÉ</b> .....	III
<b>ΠΕΡΙΛΗΨΗ</b> .....	V
<b>ACKNOWLEDGMENTS</b> .....	VII
<b>TABLE OF CONTENTS</b> .....	IX
<b>CHAPTER 1</b>	
<b>INTRODUCTION</b> .....	1
1.1 Towards H <sup>-</sup> /D <sup>-</sup> ion sources for fusion applications .....	2
1.2 State-of-the-art ion sources for the ITER NBI.....	4
1.3 Alternative negative ion source concepts .....	6
1.4 Comparative studies of negative ion sources operating with H <sub>2</sub> and D <sub>2</sub> .....	8
1.5 Negative ion production and destruction mechanisms .....	11
1.5.1 Surface production.....	12
1.5.2 Volume production .....	13
1.5.3 Surface-assisted volume production .....	17
1.5.4 Destruction mechanisms.....	18
1.6 Advantages of ECR discharges.....	19
1.6.1 Theoretical background .....	19
1.6.2 Dipolar ECR modules.....	21
1.7 Plasmas sustained in the pulsed operating regime .....	23
1.8 Thesis contribution and outline.....	26
<b>CHAPTER 2</b>	
<b>EXPERIMENTAL APPARATUS AND METHODS</b> .....	29
2.1 The “Prometheus I” reactor .....	30
2.1.1 Electrostatic (Langmuir) probe diagnostic.....	31
2.1.2 Single-beam laser-induced photodetachment technique .....	32
2.1.3 Two-beam laser-induced photodetachment technique.....	35
2.1.4 Reactor conditioning considerations .....	39
2.2 The “SCHEME-II+” reactor .....	40
2.2.1 Vacuum Ultraviolet (VUV) Fourier Transform absorption spectroscopy with synchrotron radiation .....	43
2.2.2 Pulsed plasma regime.....	49

<b>CHAPTER 3</b>	
<b>COMPARATIVE INVESTIGATION OF BASIC PARAMETERS IN H<sub>2</sub> AND D<sub>2</sub> PLASMAS</b>	55
3.1 Aspects of the analysis of the I–V characteristics	56
3.2 H <sup>-</sup> and D <sup>-</sup> production efficiency as a function of microwave power	57
3.3 H <sup>-</sup> and D <sup>-</sup> production efficiency as a function of gas pressure	64
3.4 Discussion	66
3.5 Negative ion energies in H <sub>2</sub> and D <sub>2</sub> plasmas	71
<b>CHAPTER 4</b>	
<b>EXPERIMENTAL DETERMINATION OF VIBRATIONAL DISTRIBUTION FUNCTIONS</b>	73
4.1 Analysis procedure for spectra recorded by VUV-FT absorption spectroscopy	74
4.2 VDFs in characteristic plasma conditions	88
4.3 Determining the absolute VDF	90
4.4 Other parameters derived through VUV-FT absorption spectroscopy	93
4.4.1 Gas temperature	93
4.4.2 Atom density and degree of dissociation	94
4.5 Discussion	95
<b>CHAPTER 5</b>	
<b>INTERROGATION OF PLASMAS SUSTAINED IN THE PULSED MODE OF OPERATION</b>	99
5.1 Time-resolved D <sub>2</sub> plasma parameters	100
5.2 Time-resolved measurements of the negative ion density	102
5.2.1 The case of a full quartz surface facing the plasma	102
5.2.2 The case of a full tungsten surface facing the plasma	105
5.3 Discussion	107
<b>CHAPTER 6</b>	
<b>CONCLUSIONS</b>	109
<b>BIBLIOGRAPHY</b>	113
<b>LIST OF PUBLICATIONS</b>	125
<b>Appendix A: Gas flow modeling in COMSOL</b>	127
<b>Appendix B: Validating the Langmuir probe design</b>	129

# CHAPTER 1

## INTRODUCTION

---

The following introductory chapter to the thesis entitled “*Study of the production mechanisms of hydrogen ( $H^-$ ) and deuterium ( $D^-$ ) negative ions in continuous and pulsed microwave plasmas through complementary diagnostic techniques*” contains primarily an overview of worldwide research efforts aiming to the exploration, from a fundamental point of view, of the production of  $H^-$  and  $D^-$  ions and the development of respective sources relevant to fusion studies. Among the different types of sources that exist, Electron Cyclotron Resonance (ECR) driven ones, and in particular those based on elementary dipolar ECR modules such as those studied in the framework of the present thesis, merit special attention for reasons that are thereby highlighted. Furthermore, since negative ion production in these sources is based on the so-called volume production concept, its basic theoretical aspects are presented. Eventually, the contribution and the structure of the present thesis are outlined.

## 1.1 Towards $\text{H}^-/\text{D}^-$ ion sources for fusion applications

Historically, negative ions first found application in the Van de Graaf electrostatic accelerators developed in 1929. They remain efficient, however, in studies of the spectra and structures of atom nuclei, because of the high monochromaticity of the accelerated particles [1]. Moreover, negative hydrogen beams have become the preferred means of filling circular accelerators and storage rings as well as enabling efficient extraction from cyclotrons. Several well-known facilities now have considerable experience with operating a variety of sources such as radio-frequency (RF)-, filament-, magnetron-, and Penning-type hydrogen negative ion sources. The US Spallation Neutron Source (SNS), Japan Proton Accelerator Research Complex (J-PARC), Rutherford Appleton Laboratory (RAL-ISIS), Los Alamos Neutron Science Center (LANSCE), Fermi National Accelerator Laboratory (FNAL), Brookhaven National Laboratory (BNL), numerous installations of D-Pace (licensed by TRIUMF) ion sources mainly used in on cyclotrons and the CERN-LINAC-4 injector, are representative examples of such facilities [2]. Dedicated reviews [2–5] address in detail the state-of-the-art of such negative ion sources. Nevertheless, ever since the late 1960’s, when controlled thermonuclear fusion emerged as a promising concept towards the realization of a sustainable, reliable and carbon-free source of energy, negative ion sources found a new field of application.

In the fusion reaction, energy is released when light nuclei fuse together and form a larger atom. This process powers the Sun and other stars, where hydrogen (H) nuclei fuse to create helium [6]. The plasma in the core of the Sun, attains a temperature of around 15 million °C. Mimicking this reaction on the Earth, on a laboratory scale, would require increasing the temperature by a factor of ten, to around 150 million °C. Among the possible reactions that could be considered, the deuterium-tritium (D-T) reaction is by far the most efficient one [7], [8] (Fig. 1.1(a)), during which deuterium and tritium nuclei fuse and release a helium nucleus, a neutron and 17.6 MeV of energy. Approximately 80% of the total energy released in the process is carried by the neutrons.

Fusion plasmas are harnessed in magnetic confinement devices, called tokamaks and stellarators. Currently, about 60 tokamaks and 10 stellarators are operational in laboratories involved in fusion studies worldwide [9]. Nevertheless, tokamaks have dominated over stellarators, as their design and construction is highly challenging and has yet to mature [9]. A significant milestone towards the realization of fusion energy is the commencement of the assembly of ITER (International Thermonuclear Experimental Reactor) early in 2021 in the south of France. This globe-spanning collaborative project, originally conceived in 1988 and expected to be operational by the year 2030, aims at the demonstration of the viability of a “burning plasma” (i.e. a self-sustained plasma) [10], all the while tackling significant physical and technological challenges. The return of experience from ITER will be exploited by a first-of-a-kind demonstration power plant (DEMO), whose main objective will be to prove the industrial feasibility of fusion by showing the

electricity production from the fusion reaction, the safety aspects and the Tritium self-sufficiency [10], [11].

Heating the plasma in tokamak devices up to the temperature required to achieve a self-sustained reaction is not a trivial task. Firstly, a toroidal current induced by the central transformer in the tokamak configuration ohmically heats the plasma. However, the resistivity of the plasma decreases inversely with temperature. So, as the ohmic current (and consequently the temperature) increases, the heating efficiency decreases [8]. Thus, it is imperative use auxiliary, external, methods of heating. The transmission, into the plasma, of electromagnetic radiation and the injection of highly energetic beams of neutral particles into the tokamak are the heating schemes that currently gain high research attention.

In focusing further on the concept of neutral beam injection (NBI), these beams of highly energetic neutrals can be produced either by positive or negative ions which are accelerated and consequently neutralized by passing through a gas neutralizer cell, by undergoing collisions with hydrogen molecules. However, as seen in **Fig. 1.1(a)**, the neutralization efficiency of positive ions declines rapidly after about 60 keV/nucleon, whereas the corresponding efficiency remains acceptably high (around 55%) for the negative ions even at energies above 100 keV/nucleon [12], [13]. For this reason, and despite the fact that their production is technologically challenging, negative hydrogen (deuterium) ions are the appropriate species for consideration in this application.

Historically, the development of negative ion sources began with double charge exchange sources. The complexity though associated with the design and integration of an accelerating stage in this type of sources, in due time led to their abandonment [14]. These were followed by surface conversion sources, i.e. sources in which negative ion production relies on the conversion of atomic

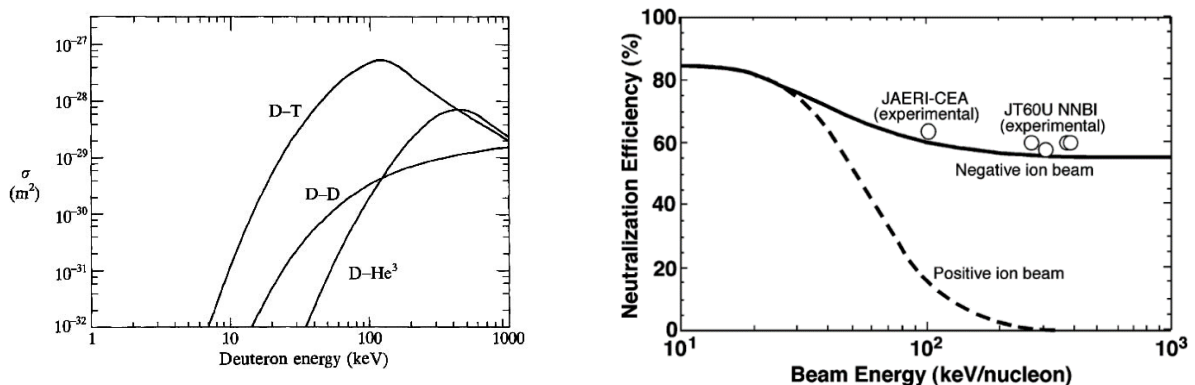


**Figure 1.1.** (a) Cross sections for different fusion reactions. The deuterium-tritium (D-T) reaction is compared to that of deuterium-deuterium (D-D) and deuterium-helium (D-He). The shown D-D cross section is the sum of two D-D possible reactions. Reprinted from [7] with the permission of Oxford Publishing Limited (License No. 92409); (b) Neutralization efficiency of positive and negative ion as a function of the beam energy. Since the beam energy is given in keV/nucleon, it applies to all the isotopes of hydrogen. Reprinted from [12] © 2005 IEEE.

or positive ionic species impinging on a surface of a low work function, termed as surface production. However, the observation, in 1977, by Nicolopoulou et al. [15], of an anomalously large concentration of negative ions in a hydrogen discharge, and its confirmation several years later by Bacal et al. [16], pointed to a new mechanism of negative ion production which was unknown at that time, that of volume production. This motivated, in the decades that followed, a great amount of experimental and theoretical works which aimed to gaining understanding on the underlying physics of both the surface and volume production mechanisms and to the development of negative ion sources based on those [17]. Concurrently, equally strong efforts are made for the development of appropriate plasma diagnostic techniques as an indispensable part of these investigations.

## 1.2 State-of-the-art ion sources for the ITER NBI

For the case of ITER, the heating and the current drive will rely on an injection of a total of 33 MW of 1MeV  $D^0$ . ITER's Neutral Beam (NB) cell will be equipped with four injectors: three Heating Neutral Beams (HNB) and a Diagnostic Neutral Beam (DNB) [18]. A cut-away conceptual view of a prototype injector and its key components is illustrated in **Fig. 1.2**. The ion source is at the heart of this device, which is expected to provide either a 1 MeV  $D^-$  or a 0.87 MeV  $H^-$  beam of an accelerated current density of  $200 \text{ A m}^{-2}$  or  $260 \text{ A m}^{-2}$  and an accelerated current of 40 A or 46 A, for a duration of 3600 s or 1000 s, respectively, operating in both cases at filling pressures of 0.3 Pa or less [13], [18], [19]. Operation in hydrogen is foreseen for the initial, non-nuclear phases of ITER [19].

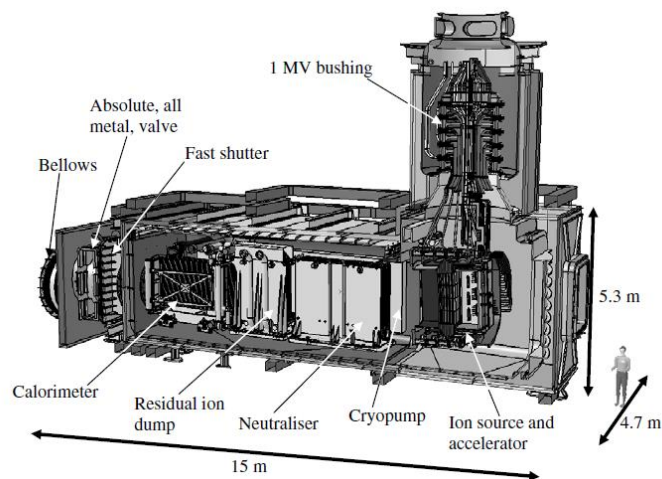


**Figure 1.2.** Conceptual cut-away view of the ITER type heating neutral beam injector. Reprinted from [13], published under an Open Access CC-BY license by IOP Publishing.

The only types of negative ion sources that have been deemed capable of meeting the aforementioned requirements for extracted negative ion current are the ceasiated arc or RF driven ones [13]. However, from those two, the RF source was finally chosen to be utilized in ITER's

injectors since it is filament free and thus there is no need for regular maintenance. This is in line with the concept for full remote handling during ITER's active phase [13], [18].

It was in 1996 that IPP-Garching (Germany) started investigating the applicability of RF-driven negative ion sources for the NBI of ITER. The experiments were started with a small prototype source with a base area of  $0.3 \text{ m}^2 \times 0.6 \text{ m}^2$  on the BATMAN (Bavarian Test Machine for Negative ions) and MANITU (Multi-Ampere Negative Ion Test Unit) test facilities [20]–[22]. **Fig. 1.3(a)** shows an illustration of the cross section of these prototype sources. In those, the plasma is generated in the cylindrical source volume, called the driver, by inductive coupling of the RF power by an external coil. The plasma then expands out of the driver into the main source chamber. Negative ions are formed mainly through the surface production process [14], [22], that is, via surface conversion of neutral atoms on the cesiated (Cs), low work function surface, of the first grid (Plasma Grid – PG) of a multigrid multiaperture extraction and acceleration system [23].

The main advantage of the driver concept is its modularity, which enables the extension to large sources by adding several drivers to one common expansion chamber [21]. **Fig. 1.3(b)** displays this concept as the prototype ion source for ITER, comprising eight driver modules, is reached. The half-ITER-size ion source of the ELISE (Extraction from a Large Ion SourcE) facility, also developed at the IPP–Garching, is an intermediate step towards the ITER NBI source that has been dedicated to experimentation since 2013 to identify and resolve issues of technical or physical nature that inhibit the fulfillment of the ITER requirements [24]. Up to date, ELISE has successfully demonstrated  $\text{H}^-$  pulses of 1000 s with a current density corresponding to 90% of the ITER goal [25]. On the other hand, the transition to deuterium has proven to be far more challenging as various complications stem from the inherent isotopic differences between hydrogen and deuterium. Some important issues are: the generally higher, inhomogeneous and less stable

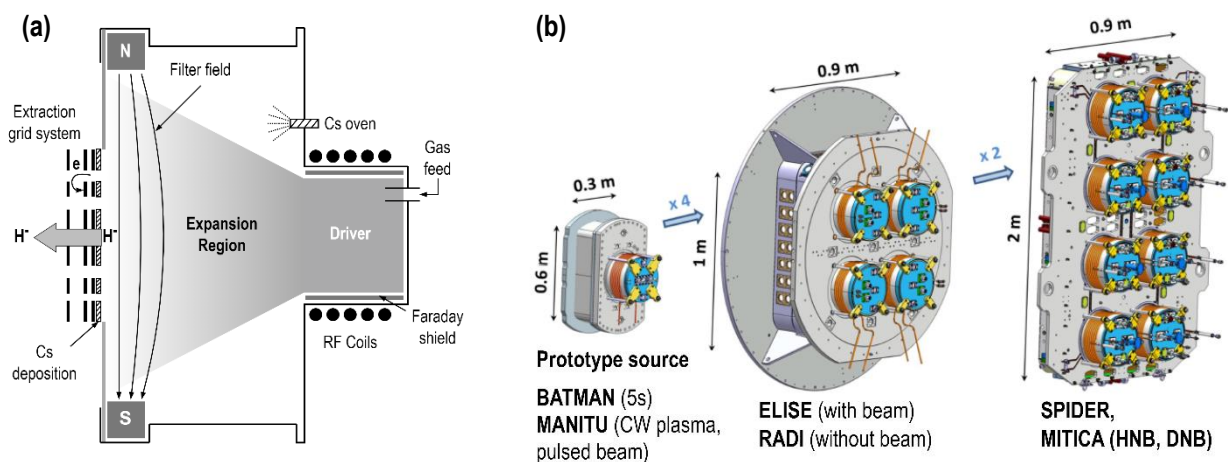


**Figure 1.3.** (a) Illustration of the cross section of the prototype source RF-driven source (Reproduced from [20], with the permission of AIP Publishing; License No. 5760110498278); (b) Modular concept of the RF source: from the prototype towards ion sources for ITER with ELISE as an intermediate step. Reprinted from [21], published under an Open Access CC-BY license by IOP Publishing.

co-extracted electron current, the significantly larger amount of Cs needed for stabilizing this current, and the Cs depletion from the reservoirs at the source walls and the PG due to the higher atomic mass of deuterium [23], [24]. Although considerable progress has been made after the application of refined Cs evaporation and distribution procedures, and though ITER requirements have nearly been reached for short  $D^-$  pulses, still only 66% of the ITER demand for negative ion current density can be extracted over a longer time span of 45 min [23], [24].

Knowledge gained from ELISE is exploited by the SPIDER (Source for Production of Ion of Deuterium Extracted from RF plasma) experiment, a full-scale injector set up at the Neutral Beam Test Facility (NBTF) at Consorzio RFX (Italy). Though only able to provide a 100 keV neutral beam, research there is focused on further optimization of the source performance, e.g. in terms of source uniformity (over a beam area of about  $1.5 \text{ m}^2$ ), negative ion current density, beam optics, beam source operation for 3600 s, and Cs distribution [25]. The operation of SPIDER began in 2018. In the span of three-years, operations in SPIDER included extensive characterization of both  $H_2$  and  $D_2$  plasmas, leading to the collection of a wealth of experimental information [26]. Insight into the source performance was provided and operational issues were detected. Some of the issues were solved or worked around during this run, while others triggered requirements for component re-design or modification and opportunities for improvements [26]. In 2021, SPIDER entered a long shut-down phase dedicated to incorporating the new learnings and resolving the arisen issues in view of extended beam operation and particularly of MITICA. MITICA (Megavolt ITER Injector & Concept Advancement) is the second test-bed at the NBTF. It is a complete full-scale prototype injector embodying all the ITER specifications, which is foreseen to exhibit the overall target performance. At the time of writing, MITICA has entered the final construction phase, with all of the auxiliary systems installed and with the final integrated test for the power supply underway [26]–[28].

### 1.3 Alternative negative ion source concepts

Although, currently only the prototype negative ion sources described in the previous section have been able to demonstrate the possibility of fulfilling the baseline requirements of a NBI system, substantial efforts are put into research for the development of alternative sources motivated by two principal aspects.

Firstly, there is a strong desire to eliminate the use of Cs on account of its several important drawbacks. Indicatively, not only could it be a source of failure in the accelerating stages of the injector, but regular maintenance is required for replenishing the Cs reservoirs. Therefore, volume production ion sources, which by definition do not rely on the injection of Cs for the production of negative ions attract much attention. In fact, recent advancements on this subject, both experimental and theoretical, are reviewed in [29].

Secondly, the design of high-power injectors with a very high wall-plug efficiency, i.e. the ratio of the neutral beam power coupled to the plasma core to the total electrical power consumed

by the beamline [30], over 60% is actively sought-after. Currently, for the injector configuration shown in Fig 1.2 this parameter is evaluated around 30%. This low value, results principally from the low rate of neutralization of the ion beam of about 55% which is imposed by the collisional neutralization with gas. Thus, research activities have also focused on investigating alternative concepts for improvement of the neutralizer efficiency, and consequently also on the development of compliant negative ion sources. Indeed, different beam neutralization concepts have been explored, among them the neutralization of the energetic negative ions by collisions with plasma electrons (plasma neutralizer) and by photodetachment (photoneutralization). If feasible, photoneutralization appears to be an ideal solution for achieving high performances, in the sense that it could offer a high beam neutralization rate ( $>80\%$ ) and a wall-plug efficiency of over 60% [31]. While the concept is attractive, there are nonetheless a number of significant technological problems that require resolution. The design of a novel photoneutralization-based neutral beam system has been proposed and extensively described by Simonin et al. [27– 29]. This new injector concept would require however the development of a negative ion source of a markedly different design with respect to the current prototypes. In particular, it would be necessary for the negative ion source to have a long and thin aspect ratio, delivering a negative ion beam comprising several thin (around 2 cm wide) laminar beamlets. This beam structure would ensure an adequate overlap with the laser beam used for the photodetachment of the negative ions. A volume production source, the Cybele source, constructed at the IRFM - CEA (Institute for Magnetic Fusion Research – Center of Atomic Energy) in Cadarache in France, was primarily conceived to demonstrate the feasibility of such a negative ion source. While initially the plasma in the Cybele source was sustained by an array of tungsten filaments, these were removed and an ICP (Inductively Coupled Plasma) driver equipped with a solenoid antenna at the extremity of the source was installed instead. In a later upgrade, the ICP driver was replaced by bird-cage helicon antenna. An identical helicon plasma generator was first utilized for the production and scrutiny of  $H_2$  and  $D_2$  plasmas in the experimental reactor RAID, installed at the EPFL in Switzerland. Among the three aforementioned plasma driving options at Cybele, the helicon driver was deemed the best candidate for the production of a dense and uniform plasma column [30], which complies with the requirements for a negative ion source for this novel injector concept. Nevertheless, a large amount of research is still necessary in order for this helicon plasma device to demonstrate the baseline requirements.

Overall, the interest and relevance of research on volume production negative ion sources is evidenced. At the same time, since operation with  $D_2$  cannot be predicted solely on the basis of simple isotope scaling with  $H_2$ , ultimately, the design of such sources benefits from studies devoted to approaching the isotopic effect from a fundamental point of view.

## 1.4 Comparative studies of negative ion sources operating with H<sub>2</sub> and D<sub>2</sub>

Despite the pertinence of the investigation of the isotope differences to the development of efficient negative ion sources, research activities, both in the past but also to this day, which focus on the development of laboratory-scale setups dedicated to the scrutiny, conducting a direct comparison, of H<sub>2</sub> and D<sub>2</sub> plasmas on a fundamental level are fairly limited. Even more so, if one refers to volume ion sources. In what follows, a concise overview of such characteristic comparative studies and of their main findings concerning the isotope differences, regardless of the type of source employed, is provided. Namely:

As regards filament-driven sources, Cs-free discharges of both gases have been examined in the sources “Camembert II” and “Camembert III” [33], [34]. The results indicate, briefly: (i) the electron density is consistently higher in D<sub>2</sub> with respect to H<sub>2</sub>, in both sources; (ii) the electron temperature shows no significant change between H<sub>2</sub> and D<sub>2</sub> discharges in the larger source, as opposed to the smaller source in which it is lower in the case of H<sub>2</sub>; (iii) the negative ion density and negative ion to electron density ratio is generally lower in D<sub>2</sub> than in H<sub>2</sub> in both sources, nevertheless these two parameters attain greater absolute values in the smaller source [34]. Observations (i) and (ii) have also been reported in the “Culham” source [35], [36]. Additionally, in this latter source, a higher plasma potential has been measured in D<sub>2</sub> while the fast electron density and temperature remain the same in both H<sub>2</sub> and D<sub>2</sub>. In another work in “Camembert II”, two-laser photo-detachment has been used to infer the H<sup>-</sup> and D<sup>-</sup> ion temperatures, with the latter being lower [37]. Pure volume production of H<sup>-</sup>/D<sup>-</sup> in a rectangular arc chamber, with an external pair of permanent magnets in front of the plasma grid serving as a magnetic filter, has been the subject of other works [35, 36]. Spatially resolved measurements with simultaneous variation of the magnetic filter field intensity revealed that the values for electron density and temperature were slightly higher in D<sub>2</sub> than in H<sub>2</sub>. Furthermore, a stronger magnetic filter field is required to control the electron temperature in the D<sub>2</sub> plasma. In other filament-driven sources the isotope scaling has been investigated based on measurements of the extracted beam properties [40], [41], along with probing of the characteristics of the plasma created in the vicinity of the extraction region [42], [43]; the bottom line in the findings is that the extracted D<sup>-</sup> ion current is constantly lower, accompanied by a larger co-extracted electron current. Moreover, the enhancing effects of Cs seeding on both H<sub>2</sub> and D<sub>2</sub> plasma properties, as opposed to Cs-free discharges, has been highlighted in studies at the “Camembert III” [44], “MANTIS” [45], and elsewhere [46]. In the filament driven “LIISA” ion source used at the “JYFL K130” cyclotron, the VUV emission spectra for both H<sub>2</sub> and D<sub>2</sub> have been compared. Neither the spectra nor the volumetric rates of ionization, excitation, production of high vibrational states, and dissociation between the two isotopes showed any significant difference. It is therefore suggested that in this source, the observed difference between the H<sup>-</sup> and D<sup>-</sup> production through dissociative electron attachment

(DEA) is attributed most likely to the difference in the diffusion properties of hydrogen and deuterium [47].

As for inductively coupled plasma setups other than the prototype ones described in the previous section, work [48] deals with the cases of  $\text{H}_2$  and  $\text{D}_2$  and shows that the atomic density is higher in  $\text{D}_2$ . Furthermore, atoms were found to be more efficiently ionized than the respective molecules, leading thus to a significantly elevated electron density in  $\text{D}_2$  compared to  $\text{H}_2$  and, consecutively, to a higher RF power transfer efficiency. Another setup, named “ACCesS”, has been employed in experiments relevant to surface production of negative ions [49]. It was concluded that, no significant isotope effect occurs regarding the surface negative ion formation. The reader is also referred to reports [50], [51] for further studies concerning a comparison between surface production of  $\text{H}^-$  and  $\text{D}^-$ .

$\text{H}_2$  and  $\text{D}_2$  discharges in RF-driven sources of a different type, i.e., helicons, have been studied in reference [52] as well as at the “RAID” source [53], [54]. In [52] the density ratio of atomic to molecular deuterium was found to be higher than the respective ratio for hydrogen. In [53] the degree of dissociation and the ion densities were higher for deuterium than for hydrogen. In [54], the electron density was higher in the case of  $\text{D}_2$ , the electron temperature appeared to be nearly the same for  $\text{H}_2$  and  $\text{D}_2$ , and the negative ion density and the negative ion to electron density ratio was lower in  $\text{D}_2$ .

Additionally, an ECR source with driven plasma rings has been studied in terms of extracted  $\text{H}^-$  and  $\text{D}^-$  ion current as a function of the pressure, the power, and the immersion depth of the plasma electrode into the plasma volume [55]. The  $\text{D}^-$  current was found to be less. Dissociative attachment of electrons to molecules at high Rydberg excited states was identified as the most probable process for  $\text{H}^-$  and  $\text{D}^-$  formation. Another ECR source, but of a tandem configuration, named “HOMER”, has been studied for the case of  $\text{H}_2$  [56], [57]. In this source, the efficiency of materials with a low work function on the surface production of negative ions has also been investigated [58], [59]. Particularly for the material MoLa,  $\text{D}_2$  was also tested and while varying the isotope had an influence on the plasma parameters, the resulting effects on the negative ion formation compensated each other leading to comparable negative ion densities [58].

On the other hand, there is an alternative concept for ECR heating of  $\text{H}_2$  and  $\text{D}_2$  plasmas, based on the use of elementary dipolar ECR modules [60]. Negative ion sources reporting the use of this kind of ECR modules are “Camembert III” [61]–[65], “ROSAE III” [65], [66], “SCHEME” [67], [68], and “Prometheus I” [17], [69]–[71]. “Camembert III” and “ROSAE III” have been operated and characterized in hydrogen only. “SCHEME”, however, has been employed in experimental campaigns (i.e. synchrotron-based VUV absorption spectroscopy) involving both  $\text{H}_2$  [67] and  $\text{D}_2$  [68]. **Table 1.1** summarizes the available data for the ECR sources of different configurations, quoted above.

**Table 1.1.** Tabulated data of the characteristic parameters of the ECR sources quoted in text. (Ext.: Extraction aperture; NI: No information; NA: Not applicable)

ECR source	Dimensions	ECR Coupling	Power (kW)	Pressure (Pa)	Gas	Ext.	Te (eV)	$n_{e(\text{cold})}$ ( $\text{m}^{-3}$ )	$n_{\text{H}^-}$ ( $\text{m}^{-3}$ )	Extr. Current (mA)
ECR source with driven plasma rings	Aluminum; $\text{\O}130 \text{ mm} \times 80 \text{ mm}$	External magnetic discs; 2.45 GHz	max. 0.25	0.02 – 0.07	$\text{H}_2$ / $\text{D}_2$	✓	50 – 60	$5 \times 10^{16}$ (0.026 Pa; $\text{H}_2$ [72]).	NI	$\leq 4.7$ ( $\text{H}_2$ ) $\leq 3.1$ ( $\text{D}_2$ ) (0.2 kW)
HOMER	Stainless steel; $\text{\O}150 \text{ mm} \times 310 \text{ mm}$ (prolonged to 410 mm in [57])	Helmholtz coils; 2.45 GHz	max. 1 (For experiments : 0.2–0.5 [56])	0.3 – 3 [58–60]	$\text{H}_2$ / $\text{D}_2$	✗	0.6 – 1; NI	$10^{16} - 10^{17}$	$\leq 3.9 \times 10^{15}$ ( $\text{H}_2$ ) [56] Above MoLa (0.3 kW, 0.3 Pa) [58]: $\leq 1.4 \times 10^{15}$ ( $\text{H}_2$ ), $\leq 1.45 \times 10^{15}$ ( $\text{D}_2$ )	NA
Camembert III	Stainless steel; $\text{\O}440 \text{ mm} \times 450 \text{ mm}$	7 ECR modules & multicusp field configuration; 2.45 GHz	max. 1.2 (for experiments : 0.5 & 1 [61], 0.9 [63], 1.05 [62])	0.13 – 1.07 [58–60]	$\text{H}_2$	✓	Within 0.2 – 1.3	In the range of $10^{14} - 10^{16}$	$\leq 2.6 \times 10^{15}$	$\leq 0.25$ (0.9 kW [63] and 1 kW [61], 0.27 Pa)
ROSAE III	Pyrex cylinder of $\text{\O}152 \text{ mm} \times 214 \text{ mm}$ housed in a stainless steel cylinder Quartz cylinder $\text{\O}152 \text{ mm}$ housed in a stainless steel cylinder [66]	4 ECR modules; 2.45 GHz Modified: 1 ECR module; 2.45 GHz	max. 1.2 (For experiments : 0.76 or 0.2 [65] & 1 [17]) max. 0.2 (for experiments : 0.075 – 0.175)	0.33 or 1.3 [65] 0.67 [17] 0.8 or 1.6	$\text{H}_2$	✗	0.9; 11 or 2; 6 1.81; 9.45	$0.13 \times 10^{16}$ or $1.4 \times 10^{16}$ $\sim 6.5 \times 10^{15}$ (Pyrex)	$0.06 \times 10^{15}$ or $1.7 \times 10^{15}$ $\sim 1.5 \times 10^{14}$ (Pyrex)	NA With quartz coverage: $\leq 3 \times 10^{13}$ or $\leq 5 \times 10^{13}$
SCHEME-II+	Stainless steel; outer dim.: $\text{\O}160 \text{ mm}$ ; inner dim. $\text{\O}124 \text{ mm} \times 220 \text{ mm}$ (quartz tube) [68]	1 ECR module; 2.45 GHz	max. 0.45 (for experiments : 0.15) [68]	0.8 [68]	$\text{H}_2$ / $\text{D}_2$	✗	$\sim 1.5$ ; $\sim 15$	$\sim 10^{15}$	$\sim 10^{13}$ (quartz coverage – $\text{D}_2$ )	NA
PROMETHEUS I	Stainless steel; $240 \times 240 \times 240 \text{ mm}^3$	5 ECR modules; 2.45 GHz	max. 0.9	0.13 – 2.67	$\text{H}_2$ / $\text{D}_2$	✗	0.5 – 2; 12.5 – 17	$\leq 4.5 \times 10^{16}$ ( $\text{H}_2$ ); $\leq 7 \times 10^{16}$ ( $\text{D}_2$ ).	$\leq 6 \times 10^{15}$	NA

## 1.5 Negative ion production and destruction mechanisms

Throughout the previous sections, the terms surface and volume production have been used to signify the two principle pathways for negative ion production. In this section it is deemed necessary to elaborate further on these processes by present the most important theoretical aspects, all the while, to a greater extent on volume production since it is of most interest in the present study. Moreover, as this work implies the study of both H<sub>2</sub> and D<sub>2</sub> plasmas, this section begins by recalling few characteristic properties of the two molecules.

The potential energy diagrams for the singlet and triplet system of the hydrogen molecule are presented in **Figs. 1.4(a)** and **(b)**, respectively. The electronic potential energy curves are supposed to be identical for H<sub>2</sub> and D<sub>2</sub> [73]. However, the vibrational and rotational structures of H<sub>2</sub> and D<sub>2</sub> are different because of the difference between their nuclear masses. Generally, the heavier isotope, D<sub>2</sub>, supports more bound vibrational levels. The number of the bound vibrational levels in the ground state, X<sup>1</sup>Σ<sub>g</sub><sup>+</sup>, and the first electronically excited state, B<sup>1</sup>Σ<sub>u</sub><sup>+</sup>, are provided in **Table 1.2**, along with several characteristic molecular constants of the H<sub>2</sub> and D<sub>2</sub> molecules.

Principally, phenomena in the discharge which can be influenced by the nuclear mass difference between H<sub>2</sub> and D<sub>2</sub> can be divided into two categories [36]. Firstly, there exist transport

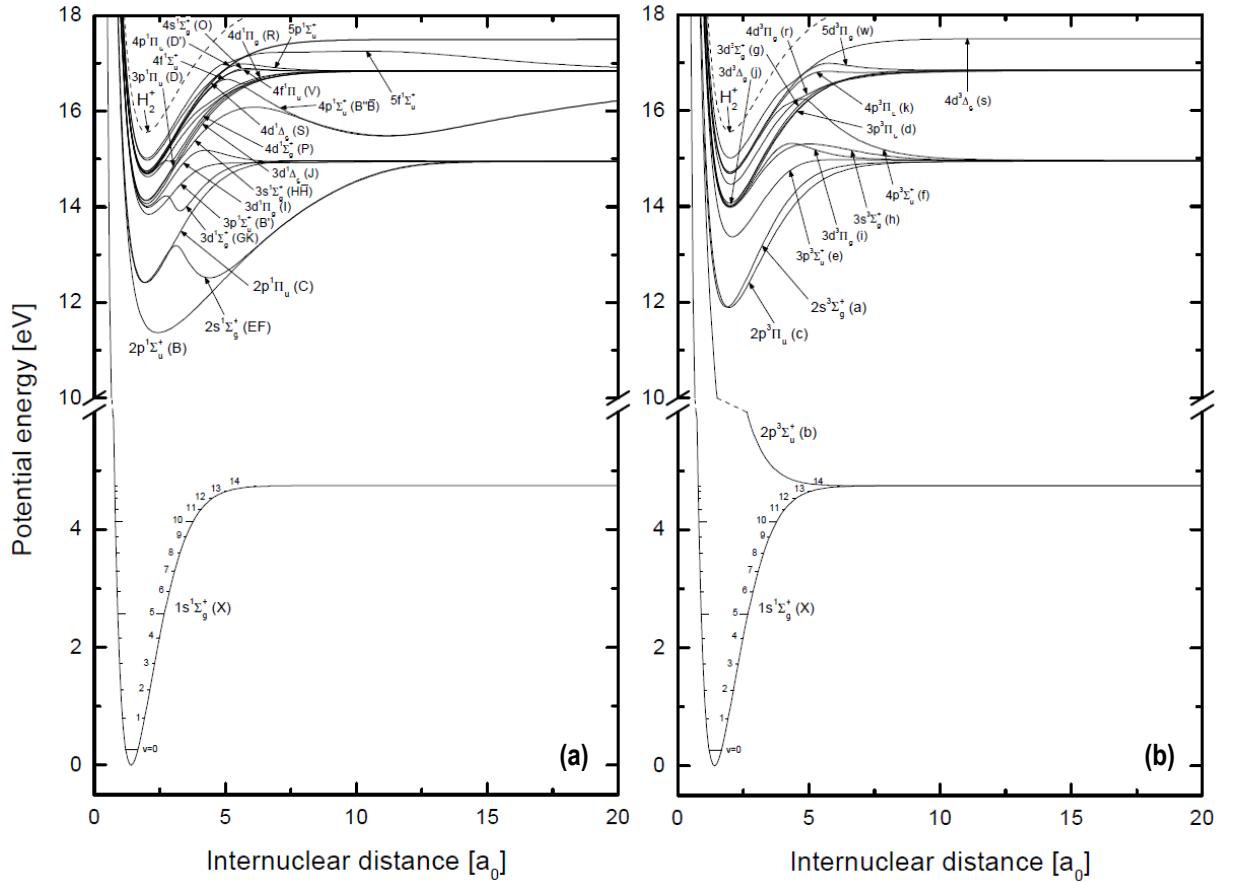


**Figure 1.5.** Potential energy diagrams of (a) the singlet system and (b) the triplet system of molecular hydrogen. Reprinted from [86].

effects, owing to the reduced mobility of the deuterium molecules, atoms, and ions, and secondly, molecular effects, due to the different vibrational and rotational structure of  $\text{H}_2$  and  $\text{D}_2$ . The latter differences in the vibrational and rotational distributions in the discharges, can in turn influence various reactions affecting thus the overall plasma chemistry of a given source.

**Table 1.2.** Molecular constants of  $\text{H}_2$  and  $\text{D}_2$  molecules [73], [74].

Molecule	$\text{H}_2$	$\text{D}_2$
Reduced mass ( $\mu$ )	0.504	1.007
Equilibrium internuclear distance ( $\text{\AA}$ )	0.7414	0.7415
Ionization potential (eV)	15.4259	15.467
Vibrational frequency ( $\text{cm}^{-1}$ )	4401.21	3115.5
Vibrational energy (eV)	0.54568	0.38628
Dissociation energy (eV)	4.478	4.556
Bound vibrational levels of the $1s^1\Sigma_g^+(X)$ electronic state	15	22
Bound vibrational levels of the $2p^1\Sigma_u^+(B)$ electronic state	40	57

### 1.5.1 Surface production

Negative ion production on surfaces comes about principally from two fundamental processes: particle reflection and ion-induced desorption of hydrogen (deuterium) atoms adsorbed onto the surface [75]. The different reactions that can take place, involving molecular ions and atomic species, are illustrated in **Fig. 1.5**. Other processes involving electrons and photons may also occur but their contribution to the total negative ion yield is expected to be little. Thus, these reactions are not represented on the schematic. However, it is worth noting that in both of the former processes, the kinetic energy of the incoming ions affects the resulting outgoing flux of  $\text{H}^-$  ions produced on the surface. Additionally, the energy of the outgoing negative ions is influenced

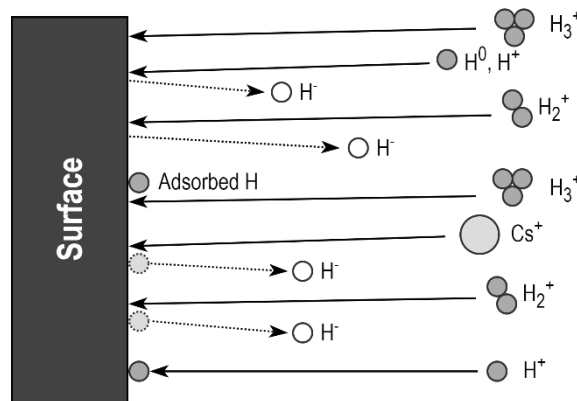


**Figure 1.5.** Schematic illustration of the different processes leading to negative ion formation via the surface production mechanism. In an ion source, atomic and molecular hydrogen (deuterium) ions as well as  $\text{Cs}^+$  ions impinge on the surface to create  $\text{H}^-$  ( $\text{D}^-$ ) ions by backscattering and ion-stimulated desorption processes. While only the hydrogen case is illustrated for clarity, the same reactions can occur in deuterium as well. Redrawn from [75] with permission from Springer Nature (License No. 5760230070960).

by the properties of the surface itself, which is commonly the first electrode of the extraction system in an ion source. In other words, the conditions of the electrode like the surface layer composition, the roughness, the adsorbate structure and thickness may all have a determining effect. Lastly, the production of negative ions on the surface can be increased when the work-function of the surface, i.e. the electrode, is lowered. Hence the common tactic to have Cs deposited on the electrode surface, which to this day and despite the numerous studies on other materials (indicatively in [58], [59], [76]) remains the element with the lowest work-function and the most effective one. For further details on the theory underlying these surface processes and for an extensive overview of the historical development of surface negative ions sources, the reader is referred to Chapters 2 and 14 of [75] and the references therein.

### 1.5.2 Volume production

A variety of processes that can lead to negative ion production are presented in **Table 1.3**. Among those probable, it is generally accepted that the predominant path for the  $\text{H}^-$  and  $\text{D}^-$  volume production is the Dissociative Electron Attachment (DEA reaction; Reactions R1 and R2), i.e. the attachment of a low-energy electron to a highly ro-vibrationally excited molecule. This process implies thus the necessity of promoting vibrational excitation of the gas, all the while ensuring the presence of low-energy electrons.

Cross sections for the DEA reaction for  $\text{H}_2$  and  $\text{D}_2$  are displayed in **Fig. 1.6**. The dependence upon the vibrational quantum level,  $v$ , and the rotational quantum level (within the first vibrational level  $v'' = 0$ ),  $J$ , of the molecular ground state correspond to insets (a) and (c), and (b) and (d), for  $\text{H}_2$  and  $\text{D}_2$  respectively. In both  $\text{H}_2$  and  $\text{D}_2$  plasmas, the cross section of the DEA reaction highly increases as the vibrational level increases and, simultaneously, the threshold electron energy for which the cross section peaks shifts to lower values. This strong enhancement of the attachment cross section on increasing the internal vibrational energy of the molecule is attributed to an increase in the range of internuclear separations over which the capture of the electron can occur. This increase occurs because of the larger amplitude of vibration for a vibrationally excited molecule [77]. Yet, the DEA cross section is larger in the case of  $\text{H}_2$ , of about two orders of magnitude for the low-lying vibrational levels but approach with those of  $\text{D}_2$  with increasing vibrational quantum number. At the same time, the reaction electron energy threshold shifts to higher values for a  $\text{D}_2$  plasma, for the levels with the same vibrational quantum number. Indicatively, near the threshold of two extreme vibrational levels, i.e.  $v'' = 0$  and  $v'' = 9$ , the following hold true for  $\text{H}_2$  vs.  $\text{D}_2$  respectively:  $1.6 \times 10^{-25} \text{ m}^2$  (3.73 eV) vs.  $3.0 \times 10^{-28} \text{ m}^2$  (3.83 eV) and  $4.8 \times 10^{-20} \text{ m}^2$  (0.13 eV) vs.  $2.3 \times 10^{-20} \text{ m}^2$  (1 eV). Rotational excitation exhibits an analogous effect. Centrifugal stretching in excited rotational levels results in a large increase of the DEA cross section from the initial rotational level to the higher ones [78], [79]. Moreover, a notable isotope effect is discerned between  $\text{H}_2$  and  $\text{D}_2$ . More specifically, the attachment cross section

increases by three orders of magnitude from the rotational level  $J'' = 0$  to  $J'' = 20$ , i.e. from  $1.6 \times 10^{-25} \text{ m}^2$  to  $5.5 \times 10^{-22} \text{ m}^2$ , and from  $3.0 \times 10^{-28} \text{ m}^2$  to  $2.5 \times 10^{-25} \text{ m}^2$ , for  $\text{H}_2$  and  $\text{D}_2$  respectively.

**Table 1.3.** Reaction set for the production and destruction of negative ions (\*RX denotes: by analogy with reaction X).

PRODUCTION			
R1.	$e + \text{H}_2\{X^1\Sigma_g^+(v,J)\} \rightarrow \text{H}_2^- \rightarrow \text{H} + \text{H}^-$	Dissociative Electron Attachment: DEA	[79], [80]
R2.	$e + \text{D}_2\{X^1\Sigma_g^+(v,J)\} \rightarrow \text{D}_2^- \rightarrow \text{D} + \text{D}^-$		
R3.	$e + \text{H}_2^+ \rightarrow \text{H}^+ + \text{H}^-$	Dissociative Recombination: DR	[81], [82]
R4.	$e + \text{D}_2^+ \rightarrow \text{D}^+ + \text{D}^-$		
R5.	$e + \text{H}_3^+ \rightarrow \text{H}_2^+ + \text{H}^-$	Dissociative Recombination: DR	[81]
R6.	$e + \text{D}_3^+ \rightarrow \text{D}_2^+ + \text{D}^-$		
R7.	$e + \text{H}_2(v,J) \rightarrow \text{H}^- + \text{H}^+ + e$	Polar Dissociation	[81]
R8.	$e + \text{D}_2(v,J) \rightarrow \text{D}^- + \text{D}^+ + e$		
R9.	$\text{H}_2 + \text{H}_2^+ \rightarrow \text{H}^- + \text{H} + 2\text{H}^+$	Ion-Molecule Collisions	[*R11]
R10.	$\text{H}_2 + \text{H}_2^+ \rightarrow \text{H}^- + \text{H}^+ + \text{H}_2^+$		[*R12]
R11.	$\text{D}_2 + \text{D}_2^+ \rightarrow \text{D}^- + \text{D} + 2\text{D}^+$		[81]
R12.	$\text{D}_2 + \text{D}_2^+ \rightarrow \text{D}^- + \text{D}^+ + \text{D}_2^+$		[81]
DESTRUCTION			
R13.	$\text{H}^- + \text{H} \rightarrow \text{H}_2 + e$	Associative Detachment: AD	[84]
R14.	$\text{D}^- + \text{D} \rightarrow \text{D}_2 + e$		
R15.	$\text{H}^- + \text{H} \rightarrow \text{H}_2(v) + e$	Associative Detachment (AD) with creation of vibrationally excited molecules	[85]
R16.	$\text{D}^- + \text{D} \rightarrow \text{D}_2(v) + e$		[*R15]
R17.	$\text{H}^- + \text{H} \rightarrow 2\text{H} + e$	non-Associative Detachment: non-AD	[86]
R18.	$\text{D}^- + \text{D} \rightarrow 2\text{D} + e$		[81]
R19.	$\text{H}^- + e \rightarrow \text{H} + 2e$	Electron Detachment: ED	[86]
R20.	$\text{D}^- + e \rightarrow \text{D} + 2e$		[81]
R21.	$\text{H}^- + \text{H}_2(v) \rightarrow \text{H}_2(v-2) + \text{H} + e, 2 \leq v \leq 6$	Electron Detachment in collisions with vibrationally excited molecules: EDV	[87], [88]
R22.	$\text{D}^- + \text{D}_2(v) \rightarrow \text{D}_2(v-2) + \text{D} + e, 2 \leq v \leq 6$		[*R21]
R23.	$\text{H}^- + \text{H}_2 \rightarrow \text{H}_2 + \text{H} + e$	Collisional Detachment: CD	[89]
R24.	$\text{D}^- + \text{D}_2 \rightarrow \text{D}_2 + \text{D} + e$		
R25.	$\text{H}^- + \text{H}^+ \rightarrow 2\text{H}$	[87], [90]	
R26.	$\text{H}^- + \text{H}^+ \rightarrow \text{H} + \text{H}(n=2, 3)$	[87], [91]	
R27.	$\text{H}^- + \text{H}_2^+ \rightarrow \text{H}_2 + \text{H}$	[87], [91]	
R28.	$\text{H}^- + \text{H}_2^+ \rightarrow 3\text{H}$	[87], [90]	
R29.	$\text{H}^- + \text{H}_2^+ \rightarrow \text{H} + \text{H}_2(v)$	[85]	
R30.	$\text{H}^- + \text{H}_3^+ \rightarrow 2\text{H}_2$	[87], [91]	
R31.	$\text{H}^- + \text{H}_3^+ \rightarrow 4\text{H}$	[87], [90]	
R32.	$\text{H}^- + \text{H}_3^+ \rightarrow 2\text{H} + \text{H}_2(v)$	[85]	
R33.	$\text{D}^- + \text{D}^+ \rightarrow 2\text{D}$	Mutual Neutralization: MN	[*R25]
R34.	$\text{D}^- + \text{D}^+ \rightarrow \text{D} + \text{D}(n=2, 3)$		[*R26]
R35.	$\text{D}^- + \text{D}_2^+ \rightarrow \text{D}_2 + \text{D}$		[*R27]
R36.	$\text{D}^- + \text{D}_2^+ \rightarrow 3\text{D}$		[*R28]
R37.	$\text{D}^- + \text{D}_2^+ \rightarrow \text{D} + \text{D}_2(v)$		[*R29]
R38.	$\text{D}^- + \text{D}_3^+ \rightarrow 2\text{D}_2$		[*R30]
R39.	$\text{D}^- + \text{D}_3^+ \rightarrow 4\text{D}$		[*R31]
R40.	$\text{D}^- + \text{D}_3^+ \rightarrow 2\text{D} + \text{D}_2(v)$		[*R32]

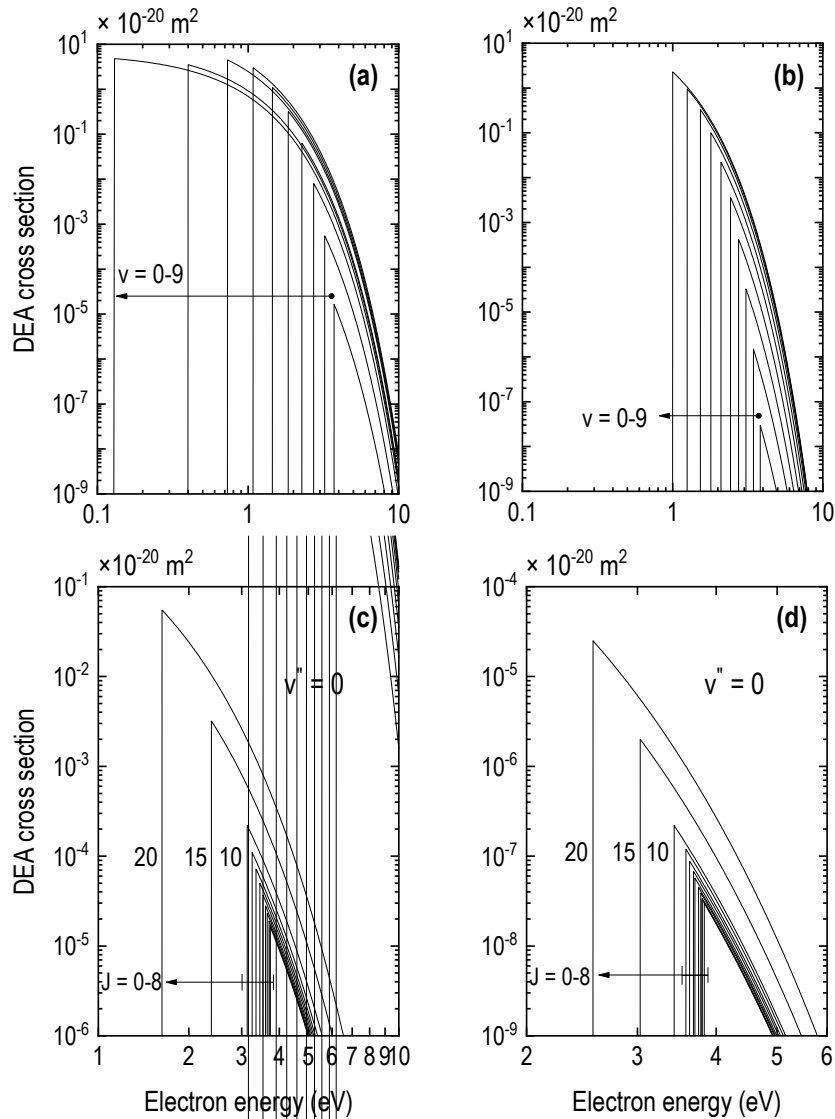


**Figure 1.6.** Cross sections of reactions (a) and (c) R1/Table 1.3 ( $\text{H}_2$  case), and (b) and (d) R2/Table 1.3 ( $\text{D}_2$  case). (a) and (b) show the dependence on the vibrational level ( $v$ ), while (b) and (c) that for the rotational levels ( $J$ ) of the ground vibrational level. The curves are drawn according to Equation 4.12 given in [80], with the use of the available data in Table 1 in [79].

With regard to the molecular precursors of the DEA reaction, they can be efficiently formed through two main channels: (i) in the plasma volume, principally via the reaction of electron excitation and radiative decay (EV reaction; reactions R43 and R44 in **Table 1.4**), and (ii) on the surfaces that face the plasma, as products of recombinative processes (reactions R45 to R50 in **Table 1.4**). Accordingly, on the basis of the two channels for vibrational excitation, volume production can be split into two sub-categories: pure volume production and surface-assisted volume production. The latter will be discussed in more depth in the following section (section 1.5.3).

With regard to the first channel, the vibrational excitation of the  $\text{H}_2$  ( $\text{D}_2$ ) molecule, by high-energy electron impact, proceeds mainly through the singlet electronically excited  $\text{B}^1\Sigma_u^+$  and  $\text{C}^1\Pi_u$  states, followed by the spontaneous (radiative) decay back to the ground state [14], [92].

**Table 1.4.** Representative reactions for the population and de-excitation of vibrational states.

<b>EXCITATION</b>			
R41.	$\text{H}_2\{\text{X}^1\Sigma_g^+(v_i, J)\} + e \rightarrow \text{H}_2\{\text{X}^1\Sigma_g^+(v_f, J)\} + e, v_f > v_i$	Resonant electron-vibration excitation: eV	[93]
R42.	$\text{D}_2\{\text{X}^1\Sigma_g^+(v_i, J)\} + e \rightarrow \text{D}_2\{\text{X}^1\Sigma_g^+(v_f, J)\} + e, v_f > v_i$		
R43.	$\text{H}_2\{\text{X}^1\Sigma_g^+(v_i, J)\} + e \rightarrow \text{H}_2\{\text{B}^1\Sigma_u^+, \text{C}^1\Pi_u\} + e \rightarrow$ $\text{H}_2\{\text{X}^1\Sigma_g^+(v_f, J)\} + e + h\nu, v_f > v_i$	Radiative decay and excitation: EV	[80]
R44.	$\text{D}_2\{\text{X}^1\Sigma_g^+(v_i, J)\} + e \rightarrow \text{D}_2\{\text{B}^1\Sigma_u^+, \text{C}^1\Pi_u\} + e \rightarrow$ $\text{D}_2\{\text{X}^1\Sigma_g^+(v_f, J)\} + e + h\nu, v_f > v_i$		
Recombinative Desorption:			
R45.	$\text{H}(\text{wall}) + \text{H}(\text{wall}) \rightarrow \text{H}_2(\text{v})$	Langmuir–Hinshelwood	[94]
R46.	$\text{D}(\text{wall}) + \text{D}(\text{wall}) \rightarrow \text{D}_2(\text{v})$		
R47.	$\text{H}(\text{gas}) + \text{H}(\text{wall}) \rightarrow \text{H}_2(\text{v})$	Eley–Rideal	[95]
R48.	$\text{D}(\text{gas}) + \text{D}(\text{wall}) \rightarrow \text{D}_2(\text{v})$		
R49.	$\text{H}(\text{wall}^*) + \text{H}(\text{wall}) \rightarrow \text{H}_2(\text{v})$	‘Hot-atom’ (Harris–Kasemo)	[96]
R50.	$\text{D}(\text{wall}^*) + \text{D}(\text{wall}) \rightarrow \text{D}_2(\text{v})$		
<i>Where, H/D(wall*), refers to a “weakly bound” atom on the surface</i>			
<b>DE-EXCITATION</b>			
R51.	$\text{H}_2(v_i) + \text{H} \rightarrow \text{H}_2(v_f) + \text{H}, v_f < v_i$	Vibrational-translational relaxation in collisions with atoms: V-t	[87], [97] [33]
R52.	$\text{D}_2(v_i) + \text{D} \rightarrow \text{D}_2(v_f) + \text{D}, v_f < v_i$		
R53.	$\text{H}_2(v_i) + \text{H}_2(v_j) \rightarrow \text{H}_2(v_i) + \text{H}_2(v_j-1)$	Vibrational-translational relaxation in collisions with molecules: V-T	[91] [33]
R54.	$\text{D}_2(v_i) + \text{D}_2(v_j) \rightarrow \text{D}_2(v_i) + \text{D}_2(v_j-1)$		
R55.	$\text{H}_2(v_i) + \text{wall} \rightarrow \text{H}_2(v_f), v_f < v_i$	Wall relaxation: WD	[87], [98] [33]
R56.	$\text{D}_2(v_i) + \text{wall} \rightarrow \text{D}_2(v_f), v_f < v_i$		

In **Figs. 1.7(a)** and **(b)** a selection of cross section data for the EV reaction for both  $\text{H}_2$  and  $\text{D}_2$ , is reproduced from [80]. The presented cross sections are resolved with respect to the final vibrational level,  $v_f$ , in which the molecule lies, while the initial one is the ground level, i.e.  $v_i = v'' = 0$ . Additional cross section data resolved with respect to  $v_i$ , are included in [80]. It is seen that, for both  $\text{H}_2$  and  $\text{D}_2$ , the cross section decreases with increasing  $v_f$ . In **Fig 1.7(c)**, the cross section value for a fixed electron energy near the peak of the curves (40 eV) is plotted against  $v_f$ , for both isotopes. While the cross section is consistently lower for the case of  $\text{D}_2$ , a converging trend between the resulting curves is evident beyond around  $v_f = 7$ . Furthermore, as it is recalled that the  $\text{D}_2$  molecule supports more bound vibrational levels, a summation of the cross section values over all the available vibrational levels finally demonstrates only a small isotope effect. This is exhibited by the star points set on the same figure, their value divided however by a factor of 10 to enable visibility on the same axis scale.

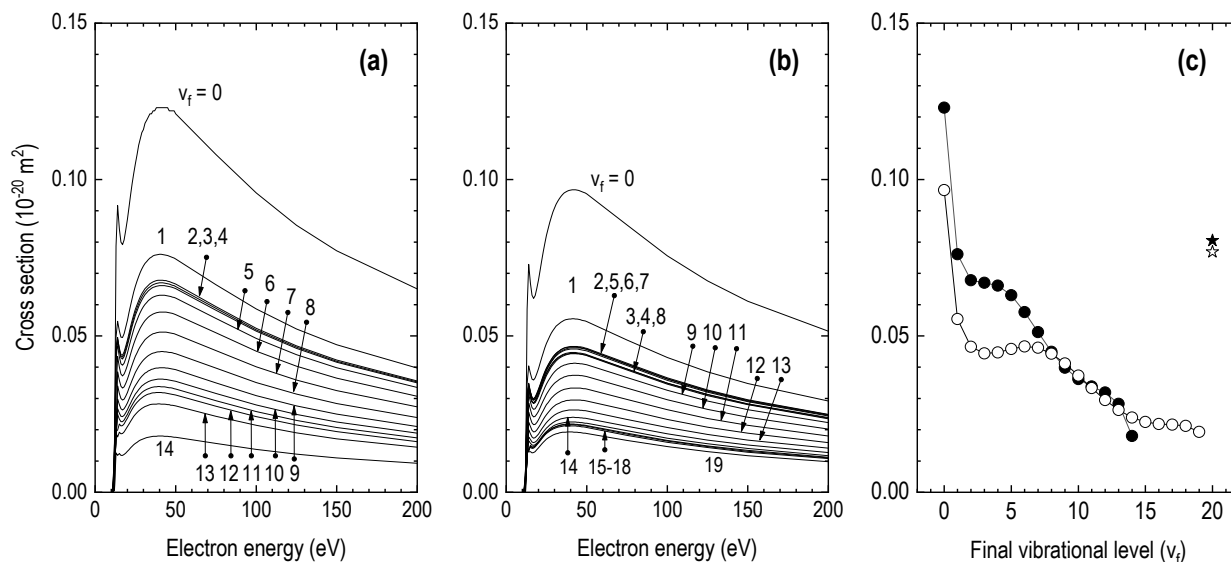


**Figure 1.7.** Cross sections of the reactions (a) R43 ( $\text{H}_2$ ) and (b) R44 ( $\text{D}_2$ ), in Table 1.3. The initial vibrational level is  $v_i = 0$ . (c) Comparison of the cross section values of  $\text{H}_2$  (solid circles) and  $\text{D}_2$  (open circles) for increasing vibrational level, at an electron energy of 40 eV where the curves peak. The star points correspond to the sum of the cross section value over all of the bound vibrational levels. Graphs (a), (b) are redrawn from the data collected from [80] with permission from Elsevier (License No. 5760260555442).

### 1.5.3 Surface-assisted volume production

It is well known that atomic species may interact varyingly with the surfaces surrounding the plasma. Firstly, when an atom impinges a surface, it will gain energy due to the interaction of the unbound electron and the surface which forms a chemical bond. Typically, the energy gained is about 2.4 eV for  $\text{H}_2$  and metallic surfaces [99]. **Fig. 1.8** illustrates the three types of reactions that these adsorbed atoms can undergo which subsequently release a ro-vibrationally excited molecule. The Langmuir-Hinshelwood [94] reaction refers to the recombination of two already adsorbed atoms on the surface releasing a molecule. The H-H bond energy is approximately 4.5 eV, making this process endothermic by 0.3 eV, with the energy supplied by the surface [99]. In Eley-Rideal [95] recombination, an atom from the gas phase impinges on the surface and reacts with an already adsorbed one to create a molecule. This process is exothermic by approximately 2 eV, as only one atom is adsorbed onto the surface during the recombination process [99]. Lastly, the “Hot-atom” reaction, first proposed by Harris and Kasemo [96], considers a “weakly bound” atom to the surface able to diffuse across it until it reaches an adsorbed atom to recombine into a molecule. As in the case of the Eley-Rideal reaction, the “Hot-atom” reaction is also exothermic, with the excess energy being distributed into various degrees of freedom, including vibrational energy levels [99]. The energetics of the surface processes and, as a consequence, the vibrational distribution of the  $\text{H}_2$  ( $\text{D}_2$ ) molecules formed in the recombination reaction critically depend on different parameters, including the nature of the bond between the adsorbed atom and surface, the impact energy of the gas-phase atoms and the surface temperature [93]. While there is a

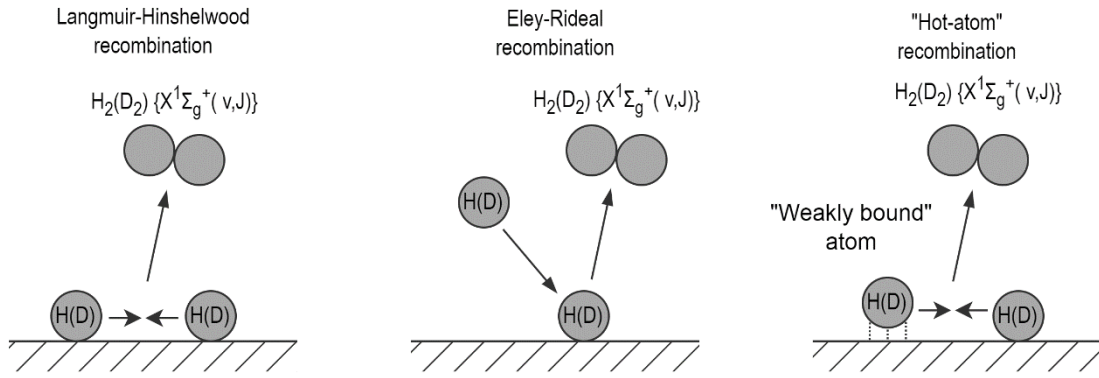


**Figure 1.8.** Representation of the three types of recombinative desorption reactions (R45 – R50 in **Table 1.3**). From left to right: (a) The Langmuir-Hinshelwood recombination: two atoms adsorbed on the surface recombine and release a molecule; (b) Eley-Rideal recombination: an atom from the gas phase impinging on the surface recombines with an adsorbed to create a molecule; (c) “Hot-atom” recombination: a “weakly bound” atom to the surface diffuses across it and reacts with an already adsorbed one to produce a molecule. The illustration is reproduced from [99] with permission from IOP Publishing (License No. 146800-2).

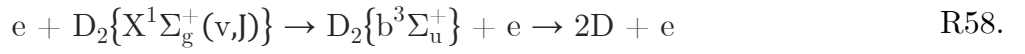
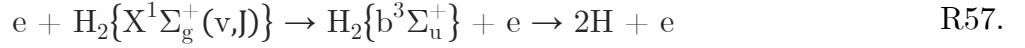
considerable amount of studies that investigate these reactions for different plasma-facing materials [93], [99]–[106], merely a few [94], [107]–[109] actually report on their effect to the vibrational distribution function (VDF). Hence the motivation behind Chapter 4 of the present thesis, which deals with the derivation of the VDFs in conditions where different materials face the plasma. Finally, it is worth noting that in the field of fusion studies, besides the application towards negative ion sources, the interest in the influence of plasma-surface interactions on the vibrational excitation attracts great attention for the molecular assisted recombination (MAR) mechanisms relevant to research on divertor plasma kinetics [110]–[112].

### 1.5.4 Destruction mechanisms

The ultimate yield of negative ions is dictated by a delicate interplay between the reactions that lead to their formation and, simultaneously, those responsible for their destruction. In principle, the latter competing mechanisms can be further classified as either *direct*, or *indirect*. The term *direct* is used to signify destructive reactions involving interactions of negative ions with atomic or ionic species. Such reactions are outlined in the lower part of **Table 1.3**. Among those, associative detachment (AD) involving atomic species, electron detachment (ED) with high-energy electrons and mutual neutralization (MN) with the positive ionic species can be identified as the most important ones. Conversely, reactions R51 through R56 of **Table 1.4**, which refer to molecular collisions with atoms, other molecules or even the surrounding walls, are characterized as *indirect*. This term arises from the fact that these reactions are accountable for the quenching of the vibrational states involved in the DEA reaction towards the formation of negative ions.

Finally, a closer inspection at R13 (R14) and R51 (R52), i.e. AD and V-t, reveals that the rates of these processes are sensitive to the atomic density. Among the many processes that may

occur, in low temperature plasmas, one of the most important electronically-inelastic processes is the excitation of the repulsive  $b^3\Sigma_u^+$  state (R57 and R58) [74]:



In turn, the effectiveness of reactions R57 and R58, and consequently the atom yield, depends on the operational parameters in a given reactor configuration, namely the gas pressure and the injected power.

Overall, in this section has laid the essential theoretical background which will be the basis upon which the interpretation of the experimental results of the present thesis will be carried out. Furthermore, it has been evidenced that the knowledge on two important particle distributions, i.e. the electron energy distribution function (EEDF), and the vibrational distribution function (VDF), can be enough to obtain a global understanding of the production pathways of the negative ions.

## 1.6 Advantages of ECR discharges

All of the mechanisms described in the previous section may occur in discharges regardless of the driving mechanism, whether it be through filaments, radio-frequencies or microwaves. However, ECR discharges in particular present several advantageous characteristics over the others and have thus prompted their study also in the framework of the present thesis. These include the lack of components with a limited lifetime which would require regular maintenance, and the capability of producing dense and homogeneous plasmas over a wide range of gas pressure and applied power. Based on the different magnetic field configurations that can be applied different configurations of ECR reactors can be distinguished. However, herein focus is laid on a special antenna-like ECR structure, that of the elementary dipolar module, whose application in particular reactors related to this study was mentioned at the end of section 1.4. But before the description of its operation, a brief overview of the basic principles underlying the ECR mechanism are presented.

### 1.6.1 Theoretical background

Waves generated near a plasma surface can propagate into the plasma or along the surface where they can be absorbed, leading to the heating of plasma electrons and heating of the discharge [113]. Prior to the description of the ECR mechanism, it is deemed necessary to establish several ground terms.

If the electrons in a plasma are displaced from a uniform background of ions, electric fields will be built up in such a direction as to restore the neutrality of the plasma by pulling the electrons back to their original positions. Because of their inertia, the electrons will overshoot and

oscillate around their equilibrium positions with a characteristic frequency,  $\omega_{ep}$ , known as the plasma frequency [114]:

$$\omega_{ep} = 2\pi f_{ep} = \sqrt{\frac{n_e e^2}{m_e \epsilon_0}} \quad (1.1)$$

This frequency is one of the fundamental parameters of a plasma, solely dependent upon the electron density,  $n_e$  [114]. In the above equation,  $m_e$ ,  $e$ , and  $\epsilon_0$  in represent the electron mass, the elementary charge and the dielectric constant of free space, respectively.

Upon irradiation of a plasma with an externally applied electromagnetic radiation ( $\omega_0 = 2\pi f_0$ ), the plasma frequency imposes an important limitation to the propagation or not of this radiation. First, the case when a magnetic field is absent is considered. If  $\omega_0 < \omega_{ep}$ , the electrons respond to the electric field and extract energy from it. If there are collisions or dissipative processes in the plasma, the wave is damped, as energy is converted into kinetic energy of the plasma constituents [115]. Moreover, electrons near the surface of the plasma may act like miniature dipoles and re-radiate the incident radiation, reflecting it from the plasma [115]. Conversely, if  $\omega_0 > \omega_{ep}$ , the electrons have too much inertia to respond to the electric field of the wave, and the radiation is able to propagate through the plasma without significant reflection or attenuation [115]. From a different point of view, solving **Eq. 1.1** with respect to  $n_e$ , gives the critical density, i.e.

$$n_{e,c} = \frac{m_e \epsilon_0}{e^2} \omega_0^2 = \frac{4 \pi^2 m_e \epsilon_0}{e^2} f_0^2 \quad (1.2)$$

equivalently denoting that propagation of an applied radiation is inhibited if the plasma density surpasses this value.

Furthermore, the introduction of a steady magnetic field  $B_0$ , in which there is a resonance between the frequency of the externally applied electromagnetic radiation, and the electron cyclotron frequency,  $\omega_{ec}$ , somewhere in the discharge, allows for operation at high density and without a cavity resonance [113]. The electron cyclotron frequency (also called gyrofrequency) is given by **Eq. 1.3**.

$$\omega_{ec} = 2\pi f_{ec} = \frac{e B_0}{m_e} \quad (1.3)$$

The fundamental principles of the propagation of electromagnetic radiation and ECR heating in magnetized plasmas are rigorously developed in [113]–[115]. In fact, there are a variety of ECR processing discharges, with somewhat different coupling of the microwave power to the resonance zone. Three categories are: i) travelling propagation wave mainly along  $\mathbf{B}_0$  (the propagation vector is parallel to  $\mathbf{B}_0$ ), ii) propagation mainly across  $\mathbf{B}$  (the propagation vector is perpendicular to  $\mathbf{B}_0$ ), and iii) standing wave excitation (mainly cavity coupled) [113]. While these distinctions are significant and could find application in various source configurations, herein, the discussion is limited to the first aforementioned case. A linearly polarized microwave field launched into the

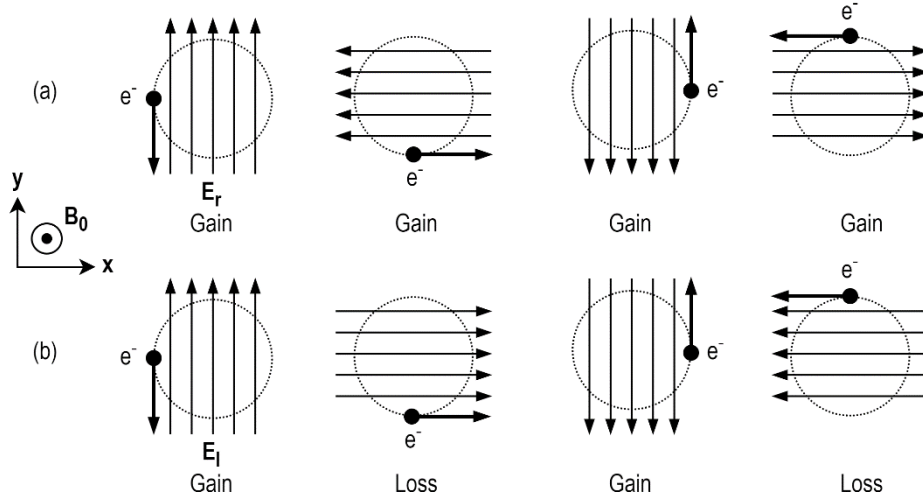


**Figure 1.9.** Basic principle of ECR heating; (a) Continuous energy gain for the electrons in the case of the RHP, and (b) net zero energy gain for the LHP. Reproduced from [113] with permission from John Wiley and Sons (License No. 5760680310681).

source chamber can be decomposed into the sum of two counter-rotating circularly polarized waves, the right-hand (RHP) and the left-hand (LHP) polarized waves. Assuming a sinusoidal steady state with the incident wave polarized along  $\mathbf{x}_0$  ( $\mathbf{x}_0$  is the unit vector along the x-axis and, similarly,  $\mathbf{y}_0$  the unit vector along the y-axis),

$$\mathbf{E}(\mathbf{r}, t) = \mathbf{x}_0 E_x(\mathbf{r}) \cos(\omega t) \quad (1.4)$$

where the complex amplitude  $E_x$  is here taken to be pure real, **Eq. 1.4** results in the expression:

$$\mathbf{x}_0 E_x = (\mathbf{x}_0 + j\mathbf{y}_0) E_r + (\mathbf{x}_0 - j\mathbf{y}_0) E_l \quad (1.5)$$

where  $E_r$  and  $E_l$  are the amplitudes of the RHP and the LHP waves, respectively, with  $E_r = E_l = E_x/2$ . The electric field of the RHP wave rotates in the right-hand sense around the magnetic field at frequency  $\omega_0$  while an electron in a uniform magnetic field  $B_0$  also gyrates in a right-hand sense at frequency  $\omega_{ec}$ . As a consequence, when  $\omega_0 = \omega_{ec}$ , the electron is accelerated by the force  $\mathbf{F} = -e\mathbf{E}$  along its circular orbit, resulting in a continuous transverse energy gain (**Fig. 1.9(a)**). Oppositely, the LHP wave field produces an oscillating force whose time average is zero (**Fig. 1.9(b)**), thus resulting in no energy gain [113]. In the former case, the sufficient energy gain by the electrons leads to reactions promoting the ionization, dissociation and excitation of the background gas.

### 1.6.2 Dipolar ECR modules

Historically, the dipolar ECR modules were originally conceived and designed by J. Pelletier and colleagues at the Laboratory of Subatomic Physics and Cosmology in the late 90's, and since then they gained notable popularity for applications related to materials processing [116]–[119]. Contrarily, their use in reactors intended for fundamental studies of hydrogen (deuterium) plasmas

is significantly more limited. A single elementary ECR module [60] is depicted in **Fig. 1.10**. It consists of two main parts, i.e. a permanent magnet (here, a samarium-cobalt magnet 20 mm in diameter and 30 mm in length is used) with an azimuthal symmetry around its magnetization axis, and a microwave applicator constituted by a coaxial line, parallel to the magnetization vector, and open on the rear pole of the magnet [60]. The inner conductor of the coaxial line penetrates inside the cylindrical magnet through a hole drilled on its axis. The magnet is encapsulated in a metallic (stainless steel) envelope and is water-cooled by using the inner tube inside the magnet. The microwave power can be thus transmitted without loss to the zone of ECR coupling in front of the rear pole of the magnet with the help of a coaxial line. There is no possibility for microwaves to be absorbed by the plasma before reaching the ECR coupling region or to radiate towards an adjacent elementary ECR module, in the case of a multi-module setup [60]. A tuner embedded on the main body of each module is used for impedance matching to maximize the power absorbed by the plasma [71]. At the microwave frequency of 2.45 GHz the magnetic field intensity needed to satisfy the ECR condition (**Eq. 1.3**) is  $B_0 = 87.5$  mT. The calculated magnetic field configuration as well as the line corresponding to a constant magnetic field intensity of 87.5 mT, are superposed on the same drawing. The field lines converge at the poles and join the two opposite poles of the magnetic dipole constituted by the magnet [60]. The “peanut-like” shape of the magnetic intensity contour corresponding to the ECR condition is attributed to end effects in combination with the length of the magnet.

With this design, the plasma is created by electrons (denoted also as “hot” electrons) that are accelerated in the zone of ECR coupling. The trajectories of these “hot” electrons around the magnetic structure have been subject to scrutiny. Briefly, the “hot” electrons oscillate within two field lines and two mirror points in front of the opposite poles of the magnet, and drift azimuthally

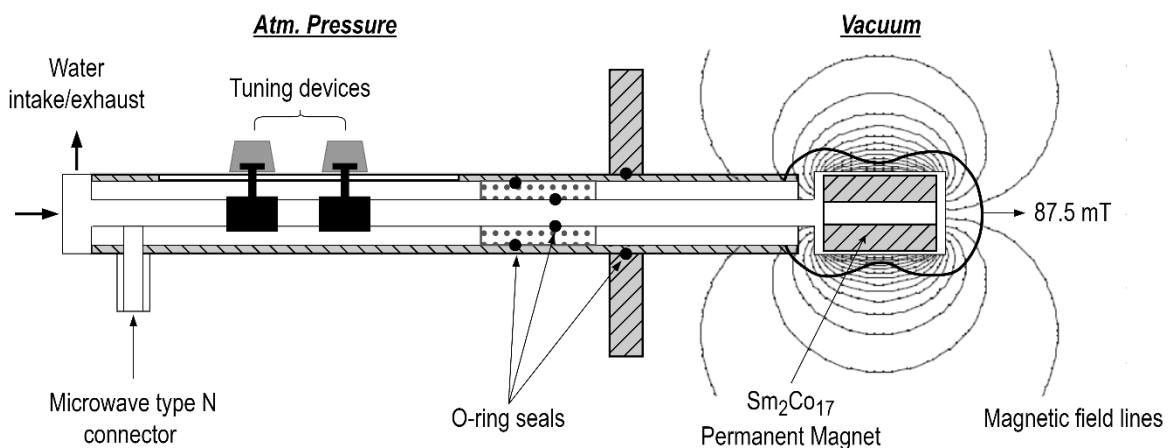


**Figure 1.10.** Schematic representation of a dipolar ECR module with details of its construction. Superposed on the drawing, around the magnet, is the configuration of the magnetic field as well as the line of constant magnetic intensity of 87.5 mT (corresponding to the ECR condition for the microwave frequency of 2.45 GHz). The latter have resulted from calculation and are reproduced from [60] with permission from IOP Publishing (License No. 1438329-1).

around the magnet acting as a tri-dimensional magnetron structure [60]. In this region, the electron energy distribution function (EEDF) can be assumed to be the sum of two electron populations (“hot” and “cold”) having Maxwellian distributions. The temperature of the “hot” population can reach more than 17 eV. This means that a significant part of the electron population includes electrons with energies much higher than twice this value [60], [120]. The plasma produced by the inelastic collisions of these electrons along their itinerary then diffuses away from the magnet. The “hot” electrons remain trapped in the magnetic field, and only the low-energy population of electrons diffuses away from the magnetic field under the influence of density gradients and the resulting space charge electric field [60], [120]. Thus, a separation of the plasma volume into two distinct regions with different characteristics is ensued. These regions, merely briefly mentioned in the cases of some reactor configurations presented in section 1.4, are commonly designated as the “driver” and “diffusion” regions. The term “driver” defines the region where the plasma is created, characterized by an elevated plasma density and electron energy. The same parameters are considerably lower in the “diffusion” region. In the above terms, in reactor configurations employing dipolar ECR modules such as those considered, these regions are respectively, the zone of ECR coupling, and the plasma in the volume that extends downstream from that.

The capability of dipolar ECR plasmas to demonstrate a plasma with such spatially resolved characteristics is crucial for efficient production of the negative ion species through the volume production process. In fact, in accordance to the principles that have been laid out in section 1.5, vibrational excitation of the gas is promoted in the “driver” region through reactions involving the “hot” electrons, while the production of negative ions occurs in the “diffusion” region through the DEA reaction for which “cold” electrons are a requisite.

## 1.7 Plasmas sustained in the pulsed operating regime

In the preceding sections, the pertinence of the spatial separation of the plasma into two different regions by means of a magnetic filter (the driver and the diffusion regions) to the production of negative ions through volume production was established. Additionally, it was highlighted that plasmas driven by elementary dipolar ECR modules inherently offer this advantageous feature. It has been proposed however, that a discharge can be filtered in time as well as in space. This is referred to as the temporal filtering technique [121], which entails pulsing the power delivered to the plasma, in the sense that the discharge is switched on and off for specific time intervals and a given repetition rate. The basic idea behind this approach for enhanced negative ion production is to control the interplay between the relaxation of the electron energy distribution function (EEDF) and the vibrational distribution of the H<sub>2</sub> (D<sub>2</sub>) molecules [122]. Nonetheless, beyond this scope, time-resolved investigations of the plasma properties may provide access to invaluable information on the kinetics of the different species, which in turn affect the elementary processes that take place inside the plasma. For this purpose, the proper synchronization, with the plasma

pulses, of various diagnostic techniques allows for interrogation of the produced plasmas in a time-resolved manner.

An appreciable amount of works has in fact been devoted to this subject, the majority of which concern filament-driven sources [121]–[130]. For the case of microwave-driven discharges in particular, surface wave discharges sustained in the pulsed mode have been scrutinized in [131], [132], whereas, from what is known, the evolution of basic plasma parameters in a hydrogen discharge in a reactor equipped with elementary dipolar ECR modules has only been dealt with in [133].

With regard to studies in filament-driven sources, in [123], the investigation of the basic plasma parameters and the temporal evolution of the EEDF in the post-discharge period, in the driver region of the source, was carried out along with a comparison of the results with those obtained when the plasma is sustained in the continuous mode. In a subsequent publication [125] and a similar source, negative ion density measurements were effected, whereby an increase of the negative ion yield in the post-discharge by a factor of two is reported. This is attributed to the favorable conditions occurring in the post-discharge which promote negative ion production via DEA (R1, R2; **Table 1.3**). Namely, a cool EEDF prevents electron-impact detachment of the negative ions but enhances the DEA rates. At the same time, the relatively long lifetime of the vibrationally excited molecules, which are destroyed mainly by several wall bounces, ensures that the negative ion production rate is maintained in the post-discharge [125]. A later study [127] at the same reactor as the one used in [123], communicated a comparison of the time-dependent properties in both H<sub>2</sub> and D<sub>2</sub> plasmas. The negative ion yield was enhanced in the early post-discharge in both gases, and in both the driver and extraction region of the source. Nevertheless, the negative ion density in deuterium is consistently about 75% of that in hydrogen [127]. Apart from using a typical boxcar waveform to drive the plasma, another series of studies [124], [126] introduced the concept of high-frequency modulation of the discharge (i.e. with bursts of pulses during the expected operating window) as a means of enhancing the negative ion yield. Measurements of the extracted negative ion current [124] in either approach reveals an increase in the post-discharge period. In particular though, and for a deuterium discharge, it was found that modulation of the discharge at a high frequency led to the increase of the extracted current by a factor of 4. In the same source, time-resolved and direct measurements of the negative ion density [126] in a hydrogen discharge further validated the trend in those findings. Furthermore, spatially-resolved investigations [121] indicated that the transport properties of the negative ions play an important role in their temporal behavior observed at different locations within the same reactor. A hydrogen discharge operated in the pulsed mode was also the subject of scrutiny in [134], where, as in the previously mentioned studies, a strong increase of the negative ion density in the post-discharge is reported. In a comparable reactor configuration operating with hydrogen gas [128], the same remark is made. At the same time, measurements with a variation of the duration of the plasma pulse as well as the time for which the discharge is turned off allow to infer, indirectly, information on the temporal evolution and lifetimes of the molecular precursors

of the negative ions. The direct detection of the species was effected in [130], where their decay times (equivalently their lifetimes) in the post-discharge period were determined. Several hundreds of microseconds were deduced for the molecules lying in the low vibrational levels, while a lifetime of around 100  $\mu\text{s}$  is deduced for the vibrational levels of the mid-range (i.e.  $v'' = 6 - 11$ ). As higher levels are approached, the lifetime drops more significantly. An analogous trend is exhibited for increasing rotational quantum number. On the other hand, in [129] the temporal evolution of basic plasma properties such as the electron and negative ion densities are followed during the plasma pulse, for various filling gas pressure values. In this study, a discrepancy between the temporal patterns of the two aforementioned species is obtained. It is claimed that this indicates that the production of the negative ions is affected not only by the electron population, but also by the neutral particle density, as assumed by the volume production mechanism of negative ions. Finally, an early theoretical report [122] addressed the behavior of the EEDF and the vibrational distribution of the molecules in the case of a deuterium plasma, with relation to the elapsed time in the post-discharge phase. The calculations indicate a rapid relaxation of the EEDF in the post-discharge in such a way that the number of electrons with small energy increases, accompanied by a less pronounced change in the VDF on the same time scale. The DEA reaction rate thus increases and so does the negative ion density.

In relation to the existing works on microwave discharges, firstly, [131], [132], [135] considers a pulsed surface wave discharge in a tubular reactor made entirely of quartz. In this special configuration, focus was mainly laid on the inspection of the neutral atomic population properties which includes exploration of the temporal evolution of the atoms [131], measurement of their lifetime in the post-discharge period at different gas pressures as well as a deduction of their surface loss probability [132], and time-resolved measurements of the gas temperature in order to gain information related to the processes of gas heating [135]. Lastly, detailed time-resolved measurements of the extracted electron and negative ion currents, and basic plasma parameters have been effected in the source “Camembert IIP” [133]. Contrary to the electron current which rises and decays rapidly with respect to the plasma pulse, the negative ion current attains longer rise and decay times. The latter fact can be attributed to the slow evolution of the vibrational distribution in the early discharge and the long lifetime of the vibrationally excited molecules in the post-discharge, preserving thus the production of the negative ions. However, unlike the abovementioned studies in filament-driven sources, therein, no important increase in the negative ion extracted current was observed during the post-discharge phase.

Evidently, as in the case of  $\text{H}_2$  and  $\text{D}_2$  discharges sustained in the continuous mode of operation, the existing works on respective pulsed discharges, even more so of those in ECR-driven sources containing elementary dipolar modules, is quite restricted. Therefore, within the framework of this thesis, a substantial step is made in treating this subject, and relevant experimentation is held at the reactor “SCHEME-II+”. A description of the application details and is included in Chapter 2 while the outcome of this study is presented in Chapter 5.

## 1.8 Thesis contribution and outline

The heating and current drive (H&CD) system is a salient component of both ITER and future fusion devices. Although an important strategic decision made at the beginning of 2020, assigned the Electron Cyclotron (EC) heating method as the heating baseline for the case of DEMO [136], the two other methods, namely Neutral Beam Injection (NBI) and Ion Cyclotron (IC) heating, will continue to be developed in the frame of a risk mitigation approach. Eventually, a final decision is expected to be made in 2024 when the potentialities of all three methods will be assessed based on physics requirements and their Technological Readiness Level (TRL) [136]. As far as research for the part of NBI systems is concerned, considerable efforts are made towards the development of negative ion sources in which the use of Cs could be eliminated, all the while fulfilling the requirements for modern NBI systems. Therefore, volume production of negative ions and the development of sources based on this mechanism draws much attention. Indeed a notable number of studies on the subject justifies this statement, though the majority of those refer to operation with hydrogen gas. Deuterium gas on the other hand is more seldom studied and direct comparative studies between the two isotopes are rather limited, especially more so if these are narrowed to ECR plasmas sustained with dipolar modules. In this direction, the main contribution of the present thesis may be summarized by the following points:

- The quantitative determination of the isotopic differences between hydrogen and deuterium plasmas, driven by dipolar ECR modules, and their correlation with the volume production of  $H^-$  and  $D^-$  negative ions.
- The parametric study, across a broad range of the operating parameters (i.e. the transmitted microwave power and working gas pressure), of a prototype reactor employing dipolar ECR modules.
- The determination of optimum operating windows with respect to the absolute density and energy of the produced fundamental particles and the stability of the plasma.
- The evaluation of the negative ion production mechanisms for the two isotopes.
- The recording of the dynamic behavior of  $H^-$  and  $D^-$  negative ions, as well as the interpretation of the existence of negative ion populations attaining different energy distributions.
- The experimental determination of the Vibrational Distribution Functions (VDFs) for different cases of materials facing the plasma. For this, the advanced diagnostic technique of vacuum ultraviolet absorption spectroscopy using synchrotron radiation is applied.
- The experimental study of prototype reactors in which plasmas are sustained in the pulsed mode of operation.

Following this first introductory chapter, **Chapter 2** contains a detailed presentation of the two prototype reactors that were studied namely, “Prometheus I” and “SCHEME-II+”, along with all the plasma diagnostic techniques that were applied. **Chapter 3** is devoted to the comparison

of the properties of  $H_2$  and  $D_2$  plasmas driven by ECR dipolar modules and their correlation with the negative ion production mechanisms. In **Chapter 4** all the necessary steps for acquiring the VDFs is unfolded, and those obtained are discussed. Then, **Chapter 5** presents the study of plasmas sustained in the pulsed mode of operation. In the closing chapter, **Chapter 6**, the main findings of this work are collected and a direction for continuation of the present work is proposed. Finally, **Appendices A** and **B** contain some information complementary to the experiments that have been conducted.



# CHAPTER 2

## EXPERIMENTAL APPARATUS AND METHODS

---

This chapter is devoted to the presentation of the two prototype reactors that have been studied within the framework of this thesis. Both utilize identical dipolar ECR modules to produce  $\text{H}_2$  and  $\text{D}_2$  plasmas, however, each reactor is oriented to the study of the DEA reaction from a different point of view, i.e. through probing the different constituents of the reaction. On the one hand, conventional diagnostics performed at the “Prometheus I” reactor (High Voltage Laboratory, University of Patras, Greece) allow for the determination of the Electron Energy Distribution Functions (EEDFs) and the principle negative ion properties in  $\text{H}_2$  and  $\text{D}_2$  plasmas. On the other hand, the “SCHEME-II+” reactor (Laboratory of Subatomic Physics and Cosmology, Grenoble, France) is especially designed for the application of Vacuum Ultra-violet Fourier Transform (VUV-FT) absorption spectroscopy in order to directly probe the molecular precursors of the negative ions. Finally, at the same reactor, plasmas sustained in the pulsed mode of operation are investigated, thus details on the necessary experimental considerations for the appropriate investigation of plasmas in this mode of operation are herein presented.

## 2.1 The “Prometheus I” reactor

**Fig. 2.1** depicts a schematic representation of the reactor “Prometheus I”, installed at the High Voltage Laboratory at the University of Patras in Greece. A photo of the reactor is shown in **Fig. 2.2(a)**.

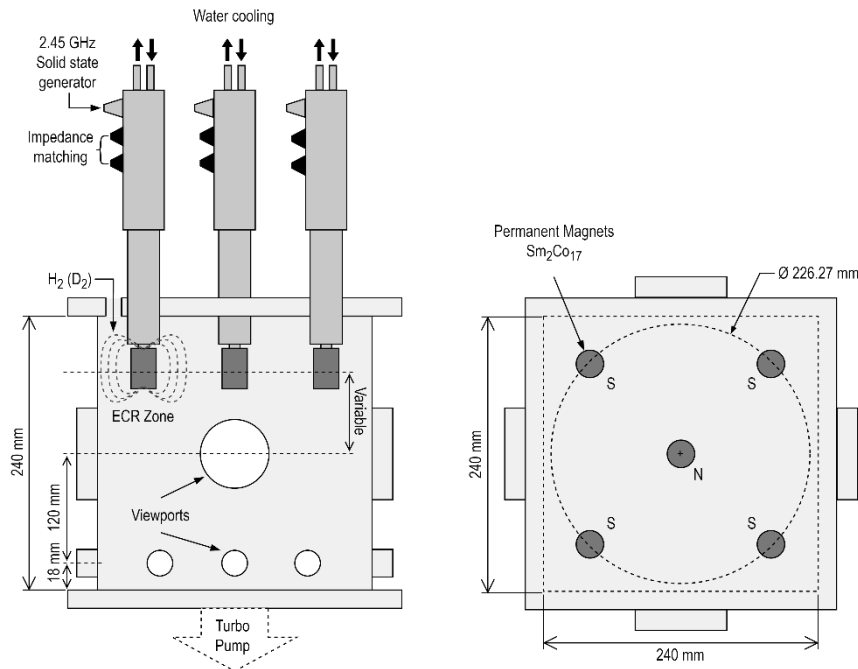


**Figure 2.1.** Schematic representation of the “Prometheus I” reactor.

It consists of a cubic stainless steel chamber (240 mm inner edge) with multiple viewports for diagnostic tool installation. A base pressure of around  $7 \times 10^{-5}$  Pa is achieved with a two-stage pumping system, comprising of a turbomolecular pump (80 l/s) fitted on the bottom flange of the reactor, backed up by a rotary oil pump. Pure  $H_2$  (99.999%) or  $D_2$  (99.8%) gas is introduced into the chamber by means of a digital mass flow controller, and the working (Plasma ON) pressure is

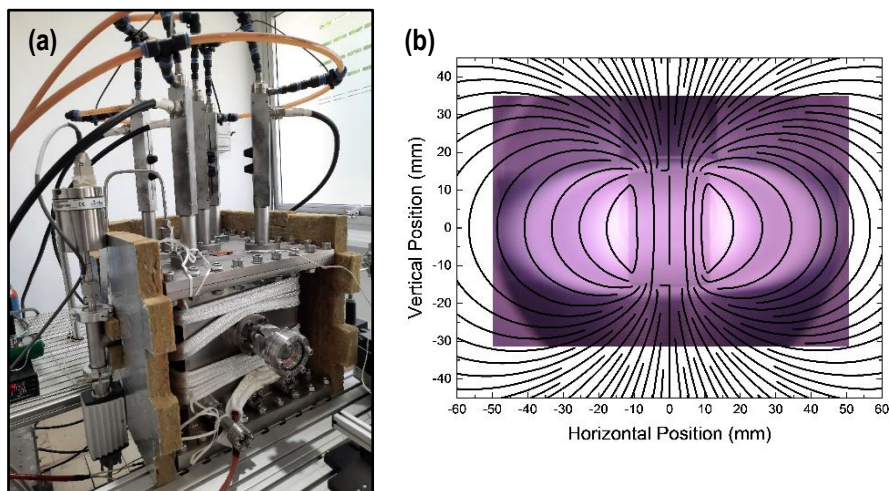


**Figure 2.2.** (a) Photo of the “Prometheus I” reactor, (b) Magnetic field streamlines superposed on a photograph of the produced plasma around the permanent magnet of the dipolar ECR module.

monitored by a Baratron<sup>®</sup> capacitance manometer. The maximum allowed working pressure is 2.67 Pa.

The plasma is sustained by a network of five elementary dipolar ECR modules, whose structure has been described in detail in section 1.6.2. Each ECR module is driven by an independent solid-state microwave power supply (2.45 GHz), able to provide up to 180 W. The magnetic field of a single ECR module, simulated using a commercial numerical suite (COMSOL Multiphysics<sup>®</sup>), is shown in **Fig. 2.2(b)**. The magnetic field streamlines are compared in the same figure with the visible plasma generated in an ECR zone. The high-energy electrons which gain their energy in the ECR zones appear to be mostly confined within the luminous region, in the vicinity of the permanent magnet, where they promote gas dissociation, excitation. Therefore, this configuration is advantageous in that the ECR magnetic field plays also the role of the magnetic filter, allowing mainly low-energy electrons and excited neutrals to diffuse into the bulk of the plasma, i.e. downstream of the ECR zones.

The properties of H<sub>2</sub> and D<sub>2</sub> plasmas produced in this reactor are studied by means of electrostatic (Langmuir) probe and laser-induced photodetachment. As for the latter, both the single-beam and the dual-beam variations of this technique have been applied. The details of the installation and application of these diagnostics are described in the following.

### 2.1.1 Electrostatic (Langmuir) probe diagnostic

An electrostatic probe, commonly referred to as a Langmuir probe (named after Irving Langmuir who alongside Harold Mott-Smith in the 1920's were the first to demonstrate the how it was possible to use the probe in order to extract the plasma parameters), in its simplest form consists of a bare metal wire inserted into a plasma. In principle, the probe is biased to different potentials with respect to a reference electrode to collect electron and/or positive ion currents [137]. The resulting current-voltage trace is known as the I-V characteristic. The subsequent analysis of this curve can unveil information on the characteristic potentials (the floating and plasma potentials), the plasma density, the electron temperature and even the electron energy distribution function (EEDF). However, the ion temperature on the other hand is inaccessible [138].

The lab-made probe used at the “Prometheus I” setup is depicted in **Fig. 2.3**. It consists of a 0.25 mm in diameter tungsten wire shaped into an L-bent configuration for alignment with a laser beam for the application of the photodetachment diagnostics described in sections 2.1.2 and 2.1.3. The tip, which is exposed to the plasma has a length of 15 mm (the bent part being 11 mm), whilst the rest of the wire is housed in a telescopic configuration of dielectrics (alumina tube inside a wider quartz tube) which insulate and protect it from the plasma. The quartz tube is supported inside a stainless-steel tube that ends in a standard Bayonet Neill-Concelman (BNC) vacuum

feedthrough. A conflat flange-to-quick connect coupling adapter makes a vacuum joint with the steel tube and at the same time allows for the linear translation of the probe.

For the entirety of the measurements carried out in the framework of this thesis (see Chapter 3), the probe is positioned 65 mm downstream of the middle plane of the permanent magnet of the central ECR module shown in **Fig. 2.1**. The magnetic field of an ECR module has

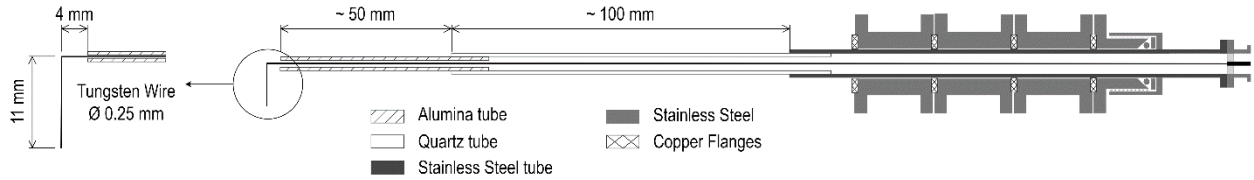


**Figure 2.3.** Construction of the Langmuir probe used at the “Prometheus I” reactor. The dimensions of the L-bent tip are specified on the magnified inset.

a vertical downward direction (**Fig. 2.2(b)**) and a magnitude of 51 Gauss, while the probe tip orientation is horizontal, i.e. perpendicular to the magnetic field. With the lowest electron temperature observed, around 0.5 eV, the corresponding Larmor radius is about 0.34 mm. Thus, even in the worst case, the probe radius (0.125 mm), is sufficiently smaller than the electron Larmor radius, validating the use of conventional non-magnetized probe theory for the processing of the current-voltage curves [139], [140]. The acquisition of the I-V characteristics is accomplished with a standalone, custom-built system [141]. Each measurement procedure includes 10 s of probe cleaning by electron-induced incandescence followed by another 10 s of cooling-down. The acquisition is realized point by point in steps of 97.6563 mV. For each point,  $2^{12}$  current-voltage samples are averaged in order to reduce the plasma-induced noise. Several important details on the curve analysis procedure are given alongside the presentation of the experimental results in Chapter 3.

### 2.1.2 Single-beam laser-induced photodetachment technique

Laser-induced photodetachment employing a single laser beam, in combination with the use of a Langmuir probe, is a well-established technique which allows for local measurements of the absolute negative  $H^-(D^-)$  ion density. A schematic of the assembly of the diagnostic at the “Prometheus I” reactor is depicted in **Fig. 2.4**.

The Nd:YAG laser (Quantel, Brilliant EaZy) employed has the following specifications: 1064 nm (1.2 eV) photon wavelength (energy), 3 mm output beam radius, 330 mJ maximum energy per pulse, 5 ns pulse width, and 10 Hz repetition rate. The beam energy is precisely adjusted either by varying the internal delay between the laser flashlamp and Q-switch or with the in-line installation of a half-wave plate and a polarizing beamsplitter. The latter concept is based on Malus’ law, according to which the attenuation of the energy of a linearly polarized laser beam is

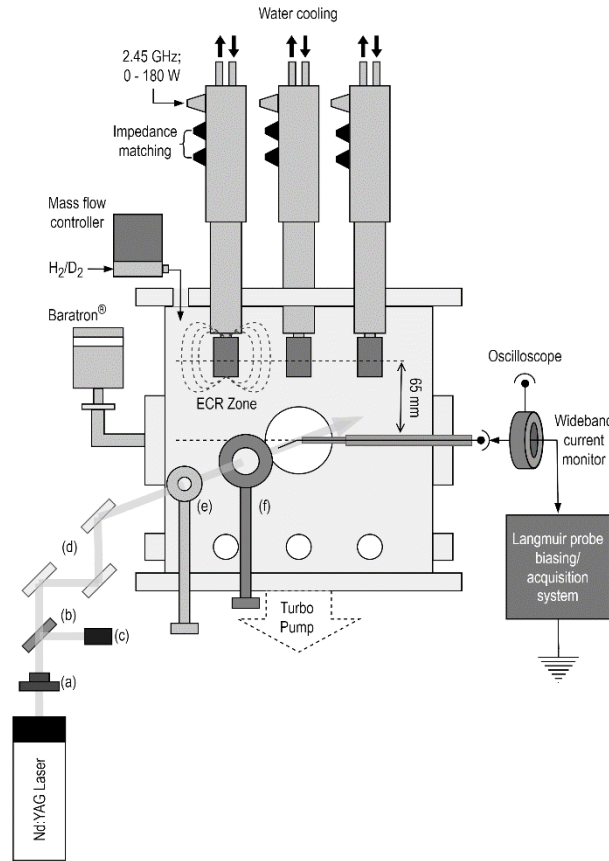


**Figure 2.4.** “Prometheus F” source and the single-laser photodetachment diagnostic. (a) Half-wave plate on precision rotation mount; (b) thin-film polarizing beamsplitter; (c) laser beam dump; (d) mirrors; (e)  $\varnothing$  5 mm diaphragm; (f) removable pyroelectric laser energy sensor.

a function of the angle between the beam’s initial direction of polarization and the axis of the polarizer. **Fig. 2.5(a)** shows the corresponding calculated and measured attenuation curves. The beam energy is measured by a pyroelectric energy meter, equipped with a diffuser for concentrated beams.

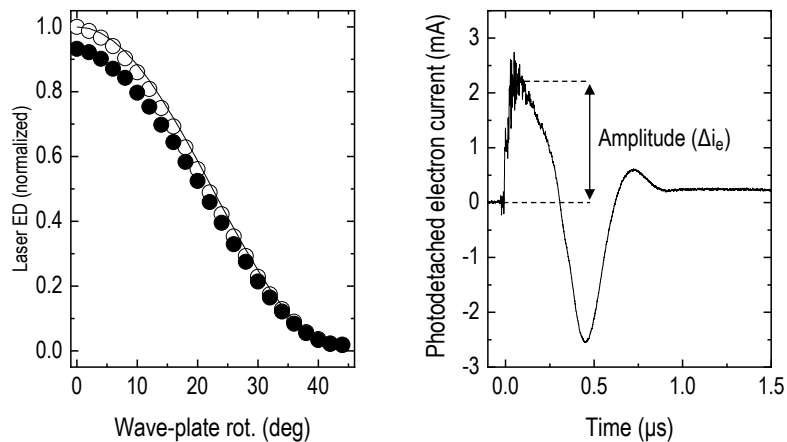


**Figure 2.5.** (a) Normalized attenuation curves of the laser beam energy density (ED). Line: Malus’ law; Open circles: measurements in front of a viewport; Solid circles: measurements behind a viewport. (b) Typical photodetachment signal. Operating conditions:  $\text{H}_2$ , 1.33 Pa, 900 W.

Special attention is paid to the proper application of the technique as stated in [142]. Accordingly: (i) the beam is concentrically aligned with the L-bent part of the tip of the probe and its radius, set to 2.5 mm, is larger than the probe collection radius (typically 0.1 mm for the conditions that are studied herein), (ii) the beam energy density, i.e. 70 mJ cm<sup>-2</sup> inside the reactor chamber after taking account approximately a 7% attenuation due to the glass viewport, suffices to detach the electrons from all negative ions present within the irradiated volume, and (iii) the probe bias, i.e. 15 V, is adequate to collect all the photodetached electrons around it. The transient current induced by the photodetached electrons, whose typical form is shown in **Fig. 2.5(b)**, is recorded by a wideband current transformer (400 Hz – 250 MHz) on a digital oscilloscope (1 GHz; 5 GSamples s<sup>-1</sup>). It is noted that, several numerical studies have been devoted to the elucidation of the kinetic phenomena that occur and are responsible for the characteristic temporal evolution, including the observed undershoot [143]–[145].

With regard to the laser beam energy density and the abovementioned chosen values, these are justified by dedicated measurements as shown in **Figs. 2.6(a)** and **(b)**. The theoretical relation of the fraction of detached electrons with respect to the beam energy density [142]:

$$\frac{\Delta n_-}{n_{-,0}} = 1 - \exp\left(-\frac{\sigma E}{h\nu S}\right) \quad (2.1)$$

where,  $h\nu$  is the photon energy,  $\sigma$  is the photodetachment cross section equal to  $4 \times 10^{17}$  cm<sup>2</sup>, and  $E/S$  is the laser pulse energy per unit area, is experimentally reproduced under typical operating conditions in **Fig. 2.5(a)**. The saturation of this fraction is predicted and also measured for energy densities as low as around 25 mJ cm<sup>-2</sup>. When choosing to work at an energy density level for

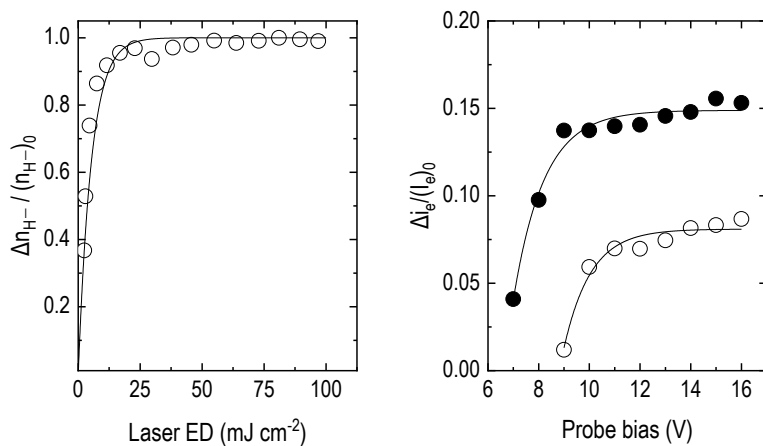


**Figure 2.6.** (a) Ratio of the photodetached negative ion density ( $\Delta n_{H^-}$ ) to the steady-state negative ion density  $(n_{H^-})_0$ , as a function of the laser beam ED. Line: theory (eq. 1); Open circles: experimental points at 2.0 Pa of H<sub>2</sub> and 0.9 kW. (b) Ratio of the photodetachment (PD) signal peak (due to the instantaneously photodetached electrons) ( $\Delta i_e$ ) to the steady-state electron current  $(I_e)_0$ , as a function of the probe biasing level. Open circles: 1.60 Pa of D<sub>2</sub> and 0.9 kW; Solid circles: 1.60 Pa of H<sub>2</sub> and 0.9 kW.

which the saturation of the ratio of **Eq. 2.1** is ensured, the amplitude of the photodetachment signal,  $\Delta i_e$ , as drawn on **Fig. 2.4(b)** is proportional to the negative ion density:

$$\frac{\Delta i_e}{(I_e)_0} = \frac{n_-}{n_e} \quad (2.2)$$

In **Eq. 2.2**,  $\Delta i_e$  is the amplitude of the photodetachment signal,  $(I_e)_0$  is the electronic current collected by the probe when biased at the potential applied for photodetachment, and  $n_e$  is the electron density derived from Langmuir probe measurements. Finally, **Fig. 2.6(b)**, shows the ratio between the peak of the photodetached electron transient impulse and the steady state electronic current with increasing probe bias. It can be seen that a 15 V bias leads to a quasi-saturation of this ratio, without inducing the probe incandescence, justifying thus the use of this value throughout the measurements that will be presented in Chapter 3.

### 2.1.3 Two-beam laser-induced photodetachment technique

Laser-induced photodetachment with the use of an additional (second) beam, allows for the full exploitation of the technique described previously in section 2.1.2. The dynamic properties of negative ions, i.e. their thermal velocities, may then be accessed. This parameter is significant in that it determines beam transport properties and emittance, while it may be much appreciated in studies concerned with the creation of numerical models for negative ions sources since it is usually estimated. On the other hand, it is a necessary parameter for the correct analysis of Langmuir probe curves obtained in electronegative plasmas, i.e. plasmas with a high negative ion to electron ratio [146], [147].

The fundamental physical concepts of this method, when a Langmuir probe is used for electron detection, implies: (i) the creation of a controlled perturbation in the negative ion density, followed by (ii) the measurement of the recovery of the negative ion density  $n_{H^-,t}$  towards its initial value  $n_{H^-,0}$ , and (iii) fitting the measured results to a physical model describing the density recovery process, in which the ion thermal drift velocity plays a central role. In practice, a first laser shot detaches all of the negative ions in the illuminated volume, and a reference photodetachment signal is acquired. A second laser shot, arriving with a delay  $\Delta t$ , subsequently detaches all of the negative ions that have managed to flow into the same illuminated volume, during  $\Delta t$ . Thus, a second photodetachment signal is generated, superposed to the reference one and lagging that by  $\Delta t$ . By increasing the delay  $\Delta t$ , the amplitude of the second signal approaches that of the reference signal, progressively, proving thus information of the negative ion recovery at different points in time. Namely, with the subtraction of the reference signal from the mixed one, the second signal is isolated, and its peak is measured. The ratio between the isolated and reference amplitudes equals  $n_{-,t}/n_{-,0}$ , where  $n_{-,0}$  is conventionally estimated by the peak of the reference photodetachment signal. Thus,  $n_{-,t}$  is determined.

The realization of this diagnostic is illustrated in **Fig. 2.7**. The beams of two independent Nd:YAG lasers (Quantel, Brilliant EaZy) are coaxially aligned by means of appropriate optical components. Additionally, the beams' energies are carefully matched at a sufficient level, ensuring that the beams' energy densities lie in the saturated part of the negative ion density saturation curve. This is accomplished in a first step, by a coarse adjustment of the internal delay between the laser Flashlamp and the Q-Switch, and then more precisely with a fine tuning of the half-wave plates situated in-line with each beam. The synchronization of the two laser units with a 4-ns resolution of is achieved by four independent external trigger pulses with specific characteristics (5V TTL signal, 10 Hz, with a pulse width of 50  $\mu$ s, and rising and falling times of 0.55  $\mu$ s and 0.65  $\mu$ s, respectively), sent to the laser Flashlamp and Q-Switch trigger inputs. These pulses are generated by a multichannel pulse/delay generator, coupled with a custom-made opto-isolating and amplifying unit [148].

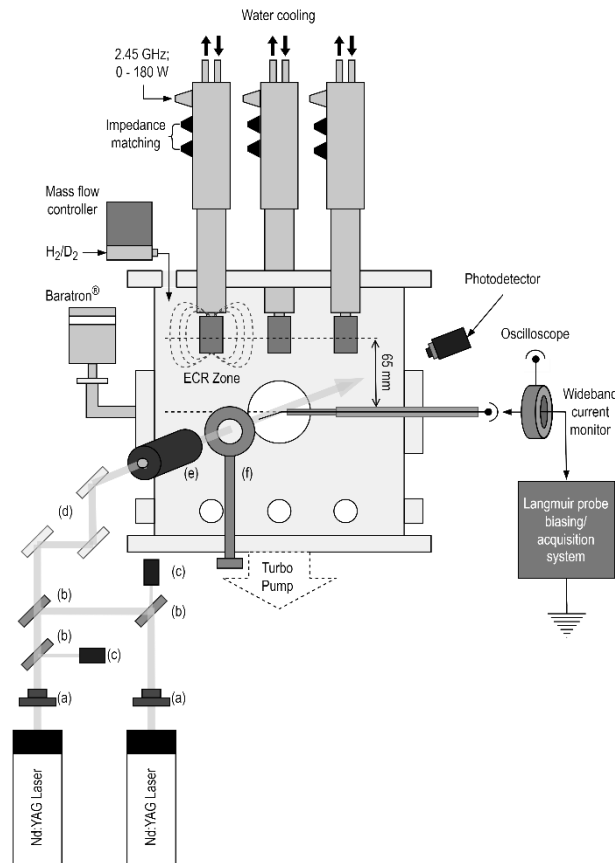


**Figure 2.7.** Two-laser diagnostic installed at the “Prometheus I” source. (a) Half-wave plates on precision rotation mounts; (b) thin-film polarizing beamsplitters; (c) laser beam dumps; (d) mirrors; (e) laser beam expander ( $\times 8$  magnification), having a  $\varnothing$  2.5 mm and a  $\varnothing$  5 mm diaphragm in the front and rear side, respectively; (f) removable pyroelectric laser beam energy sensor.

The two laser units are operated in the “Flashlamp External and Q-Switch external” mode, available by the manufacturer. First, the laser Flashlamps are triggered, with a delay between them equal to the difference in the values of the internal delays (FLQS Delay #1 and FLQS Delay #2 in **Fig. 2.8** for the first and second laser beam, respectively), i.e.  $\Delta t_{\text{energy}} = |(\text{FLQS Delay \#1}) - (\text{FLQS Delay \#2})|$ . Restricted by the ability of the laser unit’s microprocessor to treat these external signals, the Flashlamps are in fact turned on after an inherent interval of  $500\ \mu\text{s}$ . They remain on for another  $700\ \mu\text{s}$  (this is followed by the unit’s “Flashlamp OUT” output). It is within this time that the “Q-Switch IN” inputs are subsequently triggered; after FLQS Delay #1 and FLQS Delay #2 for the two lasers, respectively. Finally, the desired delay  $\Delta t$  between the two laser pulses (LASER OUT #1 and LASER OUT #2) is achieved with the addition of this delay to the pulse of the second laser. The change in the energy of the beam imposed by the addition of the extra delay  $\Delta t$  does not occur since the signal denoted as Flashlamp trigger IN #2 is equally shifted by  $\Delta t$ . A fast photodetector is used for the monitoring

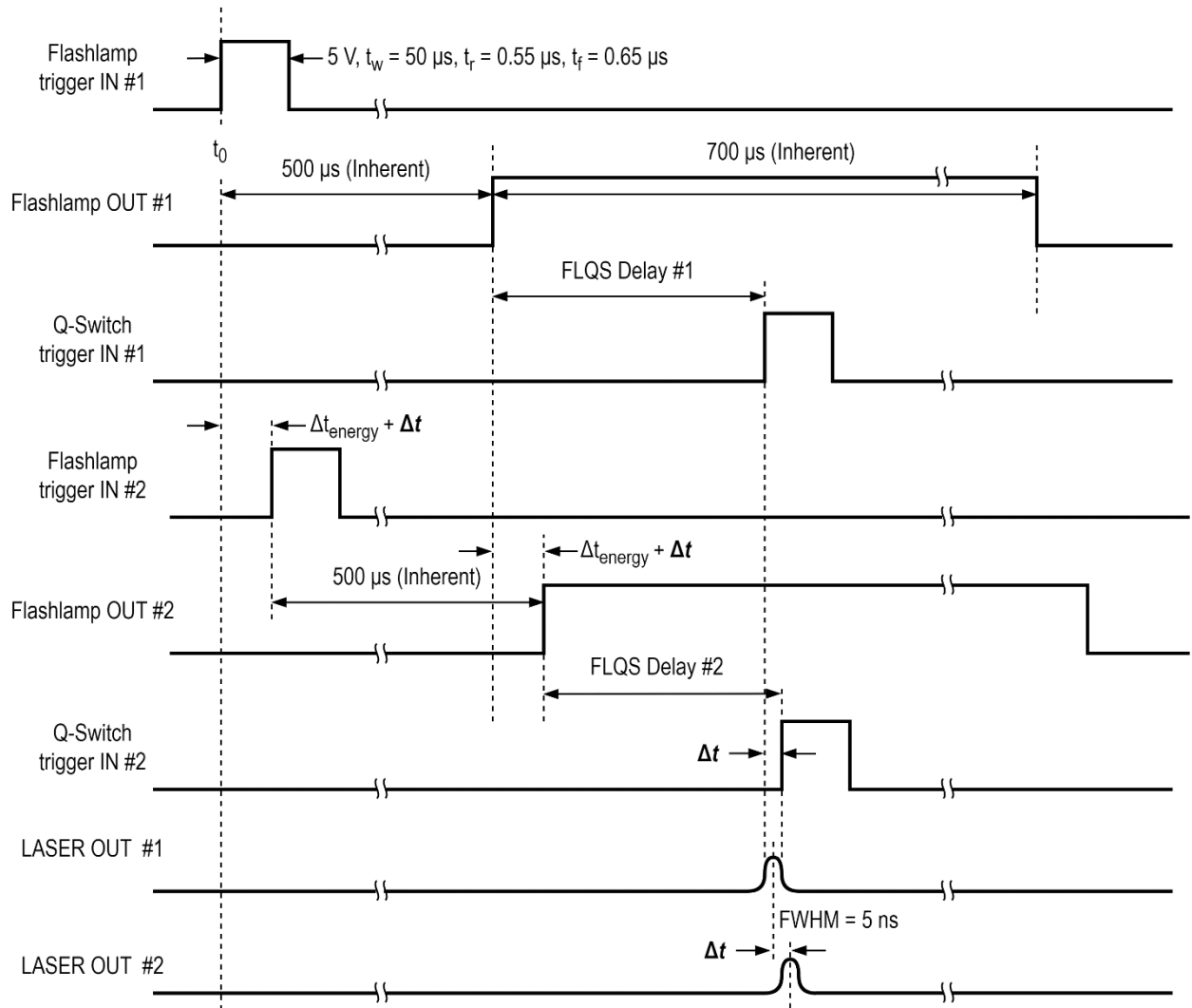


**Figure 2.8.** Timing diagram showing the synchronization scheme of the two laser units for the application of the two-laser photodetachment diagnostic.

of the temporal behavior of the laser pulses and its signal is that which triggers the probe acquisition. As in the case of the single-beam experiment, a wideband current transformer (400 Hz – 250 MHz) detects the impulses generated by the photodetached electrons, which are in turn recorded on a wideband digital oscilloscope (1 GHz; 5 GSamples s<sup>-1</sup>). All of the signals are averaged in-situ (> 200 signals averaged) in order to increase the signal-to-noise-ratio, and no further signal processing (smoothing/filtering) is applied during or after the acquisition [148].

Besides the requirements that must be met for proper application of the photodetachment diagnostic that were mentioned in the previous section, it is here underlined that the relative position of the L-shaped probe tip (vertical; horizontal; rotation) with respect to the laser beam axis is a very sensitive parameter that may lead to highly distorted photodetachment signals and, consequently, erroneous data. **Figs. 2.9(a)-(c)** depict this issue in an indicative case. In a similar manner, even if the probe is “perfectly” aligned with the laser beam axis, different beam profiles (in terms of shape or energy distribution) result in different signals. Therefore, a beam expander and two diaphragms (**Fig. 2.7**) are employed in order to provide an almost homogeneous flux of 1064 nm photons, along a 5 mm in diameter cross section path. It was observed that the amplitude of the first distinct peak of the photodetachment signal is immune to any reasonable misalignment or asymmetry. Nevertheless, these imperfections become crucial when ion dynamic effects are studied, since the tip must “see” two identical irradiative scenarios. **Fig. 2.9(d)** shows the matching photodetachment signals obtained from the two lasers, when respecting the abovementioned precautions. The signals from both lasers are periodically checked during the experiments [148].

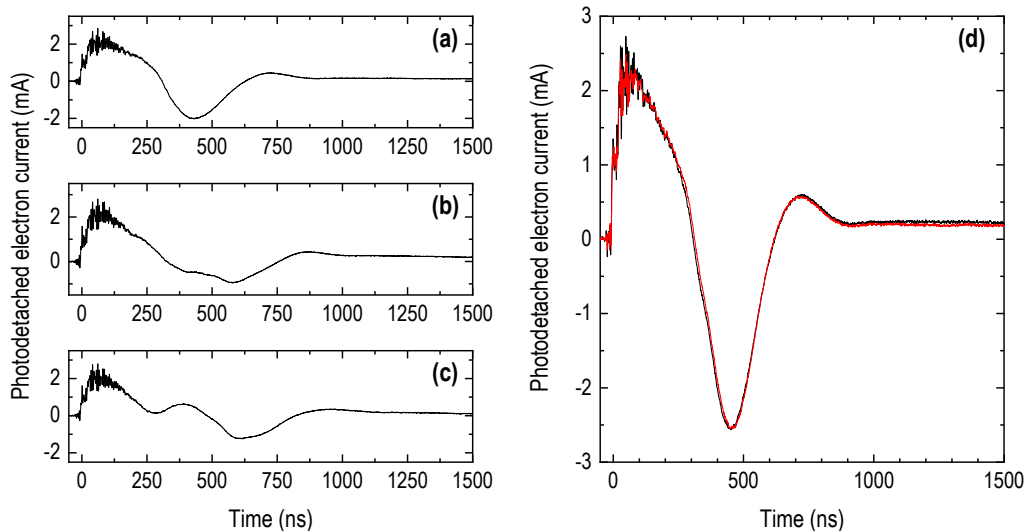


**Figure 2.9.** (a) Reference photodetachment signal, when the probe tip and the laser beam are optimally aligned. Distorted signals due to vertical, lower displacement of the laser beam for about (b) 0.5 mm and (c) 1.1 mm, with respect to (a); horizontal and rotational alignments remains as in (a). (d) Matching signals induced by two different laser beams, following the precautions mentioned in text; the red and black curves are superposed. Operating conditions: H<sub>2</sub>, 1.33 Pa, 900 W.

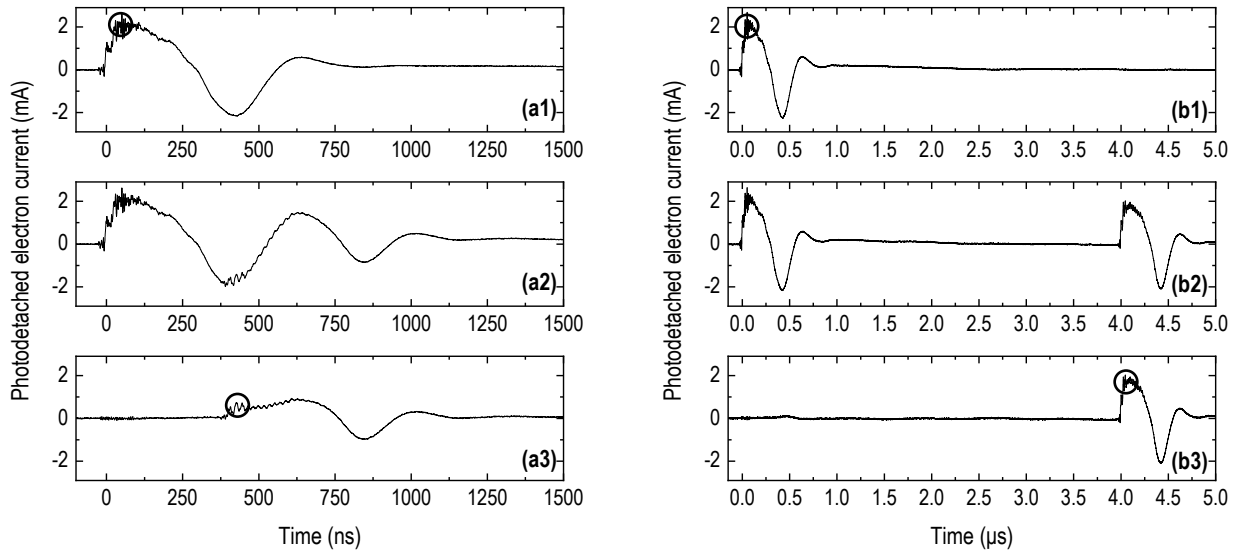


**Figure 2.10.** Typical two-laser photodetachment signals. (a1) Single-laser photodetachment signal. (a2) Two-laser photodetachment signal, with  $\Delta t = 400$  ns. (a3) Subtraction signal, i.e.  $(a2 - a1)$ . (b1) to (b3) similarly, for  $\Delta t = 4$   $\mu$ s. The inset circles define the amplitudes taken into account for the calculation of the  $n_{H^-,t}/n_{H^-,0}$  ratio. Operating conditions: 1.33 Pa, 900 W.

Typical examples of the mixed impulse induced by the photodetached electrons when both lasers are fired, for two indicative values of  $\Delta t$ , namely 400 ns and 4  $\mu$ s, are shown in **Figs. 2.10(a2)** and **(b2)** respectively. In the same figure, signals **(a1)** and **(b1)** refer to those obtained when only one laser is shot. It is seen that for  $\Delta t$  below the time required for the full evolution of the photodetachment signal two distinct ones are indiscernible, hence the use of the term mixed signal, contrary to when  $\Delta t$  attains a higher value. The subtraction signals **(a3)** and **(b3)**, carry the information for the photodetachment impulse created by the arrival of the second laser pulse after  $\Delta t$ . As predicted by the theoretical concept explained above, the faint amplitude of the photodetachment signal acquired at 400 ns is evidence of the fact that only a small fraction of negative ions have returned within the initially irradiated volume, whereas at 4  $\mu$ s, the initial negative ion density is nearly reached. This method is applied for different operating conditions of the reactor and the corresponding results are presented in Chapter 3.

### 2.1.4 Reactor conditioning considerations

Both  $H_2$  and  $D_2$  plasmas are regularly produced in the “Prometheus I” reactor. Interchanging the two working gases, however, requires special consideration and actions. Preliminary experimental attempts quickly revealed the inability to reproduce the same plasma parameters when the working gas was changed and subsequently restored to the formerly used one. This was attributed to gas retention in the stainless steel walls of the vessel. Thus, wall recovery, ensuring the stability and reproducibility of the measured plasma parameters, was deemed imperative. Gas retention as a phenomenon is well-known among the fusion community [149]–[154]. Hydrogen isotope retention is studied in particular on the basis of the evaluation of the readiness of key materials that are

currently, or are foreseen to be utilized as plasma-facing components (PFCs) in fusion devices. In particular, strict control of fuel retention in PFCs is one of the critical issues to ensure safe operation with Tritium [153].

In the said reactor, since the only available and reliable means to determine wall recovery is through monitoring the plasma parameters via systematic consecutive Langmuir probe measurements, an appropriate protocol was established as a result of a series of various trials. Ultimately, the derived protocol consists in a bake-out of the reactor at 150 °C under base-pressure conditions ( $5.33 \times 10^{-5}$  Pa), for at least 30 h. This procedure was respected upon each switch of the working gas, during the execution of the different experimental series discussed in detail later on in Chapter 3.

## 2.2 The “SCHEME-II+” reactor

The “SCHEME-II+” (Source of exCited HydrogEn MolEcules) reactor, installed at the Laboratory of Subatomic Physics and Cosmology (LPSC) at Grenoble in France, is illustrated in **Fig. 2.11** with details of its main structural properties. Actual photos of the reactor are presented in **Fig. 2.12**.

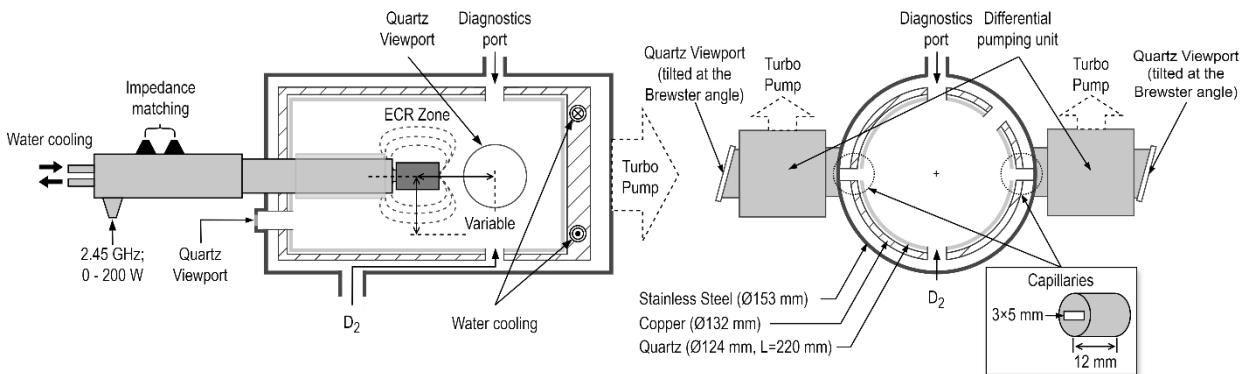


**Figure 2.11.** Schematic representation of the “SCHEME-II+” reactor, with details of its main structural properties. The quartz viewports placed on either side of the reactor are tilted at the Brewster angle so that when laser-based diagnostics are applied proper transmission of the radiation is ensured.

The reactor consists of a cylinder made of Quartz (aluminosilicate glass – Schott™ 8250), having an inner diameter of 124 mm and a length of 220 mm. Its thickness is 3 mm. Two Quartz disks are also placed on both ends of the reactor chamber, as well as another tube on the body of the ECR module. This Quartz cylinder is further enclosed in two other larger cylindrical structures; first, a cylinder made of copper while the outermost one, which is the external wall of the reactor, is made of stainless steel. These have inner diameters and thicknesses of 132 mm and 5 mm, and 153 mm and 2 mm, respectively. The copper cylinder is additionally actively cooled by a closed-loop water system at a temperature of 283 K. The reactor is evacuated by means of a

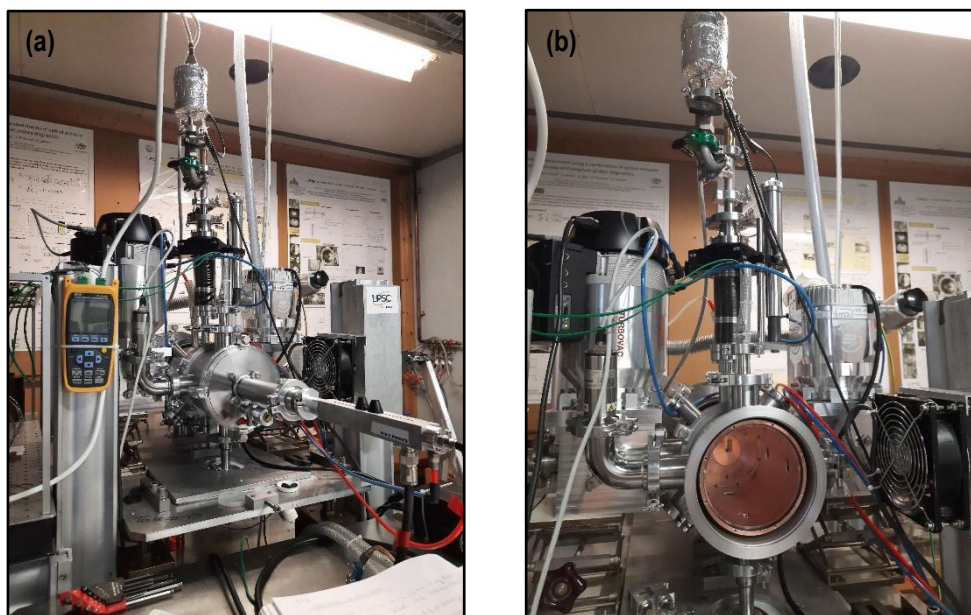


**Figure 2.12.** Photos of the “SCHEME-II+” reactor (a) with the front flange holding the dipolar ECR module in position, and (b) without the front flange so that the interior structure is visible.

two-stage pumping system comprising three turbomolecular pumps backed up by two rotary oil pumps (in the case of the experiments that are described in section 2.2.1 these are replaced by two dry rotary pumps). The main turbomolecular pump, with a maximum pumping capacity of 600 l/s, is directly fitted on the rear side of the reactor, whereas the other two, having a pumping capacity of 300 l/s, are placed on two smaller cubic chambers on either side of the reactor (see **Fig. 2.11**). It is worth noting that the main turbomolecular pump is operated at just nearly one third of its nominal speed (287 RPS) resulting in a pumping capacity of approximately 250 l/s in order to maintain a suitable pressure and to reduce the consumption of gas [68]. The differential pumping unit is completed by a set of capillaries positioned inside the feedthrough connecting the cubic chambers with the main body of the reactor, and intersecting the copper and inox cylinders. The capillaries, shown in the inset of **Fig. 2.11**, possess holes of a rectangular cross section (3 mm  $\times$  5 mm) bored in stainless steel cylinders 10 mm in diameter and 12 mm in length. The design, i.e. the choice of the dimensions, of the capillaries was refined with the aid of the COMSOL Multiphysics<sup>®</sup> software. In particular the Molecular Flow Toolbox is employed, which is generally used for simulating the gas flow in different vacuum structures the physical description of which is dependent upon on the characteristic dimensions of the modeled structure. The key intention in this case is to limit to the greatest extent possible the gas flowing outside of the capillaries and into the differential pumping unit. The entire reactor geometry is reconstructed in the software platform and all of the parameters for the gas intake and pumping are set according to the actual experimental values. For the given system dimensions the Molecular Flow Toolbox conducts calculations based on the free molecular flow regime, in which it is assumed that the gas molecules interact with the surfaces more frequently than they do with each other, and consequently the gas flow is determined by the collisions with the surfaces of the system. Thus, in the present case, the

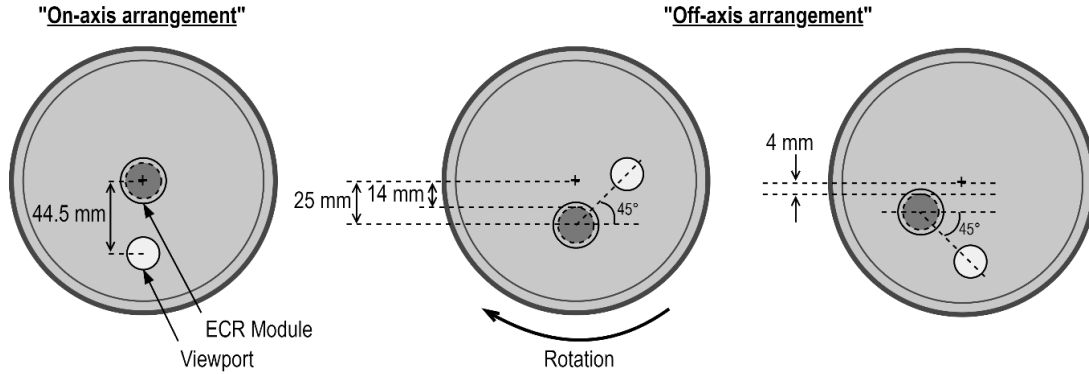


**Figure 2.13.** Illustration of the different flange configurations available for fitting on the front side of the “SCHEME-II+” reactor, on which a single ECR module is mounted. The first illustration from the left shows the standard case where the axis of the module coincides with the reactor axis. The remaining two depict the case for which the module is mounted “Off-axis”. In the latter cases, vertical displacement of the ECR module within the volume of the reactor is achieved with the rotation of the entire flange and necessitates venting the reactor.

model calculates the particle density along a specially-drawn virtual elementary surface representing the line of sight of interest, i.e. the line of sight extending across the reactor, from one side of the differential pumping unit to the other. More details on these activities are given in Appendix A.

Two Pirani gauges and a Baratron<sup>®</sup> capacitance manometer provide the means to monitor the pressure in the differential pumping chambers and the main reactor structure, respectively. Accordingly, base pressure values of  $9 \times 10^{-6}$  Pa and  $1.5 \times 10^{-4}$  Pa are routinely achieved. Pure  $D_2$  (99.9%) gas is introduced into the reactor by means of a mass flow controller.  $D_2$  plasmas are sustained by a single dipolar ECR module (identical to those employed at the “Prometheus I” reactor presented in the previous section) driven by a solid-state microwave generator (2.45 GHz) capable of supplying up to 200 W of power. The ECR module is mounted on the stainless steel vacuum flange closing the reactor from the front side via a feedthrough establishing a good vacuum joint. The feedthrough allows for the horizontal displacement of the module (forward and backward motion) while the reactor is maintained under high vacuum. Moreover, except for the standard case where the axis of the ECR module coincides with that of the reactor, a specially designed vacuum flange has been used to mount the module “Off-axis” at a distance of 25 mm from the center. In the latter case, the rotation of the flange causes the displacement of the ECR module along the reactor radius, albeit not on the same vertical axis. **Fig. 2.13** illustrates this point. The viewport on the “Off-axis” vacuum flange allows for the observation of the same region within the ECR zone regardless of the positioning of the flange. Additionally, several other viewports available around the reactor allow for the installation of different diagnostics

(e.g. Langmuir probes, Optical Emission Spectroscopy etc.), as well as the observation of the plasma and of the good operation of the ECR module.

The “SCHEME-II+” reactor has been especially designed to interrogate plasma-surface interactions, with focus on the assessment of different materials with respect to the creation of ro-vibrationally excited molecules, since the latter are integral particles in the volume production scheme of negative ions. In addition to Quartz, which serves as the reference surface, the materials whose influence is evaluated are tungsten (W) and tantalum (Ta). This means that the plasma faces a material either of low ( $\gamma - 0.004$  at 290 K for Quartz) [100], [101] or high recombination probability ( $\gamma$  up to 0.5 at 240-300 K for metallic surfaces) [100], [155]. The studied materials come in the form of commercially available metallic sheets (0.1 mm thick), which are set flat on the Quartz surface to achieve a full (100%) coverage of the reactor interior.

The details of the diagnostics that have been applied at the “SCHEME-II+” reactor in the framework of this thesis are presented in the following sections.

### **2.2.1 Vacuum Ultraviolet (VUV) Fourier Transform absorption spectroscopy with synchrotron radiation**

The key role of the ro-vibrationally excited  $\text{H}_2/\text{D}_2$  molecules on the creation processes of the corresponding negative ions was explained in detail in section 1.5 of the introductory chapter. Thus, probing these species is imperative. In fact, two main approaches can be considered. On the one hand, there are methods which can indirectly provide information on the formation of the ro-vibrationally excited molecules. Principally, this implies probing by-products of reactions in which these molecules are involved. The laser-induced photodetachment technique is the best example, since knowledge on the behavior of the negative ion population can be traced back to their origin, i.e. the molecular species. On the other hand, there are several techniques that can access, directly, the ro-vibrationally excited molecule population.

A concise review of works devoted to this subject is given in [68]. Epigrammatically, multi-photon ionization (MPI), resonantly-enhanced MPI (REMPI), Vacuum ultraviolet (VUV) laser absorption spectroscopy, Coherent Anti-Stokes Raman (CARS) spectroscopy, laser-induced fluorescence (LIF) with VUV laser beams generated via stimulated anti-Stokes Raman scattering (SARS) in a cold high-pressure hydrogen Raman cell, and photon-induced fluorescence spectroscopy (PIFS) using synchrotron radiation are diagnostics that can be used to access this information.

Béchu et al., first in 2016 [67], demonstrated the possibility to use synchrotron radiation to perform VUV absorption spectroscopy and access the rotationally and vibrationally excited levels of the ground state hydrogen molecule. The experiments were carried out at the state-of-the-art DESIRS (Dichroisme et Spectroscopie par Interaction avec le Rayonnement Synchrotron)

undulator-based beamline at the SOLEIL synchrotron facility (St. Aubin, France) [156], [157]. Despite the success of this first experimental attempt, the number of observable bands was limited to five transitions  $\text{H}_2 \{B^1\Sigma_u^+(v'=0)\} \leftarrow \text{H}_2 \{X^1\Sigma_g^+(v''=2 \text{ to } 6)\}$  and in the best case restricted from  $J''=0$  to 4 or to 5 [68]. In subsequent experimental campaigns (held in 2018 and in 2020) during which the “SCHEME-II+” reactor is used, the exploitation of the wave-front division-based interferometer Fourier-Transform Spectrometer (FTS), a permanent end-station at the DESIRS beamline, significantly broadened the capabilities. The installation of the reactor downstream the beamline is shown in **Fig. 2.14**.

The photon source is a 10 m long pure electromagnetic variable polarization undulator providing, at the sample location, fully calibrated quasi-perfect horizontal, vertical and circular

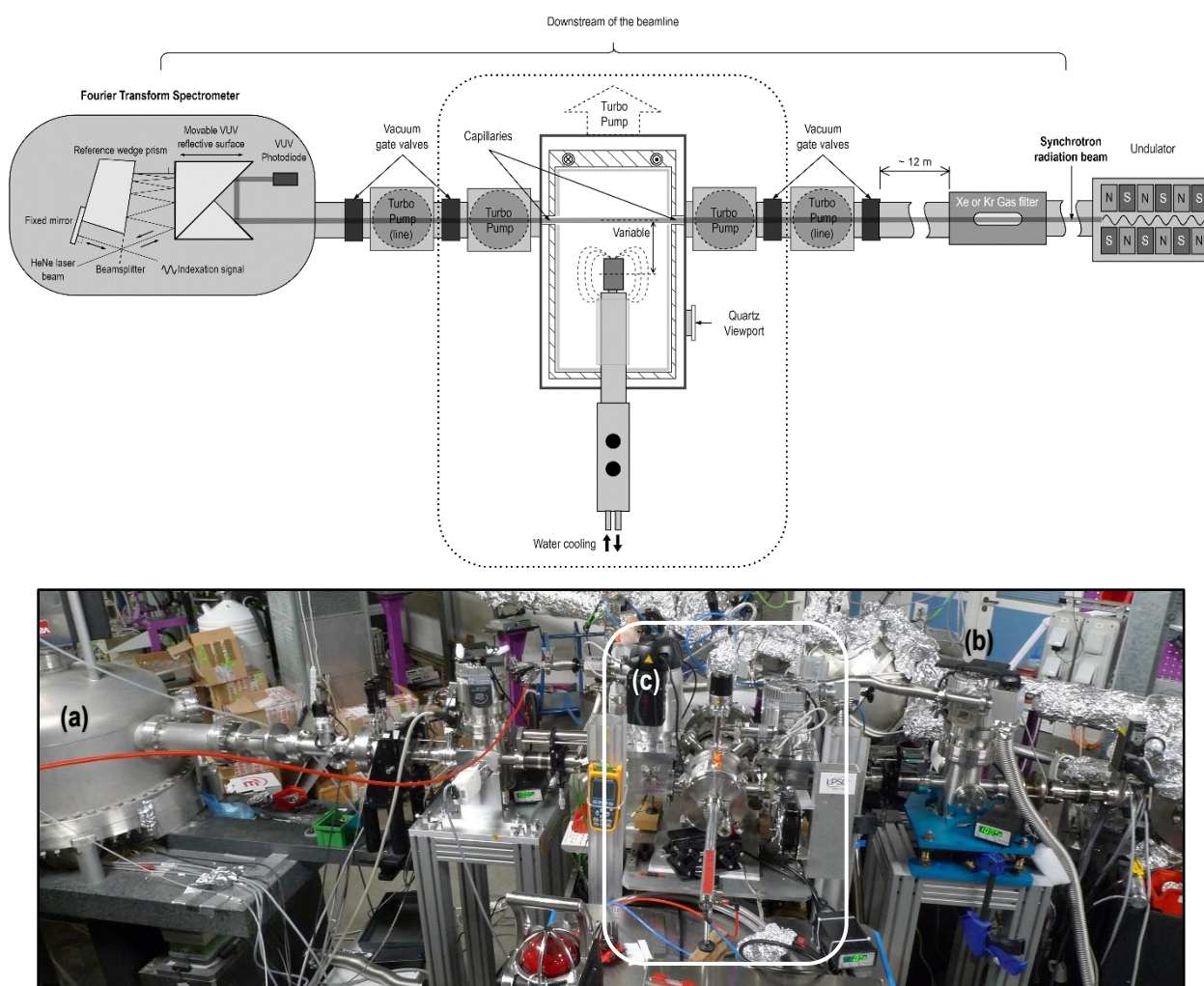


**Figure 2.14.** Top: Schematic of the installation of the “SCHEME-II+” reactor along the DESIRS beamline at the SOLEIL synchrotron facility. The dotted frame distinguishes the components of the beamline from those belonging to the experimental setup. Bottom: Photo of the actual setup corresponding to the part from the FTS to the turbomolecular pump of the beamline on the right side of the reactor as illustrated on the schematic; (a) the FTS, (b) the turbomolecular pump of the line, and (c) the box marks the boundaries of the “SCHEME-II+” reactor setup.

polarizations [156]–[158]. The optical design includes a beam waist allowing the implementation of a rare gas (Xenon or Krypton) filter to suppress the higher harmonics emitted by the undulator [156], [157], [159]. Finally, the radiation delivered is of a quasi-Gaussian shape with a Full Width Half Maximum (FWHM) of around 7% around its central frequency. The central frequency of the radiation is altered by imposing different values of the current flowing through the undulator. This harmonic-free radiation is then steered towards the FTS for absorption experiments [156]. The FTS is a unique instrument, which offers an unprecedented resolving power ( $R = \lambda/\delta\lambda$ ) in the  $10^6$  range, covers a broad range of wavelengths from 250 nm to 40 nm, has an extrinsic absolute wavelength accuracy of  $1 \times 10^{-7}$  nm and a high signal-to-noise ratio [160]. Typically, a FTS instrument is based on a Michelson interferometer in which one mirror is moved to vary the optical path difference (OPD) between the interfering beams. One records the interferometric signal versus the OPD to get the interferogram. The spectrum is then recovered from the interferogram by an inverse FT operation. The construction of the FTS instrument [160], [161] of the DESIRS beamline is based exclusively on reflective optical surfaces giving access to the UV-VUV spectral range offered by the beamline, provided however that no additional window is inserted along its path [68]. The exploitation of this range at the “SCHEME-II+” reactor implies its coupling to the beamline in a window-less mode, whilst special measures are taken to prevent any perturbation of the ultra-high vacuum of the FTS and the beamline. Firstly, the “SCHEME-II+” reactor implements a differential pumping system, described before, with a set of turbomolecular pumps (300 l/s) and capillaries placed on either side of the reactor. Already, with this first differential pumping stage the pressure is reduced to  $1.6 \times 10^{-3}$  Pa when, at the interior, the reactor is at a pressure of 1.6 Pa. A second differential pumping stage, comprising a set of turbomolecular pumps (300 l/s) and rectangular tubes shaping the incident beam ( $8 \times 5$  mm<sup>2</sup>, 150 mm long), are placed on the synchrotron beam exit and on the FTS entrance sides, respectively. Thus, the differential pumping system is completed allowing for a final pressure of around  $6 \times 10^{-6}$  Pa. For added safety, vacuum gate valves are used to isolate both the two differential pumping stages from the rest of the beamline, and the two stages themselves.

In the frame of this work, the molecular absorption transitions which are examined are limited to those from the ground  $X^1\Sigma_g^+$  state to the singlet  $B^1\Sigma_u^+$  state (see **Fig. 1.4**), known as the Lyman band. Hereafter,  $BXv'-v''$  will be used throughout the text for simplicity, denoting the transitions from the ground  $X^1\Sigma_g^+$  state, at the  $v''$  vibrational level to the singlet  $B^1\Sigma_u^+$  state and at the  $v'$  vibrational level. Although, also transitions to the singlet  $C^1\Pi_u^-$  state are present and observable in the probed UV-VUV range, they are not examined since those spectra are more dense and blending effects are common [68]. However, besides the BX transitions, up to seven absorption lines corresponding to the atomic Lyman series can be discerned and evaluated to infer the absolute population of the atoms lying in the ground state, i.e. in the  $D(n=1)$  level.

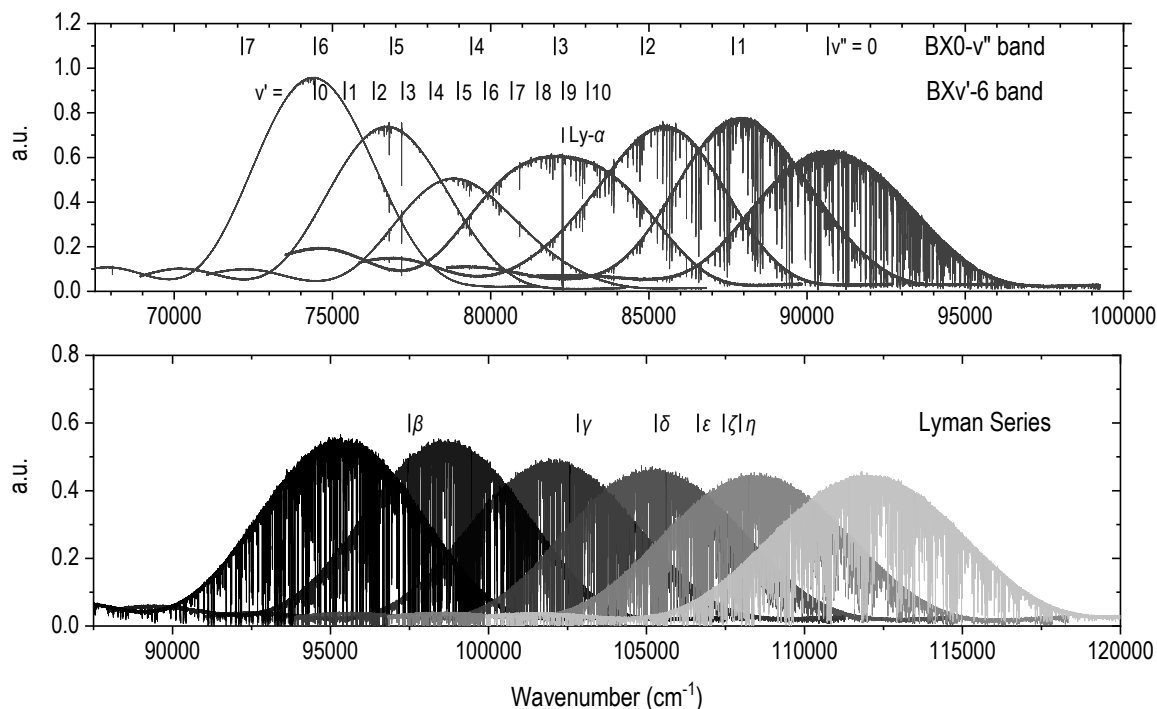


**Figure 2.15.** Raw absorption spectra obtained from VUV-FTS for thirteen undulator settings, covering the 66000-122000  $\text{cm}^{-1}$  energy range. The experimental conditions to which they correspond are:  $\text{D}_2$  gas, 1.6 Pa, 150 W with a 100% Quartz surface facing the plasma. Above the spectra, vertical lines note the positions of the  $\text{BX0-v}''$ ,  $\text{BXv}'-6$ , and the seven first atomic Lyman transitions.

An example of the synthesis of thirteen raw absorption spectra, corresponding to thirteen different undulator settings, is shown in **Fig. 2.15**. In the raw spectra, the absorption lines appear as sharp decreases in the Gaussian-like illumination intensity. On the same figure, vertical lines indicate, as an example, the wavenumbers of the transitions  $\text{BX0-v}''$  and  $\text{BXv}'-6$ , and those of the first seven atomic Lyman lines, among the multitude of the existing absorption lines. Typically the recording of a spectrum has a duration of 10-15 min, depending however on the parameters used in the software for the acquisition of the spectra such as the sampling rate and the scanning speed (i.e. the speed of the movement of the reflective surface, typically around  $0.15 \text{ mm s}^{-1}$ ). The recording of the thirteen spectra, covering the entire energy range of interest may take up to 3 hours. Processing of the acquired spectra towards the determination of the distribution of the molecule population over the vibrational levels of the ground electronic state requires a meticulous analysis procedure, which will be further discussed in Chapter 4.

In the course of that analysis, it will be seen that it is useful to have knowledge on the gas temperature. While there are several different diagnostic techniques with which it can be inferred, in the present thesis Tunable Diode Laser Absorption Spectroscopy (TDLAS) was employed to have an estimation. Since there is no such laser that can generate radiation in the VUV region so as to directly probe the atomic ground state, the method is applied to the  $n = 2$  level, i.e. to the Balmer- $\alpha$  transition  $\text{D}(n = 3) \leftarrow \text{D}(n = 2)$  at a wavelength of 656.1 nm, and the gas temperature

is deduced from the Doppler broadening of this line. The reasons behind the justification of the fact that the velocity of the atom population in the  $n = 2$  level is linked to that of the ground state D atoms is based on the identification of the main mechanism leading to the atom formation, and on whether their lifetime is sufficiently long for them to come to thermal equilibrium with the rest of the gas.

**Fig. 2.16** illustrates the installation of the TDLAS diagnostic at the “SCHEME-II+” reactor. Laser radiation is emitted by a tunable diode laser (Toptica; DL 100) at a wavelength that can be finely regulated by the control of the diode’s current and/or temperature. The laser head is cooled by a closed-loop water circuit at a temperature of approximately 290 K. A free space isolator firstly intercepts the laser beam in order to prevent any back-reflection of the beam into the laser. Subsequently two non-polarizing beamsplitters are placed in the laser path. The first branch is steered into a Fabry-Perot interferometer (630 nm – 824 nm; FSR (Free Spectral Range) equal to 1.5 GHz). The second branch is directed towards a light detector (photodiode) and acts like a reference branch, while the rest of the main beam is routed by means of a high-energy reflective mirror into the reactor, through the left differential pumping unit, the capillaries and the right differential pumping unit. As the beams exits, a second high-energy reflective mirror is placed nearly perpendicularly to the beam so as to reflect it back through same optical path. In practice, there is a slight angle between the incident and returning beams (exaggerated in **Fig. 2.16** for clarity) so that its path does not meet the mirror placed on the entrance side, but

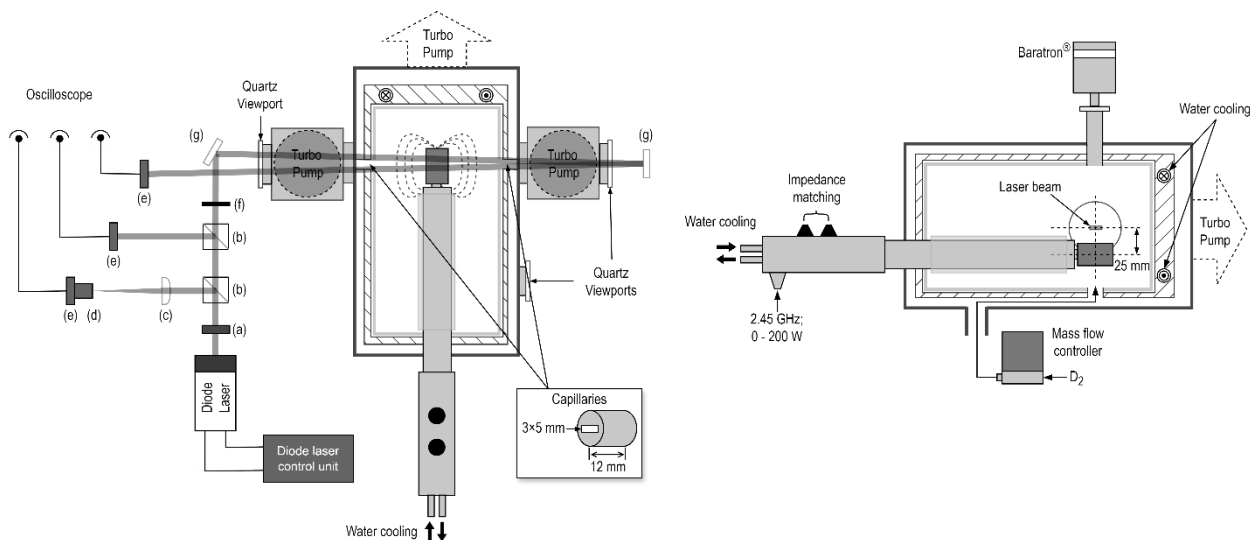


**Figure 2.16.** Illustration of the installation of the TDLAS diagnostic at the “SCHEME-II+” reactor. The optical components used are: a) free space isolator, (b) cage mount non-polarized cube beamsplitter, (c) plano-convex lens, (d) Fabry-Perot interferometer, (e) Light detector, (f) intensity filter, and (g) high-energy mirror. It is noted that the angle between the incident and returning beam, traversing the reactor through the viewports which are tilted at the Brewster angle, is exaggerated here for clarity. On the right side of the figure, a cross section of the reactor structure reveals the particular configuration under which measurements were carried out.

instead passes it and reaches a second light detector which records the absorption signal. It is opted to traverse the reactor twice because this can increase the sensitivity of the method.

An example of the signals recorded from the Fabry-Perot interferometer and the last light detector tracing the laser beam intensity on the oscilloscope is given in **Fig. 2.17(a)**. For the signals coming from the light detector two cases are distinguished in the same figure, one without and one with the presence of a plasma. In the first case, i.e. in the absence of a plasma the light intensity follows the characteristic ramp shape imposed by the same the diode current as the wavelength is scanned in the desired narrow range. When a plasma is present, a drop in the recorded laser beam intensity is evident, which corresponds to the absorption profile of the light by the probed atomic transition.

**Figs. 2.17(b)-(d)** subsequently show the procedure that is used to determine the gas temperature, symbolized as  $T_g$  hereafter. Firstly, a single side of the ramp-like absorption signal is isolated. At the same time, the ordinate is converted into units of frequency based on the knowledge of the FSR of the Fabry-Perot interferometer which gives the optical frequency between two successive peaks in the signal displayed in **Fig. 2.17(a)**. An example of an isolated absorption line is given in **Fig. 2.17(b)**. The next step consists in fitting a linear baseline to this part of the signal (dashed line on the same subfigure), and then subtracting it. **Fig. 2.17(c)** displays the final step, in which a Gaussian profile is fit to the absorption line and the FWHM is calculated. It is noted that at this point the signal amplitude has been normalized to unity, and the data is centered around the frequency of the peak. Once determined,  $T_g$  is deduced through the relation linking the two parameters [135]:

$$\frac{\Delta v}{v_0} = 7.16 \times 10^{-7} \sqrt{\frac{T_g}{m}} \quad (2.3)$$

where  $\Delta v$  is equal to the FWHM,  $v_0$  is the frequency of the Balmer- $\alpha$  transition for deuterium (456.793 GHz), and  $m$  is the molar mass of the particle (2 for deuterium). The described procedure

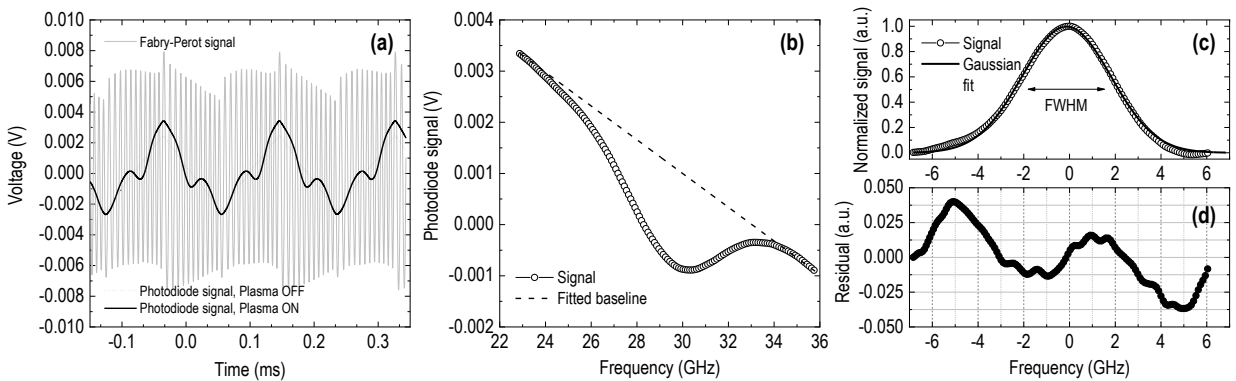


**Figure 2.17.** (a) Indicative signals obtained with the TDLAS installation. Among them the absorption signal recorded by the photodiode is distinguished. (b)-(d) illustration of the steps in the procedure for the extraction of the gas temperature, described in detail in text.

can be then repeated for the number of ramps observable in the time-window in order to additionally derive an error.

## 2.2.2 Pulsed plasma regime

Section 1.7 introduced the concept of plasmas sustained in the pulsed mode of operation, and evidenced that investigation of the parameters of a discharge in a time-resolved manner can unveil invaluable information related to the evolution of the plasma chemistry and the kinetics that govern different species. At the “SCHEME-II+” reactor, the feasibility to scrutinize  $D_2$  plasmas in such an operational regime is demonstrated. Primarily, special attention was paid to achieve the synchronization of the discharge pulses with the diagnostic techniques that would be used. In the present study, this entails the synchronization to the plasma pulses of the Langmuir probe and the laser-induced photodetachment diagnostics. The installation of these two is described in the following paragraph prior to the presenting the synchronization scheme.

**Fig. 2.18** presents a schematic representation of the installation of the two aforementioned diagnostics at the “SCHEME-II+” reactor. The Langmuir probe is inserted into the reactor through a standard feedthrough, 16 mm in diameter, positioned on the top and 42 mm from the back of the reactor. Additionally, it is fitted onto a vertical translator, allowing for its radial displacement. Since, on top of that, the ECR module can also be moved along the axis and off-axis to different positions, several different configurations of the reactor can be achieved. In the frame of this work, one particular configuration has been investigated with respect to these techniques and is displayed in **Fig. 2.19**. In the same figure, details are given regarding the

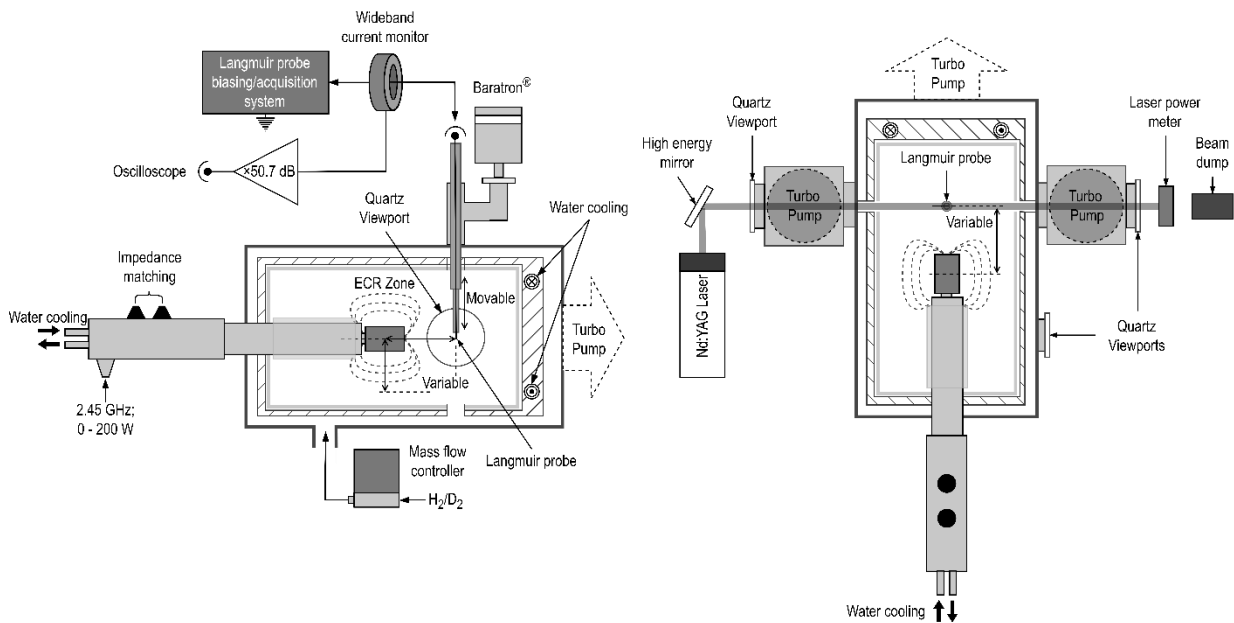


**Figure 2.18.** Illustration of the installation of the Langmuir probe and the single-beam laser-induced photodetachment diagnostics, at the “SCHEME-II+” reactor. It is important to note that the two quartz viewports through which the laser beam passes are tilted at the Brewster angle.

construction of the probes that are used. The probes are custom-made in the laboratory, and so is the system (hardware and software) for the acquisition of the characteristic probe current-voltage curves. In general, the probes consist of a tantalum wire 0.5 mm in diameter, housed in a telescopic arrangement of alumina tubes. This structure is further supported inside a stainless steel tube that ends in a standard BNC vacuum feedthrough. A conflat flange to quick-connect coupling adapter makes a vacuum joint with the steel tube. In the present configuration the plasma region being probed is that 75 mm downstream of the middle plane of the magnet of the dipolar ECR module, i.e. the diffusion zone, where negative ion production is expected to take place. The dipolar ECR module is aligned with the axis of the reactor itself.

The laser-induced photodetachment technique is based on a Nd:YAG laser (Quantel, Brilliant) with the following specifications: 1064 nm wavelength, 150 mJ max. energy per pulse, 10 ns pulse duration, and a repetition rate of 50 Hz. The laser beam is directed by means of high-energy mirrors, and traverses the reactor through the Quartz viewports and the capillaries situated on either side of the differential pumping chambers. Fine adjustments to the positioning of the mirror ensure the good alignment of the beam, which due also to the capillaries obtains a rectangular cross-section. The laser beam energy is monitored with a high energy-density thermal detector connected to an energy meter, placed on the exit (right) side of the installation. The beam energy is regulated to the desired level by adjusting the inherent delay between the laser Flashlamp fire and the Q-Switch output, or by tuning of the built-in energy regulation system which is integrated on the laser head. Typically, an energy density inside the reactor of around 70 to 75 mJ cm<sup>-2</sup> is opted for, which is calculated after taking into account a beam cross-section of 15 mm<sup>2</sup> imposed by the capillaries and an attenuation of the laser beam energy of about 7% due to the presence of the Quartz viewport. In essence, these choices are made based on the same criteria that have been laid out for the case of the “Prometheus I” reactor, presented in section 2.1.2. In the absence of the pyroelectric sensor head, a beam dump restricts the further propagation of the laser beam. It should be noted that the application of the photodetachment

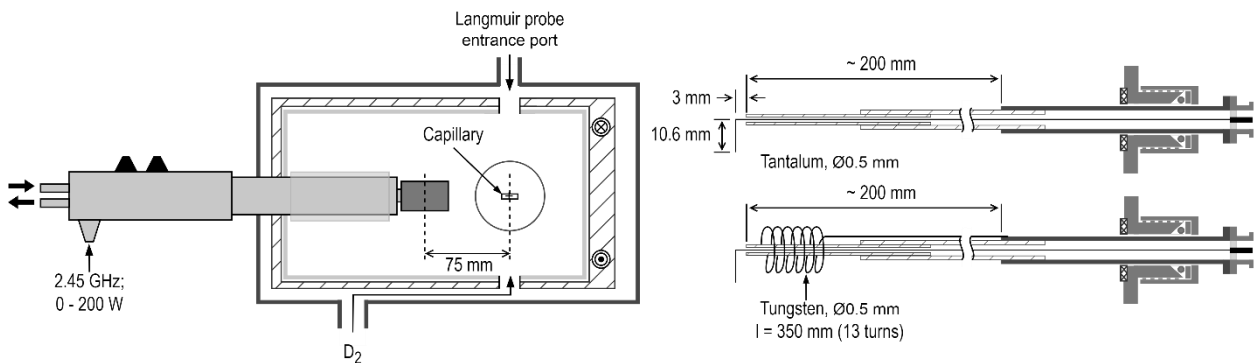


**Figure 2.19.** Schematic representation of the configurations of the “SCHEME-II+” reactor for which the Langmuir probe and laser-photodetachment diagnostics have been applied. On the right: there are presented the construction details of the Langmuir probes that have been used.

technique necessitates that the tip of the Langmuir probe is of an L-bent topology, so that the bent –and greater in length– part can be co-axially aligned with the laser beam. The impulse current imposed by the photodetached electrons, is detected by a wideband current monitor (Pearson™ Electronics; 300 Hz – 200 MHz), subsequently amplified by an operational amplifier based circuit (3 ns signal propagation delay; 2 kHz – 80 MHz; 50.7 dB gain), and finally recorded on a digital oscilloscope (400 MHz, 2.5 GSamples s<sup>-1</sup>).

Furthermore, afore-presented reactor configurations, the cases for either a 100% Quartz or 100% metallic coverage of the interior are studied. The application of the Langmuir probe diagnostic and the recording of current-voltage curves especially in the former case requires caution. The particularity arises from the dielectric nature of Quartz, unlike the case of a fully metallic interior, which makes no electrical contact with the rest of the vessel walls which are grounded. Therefore, the standard circuitry requirements for the proper application of Langmuir probe measurements is not satisfied. This necessitates the insertion of a supplementary electrode, connected to the ground, which would serve as a reference. Additional requisites include firstly, this electrode to be placed relatively close but in such a way that it would not come in contact with the tip of the probe, and secondly, it should not impede the vertical displacement of the probe within the reactor. The design that was deemed to simultaneously satisfy the above criteria was that of a coil, as shown in **Fig. 2.19**. The coil is made out of a tungsten wire 0.5 mm in diameter and about 350 mm in length. Alternatively, the use of a double-probe would be efficient to extract the plasma parameters, but would be restricting in that photodetachment measurements would not be feasible since a double probe cannot be biased above the plasma potential [138], [163]. A separate series of measurements, available in Appendix B, was carried out to validate the correctness of the use of this custom-made probe. However, the coil is removed in the case where the interior of the reactor is covered fully (100%) by a metallic surface.

As far as the appropriate synchronization of the techniques with the plasma pulses is concerned, the detailed block diagram of the sequence of events is given in **Fig. 2.20**. The solid-state microwave generator that is used to drive the single ECR module was manufactured based on special, custom, requirements tailored to the present application. Namely, it has the ability to deliver a maximum of 200 W of microwave power (2.45 GHz), both in the continuous-wave mode of operation or in bursts in the up to the kHz range with very fast response times.

In particular for the generation of microwave pulses, the generator is controlled via an externally applied pulse of desired frequency and duty cycle. The characteristics of the latter are determined in a dedicated users interface (LabView) linked to (NI) device for the output of the final analog command pulse. A generator response time as well as rapid rising and falling times of the microwave pulses of 5  $\mu$ s provide seemingly few limitations for the frequency and the duty

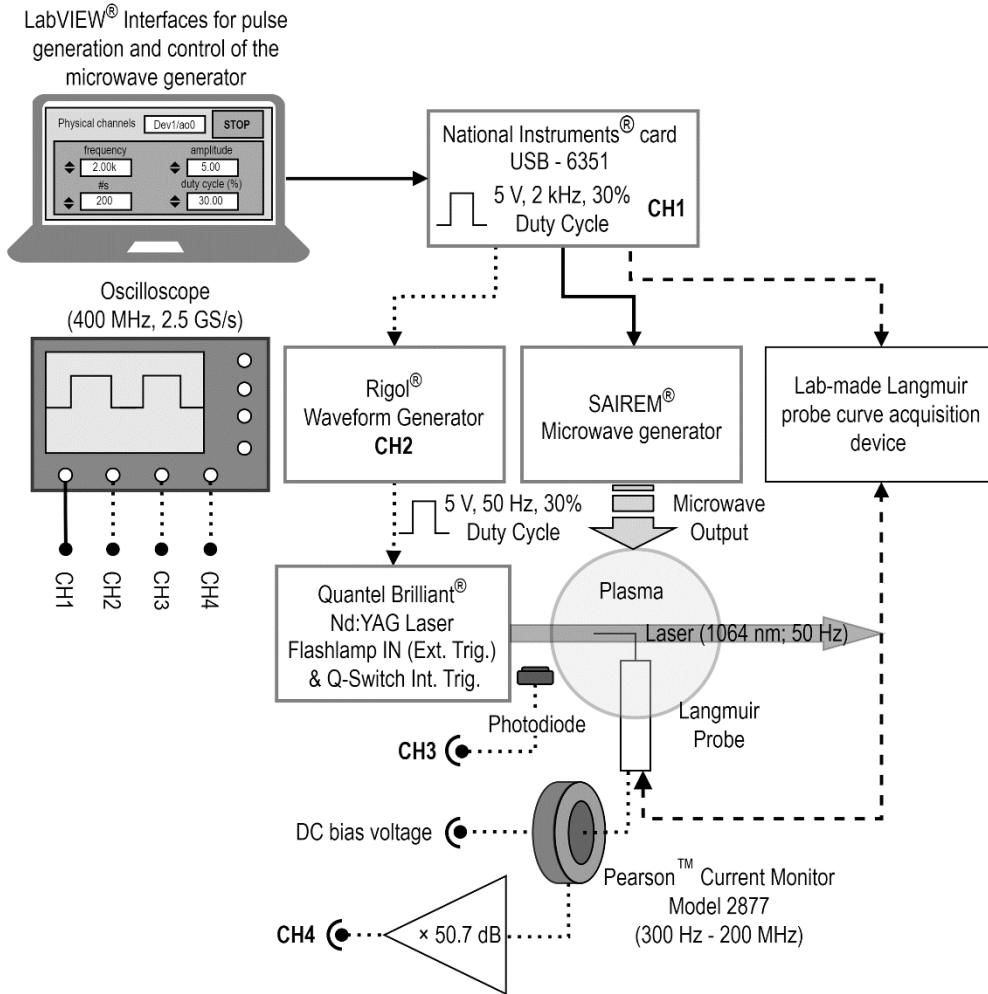


**Figure 2.20.** Block diagram of the synchronization scheme between the plasma pulses and the applied diagnostics, i.e. Langmuir probe measurements and laser-induced photodetachment.

cycle that can be chosen for operation. This command pulse is then considered as the “master” pulse which serves as the reference signal for the synchronization of the rest of the instruments, which in this case is the Langmuir probe biasing and acquisition system and the laser used for the photodetachment measurements.

Recording current-voltage curves with the Langmuir probe at different time points within the plasma pulse is made possible with a special built-in routine in the software of the lab-made curve acquisition system. More precisely, reception of the aforementioned command pulse at the external trigger input of the device signals the beginning of the acquisition procedure. The voltage range as well as the total number of points of a curve are given as initializing parameters in the routine. Time-resolved measurements are carried out by setting a specific time delay,  $\Delta t$ , for the beginning of the acquisition. Essentially this delay denotes the time interval between the reception of the command (trigger) signal by the probe system and the recording of a current-voltage sample. In principle, after the arrival of a command pulse the system waits  $\Delta t$  to then bias the probe and

sample the current. This is repeated for each point on a single curve, while the entire process can be iterated for a specific number of curves.

On the other hand, the synchronization of the laser unit with the plasma pulses for the time-resolved photodetachment measurements is a more intricate task. First of all, the operating frequency of the laser unit (50 Hz) should be respected at all times. Therefore, the command pulse, often lying in the kHz range, is inappropriate to directly trigger the laser unit. An intermediate step is thus necessary. The waveform generator shown in **Fig. 2.20** plays this role; it receives the command pulse and generates a synchronous pulse at the frequency of the laser unit, i.e. 50 Hz. This second pulse is used to control the laser unit which operates in the mode where the Flashlamp is triggered externally and the Q-Switch internally. The laser Flashlamp is turned on upon arrival of the external pulse from the generator but laser radiation is emitted after a given, regulated, delay *FLQS Delay*. The latter delay is crucial since it also determines the laser beam energy. Thus, *FLQS Delay* is set such that the beam energy density measures around  $70 - 75 \text{ mJ cm}^{-2}$ . The analytic timing diagram for the synchronization of the laser unit with the plasma pulses is given in **Fig. 2.21**. It is noted that for this diagram various secondary delays (e.g. inherent delays induced by the waveform generator) are omitted for simplicity. However, it is important to identify such small delays and compensate for them by monitoring at any given time, simultaneously, the

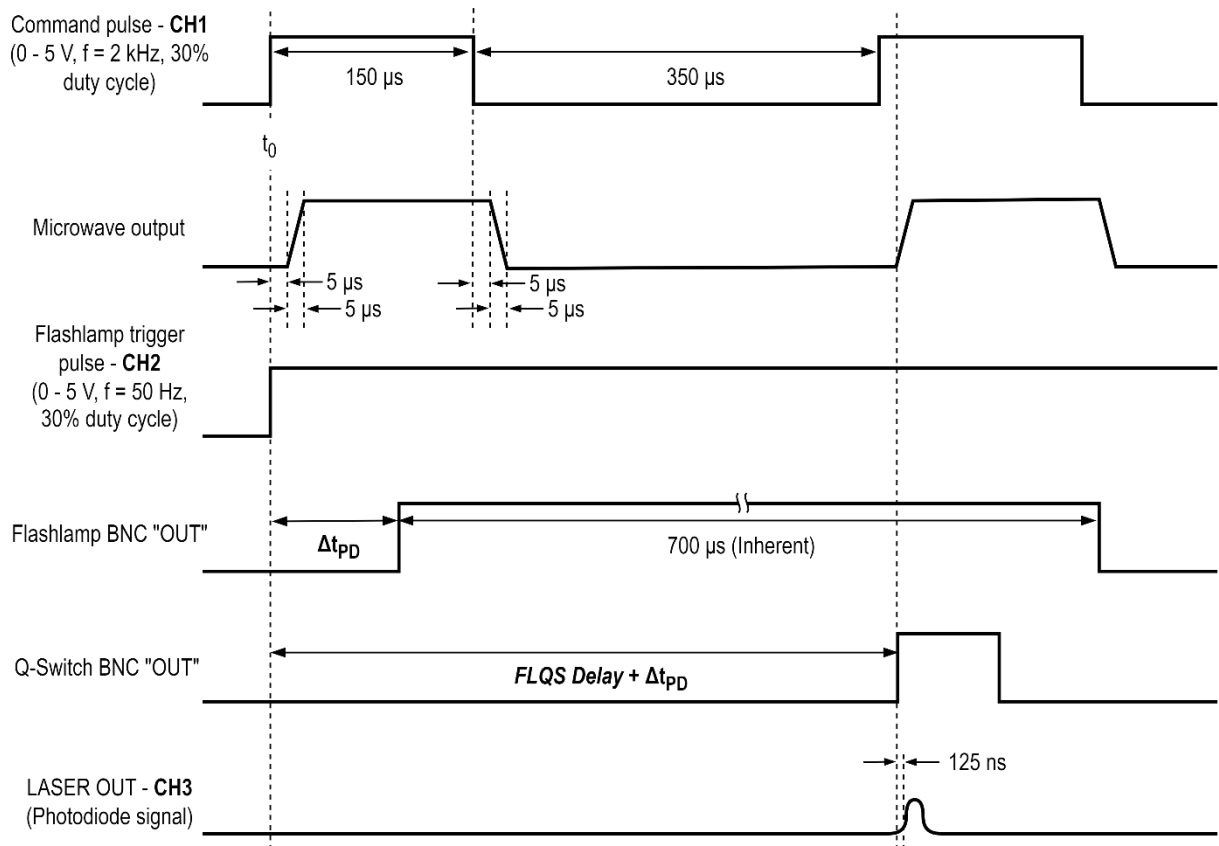


**Figure 2.21.** Timing diagram for the synchronization of the laser unit with the plasma pulses, for the performance of time-resolved photodetachment measurements.

command pulse given to the microwave generator, the pulse driving the laser Flashlamp and the signal originating from the photodiode which follows the actual laser pulse. Finally, the addition of an extra delay  $\Delta t_{pd}$  to the pulse driving the Flashlamp will shift the laser pulse to the desired point in time, allowing for the recording of a photodetachment signal exactly then.

Chapter 5 collects the results of time-resolved investigations of the basic plasma parameters and the negative ion yield, in the most characteristic configurations and operating conditions of the “SCHEME-II+” reactor.

## CHAPTER 3

# COMPARATIVE INVESTIGATION OF BASIC PARAMETERS IN H<sub>2</sub> AND D<sub>2</sub> PLASMAS

---

H<sub>2</sub> and D<sub>2</sub> plasmas produced in the “Prometheus I” reactor are investigated by means of the Langmuir probe and laser-induced photodetachment techniques, and the results are reported in the present chapter. The properties of the two plasmas have been studied parametrically as a function of the reactor’s operational parameters, i.e. the gas pressure and the microwave power delivered to the plasma. Beyond the identification of operational optima, the existing isotope effect is elucidated. Ultimately, these aspects are evaluated with respect to the main processes governing negative ion production on the basis of the volume production mechanism.

### 3.1 Aspects of the analysis of the I–V characteristics

Sections 2.1.1 and 2.1.2 in the previous chapter provided a thorough description of the installation of both Langmuir probe and laser-induced photodetachment diagnostics, used to scrutinize H<sub>2</sub> and D<sub>2</sub> plasmas produced in the reactor “Prometheus F”. Nonetheless, it is deemed important to underline here several additional details regarding the approach which is adopted for the analysis of the I-V characteristics obtained by means of the Langmuir probe diagnostic.

Examples of typical I-V characteristics obtained from H<sub>2</sub> and D<sub>2</sub> plasmas are depicted in **Figs. 3.1(a)** and **(b)**, respectively. A customized software, developed in-house, is used to process these curves in order to extract the basic plasma parameters, i.e. the characteristic potentials of the plasma, the plasma density and electron temperatures. In brief, the floating potential,  $V_f$ , is defined as the potential for which the current collected by the probe equals zero, while the plasma potential,  $V_p$ , is determined from the maximum of the first derivative of the I-V curve. It is then necessary to isolate the current induced by electron collection from the total recorded current. Thus, the ionic

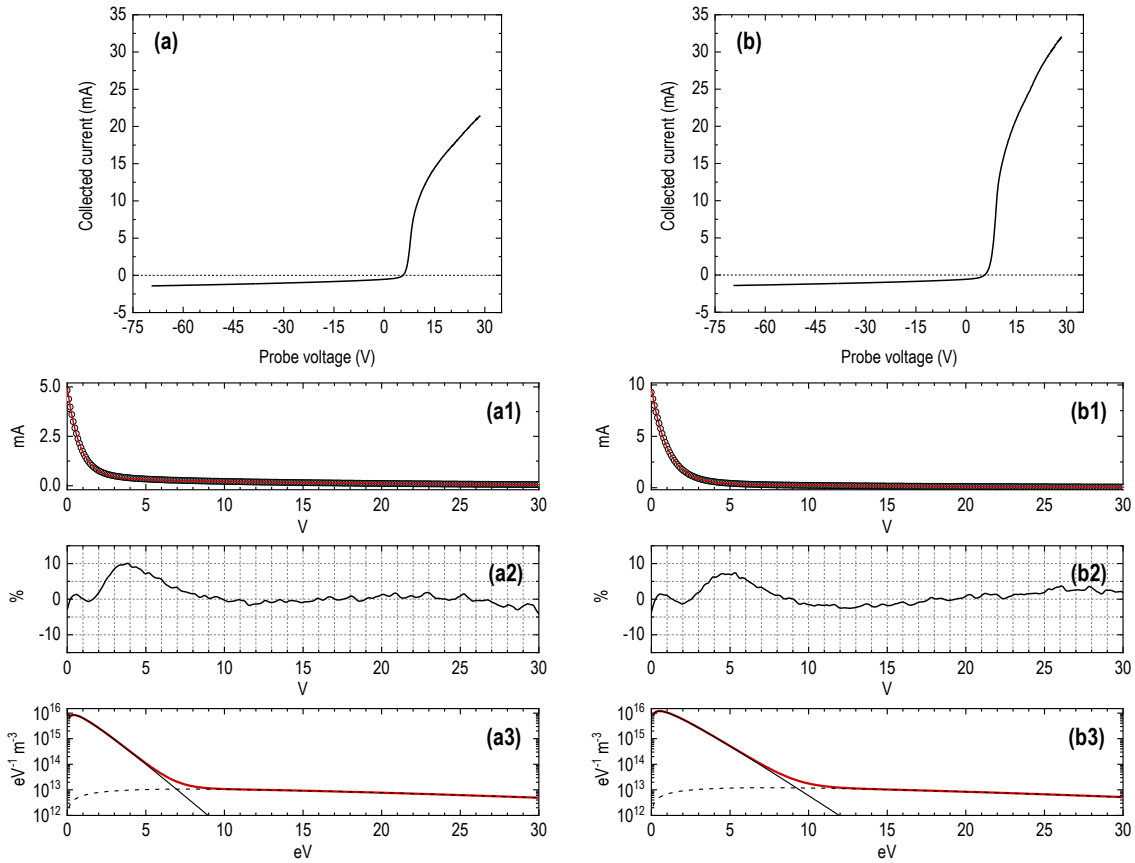


**Figure 3.1.** Representative examples of the current-voltage curves obtained in (a) H<sub>2</sub> and (b) D<sub>2</sub> plasmas, at 1.07 Pa and 0.75 kW. Accordingly, for the two cases: (a1), (b1) Bi-Maxwellian fitting (red line) to the experimentally determined electron current (black line), versus the absolute value of the difference between the probe bias and the plasma potential. (a2), (b2) Percentage of the residuals of the fitting process. (a3), (b3) EEDF (red line) based on the bi-Maxwellian assumption; cold population part (black solid line; 0.81 eV); hot population part (black dashed line; 15.32 eV).

current should be subtracted. A popular approach for the estimation of the ionic current is the extrapolation of a straight line through the region of high retarding potentials up to the plasma potential. Despite its simplicity, [139] communicates the concern about the ambiguity introduced by this method and the potential error that is propagated in the calculation of the EEDFs. Perhaps more accuracy can be achieved by the application of one of the existing theories for ion collection by cylindrical probes, i.e. either the Orbital-Motion-Limited (OML) theory of Langmuir, the Allen-Boyd-Reynolds (ABR) theory, or the theory developed by Laframboise. However, [138] states that refinements to the method of linear extrapolation are usually not necessary since they affect only the high energy tail of the EEDF. Be that as it may, in this study due to the ease of implementation this method has been deemed appropriate. Therefore, following the subtraction of the ionic current, the remaining (electron) current is fitted as the sum of two exponentials, constituting a bi-Maxwellian EEDF. A low- and a high-energy component is thus discerned, corresponding to a “cold” and “hot” electron population, respectively. The values of the electron densities and temperatures for the two populations, i.e.  $n_{e(\text{cold})}$ ,  $kT_{e(\text{cold})}$  and  $n_{e(\text{hot})}$ ,  $kT_{e(\text{hot})}$ , accordingly, are extracted from the resulting values of the fitting parameters of each exponential component. EEDFs from the I-V characteristics are also constructed by using the Druyvesteyn method. The Druyvesteyn formula states that the EEDF is proportional to the second derivative of the characteristic curve [139]:

$$F(\text{eV}) = - \frac{4}{e^2 S_p} \sqrt{\frac{\text{mV}}{2e}} \frac{d^2 I_e}{dV^2} \quad (3.1)$$

Concerning the former way (i.e. the bi-Maxwellian fitting procedure), an agreement better than 10% is achieved between the experimentally recorded electron curves and the theoretically considered fitting functions, as seen in **Fig. 3.1(b)** and **(c)**.

In the sections of the present chapter that follow, the properties H<sub>2</sub> and D<sub>2</sub> plasmas produced in the “Prometheus I” reactor extracted through Langmuir probe measurements using the analysis procedure outlined above, as a result of thorough parametric studies as a function of the basic operational parameters of the reactor will be presented and scrupulously discussed.

### 3.2 H<sup>-</sup> and D<sup>-</sup> production efficiency as a function of microwave power

In this section the properties of H<sub>2</sub> and D<sub>2</sub> plasmas, as a function of the delivered microwave power for several characteristic values of the working pressure of the “Prometheus I” reactor are presented. In particular, the plasma properties are extracted for three representative values of the operating power throughout the available range (0.53 Pa, 1.07 Pa and 1.60 Pa) as the delivered microwave power is varied from 30 W to 180 W per ECR module (0.15 kW to 0.9 kW in total). It is noted that during the experiments the temperature of the reactor walls is not controlled in any way, therefore it is solely influenced by the operational parameters and the measurement

sequence. Nonetheless, for consistency reasons it is monitored with the use of a thermocouple. In between measurements, a 20-min interval is allowed for the thermal stabilization of the reactor. **Table 3.1** provides collective information on the experimental conditions for each value of working pressure and for the minimum and maximum power settings.

**Table 3.1.** Tabulated information of representative experimental conditions (H<sub>2</sub>/D<sub>2</sub>).

Pressure (Pa / mTorr)	0.15 kW		0.9 kW	
	Flow rate (scm) (H <sub>2</sub> / D <sub>2</sub> )	Wall Temp. (°C) (H <sub>2</sub> / D <sub>2</sub> )	Flow rate (scm) (H <sub>2</sub> / D <sub>2</sub> )	Wall Temp. (°C) (H <sub>2</sub> / D <sub>2</sub> )
0.53 / 4	6.9 / 8.6	42 / 44	7.4 / 9.2	116.5 / 128.2
1.07 / 8	11.8 / 15.0	41.7 / 43	12.5 / 15.3	119.3 / 120.6
1.60 / 12	16 / 20.1	40.8 / 41.7	16.8 / 20.7	117.4 / 122.2

With regard to the characteristic potentials of the plasma, first it is shown in **Fig. 3.2** that the floating potential does not differ greatly from one gas to the other and for increasing pressure. In fact, it attains values in the range of 4–6 V for each of the pressures studied, while with increasing power there is only a slight increase. On the contrary, **Fig. 3.3** shows that the plasma potential is consistently higher in the case of a D<sub>2</sub> plasma, regardless of the operational conditions. With increasing power there is a global increase of the plasma potential of about 2–3 V, but remains in the same value range with respect to the operating pressure.

As it has already been mentioned (c.f. section 1.5), a special feature of the reactors utilizing the dipolar ECR modules is the production of two electron populations to which two different temperatures can be assigned. **Fig. 3.4** gives the evolution of the cold electron population as a function of the microwave power. The density lies between 10<sup>16</sup> and 10<sup>17</sup> m<sup>-3</sup>, while a D<sub>2</sub> plasma

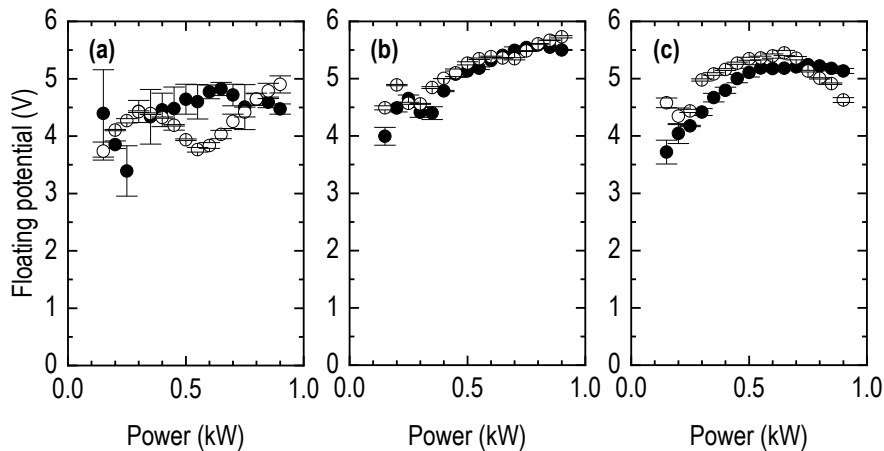


**Figure 3.2.** Floating potential as a function of the microwave power at (a) 0.53 Pa, (b) 1.07 Pa, (c) 1.60 Pa. Solid circles: H<sub>2</sub> plasma. Open circles: D<sub>2</sub> plasma. Mean values and standard deviations are derived from four series of experiments (2 sets on 2 different dates).

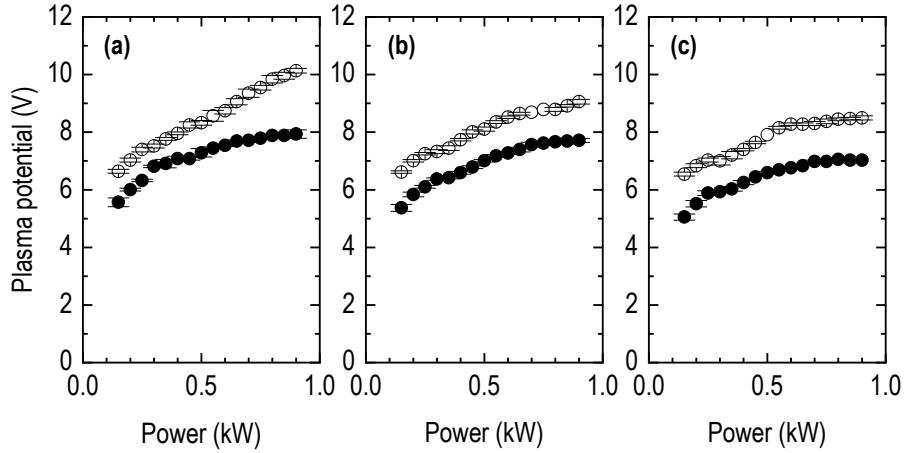


**Figure 3.3.** Plasma potential as a function of the microwave power at (a) 0.53 Pa, (b) 1.07 Pa, (c) 1.60 Pa. Solid circles: H<sub>2</sub> plasma. Open circles: D<sub>2</sub> plasma. Mean values and standard deviations are derived from four series of experiments (2 sets on 2 different dates).

is associated with higher cold electron densities independently of the pressure and the power level. In general, higher power or pressure leads to increased cold electron densities.

**Fig. 3.5** presents the corresponding to **Fig. 3.4** results for the hot electron density. It is recalled that the present measurements deal with the negative ion production region, i.e. the region downstream of the ECR driver region, and thus the hot electron population is not probed in its totality. The absolute density was found to be two orders of magnitude lower than that of the cold electrons. Furthermore, higher power or pressure leads to increased hot electron densities, similar to the cold electron case. On the other hand, the isotope effect seems to be less pronounced in the case of the hot population, since its density in H<sub>2</sub> and D<sub>2</sub> plasmas deviates less (compare **Figs. 3.4** and **3.5**).

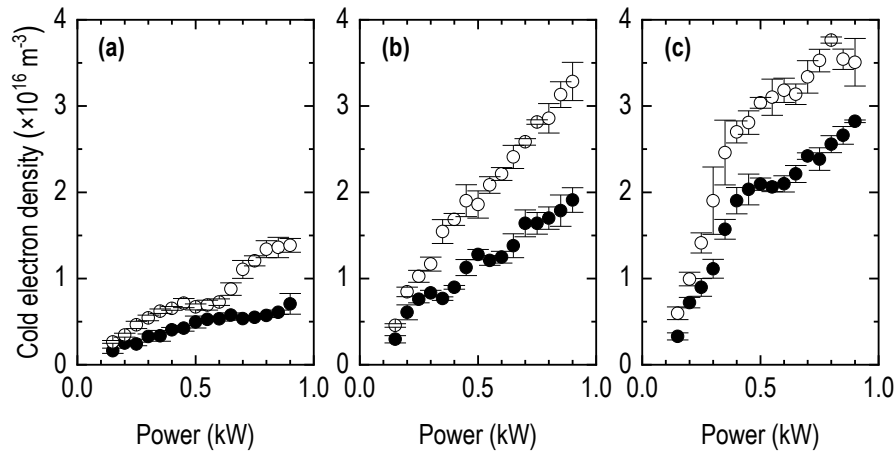


**Figure 3.4.** Cold electron density as a function of the microwave power at (a) 0.53 Pa, (b) 1.07 Pa, (c) 1.60 Pa. Solid circles: H<sub>2</sub> plasma. Open circles: D<sub>2</sub> plasma. Mean values and standard deviations are derived from four series of experiments (2 sets on 2 different dates).

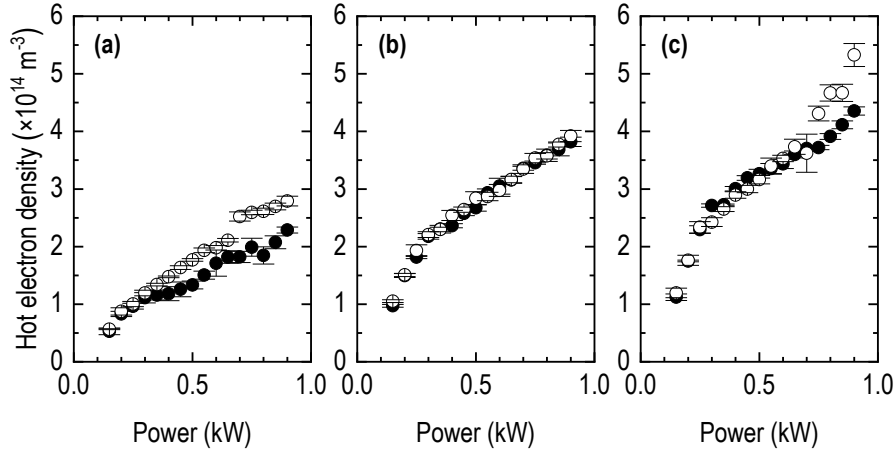


**Figure 3.5.** Hot electron density as a function of the microwave power at (a) 0.53 Pa, (b) 1.07 Pa, (c) 1.60 Pa. Solid circles: H<sub>2</sub> plasma. Open circles: D<sub>2</sub> plasma. Mean values and standard deviations are derived from four series of experiments (2 sets on 2 different dates).

The representative results of **Fig. 3.1**((a1–a3) and (b1–b3)), as well as previous studies [71], have shown that, the above-mentioned two populations follow quasi-Maxwellian distributions. This fact has been confirmed over all of the operational windows studied herein. **Figs. 3.6** and **3.7** provide a direct comparison of the EEDFs obtained in H<sub>2</sub> and D<sub>2</sub> plasmas.

To the extent of what is known, a main gap exists in the literature with regard to the isotope effect on the EEDFs. Thus, the present results suggest a divergence between the H<sub>2</sub> and D<sub>2</sub> plasma EEDFs. As is expected, EEDFs are also pressure and power dependent (only the pressure dependence can be discerned from **Figs. 3.6** and **3.7**). Such differences can regulate the production and destruction processes of the H<sup>-</sup> and D<sup>-</sup> ions. More about this subject will be discussed in section 3.5.

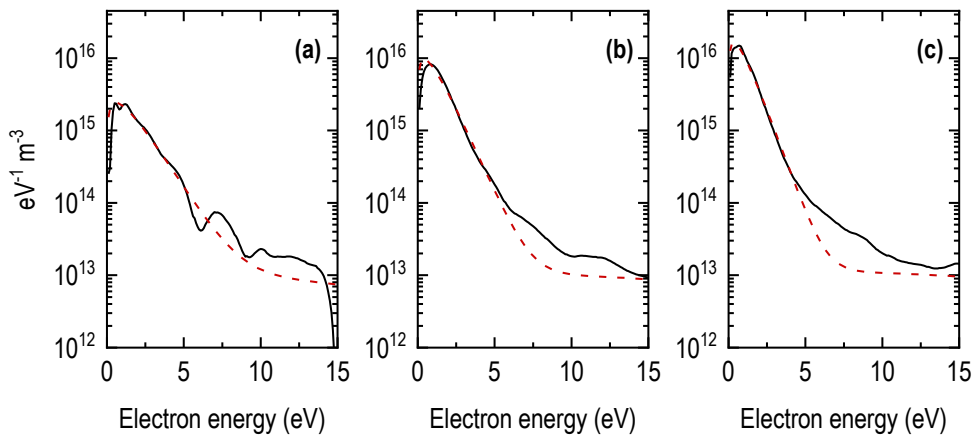


**Figure 3.6.** Representative EEDFs from the H<sub>2</sub> ECR plasmas. (a) 0.53 Pa; 0.75 kW, (b) 1.07 Pa; 0.75 kW, (c) 1.60 Pa; 0.75 kW. Solid black lines: Druyvestyn method. Dashed-red lines: bi-Maxwellian assumption.

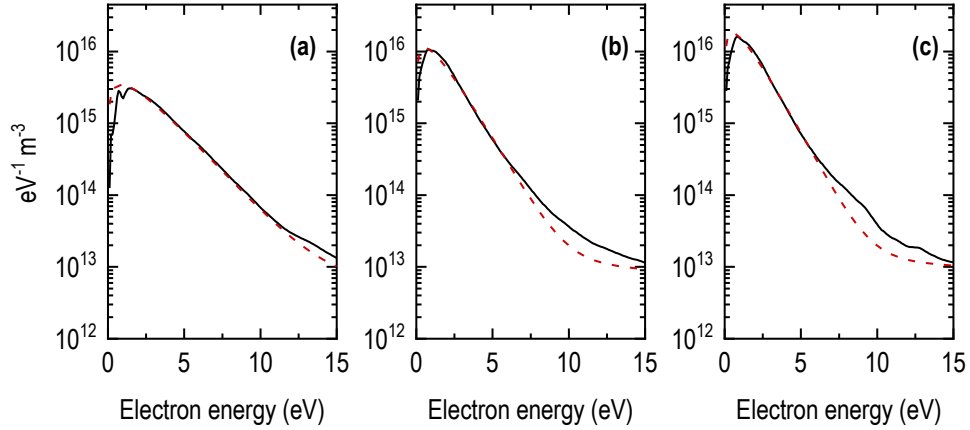


**Figure 3.7.** Representative EEDFs from the D<sub>2</sub> ECR plasmas. (a) 0.53 Pa; 0.75 kW, (b) 1.07 Pa; 0.75 kW, (c) 1.60 Pa; 0.75 kW. Solid black lines: Druyvestyn method. Dashed-red lines: bi-Maxwellian assumption.

The existence of an isotope effect for the EEDFs, as it is demonstrated by **Figs. 3.6** and **3.7**, is further supported if one considers the pressure and power dependence of the cold and hot electron temperatures in H<sub>2</sub> and D<sub>2</sub>, and correlate them with the corresponding densities (**Figs. 3.4** and **3.5**). **Fig. 3.8** displays the existence of higher cold electron temperatures in D<sub>2</sub> plasmas. Otherwise, the ECR heating leads to higher electron temperatures versus the microwave power in both gases. The temperature of the hot electrons, downstream of the ECR zones, is almost constant (around 15 eV) at any experimental condition (**Fig. 3.9**) (see further commentary in section 3.5).

To summarize, D<sub>2</sub> plasma gives cold electrons of higher density and temperature than H<sub>2</sub> does under identical operating conditions. H<sub>2</sub> and D<sub>2</sub> plasmas give, downstream of the ECR zones, hot electrons of comparable temperature whereas their density is either equal (**Fig 3.10(b)**) or slightly higher (**Figs. 3.10(a)** and **3.10(c)**), under identical working conditions. These features are

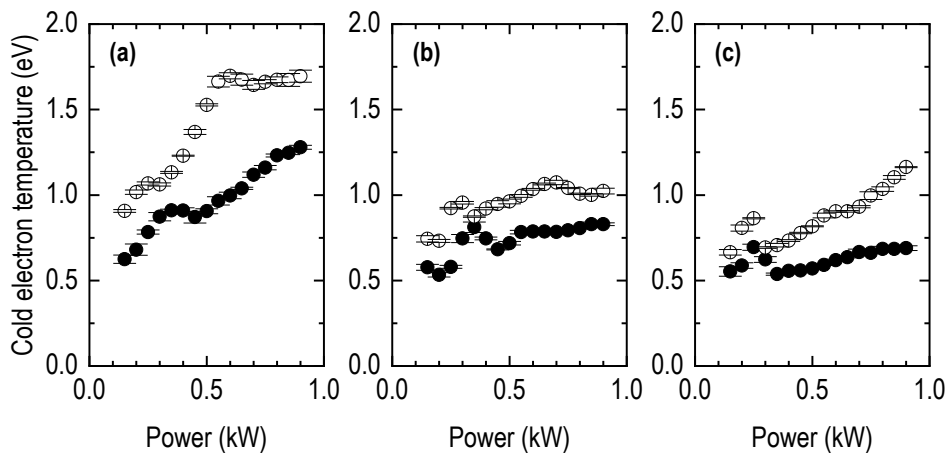


**Figure 3.8.** Cold electron temperature as a function of the microwave power at (a) 0.53 Pa, (b) 1.07 Pa, (c) 1.60 Pa. Solid circles: H<sub>2</sub> plasma. Open circles: D<sub>2</sub> plasma. Mean values and standard deviations are derived from four series of experiments (2 sets on 2 different dates).

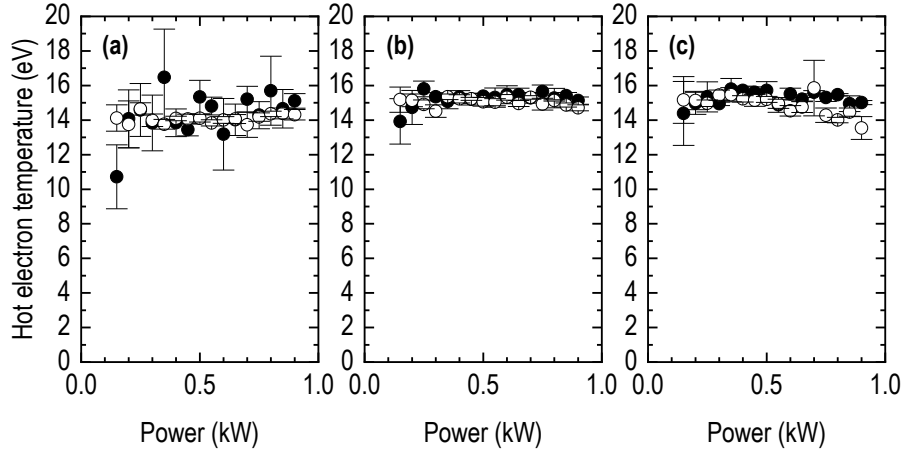


**Figure 3.9.** Hot electron temperature as a function of the microwave power at (a) 0.53 Pa, (b) 1.07 Pa, (c) 1.60 Pa. Solid circles: H<sub>2</sub> plasma. Open circles: D<sub>2</sub> plasma. Mean values and standard deviations are derived from four series of experiments (2 sets on 2 different dates).

reflected on the EEDFs (**Figs. 3.6** and **3.7**). The EEDFs with respect to the negative ion production/destruction are commented in section 3.4.

**Fig. 3.10** unveils the H<sup>-</sup> and D<sup>-</sup> negative ion density as either the microwave power or the gas pressure increases. Higher values of both working parameters lead to higher negative ion densities. It is worth noticing that the densities are either equal (**Fig. 3.10(b)**) or slightly higher (**Figs. 3.10(a)** and **3.10(c)**) in H<sub>2</sub>. In any case, values up to about  $0.4 \times 10^{16} \text{ m}^{-3}$  are reached in both the H<sub>2</sub> and D<sub>2</sub> plasmas.

Despite the close negative ion densities obtained in H<sub>2</sub> and D<sub>2</sub>, the ratio of the negative ion to cold electron density is higher in the H<sub>2</sub> plasmas for any pressure and power level (**Fig. 3.11**). This ratio is an important parameter affiliated with the ratio of the negative ion to co-extracted electron currents in ECR-driven sources [63]. Thus, as **Fig. 3.11(b)** attests, a ratio of  $\sim 0.225$  is

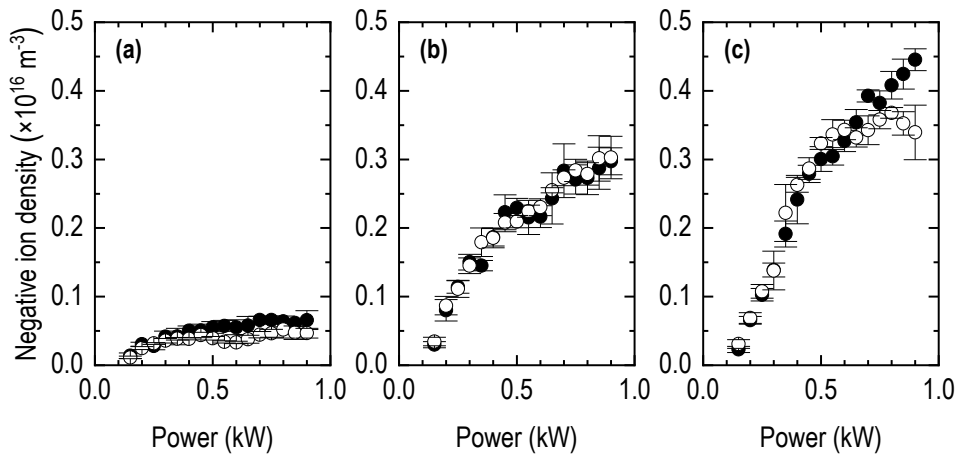


**Figure 3.10.** Negative ion density as a function of the microwave power at (a) 0.53 Pa, (b) 1.07 Pa, (c) 1.60 Pa. Solid circles: H<sub>2</sub> plasma. Open circles: D<sub>2</sub> plasma. Mean values and standard deviations are derived from four series of experiments (2 sets on 2 different dates).

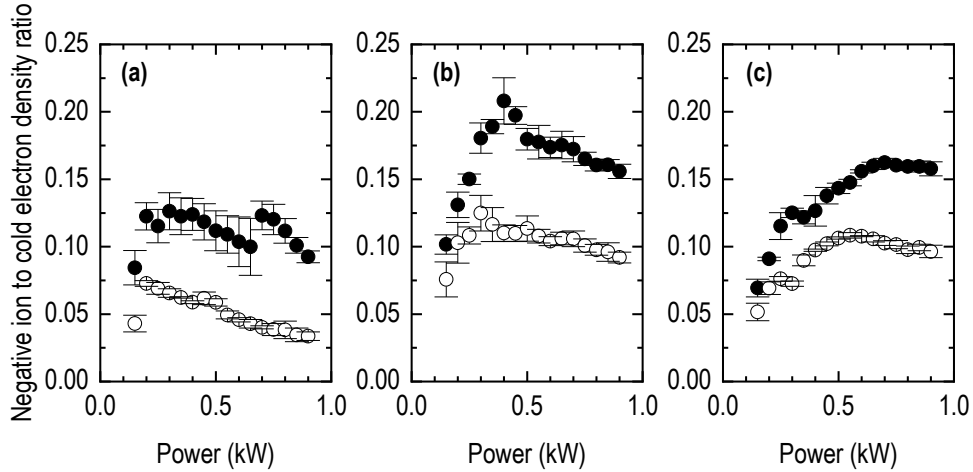


**Figure 3.11.** Negative ion to cold electron density ratio as a function of the microwave power at (a) 0.53 Pa, (b) 1.07 Pa, (c) 1.60 Pa. Solid circles: H<sub>2</sub> plasma. Open circles: D<sub>2</sub> plasma. Mean values and standard deviations are derived from four series of experiments (2 sets on 2 different dates).

optimally achieved in H<sub>2</sub> versus  $\sim 0.125$  in D<sub>2</sub>. Additionally, the data of **Fig. 3.11** disclose that intermediate pressure and temperature are needed for maximizing this ratio. In **Fig. 3.11** the optima are 1.07 Pa/0.4 kW for H<sub>2</sub> and 1.07 Pa/0.3 kW for D<sub>2</sub>. A more extensive inspection of the dependence of the plasma properties on the working pressure is given in the next section.

Finally, a decoupling from the operating parameters and a direct comparison of the negative ion yield in the H<sub>2</sub> and D<sub>2</sub> discharges in terms of endogenous plasma properties, may be attained by plotting the negative ion density versus the plasma density. This is shown in **Fig. 3.12**. A H<sub>2</sub> plasma allows to produce higher negative ion density than a D<sub>2</sub> plasma does for a given cold electron density (**Fig. 3.12(a)**). At the same time, the negative ion densities are neared when the hot electron density is considered (**Fig. 3.12(b)**).

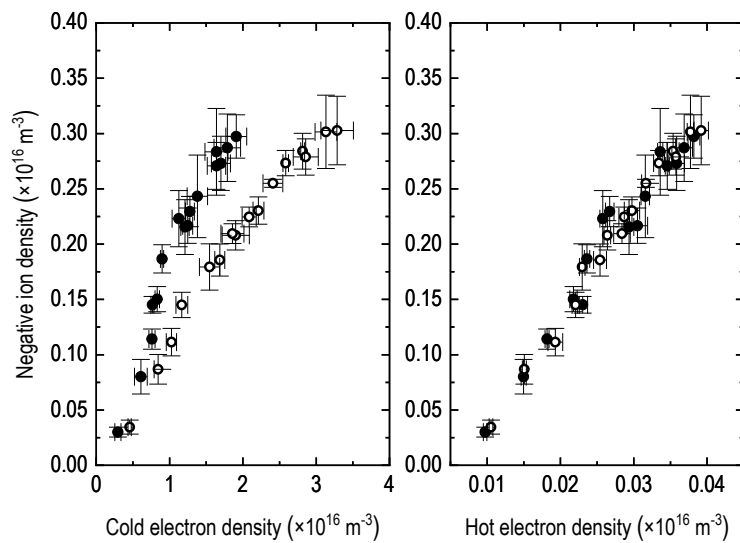


**Figure 3.12.** Negative ion density as a function of: (a) the cold electron population, (b) hot electron population. Solid circles: H<sub>2</sub> plasma. Open circles: D<sub>2</sub> plasma. Mean values and standard deviations are derived from four series of experiments (2 sets on 2 different dates). 1.07 Pa.

### 3.3 H<sup>-</sup> and D<sup>-</sup> production efficiency as a function of gas pressure

The properties of the H<sub>2</sub> and D<sub>2</sub> plasmas produced in the “Prometheus I” reactor are further investigated with respect to the working pressure. This section collects the corresponding results. The working pressure is varied across the available range, from 0.27 Pa to 2.67 Pa (2 mTorr to 20 mTorr) with a step of 0.27 Pa. At the same time, the injected microwave power is kept constant during the measurements, i.e. 180 W per ECR module (0.9 kW in total).

The evolution of the characteristic potentials in the H<sub>2</sub> and D<sub>2</sub> plasmas is displayed in **Fig. 3.13**. The floating potential (**Fig. 3.13(a)**) lies in the range of 3.5 V to 6.5 V. Neither a particular difference is displayed between the two gases, nor a specific trend throughout the

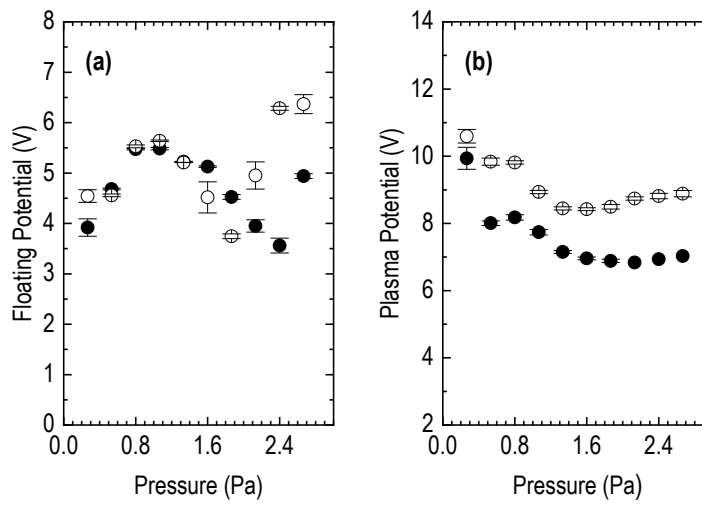


**Figure 3.13.** (a) Floating and (b) plasma potential as a function of the working pressure for a constant microwave power of 0.9 kW. Solid circles: H<sub>2</sub> plasma. Open circles: D<sub>2</sub> plasma. Mean values and standard deviations are derived from four series of experiments (2 sets on 2 different dates).

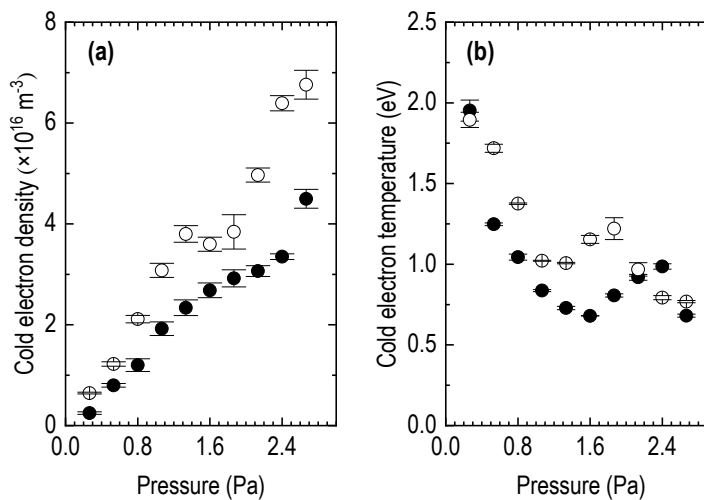


**Figure 3.14.** Cold electron (a) density and (b) temperature as a function of the working pressure for a constant microwave power of 0.9 kW. Solid circles: H<sub>2</sub> plasma. Open circles: D<sub>2</sub> plasma. Mean values and standard deviations are derived from four series of experiments (2 sets on 2 different dates).

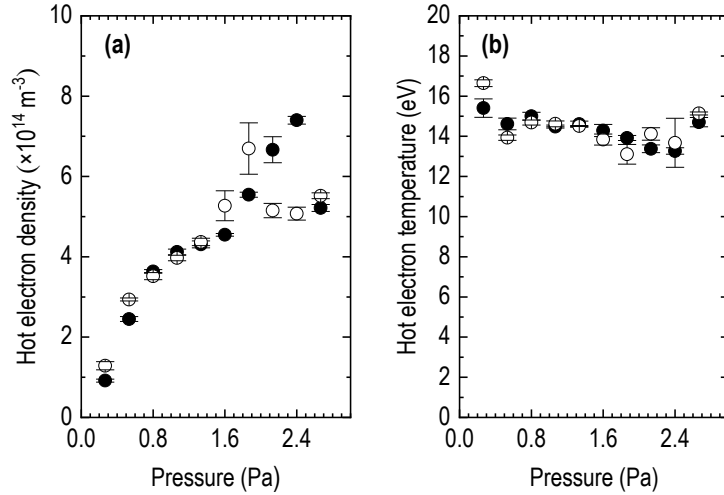


**Figure 3.15.** Hot electron (a) density and (b) temperature as a function of the working pressure for a constant microwave power of 0.9 kW. Solid circles: H<sub>2</sub> plasma. Open circles: D<sub>2</sub> plasma. Mean values and standard deviations are derived from four series of experiments (2 sets on 2 different dates).

investigated pressure range. Contrarily, the plasma potential (**Fig. 3.13(b)**) appears to drop slightly as the pressure increases, all the while being higher in the case of D<sub>2</sub> plasmas.

**Figs. 3.14(a)** and **3.15(a)** show the densities of the two electron populations versus the working pressure. Both populations in both discharges exhibit a linear increase in their density with increasing pressure, however, when compared to H<sub>2</sub> plasmas, D<sub>2</sub> plasmas are characterized by a consistently higher cold electron density over the entire pressure range. This observation matches that made for the dependency of the electron density upon the microwave power, indicated in **Figs. 3.4** and **3.5**. It is worth noting once again that, while the cold electron density

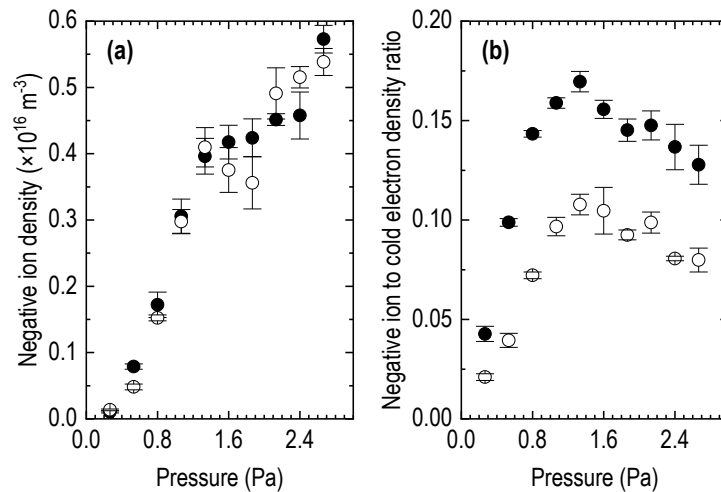


**Figure 3.16.** (a) Negative ion density and (b) negative ion to cold electron density ratio as a function of the working pressure for a constant microwave power of 0.9 kW. Solid circles: H<sub>2</sub> plasma. Open circles: D<sub>2</sub> plasma. Mean values and standard deviations are derived from four series of experiments (2 sets on 2 different dates).

attains values of the order of  $10^{15} - 10^{16} \text{ m}^{-3}$ , as a rule, the hot electron density is two orders of magnitude lower.

Accordingly, the temperatures of the two electron populations are presented in **Figs. 3.14(b)** and **3.15(b)**. As expected, with increasing pressure the temperature of the cold electron population in both gases decreases, since electrons lose their energy in more frequent collisions. However in the case of a D<sub>2</sub> plasma, the temperature of the cold electrons is measured to be higher than that in a H<sub>2</sub> plasma. These conclusions correspond to those made when the microwave power is ramped up (compare with **Fig. 3.8**). On the other hand, a similar yet less pronounced decreasing trend can be discerned for the temperature of the hot electron population in both discharges with increasing pressure. Nonetheless, equal hot electron temperatures are obtained in the H<sub>2</sub> and D<sub>2</sub> plasmas.

Moreover, the influence of the pressure variation on the negative ion density and the negative ion to cold electron ratio is displayed in **Figs. 3.16(a)** and **(b)**, respectively. As the pressure increases, a steep negative ion rise followed by a quasi-saturation phase is evident. The curves are nearly independent of the isotope, in line also with the data of **Fig. 3.10**. Finally, with regard to the negative ion to cold electron ratio, a distinct optimum at around 1.33 Pa is present for both discharges (H<sub>2</sub> and D<sub>2</sub>), albeit less for the case of D<sub>2</sub>.

### 3.4 Discussion

Following the presentation of the experimental results on the evolution of H<sub>2</sub> and D<sub>2</sub> plasma properties versus the basic operational parameters (microwave power, microwave pressure) and the primary conclusions drawn from their observation, it is pertinent to correlate them hereafter with the production and destruction mechanisms of the H<sup>-</sup> and D<sup>-</sup> ions.

The concept of ECR heating and the way this is implemented with the use of the dipolar ECR modules in the reactors under study was amply explained in the introductory chapter (see section 1.5). It was noted, and is evoked here once more, that in principle the hot electrons remain trapped in the magnetic field whereas the cold electrons are able to diffuse away from it under the influence of density gradient and the resulting space charge electric field. This fact may explain the much lower density (**Figs. 3.5** and **3.15(a)**) as well as the almost constant temperature (**Figs. 3.9** and **3.15(b)**) of the hot electron population found downstream of the ECR zone, i.e. it is likely that merely the portion of the hot electrons that are capable of escaping the “magnetic trap” are probed.

Regarding the isotope effect for the EEDFs shown in **Figs. 3.6** and **3.7**, this may be due to both the different total ionization cross section values for H<sub>2</sub> and D<sub>2</sub> and the difference in the ion confinement time in the two discharges. With regard to the former statement, the total (i.e. including the contributions from both dissociative and non-dissociative ionization, in the ECR

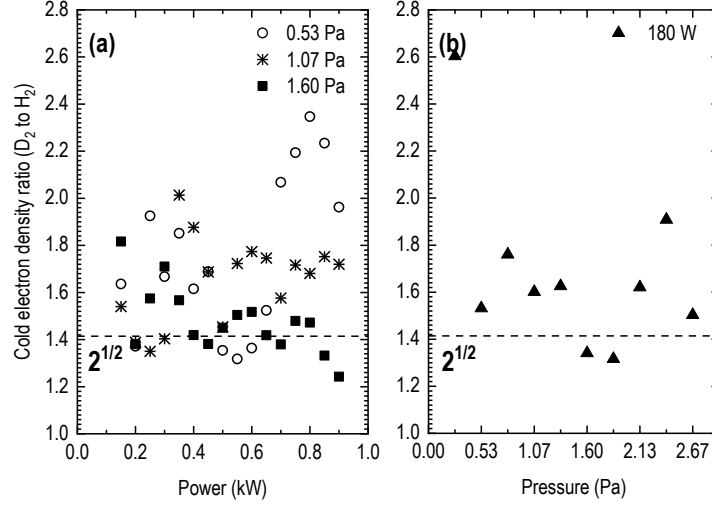


**Figure 3.17.** Ratio of the cold electron densities measured in the D<sub>2</sub> plasma to the cold electron densities measured in the H<sub>2</sub> plasma, from **Figs. 3.4** and **3.14** as a function of (a) the microwave power at three different pressures, and (b) the working pressure for a microwave power of 180 W. The level of  $\sqrt{2}$  is given in both figures for reference.

zones) ionization cross section values from H<sub>2</sub> and D<sub>2</sub>, which gave an isotope effect near the threshold electron-impact energies [73]. As predicted theoretically,  $Q_{\text{ion}}^{\text{D}_2} > Q_{\text{ion}}^{\text{H}_2}$  up to 25 eV of energy but the cross sections at electron energies larger than 25 eV become equal. Indicative values of the total ionization cross section include  $Q_{\text{ion}}^{\text{D}_2}/Q_{\text{ion}}^{\text{H}_2} = 1.147$  at 16 eV and  $Q_{\text{ion}}^{\text{D}_2}/Q_{\text{ion}}^{\text{H}_2} = 1.041$  at 22 eV [73]. On the other hand, the ion confinement time in D<sub>2</sub> is  $\sqrt{2}$  times higher than in H<sub>2</sub> due to the square root of the mass ratio of the two molecules [33], [73], while the positive ions are destroyed by transport to the walls where they are neutralized. Thus, the positive ions are consistently higher in a D<sub>2</sub> plasma. In other words, the plasma density should be consistently higher in D<sub>2</sub> than in H<sub>2</sub> and their ratio should differ by a factor of about  $\sqrt{2}$ . A direct comparison of the plasma density ratio resulting from the measurements presented in the previous sections is provided in **Fig. 3.17**. The ratio approaches but does not precisely equal  $\sqrt{2}$ , depending on the operating conditions. It is an indication that other factors (e.g. the presence of the magnetic field, isotope effects in some ion-loss cross sections, etc.) may be significant [33], [73].

**Table 1.3** in Chapter 1 summarized the main production processes for the H<sup>-</sup> and D<sup>-</sup> negative ions. It was furthermore underlined that in the volume production scheme the DEA process (reactions R1 and R2; **Table 1.3**) is the predominant path for negative ion production. For the case studied herein, a direct comparison of exemplary EEDFs corresponding to the cold electron population and the DEA reaction cross sections (**Fig. 3.18**) shows that the cold populations produced both in the H<sub>2</sub> and D<sub>2</sub> plasmas have energies that promote reactions R1 and R2.

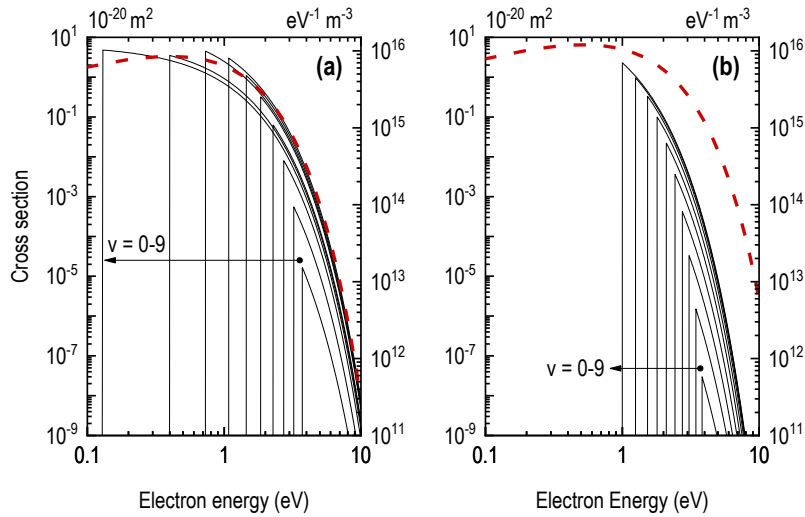


**Figure 3.18.** Indicative EEDFs of the cold electron population (red dashed lines) plotted against the cross sections of the DEA reaction; (a) H<sub>2</sub>, and (b) D<sub>2</sub>.

At the same time, it was accentuated that the DEA cross section is higher for H<sub>2</sub> than for D<sub>2</sub> for every vibrational level and the energy threshold is lower for the same vibrational level. **Fig. 3.19(a)** presents the average H<sup>-</sup> and D<sup>-</sup> ion densities measured within evenly spaced intervals of electron temperature. This figure is obtained as follows: for the optimal pressure identified from the measurements versus the microwave power, i.e. 1.07 Pa (see **Fig. 3.4**), the data from **Figs. 3.4(b)** and **3.8(b)** are combined by eliminating the power and give the data provided in **Fig. 19(a)**. From this figure, the negative ion densities are averaged within 0.1 eV intervals (see gridlines). From the resultant figure (**Fig. 3.19(b)**) it is deduced that the cold

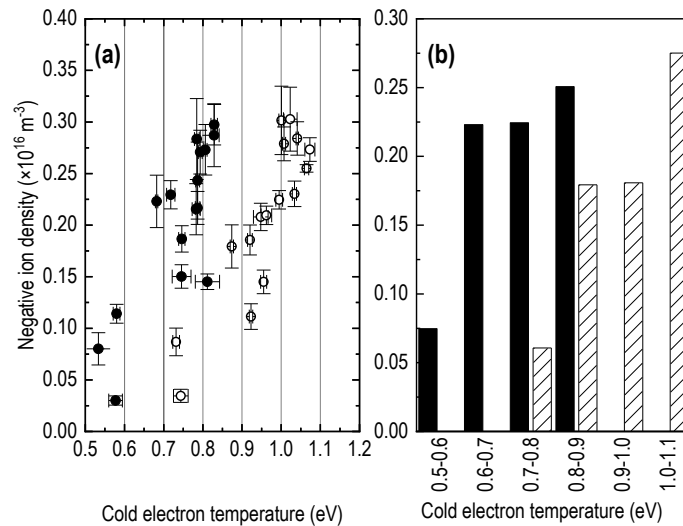


**Figure 3.19.** (a) Negative ion density as a function of cold electron temperature (the data of **Figs. 3.10(b)** and **3.8(b)** are combined) by eliminating the power. The grid lines define the intervals where the negative ion density is averaged for getting the histograms of (b). (b) Histograms of the average values of the negative ion densities over 0.1 eV temperature intervals of the cold electron population; H<sub>2</sub> (solid bars) and D<sub>2</sub> (hatched bars); 1.07 Pa.

electron temperatures that yield negative ions lies within the 0.5–0.9 eV range for H<sub>2</sub>, whereas for D<sub>2</sub> it lies within the 0.7–1.1 eV range. According to **Figs. 3.18(a)** and **(b)**, these values correspond to the cold electrons that participate in the DEA reaction with molecules heated at the vibrational levels  $v \geq 7$  and  $v \geq 9$ , respectively. However, although it is seen that the higher DEA cross sections and the span of the cold electron temperature in H<sub>2</sub> may favor negative ion production, this may nonetheless be partially compensated for the lower cold electron density in the H<sub>2</sub> plasma, compared to the D<sub>2</sub> plasma, as it was seen from the measurements. This could explain the relatively close densities of H<sup>-</sup> and D<sup>-</sup> ions displayed in **Figs. 3.10** and **3.16(a)**, as opposed to the apparent higher H<sup>-</sup> density in **Fig. 3.12(a)** where any difference in the cold electron temperatures has been eliminated. This is also in line with the lower negative ion to cold electron density ratio presented in **Figs. 3.11** and **3.16(b)**. More specifically, this ratio becomes higher in the H<sub>2</sub> plasma than in the D<sub>2</sub> plasma since the numerator is almost constant whereas the denominator is lower by a factor of  $\sqrt{2}$  (**Fig. 3.17**). Based on **Fig. 3.11(b)**, a ratio of up to  $\sim 0.225$  in H<sub>2</sub> versus  $\sim 0.125$  in D<sub>2</sub> is observed (at 1.07 Pa and 0.4 kW and 0.3 kW, respectively), while **Fig. 3.16(b)** shows that a ratio of  $\sim 0.169$  in H<sub>2</sub> and  $\sim 0.107$  in D<sub>2</sub> is obtained (at 1.33 Pa and 0.9 kW). This corresponds to a factor 1.8 and 1.58 higher in H<sub>2</sub> for the two cases, respectively. For the same conditions, **Fig. 3.17(a)** gives an average cold electron density of  $\sim 1.77$ , and **Fig. 3.17(b)** of  $\sim 1.62$ , times higher in the D<sub>2</sub> plasma.

With the measurements described in the previous sections, information on the EEDFs is acquired but not on the ro-vibrational heating of the two plasmas. Hence DEA cross sections and cold electron densities/temperatures alone fail to describe the entire DEA process. This would require the direct measurement of the vibrational distribution functions (VDFs). This subject has been studied in similar conditions at the “SCHEME-II+” reactor, and the corresponding findings shall be laid out in the next chapter. Nonetheless, **Table 1.4** gathered the main reactions that lead to the H<sub>2</sub> and D<sub>2</sub> molecules’ excitation and de-excitation, and they can be correlated with the present results. Reactions R43 and R44 have been recognized as the principle ones that lead to the formation of the ro-vibrationally excited molecules, while the cross sections of these reactions were displayed in **Figs. 1.6(a)** and **(b)**. A direct comparison of **Figs. 3.9** and **3.15(b)** with **Fig. 1.6(a)** and **(b)** shows that the hot electron population produced in both ECR plasmas attains a temperatures that exceed the threshold energy of the two reactions. It is repeated that the measurements refer to the diffusion region of the reactor, i.e. downstream of the ECR zones, which means that in the ECR zones the electron density should be higher and that they should obtain energies even higher than those probed. Thus, H<sub>2</sub> and D<sub>2</sub> gases can be efficiently heated vibrationally in the ECR zones.

On the other hand, it is crucial to also consider the negative ion destruction processes. In **Tables 1.3** and **1.4** the possible reactions that contribute to negative ion loss have been listed. It has been estimated that among the multitude of direct reactions, associative detachment

(AD: R13, R14) and mutual neutralization (MN: R25 – R40) should play the dominant role in the present reactor [71]. As far as the indirect mechanisms, i.e. those of molecular relaxation, it is assumed that the V-t process (R51, R52) is the principle one. In restricting the analysis to the AD and V-t reactions, a simplistic consideration of negative ion destruction may be derived. It becomes evident that the rates for both reactions are sensitive to the atomic density which depends both on the gas pressure and the injected microwave power and, by extension, may be associated with the limitations in the H<sup>-</sup> and D<sup>-</sup> production and the observed operational optima (see **Figs. 3.10, 3.11** and **3.16**). It is recalled from section 1.4 that reactions R57 and R58, describing the process of electron-impact dissociation proceeding through the  $b^3\Sigma_u^+$  state, are the key reactions that lead to the creation of the atomic fragments, while at below about 12 eV this process is believed to be the sole path for the dissociation of the H<sub>2</sub> and D<sub>2</sub> molecules into these neutral fragments. Based on the acquired EEDFs (**Figs. 3.6** and **3.7**) this process should be active in the “Prometheus I” reactor.

In ECR reactors [56], [57], [71] operating with hydrogen, an increase of the atomic density and a decrease in the atomic-to-molecular density for increasing pressure have been reported, whereas the latter was found to increase for increasing power [71]. At the same time, AD and MN reaction rates have been found to increase with hydrogen pressure [71], [87]. These findings are consistent with **Fig. 3.16(a)** where the H<sup>-</sup> and D<sup>-</sup> ion production is constricted with the increase in gas pressure. The parallel increase of the plasma density (**Figs. 3.4** and **3.14(a)**) lead to the optima shown in **Fig. 3.16(b)**.

With regard to the isotope effect between reactions R57 and R58, the atomic-to-molecular density ratio is found to be constantly higher in the case of D<sub>2</sub> plasmas both by means of experiments [22], [48], [58] and theoretical analyses [33], [53]. Recent calculations [74], [164] have shown that the cross section of R58 (for D<sub>2</sub>) is close to or even lower than that of R57 (for H<sub>2</sub>). Thus, the commonly observed higher atomic density in D<sub>2</sub> plasmas should be justified by the difference on the transport properties of H and D atoms [165] and points to more intense AD and MN losses in D<sub>2</sub>, in agreement with the lower negative ion density for a given plasma density showcased in **Fig. 3.12(a)**.

To conclude, several statements can be made which recap the differences between the H<sub>2</sub> and D<sub>2</sub> plasmas, as they are ensued by the preceding comparative investigations. Two electron populations, quasi-Maxwellian, are produced, independently of the gas, the pressure, and the microwave power employed. The cold electron population is constantly higher in the D<sub>2</sub> plasma, and this is attributed to the higher confinement time of the respective positive ions. H<sup>-</sup> and D<sup>-</sup> negative ion densities are not substantially different in the two plasmas under the same operating conditions, although the H<sup>-</sup> negative ion yield is higher for a given plasma density. A strong isotope effect exists when the negative ion to electron density ratio is considered, and the

latter may be up to 80% higher in the H<sub>2</sub> plasma. Finally, similar optimal operating windows for enhanced negative ion production exist in both gases, reflecting the interplay between the production and destruction processes.

### 3.5 Negative ion energies in H<sub>2</sub> and D<sub>2</sub> plasmas

The application of the two-beam laser-induced photodetachment diagnostic, the details of which were described in section 2.1.3, led to the measurement of the H<sup>-</sup> and D<sup>-</sup> ion energies in several characteristic operating conditions in the “Prometheus I” reactor. More specifically, the working gas pressure was kept constant at 1.33 Pa as the injected microwave power was varied between a total of 300, 600, or 900 W (accordingly 60, 120, or 180 W set on each of the five dipolar ECR modules of the reactor).

Based on the synchronization scheme presented in **Fig. 2.7** and the theory laid out in the same section, mixed photodetachment signals (see **Fig. 2.9(a2)** and **(b2)**) are recorded in each of the studied conditions whilst the delay between the two laser beams,  $\Delta t$ , is varied from 200 ns up to 5  $\mu$ s. This results in the acquisition of a bundle of such signals which are treated as discussed therein. For each of them the ratio  $n_{-,t}/n_{-,0}$  is calculated and plotted versus  $\Delta t$ , which constitutes the so-called recovery curve. Two recovery curve examples are given in **Fig. 3.20(a)** and **(d)**.

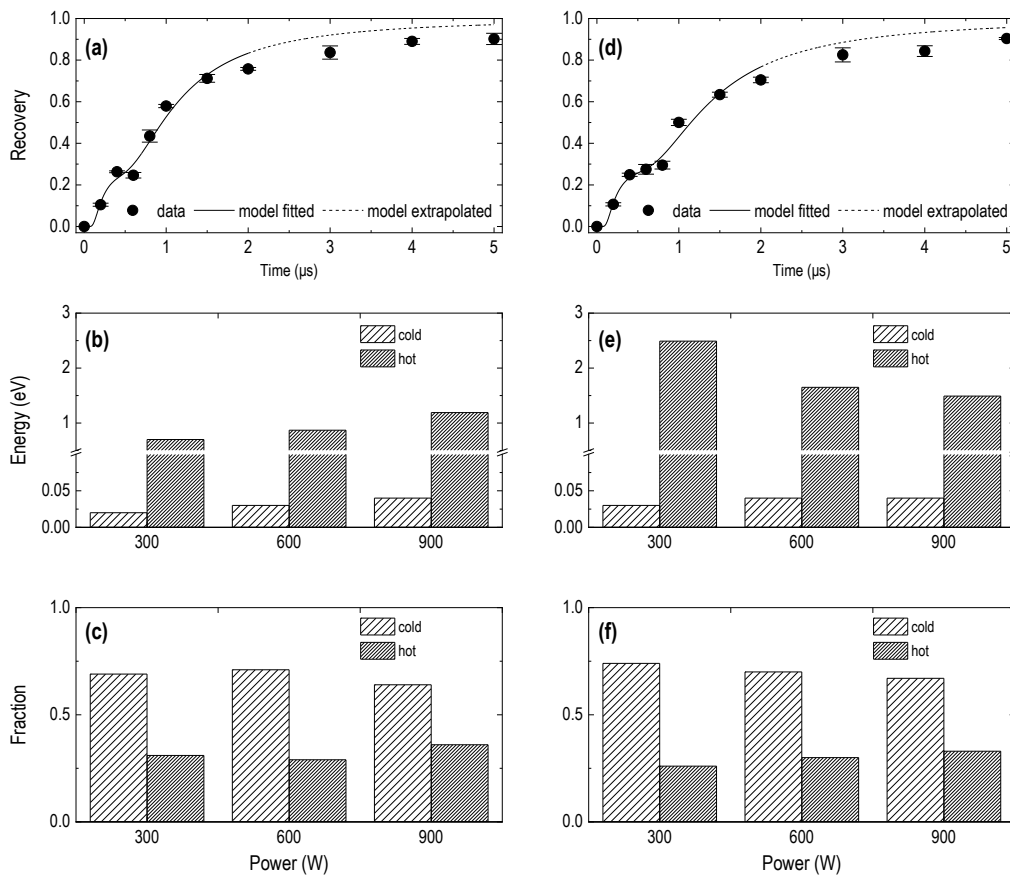


**Figure 3.20.** Ion density recovery in (a) H<sub>2</sub>, and (b) D<sub>2</sub>; (600W). Ion energy versus MW power (note the break on the vertical axis) for (c) H<sup>-</sup>, and (d) D<sup>-</sup>. Ion fraction versus MW power for (e) H<sup>-</sup>, and (f) D<sup>-</sup>.

It is here attempted to fit to the data a ballistic model [143], assuming two ionic populations of different temperatures [166]:

$$\frac{n_{-,t}}{n_{-,0}} = a \exp\left(-\left(\frac{R_L}{V_{th,\alpha} t}\right)^2\right) + \beta \exp\left(-\left(\frac{R_L}{V_{th,\beta} t}\right)^2\right) \quad (3.2)$$

with:

$$V_{th} = \sqrt{\frac{2(kT)_-}{M_-}} \quad (3.3)$$

Where  $a$  and  $\beta$  express the fractions for each of the two populations,  $R_L$  is the Langmuir probe radius,  $V_{th}$  is the thermal velocity,  $M_-$  is mass of the ion (either of H<sup>-</sup> or D<sup>-</sup>),  $(kT)_-$  represents the energy of the ion. Ultimately, the fitting procedure provides the values  $a$ ,  $\beta$ ,  $V_{th,\alpha}$ , and  $V_{th,\beta}$  and from the latter, via **Eq. 3.3** the energies of the two different negative ion populations are derived. Under the present conditions, the model (**Eq. 3.2**) traces acceptably the data up to about 2  $\mu$ s (**Fig. 3.20**). Fitting for longer recovery times, increases the overall least squares error significantly. According to this model, “cold” ions have energy less than 0.05 eV in both H<sub>2</sub> and D<sub>2</sub> plasmas, whereas “hot” ions achieve higher energies in D<sub>2</sub>. In any case, the “cold” negative ions dominate the “hot” ones, with a fraction of about 65–70% (**Fig. 3.20**). Besides, it has been already shown that two electronic populations are observed. From section 3.2 the exact values of the plasma features for the case of 1.33 Pa and 900 W, in H<sub>2</sub> | D<sub>2</sub>, are:  $V_p = 7.1$  |  $8.4$  V;  $n_{e,cold} = 2.3$  |  $3.8$  ( $\times 10^{16}$  m<sup>-3</sup>);  $n_{e,hot} = 4.3$  |  $4.4$  ( $\times 10^{14}$  m<sup>-3</sup>);  $kT_{e,cold} = 0.7$  |  $1.0$  eV;  $kT_{e,hot} = 14.6$  |  $14.5$  eV; and  $n_{-,0} = 3.9$  |  $4.1$  ( $\times 10^{15}$  m<sup>-3</sup>).

The production of two ionic populations and the elevated energy of the hot ions, should be traced back to their origin. It has been established that in the ECR zones, inelastic collisions with hot electrons lead to vibrationally excited molecules which diffuse downstream, where the present measurements are realized. There, H<sup>-</sup> or D<sup>-</sup> ions are formed through the DEA reaction (R1, R2; **Table 1.3**), which are expected to acquire only the energy of formation by DEA, being thus cold. On the other hand, recombinative desorption processes on the metallic walls as a source of a wide spectrum of ro-vibrationally excited molecules have been recognized. Ions formed this time near the walls, again by DEA, are accelerated by the positive plasma potential difference, moving towards the bulk plasma, being thus hot(ter). This is in line with the constantly higher plasma potential measured in D<sub>2</sub> and the higher hot ion energy obtained, with respect to the H<sub>2</sub> case (cf. **Fig. 3.3**). Furthermore, the same figure revealed increasing plasma potential versus the MW power, in both gases. Thus, higher power should lead to higher acceleration and finally increased energy for the hot ions. While this holds true in the H<sub>2</sub> case, the trend is different in the D<sub>2</sub> case. This implies that the accelerating ions are subject to various transport mechanisms in each gas-plasma, and it is another explicit difference with respect to the cold negative ions.

## CHAPTER 4

# EXPERIMENTAL DETERMINATION OF VIBRATIONAL DISTRIBUTION FUNCTIONS

---

The vibrational distribution functions (VDFs) are pertinent to the production of negative ions through the DEA reaction. In the case of the “SCHEME-II+” reactor and in particular a  $D_2$  plasma, these are accessed through the analysis of the spectra obtained by Vacuum Ultra-Violet Fourier transform absorption spectroscopy using synchrotron radiation. This chapter gives a detailed description of the sequence of steps that are followed for their extraction and finally discusses their shape and their dependence on different materials exposed to the plasma.

## 4.1 Analysis procedure for spectra recorded by VUV-FT absorption spectroscopy

Previously, in Section 2.2.1 of Chapter 2, the absolute necessity of having direct measurements of the vibrational distribution functions (VDFs) was emphasized. Moreover, it was mentioned how, in the framework of this thesis, these distributions can be determined experimentally through an unparalleled spectroscopic technique which calls for the use of synchrotron radiation; VUV Fourier Transform Absorption Spectroscopy. Following the detailed description of the instruments used for the application of this technique, this chapter aims to firstly provide a concise but in-depth description of the steps that are followed to extract the information on the VDFs from the experimentally acquired spectra, and secondly to present and assess the resulting distributions with respect to the mechanisms of negative ion production laid out in the introductory chapter. Although the entire analysis and results will refer to  $D_2$ , it should be noted that the same procedure can be followed for the case of  $H_2$  provided the molecular parameters are changed where necessary.

The construction of the VDFs from the absorption spectra acquired through the VUV-FT absorption spectroscopy technique (**Fig. 2.13**) results from a sequence of meticulous steps which are hereafter described in detail. It is noted that the procedure has been developed on MathWorks's MATLAB computing platform.

According to the Beer-Lambert law for the absorption of light from a medium, the optical depth,  $\tau = \ln(I_0(\nu)/I(\nu))$ , is correlated to the thickness and physical properties of the latter by:

$$I(\nu) = I_0(\nu)e^{-k_\nu(\nu)L} \quad (4.1)$$

where  $I(\nu)$  and  $I_0(\nu)$  are the transmitted and incident intensities at a frequency  $\nu$ ,  $L$  the length of the absorbing medium, and  $k_\nu(\nu)$  is the spectral absorption coefficient. Thus, first of all, the raw

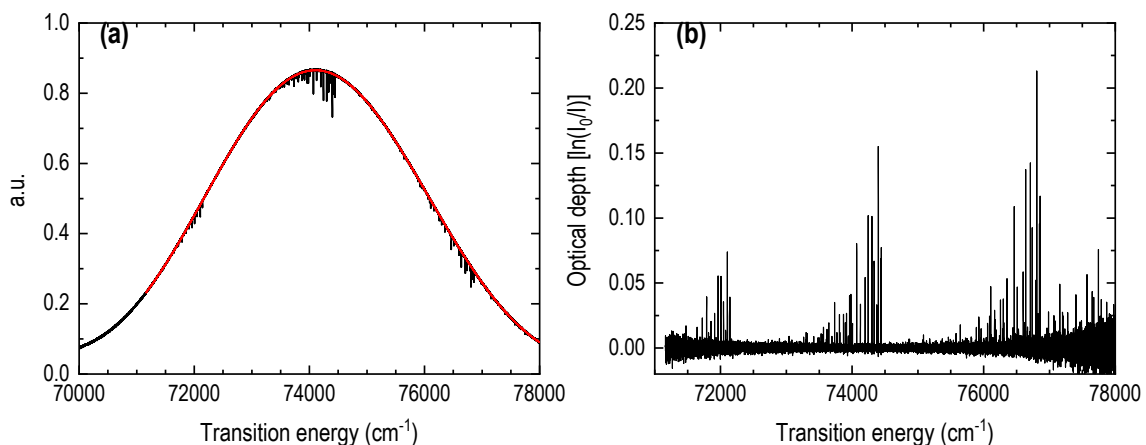


**Figure 4.1.** (a) Example of the fit of a baseline (red solid line) to the raw spectrum (black solid line) obtained by the VUV-FTS for a single undulator setting. The baseline follows the characteristic quasi-Gaussian profile of the synchrotron radiation emission. The current of the undulator is set at 491 A, thus the illumination is centered on a transition energy of 74200  $cm^{-1}$ . (b) The obtained spectrum, after the suppression of the baseline, expressed as a measure of optical depth.  $D_2$  plasma; 1.6 Pa, 150 W.

absorption spectra (of intensity  $I$ ) are converted into optical depth spectra. This is done by determining the baseline of intensity  $I_0$  for each of the spectra, corresponding to the continuum imposed, and by then applying the aforementioned formula. While the shape of this continuum is quasi-Gaussian (see section 2.2.1), the method applied for its determination is based on a locally weighted linear regression algorithm as opposed to simply an adjustment of a Gaussian function. **Fig. 4.1(a)** presents an example of the result of this procedure. The red solid line superposed upon the raw spectrum is subsequently considered as the baseline of the spectrum. The closer scrutiny, in **Fig. 4.2**, of a part of the spectrum shown initially in **Fig. 4.1(b)**, confirms the high resolving power of the FTS instrument, since the absorption lines are distinguished with a resolution of about  $0.5 \text{ cm}^{-1}$ . This high resolution provided by the instrument ensures the observation of the absorption lines with as few as possible blends between lines of different transitions.

Next follows the identification of the observed spectral lines. The MOLAT atomic and molecular database [167] provides the data on the transition energies from the rovibrational levels ( $v', J'$ ) of the upper electronic states (B, C, B', D) towards the rovibrational levels ( $v'', J''$ ) of the ground electronic state X, for both the  $\text{H}_2$  and  $\text{D}_2$  molecules. More specifically, the data is found in the section of the database entitled “VUV Spectra of small molecules”, which is based, among others on the theoretical works of Roncin and Launay [168] and Abgrall et al. [169]. As it was mentioned in section 2.2.2, focus is laid on the molecular Lyman system,  $\text{B}^1\Sigma_u^+(v', J') \leftarrow \text{X}^1\Sigma_g^+(v'', J'')$  (denoted as  $\text{BX}v'-v''$  for simplicity). **Table 4.1** for example lists the wavenumbers of the first ten R- and P-branch components of the BX0-6 vibrational band. It is reminded that the R-, and P-branches correspond to rotational transitions for which  $\Delta J = +1$  and  $\Delta J = -1$  respectively. Correspondingly, **Fig. 4.2** displays a portion of the rotational spectrum of the BX0-6 vibrational band, where the first six R and three P components are distinguished.

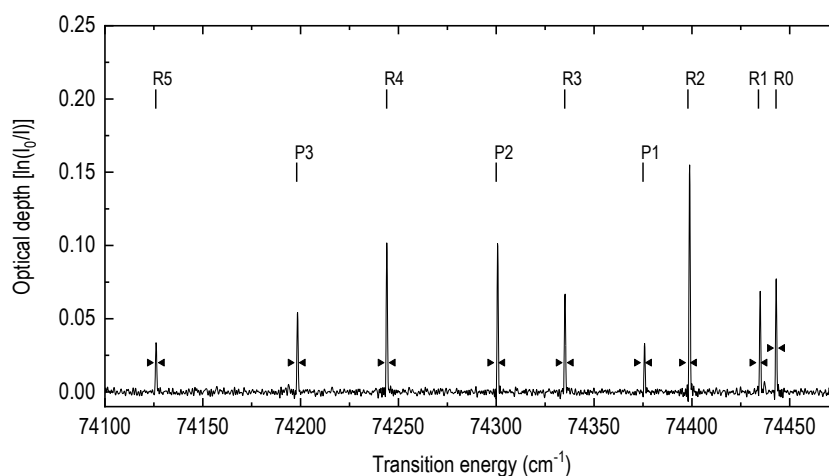


**Figure 4.2.** A portion of the spectrum shown in **Fig. 4.1** demonstrating the high resolving power of the VUV-FTS system. The first six and three components of the R and P rotational branches, respectively, of the BX0-6 vibrational band are discerned. The arrows on either side of each line represent the boundaries of integration of each spectral line.

**Table 4.1.** Wavenumbers of the first ten components of the R and P rotational branches of the BX0-6 vibrational band.

BX0-6 0	1	2	3	4	5	6	7	8	9	10	
R	74443.06	74434.93	74398.83	74335.2	74244.17	74126.33	73981.92	73812.29	73617.68	73399.2	73157.83
P	–	74375.87	74300.71	74198.49	74069.55	73914.65	73734.16	73529.59	73301.3	73050.52	72778.31

Nonetheless, a crucial point in the identification procedure is the inspection for potential blends of the spectral lines under study with lines of other transitions. For this purpose, potential coincidence of the Lyman system transitions with others belonging to the same system but also with those of the Werner system,  $C^1\Pi_u(v', J') \leftarrow X^1\Sigma_g^+(v'', J'')$  (denoted as CXv'-v''), the  $B^1\Sigma_u^+(v', J') \leftarrow X^1\Sigma_g^+(v'', J'')$  band (denoted B'Xv'-v''), and the  $D^1\Pi_u(v', J') \leftarrow X^1\Sigma_g^+(v'', J'')$  band (denoted DXv'-v'') are carefully examined. Therefore, in order to identify the existence of a blend, the fulfillment of two conditions is considered. Specifically, a blend is deemed to be present if it is found that the transition energies of two spectral lines differ less than  $0.5 \text{ cm}^{-1}$  and if simultaneously the ratio of the oscillator strengths of the two transitions corresponds to more than 10%. The values of the abovementioned constraints have been chosen arbitrarily after a series of trials. If a blend is indeed detected, the contribution of the “stray” line is evaluated and then removed. If on the contrary these conditions are not fulfilled, no blend is considered. A practical example demonstrating this approach follows.

**Figs. 4.3(a)-(c)** provide a closer inspection of the obtained absorption spectrum in the transition energy ranges for which the R(1), R(2), and P(1) rotational components of the BX0-6 band are present. On the same figure, vertical markers indicate the theoretical positions of the various transitions that could be found in the particular energy ranges. **Tables 4.2 – 4.4** collect

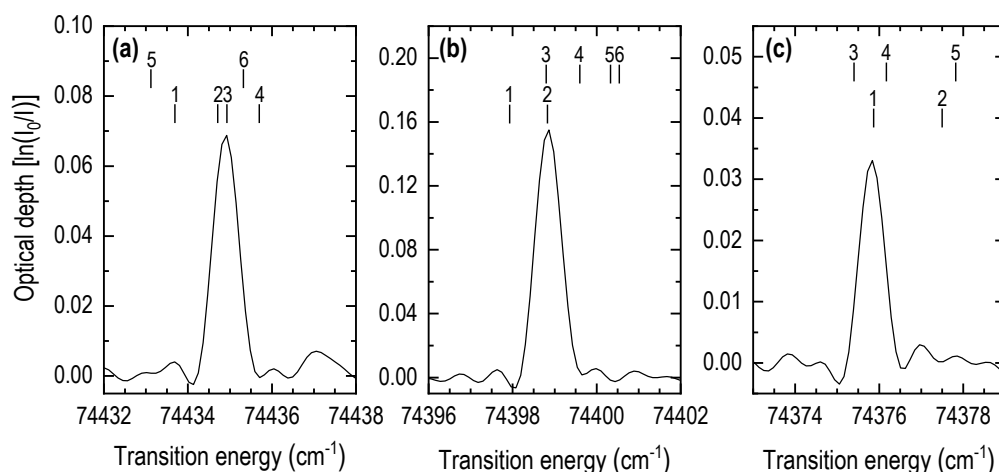


**Figure 4.3.** Magnification of three absorption lines within the  $74100 - 74450 \text{ cm}^{-1}$  energy range corresponding to (a) the R(1), (b) the R(2), and (c) the P(1) rotational components of the BX0-6 transition. In each subfigure, the numbered vertical markers indicate the positions of transitions whose energies lie within the corresponding range, and between which potential blends are examined.

the information on the characteristic parameters, i.e. the transition energy, the transition probability and the oscillator strength, regarding each of these potential transitions. It is noted that the numbers on the first row of the said tables correspond to the numbers above the markers in each of the subfigures of **Fig. 4.3**. In the second row, the formal notation of each transition as it has been determined herein is given, i.e., either BX( $v'-v''$ ,  $J'-J''$ ) or CX( $v'-v''$ ,  $J'-J''$ ) is specified. For the case presented in **Fig. 4.3(a)** one can observe that it is most likely that there is a blend between the lines indicated as #2 and #3. Upon closer examination of the data provided in **Table 4.2** it is seen that firstly, the transition energies differ by  $0.22 \text{ cm}^{-1}$ , and secondly that the ratios of the transition probabilities and the oscillator strengths attain a value of 3.83% and 0.025%, respectively. In this example, and by recalling the constraints that are set in the semi-automated procedure mentioned in the previous paragraph, the possible effect of transition #3 is disregarded and thus the absorption line is considered to result from transition #2, which belongs to the BX0-6 band. Similar reasoning can be applied for the cases presented in **Fig. 4.3(b)** and **(c)**. For the former, once again, transitions #2 and #3 are most likely to be interlaced. **Table 4.3** attests that the differences also evaluated before have a value of  $0.03 \text{ cm}^{-1}$ , 0.006%, and 0.0043%, respectively. Despite the fact that the transition energy difference is below the limit value of  $0.5 \text{ cm}^{-1}$ , the difference in the transition probabilities and oscillator strengths is so small that in this instance too, transition #2, associated to the BX0-6 band, is considered as the dominant one. The last case is slightly more complicated, since a check is performed between three lines consisting two pairs. The transition pairs under investigation consequently are: #1 with #3, and #1 with #4. From **Table 4.4**, the following values of the differences in the characteristic parameters are deduced for the respective pairs:  $0.47 \text{ cm}^{-1}/0.3 \text{ cm}^{-1}$ , 0.01%/0.002%, and 0.036%/0.006%. On account of the very low similarity observed from the ratios of the transition probability and oscillator strength, the conclusion is that finally the absorption profile should be attributed to transition #1 belonging again to the BX0-6 band under study.

**Table 4.2.** Characteristic parameters of the transitions indicated by the markers in Fig. 4.3(a) [167], [170].

	1	2	3	4	5	6
<b>Transitions</b>	BX(15-12,6-5)	BX(13-11, 8-7)	BX(0-6,2-1)	BX(0-5, 11-12)	CX(2-12,8-7)	CX(4-14,7-6)
Transition energy ( $\text{cm}^{-1}$ )	74433.69	74434.71	74434.93	74435.7	74433.12	74435.32
Transition probability, A ( $\text{s}^{-1}$ )	$3.20224 \times 10^6$	$6.05305 \times 10^6$	$1.58424 \times 10^8$	$1.73393 \times 10^8$	$2.63921 \times 10^4$	$1.66157 \times 10^5$
Oscillator Strength	$1.025 \times 10^{-3}$	$1.857 \times 10^{-3}$	$7.148 \times 10^{-2}$	$4.318 \times 10^{-2}$	$8.098 \times 10^{-6}$	$5.19 \times 10^{-5}$

**Table 4.3.** Characteristic parameters of the transitions indicated by the markers in Fig. 4.3(b) [167], [170].

	1	2	3	4	5	6
<b>Transitions</b>	BX(25-17, 6-5)	BX(0-6, 3-2)	CX(5-15, 2-2)	CX(2-12, 1-0)	CX(3-13, 8-7)	CX(7-18, 11-12)
Transition energy ( $\text{cm}^{-1}$ )	74397.93	74398.83	74398.8	74399.6	74400.33	74400.54
Transition probability, A ( $\text{s}^{-1}$ )	$4.5484 \times 10^6$	$1.7003 \times 10^8$	$1.01246 \times 10^4$	$4.56865 \times 10^3$	$1.26103 \times 10^5$	$1.31378 \times 10^5$
Oscillator Strength	$1.457 \times 10^{-3}$	$6.451 \times 10^{-2}$	$2.744 \times 10^{-6}$	$3.714 \times 10^{-6}$	$3.873 \times 10^{-5}$	$3.275 \times 10^{-5}$

**Table 4.4.** Characteristic parameters of the transitions indicated by the markers in Fig. 4.3(c) [167], [170].

Transitions	1	2	3	4	5
	BX(0-6, 0-1)	BX(5-7, 11-12)	CX(3-13, 11-10)	CX(5-15, 5-5)	CX(0-10, 8-8)
Transition energy (cm <sup>-1</sup> )	74375.87	74377.5	74375.4	74376.17	74377.82
Transition probability, A (s <sup>-1</sup> )	3.92864×10 <sup>8</sup>	5.54019×10 <sup>7</sup>	4.3623×10 <sup>4</sup>	7.84265×10 <sup>3</sup>	0.12774
Oscillator Strength	3.551×10 <sup>-2</sup>	1.382×10 <sup>-2</sup>	1.296×10 <sup>-5</sup>	2.127×10 <sup>-6</sup>	3.464×10 <sup>-11</sup>

For the range of the experimental parameters (e.g. working gas pressure, microwave power) investigated in the frame of the present thesis, which will be referred to in more detail in the next section of this chapter, transitions involving even up to the  $v'' = 11$  vibrational level are observable. Since, for each transition, about nine lines of the R-branch and ten lines of the P-branch are discernable, nearly a total of three-thousand lines are identified and processed in order to construct a VDF. This complexity is a testament to the necessity of an automated, to the maximum degree possible, processing scheme.

The identification of the lines is followed by the determination of the “real” absorption profile each of the lines’ profiles individually. The absorption profile of each line comprises a component related to the inherent instrumental response. Thus this contribution, referred to as the instrumental function, must be deconvoluted from each of the observed line. In the present case, the instrumental function has a sine cardinal ( $\text{sinc} = \sin x/x$ ) form which is characteristic of the Fourier Transform [68]. It is accurately derived from a calibration procedure based on the observation of the atomic lines of Xe, which is present in the gas filter installed downstream of the beamline (see [159] and Chapter 2 for explanation), due to their natural narrow line-widths. The deconvolution of a Gaussian profile from the observed spectral profile of the Xe atomic line gives in the end the pure profile of the instrumental function. From this procedure, the FWHM (full width at half maximum) of the instrumental function is derived and is equal to about

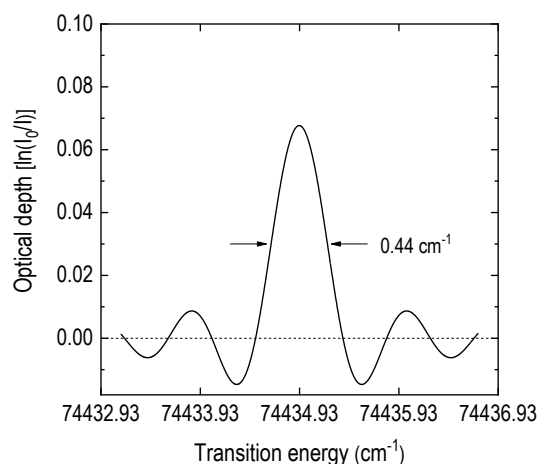


**Figure 4.4.** The instrumental function attaining a characteristic sinc form, obtained from the absorption line for atomic Xe as described in [68]. The function is centered at the transition energy which corresponds to the R(1) rotational component of the BX0-6 transition. The FWHM of this profile is equal to 0.44 cm<sup>-1</sup>.

$0.44 \text{ cm}^{-1}$ . **Fig. 4.4** shows the assumed instrumental function profile centered at the transition energy for which the R(1) rotational component of the BX0-6 transition is present i.e., at  $74434.93 \text{ cm}^{-1}$ . Nonetheless, regardless of the transition energy, the instrumental function remains the same, and consequently has the same effect on all of the absorption.

The remaining experimental absorption profile is approached by a pseudo-Voigt function. In principle, a Voigt profile is defined as the convolution of a Gaussian and a Lorentzian profile, each of which is related to different physical mechanisms contributing to the broadening of a spectral line. However, in this case the Voigt function is approximated by the pseudo-Voigt function, which is simply the linear combination of the two contributing profiles. In practice, the semi-automated routine implements a non-linear adjustment to the experimentally measured profile of the pseudo-Voigt profile convoluted with the previously deduced instrumental function. However, if a blend is identified as discussed before, then an additional pseudo-Voigt function is introduced and thus the resulting profile consists in the convolution of a total of two pseudo-Voigt profiles and the instrumental function. This way, the two contributions are isolated and then the only the pseudo-Voigt profile corresponding to the transition of interest is taken into account. It is noted that the position, the intensity, and the FWHM of the pseudo-Voigt functions are adjustable parameters in the routine. The non-linear adjustment between the experimental profile and the pseudo-Voigt profile convolute with the instrumental function (sinc) continues until criteria both on the minimal

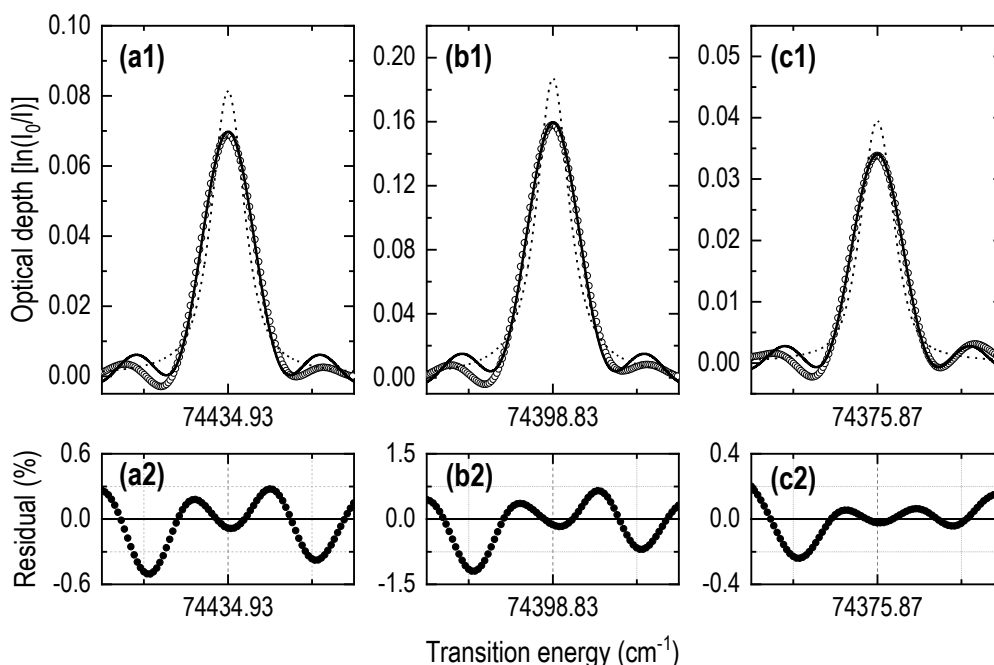


**Figure 4.5.** Examples of the results from the procedure of obtaining the deconvoluted absorption profile for three different absorption lines: (a1) the R(1), (b1) the R(2), and (c1) the P(1) rotational components of the BX0-6 transition. Open circles: experimental profile; dashed line: considered pseudo-Voigt profile; solid line: convolution of the pseudo-Voigt profile with the instrumental profile. The FWHM is the same for all three lines and is equal to  $0.4620 \text{ cm}^{-1}$ . Subfigures, (a2)-(c2) display the residuals from the comparison of the fitted function and the experimental data in the respective cases.

step and values of the objective function obtained between two successive steps are reached; criteria are  $10^{-8}$  and  $10^{-6}$  for the minimal step and the objective function, respectively. During this non-linear fitting procedure, the FWHM, the line position and the intensity of the Gaussian and the Lorentzian profiles are fixed parameters but the MatLab simplex procedure could alter them.

This process is repeated for all of the identified absorption lines. **Figs. 4.5(a1)-(c1)** illustrate the result of the fitting procedure for the three absorption lines mentioned before, the R(1), the R(2), and the P(1) rotational components of the BX0-6 transition (**Fig. 4.3**). The dotted lines represent the considered pseudo-Voigt profile, which upon its convolution with the instrumental function (solid line) results in a profile that is in good agreement with the experimental one (open circles). The efficiency of the fitting procedure is confirmed by the low residual (lower or near to 1%) that is obtained and displayed respectively in **Figs. 4.5(a2)-(c2)**.

Returning to the Beer-Lambert law (**Eq. 4.1**) and solving for the spectral absorption coefficient **Eq. 4.2** is obtained:

$$k_v(\nu) = \frac{1}{L} \ln \left( \frac{I_0(\nu)}{I(\nu)} \right) \quad (4.2)$$

This parameter, is identified as the governing quantity which characterizes the absorption of light, as a function of wavelength. It is recalled that based on a two-state scheme for the absorption of radiation, the conventional notations for the lower (in the ground electronic state) and upper (in an excited electronic state) rotational (vibrational) levels are:  $J''(v'')$  and  $J'(v')$ , respectively. For a single line (rotational transition)  $k_v(\nu)$  is given by [171]:

$$k_v(\nu) = k_0 \varphi(\nu) \left( n_{J''} - \frac{g_{J''}}{g_{J'}} n_{J'} \right) \quad (4.3)$$

Where  $n_{J''}$  and  $n_{J'}$  are the population densities in the lower and the upper rotational level and accordingly  $g_{J''}$  and  $g_{J'}$  are the statistical weights of those levels, and  $\varphi(\nu)$  is the normalized lineshape function. More specifically, the normalized lineshape function, is defined as:

$$\varphi(\nu) = k_v / \int_{\text{line}} k_v(\nu) d\nu, \text{ so that } \int_{\text{line}} \varphi(\nu) d\nu = 1 \quad (4.4)$$

The lineshape function, whose integral over the line is equal to 1, provides a useful way of characterizing the shape of a line regardless of the type (Gaussian, Lorentzian, or Voigt) [172].

$k_0$  is a factor related to the absorption ( $B_{J''J'}$ ) and emission ( $A_{J'J''}$ ) Einstein coefficients, the oscillator strength of the line ( $f_{J''J'}$ ), or the transition dipole momentum ( $\mu$ ) according to the relation [171]:

$$k_0 = \frac{h\nu}{c} B_{J''J'} = \frac{g_{J'} \lambda^2}{g_{J''} 8\pi} A_{J'J''} = \frac{1}{4\pi\epsilon_0} \frac{\pi e^2}{m_e c} f_{J''J'} = \frac{g_{J''}}{g_{J'}} \frac{2\pi^2}{3\epsilon_0 h \lambda} |\mu|^2 \quad (4.5)$$

In **Eq. 4.5**  $\lambda$  is the wavelength,  $\epsilon_0$  the permittivity of free space,  $m_e$  and  $e$  the electron mass and elementary charge,  $c$  the speed of light, and  $h$  Planck's constant. **Eq. 4.3** evidences that the measured absorption is always related to the population difference between the lower and the upper level of a transition. However, when dealing with electronic transitions where the energy difference is larger than the gas temperature, usually  $n_{J'} \ll n_{J''}$  is satisfied so that the second term in the parenthesis in **Eq. 4.3** can be omitted. If a Boltzmann equilibrium is considered within the rotational levels, then:

$$\frac{n_{J'}}{n_{J''}} = \frac{g_{J'}}{g_{J''}} \exp\left(-\frac{h\nu}{k_B T_g}\right) \quad (4.6)$$

where  $k_B$  is the Boltzmann constant and  $T_g$  is the gas temperature. With a measured gas temperature in this reactor of about 400K (see section 4.3.2 for details) and since the energy of transitions between the BX states exceed 5 eV, in fact, the aforementioned assumption holds true. Combining this fact with the expression for  $k_0$  using the transition oscillator strength from **Eq. 4.5**, the following formula is deduced:

$$k_\nu(\nu) = \frac{1}{4\pi\epsilon_0} \frac{\pi e^2}{m_e c} f_{J''J'} \varphi(\nu) n_{J''} \quad (4.7)$$

In the case of diatomic molecules, taking the integral of the optical depth for a given line, and applying **Eqs. 4.2 – 4.7** ultimately gives:

$$\int_{J' \leftarrow J''}^{\square} \ln\left(\frac{I_0(\nu)}{I(\nu)}\right) d\nu = L \int_{J' \leftarrow J''}^{\square} k_\nu(\nu) d\nu = L \frac{1}{4\pi\epsilon_0} \frac{\pi e^2}{m_e c} f_{J''J'} n_{J''} \quad (4.8)$$

Thus, a relation between the integral of an absorption line in terms of optical depth and the relative population density in the probed level is established.

**Fig. 4.6** displays the resulting integrated absorption values for the R- and P-branches of several transitions in the BXv'-6 band. Such plots can, in fact, be generated for all of the studied transitions. A closer observation of the resulting intensity distributions validates what is established by theory. In particular, it is seen that the intensities of the rotational components of the R and P branches alternate in intensity, for the most part at least, which is typical for homonuclear molecules such as H<sub>2</sub> and D<sub>2</sub>. While it is beyond the scope of this text to delve into the theoretical details, several brief comments should suffice to clarify this occurrence. Firstly, theory dictates [173] that for homonuclear molecules with a total orbital angular momentum  $\Lambda$  equal to zero (i.e. for the  $\Sigma$  states), either the even-numbered or the odd-numbered rotational levels have a greater statistical weight. In this sense, they are referred to as "strong" or "weak". In the case of D<sub>2</sub> in particular, it has been shown that the even-numbered (symmetric) levels have the greater statistical weight. The opposite holds true for H<sub>2</sub>. Moreover, on account of the selection rule which states that symmetric levels may combine only with symmetric ones, and anti-

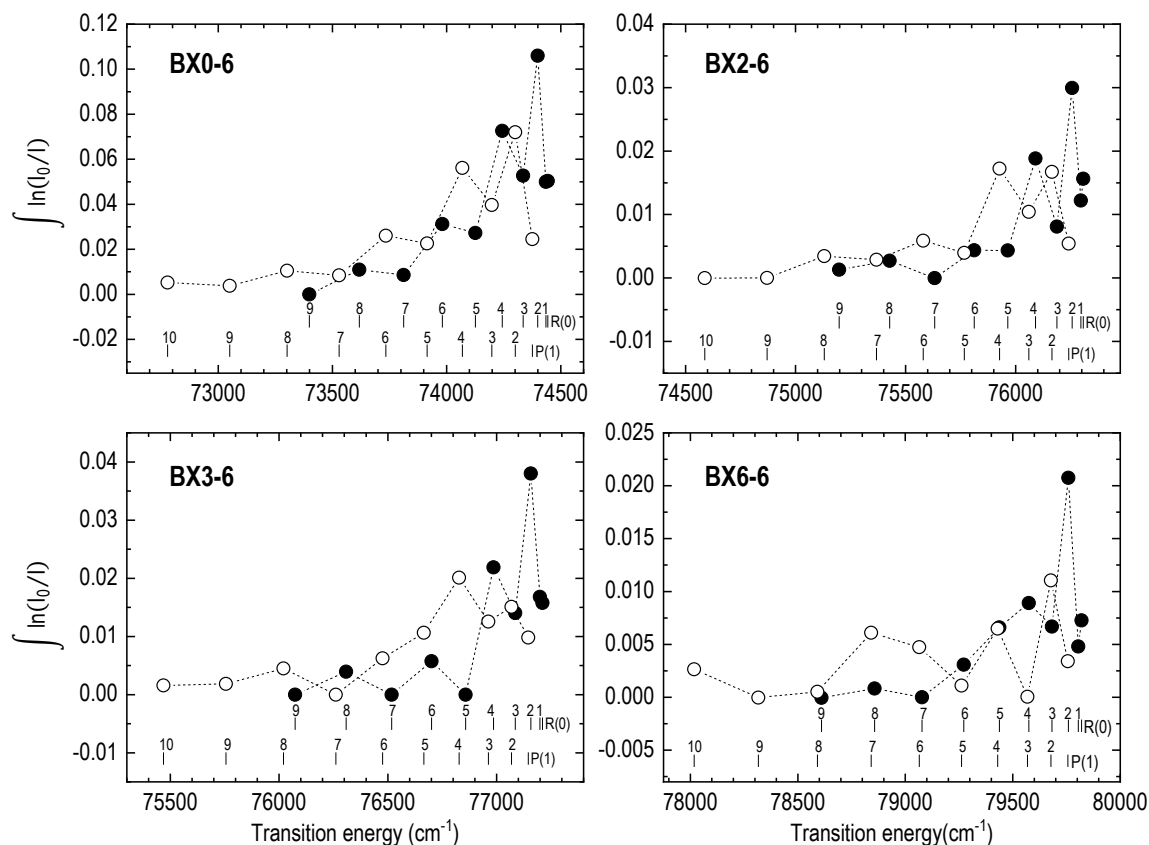


**Figure 4.6.** Intensity distribution of the rotational components of several transitions within the BXv'-6 band. Filled circles: R-branch components; Open circles: P-branch components.

symmetric with anti-symmetric ones, “strong” levels combine only with “strong” ones and “weak” levels with “weak” ones. Since, in addition, the selection rule  $\Delta J = \pm 1$  holds for the rotational branches, two electronic  $\Sigma$  states may combine with each other only if in one the even-numbered levels are the “strong” ones and in the other the odd-numbered levels are the “strong” ones [173].

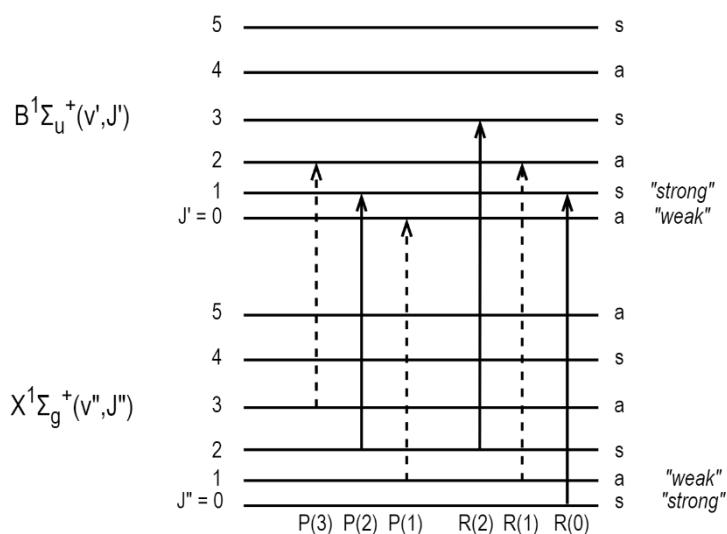


**Figure 4.7.** Principle of the intensity alternation in the rotational transitions of the  $B^1\Sigma_u^+ - X^1\Sigma_g^+$  electronic band. The symmetric (“strong”) and anti-symmetric (“weak”) levels are denoted with the letters s and a, respectively. The three first components of each of the R and P rotational branches are shown; the solid arrows represent a “strong” transition whereas the dashed lines a “weak” one.

For the BX transitions examined herein, the illustration in **Fig. 4.7** may ease the comprehension of this phenomenon. Therefore, overall, since the statistical weights of the rotational levels both in the upper and lower electronic states alternate, an alternation in intensity must occur [173].

In returning to the methodology for the spectra analysis, as it was mentioned at the beginning of this section, typically the value of the current flowing through the undulator of the synchrotron beamline is regulated so that the synchrotron illumination is centered around the center of the transition energy range for which a particular vibrational band can be observed. However, it so happens that, there is an overlap in the transition energy regions covered by illuminations from different undulator settings. In **Fig. 4.8** for example it is demonstrated how the rotational components of the BX3-6 transition are discernable in spectra obtained with three different undulator settings, i.e. from three spectra centered on different transition energies. The importance of this lies in that, in cases such as these, the treatment of a single transition through multiple spectra can provide an estimation of the error between different measurements. Thus, a correlation with the overall stability of the plasma in the course of the measurements, since typically the different spectra can be recorded with an interval of nearly half an hour, can be established. This aspect will be better understood in the following part of the analysis procedure.

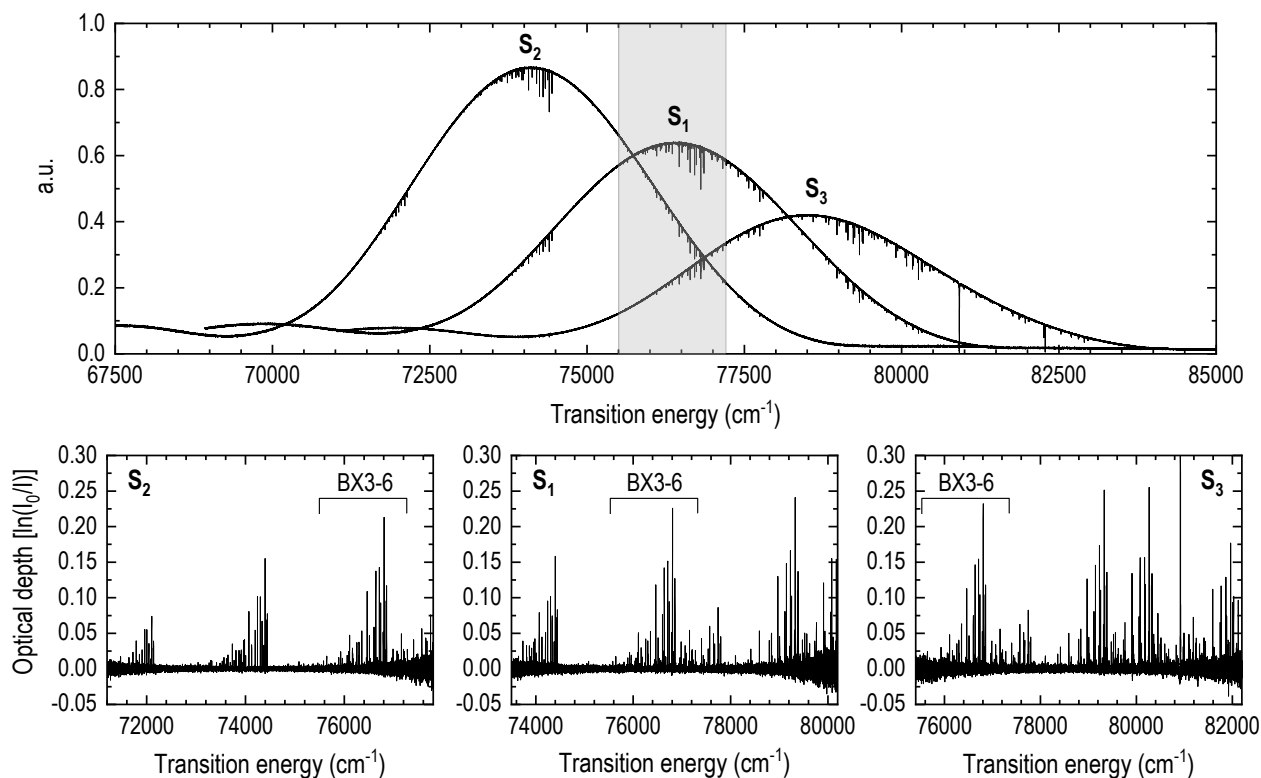


**Figure 4.8.** Top: Raw spectra ( $S_1$ ,  $S_2$ , and  $S_3$ ) obtained with three different settings of the undulator current;  $S_1$  is centered around  $76462 \text{ cm}^{-1}$ ,  $S_2$  around  $74197 \text{ cm}^{-1}$ , and  $S_3$  around  $78596 \text{ cm}^{-1}$ . The shaded rectangle marks the transition energy range which is covered by all three spectra and within which the rotational components of the BX3-6 transition are observed. Bottom: Transformed, to units of optical depth, spectra. In each, the position of the rotational components of the BX3-6 transition is indicated.

In order to deduce the population density in a given vibrational level  $v''$  of the ground state, it is necessary subsequently to perform a summation of the integrals previously calculated for all of the rotational R- and P-branch components of vibrational transitions associated to that level from **Eq. 4.8**. This may be expressed by:

$$\sum_{J''} \left[ \int_{J' \leftarrow J''}^{(R)} \ln \left( \frac{I_0(\nu)}{I(\nu)} \right) d\nu + \int_{J' \leftarrow J''}^{(P)} \ln \left( \frac{I_0(\nu)}{I(\nu)} \right) d\nu \right] = L \frac{1}{4\pi\epsilon_0} \frac{\pi e^2}{m_e c} f_{v''v'} n_{v''} \quad (4.9)$$

**Fig. 4.9** displays the values of these sums (hereafter symbolized as  $S_{v''v'}$ ), calculated according to **Eq. 4.9**, for the BX transition and for the first ten vibrational levels of the ground electronic state (i.e. for  $v'' = 0$  to 10) as a function of the vibrational level of the upper electronic state ( $v'$ ). The distributions of these sums of the integrated optical depth presented in **Fig. 4.9** are governed by the Franck-Condon principle, the concept of which is briefly explained in the next paragraph.

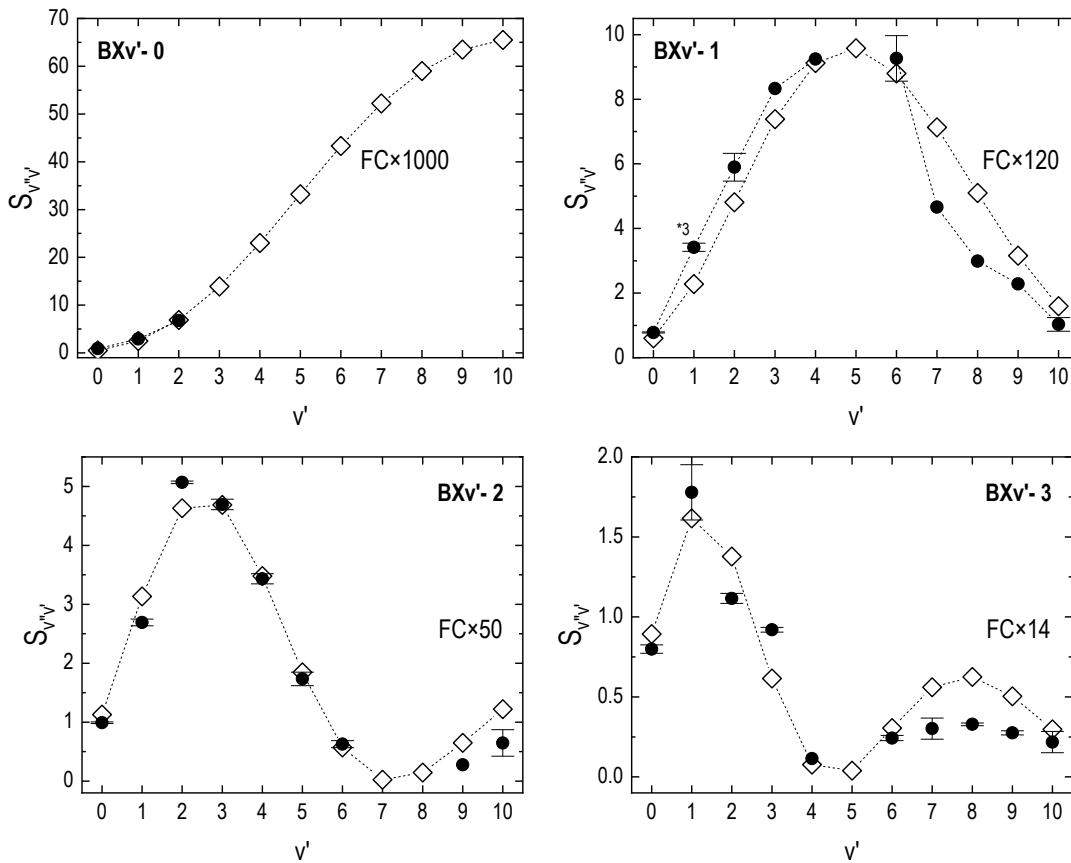


**Figure 4.9.** Each subfigure shows for each of the first ten vibrational levels in the ground electronic state,  $v''$ , the sum of the integrated optical depths of all of the R- and P-branch rotational components of the vibrational transitions associated to that given level (closed circles). The error bars, unless otherwise specified by a number next to the data point, result from the processing of two different spectra obtained with different undulator settings. These data points are superposed upon the scaled (by a factor given in each subfigure) theoretical values of the FC factors.

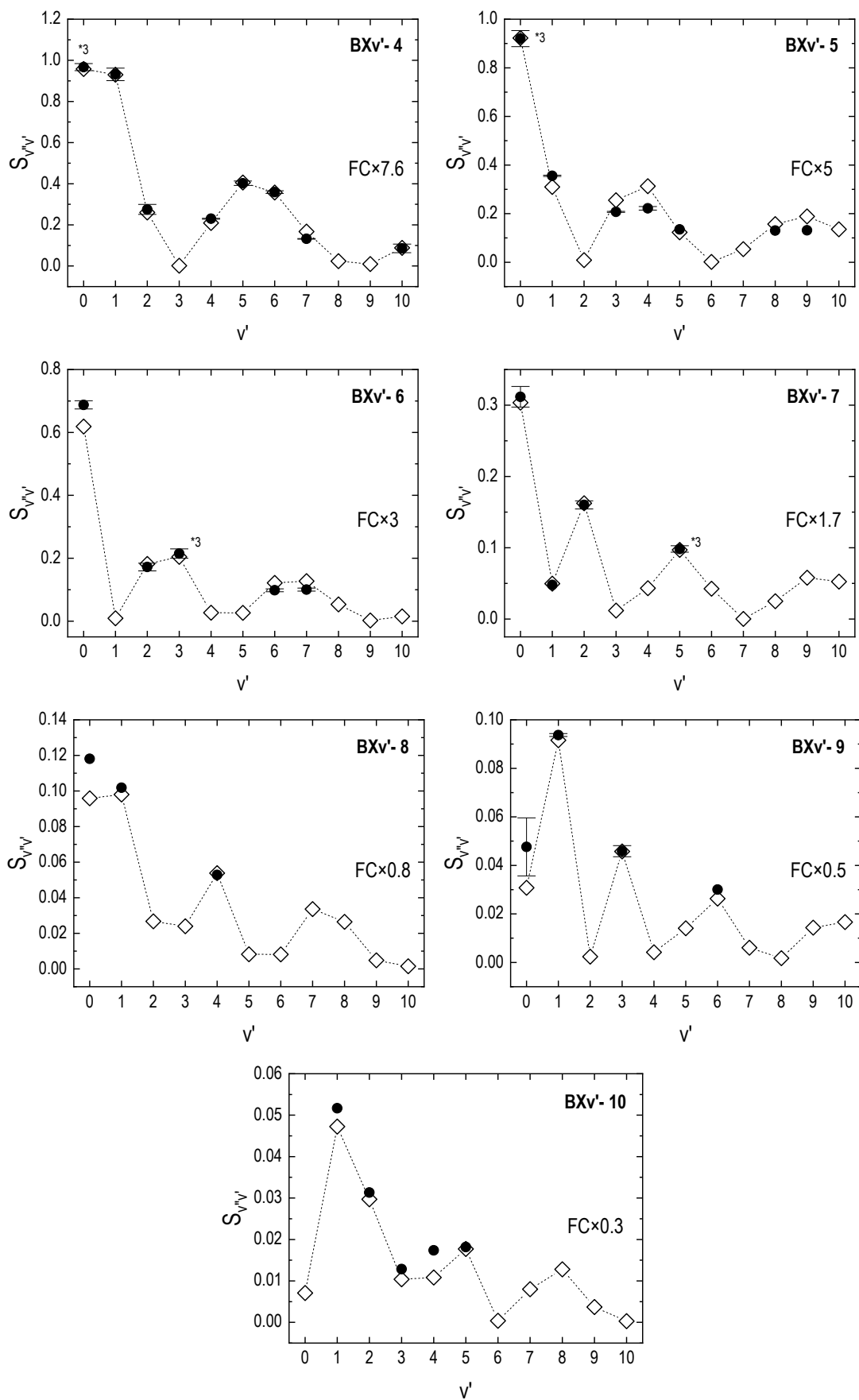
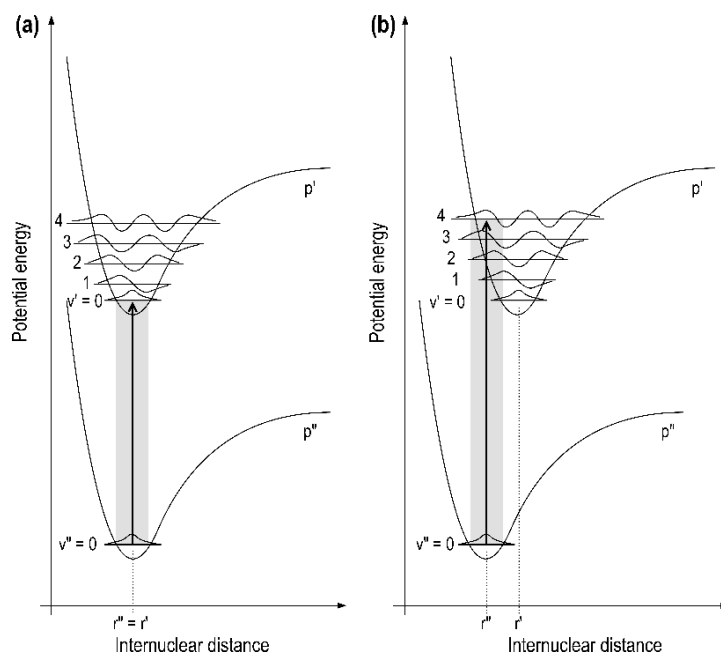


Figure 4.9. Continued.



**Figure 4.10.** Illustration of the FC principle for a transition from an electronic state  $p''$  to a higher electronic state  $p'$ , for two different cases depending on the relation between the initial and final internuclear distance: (a)  $r' = r''$  demonstrating that the transition 0-0 is the most probable, and (b)  $r' > r''$  showing that the 4-0 transition is most probable.

Franck's main idea, which was developed mathematically and later given a wave-mechanical basis by Condon states that the electron "jump" in molecule takes place so rapidly in comparison to the vibrational motion that immediately afterwards the nuclei still have very nearly the same relative position and velocity as before the "jump" [173]. This is more easily understood from the illustration of **Fig. 4.10**. The potential curves of the upper and lower electronic state involved are drawn, for two typical cases. In the first case (**Fig. 4.10(a)**), the minima of the two curves lie very nearly one above the other (corresponding to no change in the internuclear distance of the atoms,  $r' = r''$ ) whereas in the second case (**Fig. 4.10(b)**), the minimum of the upper state lies at a somewhat greater distance than that of that the lower state ( $r' > r''$ ) [173], [174]. In quantum-mechanic terms, the Franck-Condon (FC) factor,  $q_{v''v'}^{p''p'}$ , is defined as the overlap integral of the two vibrational wavefunctions in different electronic states for an electronic transition from  $p''$  to  $p'$  [175]:

$$q_{v''v'}^{p''p'} = \left| \int_0^\infty \psi_{v'}^{*p'}(r) \psi_{v''}^{p''}(r) dr \right|^2 \quad (4.10)$$

In other words, the greater the value of the FC factor, the greater the transition probability. In addition, **Table 4.8** reproduces from [175] the calculated FC factors for the  $BXv'-v''$  band transitions implicating the first ten vibrational levels of both electronic states.

**Table 4.8.** Franck-Condon factors for the  $D_2 B^1\Sigma_u^+(v', J') \leftarrow X^1\Sigma_g^+(v'', J'')$  transition. Reprinted from [175] with permission from Elsevier (License No. 5762350133793).

$v''$											
$v'$	0	1	2	3	4	5	6	7	8	9	10
0	0.00052	0.0050	0.02258	0.06379	0.12602	0.18449	0.20629	0.17861	0.11985	0.06159	0.02357
1	0.00253	0.01904	0.06268	0.11541	0.12236	0.06203	0.00299	0.02920	0.12247	0.18306	0.15753
2	0.00689	0.04012	0.09255	0.09841	0.03419	0.00166	0.06062	0.09546	0.03337	0.00481	0.09895
3	0.01388	0.06146	0.09368	0.04394	0.00024	0.05095	0.06813	0.00704	0.02999	0.09145	0.03465
4	0.02299	0.07596	0.06955	0.00550	0.02750	0.06260	0.00886	0.02550	0.06730	0.00835	0.03614
5	0.03321	0.07982	0.03687	0.00283	0.05344	0.02462	0.00878	0.05701	0.01029	0.02824	0.05899
6	0.04330	0.07326	0.01139	0.02183	0.04702	0.00035	0.04064	0.02502	0.01016	0.05259	0.00126
7	0.05216	0.05941	0.00046	0.03999	0.02202	0.01075	0.04242	0.00008	0.04199	0.01206	0.02666
8	0.05903	0.04249	0.00292	0.04463	0.00314	0.03136	0.01780	0.01471	0.03308	0.00352	0.04264
9	0.06349	0.02627	0.01301	0.03595	0.00122	0.03770	0.00079	0.03410	0.00597	0.02873	0.01234
10	0.06554	0.01329	0.02441	0.02122	0.01162	0.02705	0.00503	0.03090	0.00193	0.03329	0.00097

The oscillator strength term now introduced in **Eq. 4.10** refers to a “band oscillator strength” which is furthermore given as a function of the FC factor by [176]:

$$f_{v''v'} = \frac{8\pi^2 m_e c a_0^2}{3h} \bar{\nu}_{v''v'} \frac{(2 - \delta_{0, \Lambda' + \Lambda''})}{(2 - \delta_{0, \Lambda'})} q_{v''v'} R_e^2(\bar{r}_{v''v'}) \quad (4.11)$$

Where the ratio  $(2 - \delta_{0, \Lambda' + \Lambda''}) / (2 - \delta_{0, \Lambda'})$  is equal to 1 for  $\Sigma$ - $\Sigma$  transitions such as the BX one,  $\bar{\nu}_{v''v'}$  is the averaged value for the wavenumber for the vibrational band, and  $R_e$  is the electronic transition moment in atomic units of  $e \times a_0$ . The substitution of **Eq. 4.11** into **Eq. 4.9** finally gives:

$$S_{v''v'} = L \frac{2e^2 \pi^2 \alpha_0^2}{3h \epsilon_0} \bar{\nu}_{v''v'} q_{v''v'} R_e^2(\bar{r}_{v''v'}) n_{v''} \quad (4.12)$$

Thus, the comparison in **Fig. 4.9** of the band strengths with the FC factors is relevant. Indeed, the experimentally derived results are superposed on the corresponding FC factors in the same figure. By observing **Eq. 4.12** it can be seen that the ratio of the sum of the integrals across all rotational levels linked to a given  $v''$  level to the respective FC factor is directly proportional to the relative population in the leading vibrational level of each band, i.e.:

$$\frac{S_{v''v'}}{q_{v''v'}} \propto n_{v''} \quad (4.13)$$

On the basis of this last analogy that holds true, an intermediate step towards the relative VDF can be deduced. In practice, once the graphs of **Fig. 4.9** have been derived, for each vibrational band the individual ratios of the available band strengths to the FC factors are calculated. This results in a number of different values across  $v'$  for the said ratio. The mean value from the multiple points is calculated along with an uncertainty. The former ultimately corresponds to a

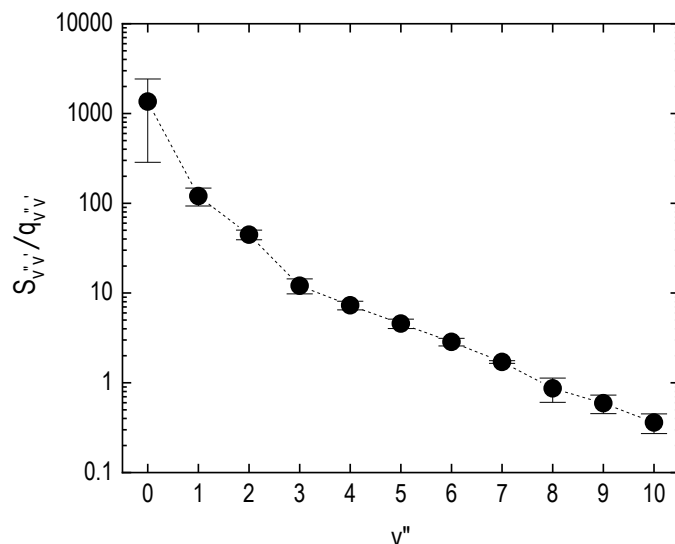


**Figure 4.10.** Plot of the distribution of the  $S/q$  ratios over the vibrational levels of the ground state mirroring the VDF. A thorough explanation for the derivation of the data points and their error bars is given in text.  $D_2$  plasma; 1.6 Pa, 150 W (see also next section for details).

value that is proportional to the population density of the level  $v''$  for which the computation is being made. This means that with knowledge on all of the other factors in **Eq. 4.12** it would be possible to deduce the absolute value of  $n_{v''}$ . Based on this procedure and the data in **Fig. 4.9**, the resulting distribution of the  $S/q$  ratios over the vibrational levels of the ground electronic state is presented in **Fig. 4.10**. The error bars on each of the points are derived from the application of a Student's  $t$ -test when defining a 95% confidence interval.

## 4.2 VDFs in characteristic plasma conditions

In the present section, the distributions of the  $S/q$  ratios which are directly proportional to the absolute VDFs (hereafter denoted as intermediate VDFs), obtained in  $D_2$  plasmas produced in

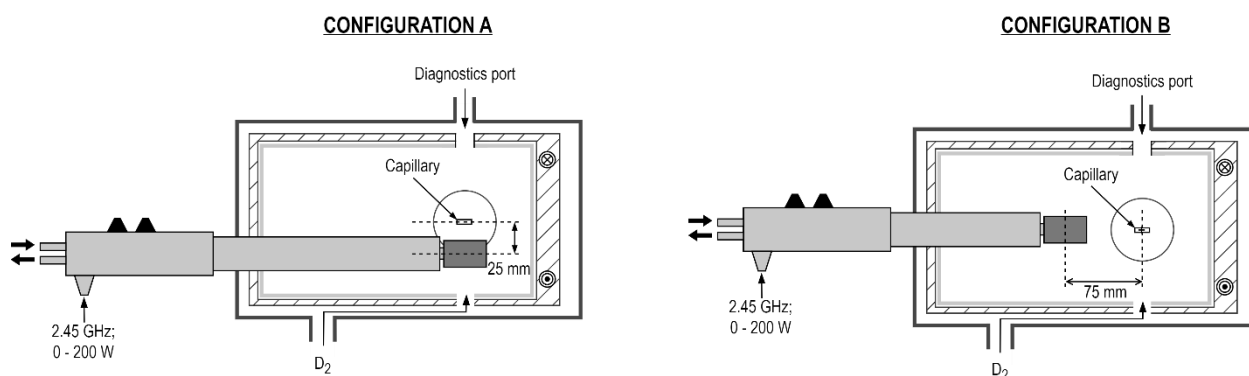


**Figure 4.11.** Detailed illustration of the two characteristic configurations of the “SCHEME-II+” reactor for the investigation of the VDFs in there produced  $D_2$  plasmas. It is reminded that the synchrotron radiation beam passes through the capillaries on each side of the reactor, that is in a direction perpendicular to this page.

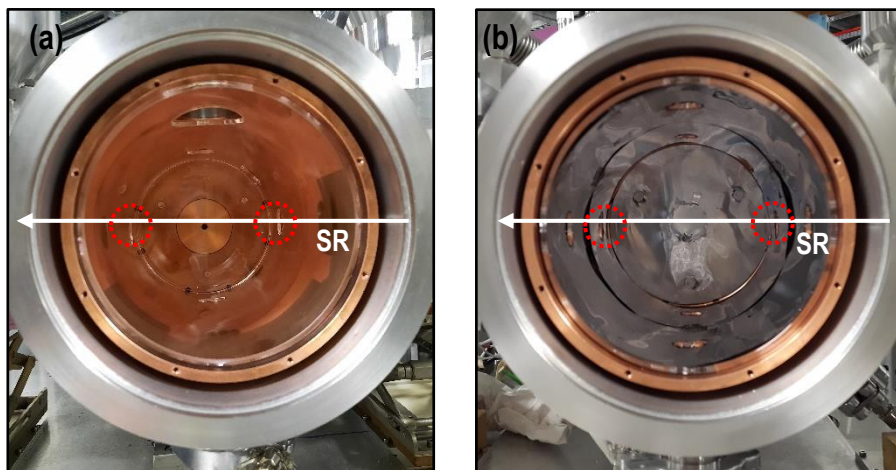


**Figure 4.12.** Real photos of the interior of the “SCHEME-II+” reactor depicting the two cases of materials that are investigated. (a) The Quartz cylinder is set in place thus constituting a full quartz interior, and (b) Tantalum foils (0.1 mm thick) are set on top of the quartz surface so that a full metallic coverage is achieved. The white arrows on the pictures indicate the position and direction of the synchrotron radiation (SR) beam, while the red dotted circles that of the capillaries.

the “SCHEME-II+” reactor via VUV-FT absorption spectroscopy and by using the methodology described in the preceding sections will be presented. In particular, these have been deduced for four characteristic operating conditions detailed hereafter. More specifically, as it is illustrated in **Fig. 4.11**, two principle configurations of the “SCHEME-II+” reactor which differ with respect to the position of the dipolar ECR module inside the reactor structure. It is reminded that the synchrotron radiation beam which is used for the absorption measurements traverses the reactor structure through the two capillaries (noted on **Fig. 4.11**) that complete the differential pumping unit, in a sense perpendicular to the present page. In addition to the aforementioned distinction, in both configurations, the influence of two different materials on the VDFs is assessed. Namely, quartz (Q) which notably in this case serves as a reference material, and Tantalum (Ta). In either case, special attention is paid so that the plasma faces entirely (100%) a Q or Ta surface (**Fig. 4.12**). For the case of Q this is slightly easier since, by design a Q cylinder is always placed inside the reactor as it has been discussed in the description of the “SCHEME-II+” reactor in section 2.2 of the second chapter. For the case for which Ta should be investigated, thin foils (0.1 mm thickness) are acquired, cut and shaped in such a way as to fully coat the interior of the quartz cylinder. In other words, the foil is made sure to cover all of the quartz parts, and thus it is considered that the plasma faces an entirely metallic surface. During the experiments it is also important to note that the basic plasma operating parameters are kept constant, i.e. the working gas pressure is regulated at 1.6 Pa and the transmitted microwave power is 150 W. Following the acquisition of the absorption spectra and their processing which has been described in sections 2.2.1 and 4.1, respectively, the resulting intermediate VDFs for the four different operating conditions mentioned before are displayed in **Fig. 4.13**.

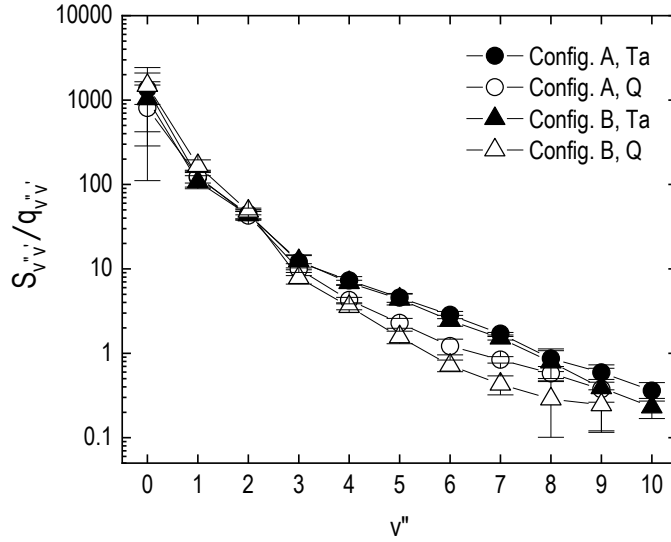


**Figure 4.13.** Plot of the intermediate VDFs for a D<sub>2</sub> plasma (1.6 Pa; 150 W) for four characteristic configurations of the “SCHEME-II+” reactor.

### 4.3 Determining the absolute VDF

**Eq. 4.12** suggests a straightforward way to deduce the population density  $n_{v''}$  in the vibrational levels of the electronic ground state for the D<sub>2</sub> molecule, since the rest of the terms in the equation are constant:

$$n_{v''} = \frac{S_{v''v'}}{L \frac{2e^2\pi^2\alpha_0^2}{3h\epsilon_0} \bar{v}_{v''v'} q_{v''v'} R_e^2(\bar{r}_{v''v'})} \quad (4.14)$$

However, in reality the absorption length  $L$  is the sole parameter which can be questioned and there is some ambiguity surrounding its correct determination. Primarily, due to the fact that the “SCHEME-II+” reactor is installed along the synchrotron beamline for measurements in a windowless mode, the passive gas (see section 2.2 for details) flowing outside of the structure through the two capillaries set on either side of the differential pumping unit makes it difficult to clearly define a value for  $L$ .

This issue can be circumvented by performing a calibration procedure in which absorption measurements are performed in the absence of the plasma, in pure D<sub>2</sub> gas. It is known that, when the plasma is not ignited the entire molecule population lies in the ground state  $X^1\Sigma_g^+(v''=0, J'')$  levels. By applying the ideal gas law considering the pressure of 1.6 Pa and a temperature of 294 K (room temperature of 21 °C), the population density of the molecules, let it be denoted as  $n_{i,off}$ , is found equal to  $3.94 \times 10^{20} \text{ m}^{-3}$ . The application of the analysis of section 4.1 in the case of the investigation of only the  $BXv'-0$  transitions when the plasma is not ignited yields the  $S/q$  ratios (**Eq. 4.13**) from which a mean value for  $S/q$  can be calculated for the  $v''=0$  level, which is then proportional to the entire molecule density, i.e.  $3.94 \times 10^{20} \text{ m}^{-3}$ .

**Table 4.9.** Measured values for the band strength for the  $BXv'-0$  ( $v' = 0, 1$ ) transitions. Two measurements per band exist from two different spectra obtained with two different undulator settings. The band strength is divided by the FC factor and a mean value and an uncertainty (derived from a Student's t-test) is calculated.

Band	$S_{0v'}$	$q_{0v'}$	$S_{0v'}/q_{0v'}$
BX0-0 <sub>(1)</sub>	1.032	0.0005	2063.10
BX0-0 <sub>(2)</sub>	1.045	0.0005	2090.25
BX1-0 <sub>(1)</sub>	4.36	0.0025	1743.06
BX1-0 <sub>(2)</sub>	4.76	0.0025	1903.27
<b>Mean</b>			<b>1950</b>
<b>Uncertainty</b>			<b>255</b>

**Table 4.9** summarizes these results for the experimental conditions (1.6 Pa, 150 W) studied herein. According to the former statement, the mean value of 1950 (**Table 4.9**) is directly related to a molecular density of  $3.94 \times 10^{20} \text{ m}^{-3}$ . That is, when considering a given absorption length  $L$  which also includes the contribution of the passive gas. It is reminded here that the term passive gas refers to the gas flowing outside of the capillaries of the differential pumping unit employed at the "SCHEME-II+" reactor. Similar measurements, which are not included in this work, in several other pressures as well (0.06 Pa, 0.66 Pa, and 0.8 Pa) evidenced a linear increase of the  $S/q$  ratio as a function of pressure. This is proof both for the good performance of the analysis that is carried out and the absence of saturated spectral lines.

While by direct analogy the absolute density of all of the levels could be derived, this would lead to erroneous results. In fact,  $L$  is not constant but actually decreases with increasing vibrational level. This is due to the decreasing lifetime of the higher vibrational levels as it has been reported in [130]. This study revealed that the vibrationally excited molecules have lifetimes of a few hundred microseconds. More specifically, the lifetime falls from  $350 \mu\text{s}$  for  $v'' = 4$  to about  $100\text{-}150 \mu\text{s}$  for the intermediate levels  $v'' = 6\text{-}11$ , and finally plummets to several tens of microseconds for higher levels. Thus, an absorption length equal to  $L$  is to be considered only for the  $v'' = 0$  level while only a fraction of  $L$ ,  $L'$ , for the higher levels. **Table 4.10** collects the data corresponding to each of the points in **Fig. 4.13**, i.e. the experimental values for the  $S/q$  ratios in the ten first vibrational levels of the ground electronic state for the  $D_2$  molecule, for the four studied conditions. At the same time, at the end of **Table 4.10** the value for the summation of the  $S/q$  ratios over all of the observed vibrational levels is given. In all of the studied cases, in the presence of the plasma, this sum is lower than that in the absence of the plasma. On the one hand, one explanation would be that there are several other vibrational levels that are populated and are not accounted for since they are not observable. However, their small contribution is not expected to compensate for the difference. On the other hand, there is a loss of a portion of the molecule population when the plasma is ignited. In fact, this is expected on account of the

combined action of a few mechanisms such as dissociation of the gas, ionization and excitation to triplet states [68].

**Table 4.10.** Experimental values of  $S_{v''}/q_{v''}$  in the different experimental conditions studied herein. D<sub>2</sub> plasma, 1.6 Pa; 150 W.

$v''$	Without plasma	Quartz (Q)		Tantalum (Ta)	
		Config. A	Config. B	Config. A	Config. B
0	1950	807.4504	1488.1	1355.5	1035.4
1		123.8621	167.1918	120.3785	108.0885
2		42.7625	48.0652	44.7241	43.6122
3		9.9201	7.8389	12.0649	12.4874
4		4.2756	3.5668	7.294	6.8551
5		2.287	1.5628	4.5657	4.3836
6		1.2158	0.7184	2.8527	2.4522
7		0.8393	0.4303	1.7067	1.5095
8		0.5794	0.287	0.867	0.7874
9		0.3763	0.2447	0.592	0.3907
10		--	--	0.3609	0.2307
$\sum_{v'' > 0} v''$		186.1181	229.9059	195.4065	180.7973
$\sum v''$	1950	993.5685	1718.0059	1550.9065	1216.1973

Based on the discussion in the preceding paragraphs, it is evident that with the current knowledge one can derive with certainty the absolute population density of only the  $v'' = 0$  level. It is noted that it is because L does not change between the calibration procedure based on the measurements in the absence of the plasma and on the measurements when the plasma is ignited, only for  $v'' = 0$ . Thus, the values in the first row of **Table 4.10** are finally transformed to absolute molecule densities as given in **Table 4.11**.

**Table 4.11.** Absolute values for the D<sub>2</sub> molecule density in the fundamental vibrational level of the  $X^1\Sigma_g^+$  state (1.6 Pa, 150 W).

$v''$	Without plasma	Quartz (Q)		Tantalum (Ta)	
		Config. A	Config. B	Config. A	Config. B
0	$3.9 \times 10^{20} \text{ m}^{-3}$	$1.6 \times 10^{20} \text{ m}^{-3}$	$3.0 \times 10^{20} \text{ m}^{-3}$	$2.7 \times 10^{20} \text{ m}^{-3}$	$2.1 \times 10^{20} \text{ m}^{-3}$

For the higher vibrational levels, in the end, the most accurate way to deduce their population density would be through **Eq. 4.14** after having properly defined the absorption length for each level in taking into account the factors that influence it. For that, dedicated experimental and modeling efforts would be of great value. In this work, it will suffice to say that even if the correction for the higher vibrational levels could be effected it is not expected to significantly alter the shape of the distribution. In other words, it would maintain that of **Fig. 4.13** and the relations between the different experimental configurations would be the same. Thus, the discussion that will follow in section 4.5 is made on the basis that the absolute VDFs would have the form of those in **Fig. 4.13**.

## 4.4 Other parameters derived through VUV-FT absorption spectroscopy

A unique aspect of the VUV-FTS measurements described in this chapter is furthermore the ability to observe up to eleven atomic Lyman lines, i.e. the transitions from  $n = 1$  up to  $n = 12$ . Therefore, it is possible to infer the atomic density in the ground state and from that the degree of dissociation of the gas. However, in order to do so it is necessary to also have knowledge on the gas temperature. Thus, before presenting the results on the atomic density and the degree of dissociation, the following section is dedicated to the description of the derivation of an estimate of the gas temperature experimentally in the “SCHEME-II+” reactor.

### 4.4.1 Gas temperature

An estimation of the gas temperature is derived from applying the tunable diode-laser absorption spectroscopy diagnostic whose validity and details on its implementation at the “SCHEME-II+” reactor were discussed in section 2.2.1. In particular, the left side of **Fig. 4.11** showed the configuration of the reactor under which the measurements were made. It corresponds to one of the two for which the VDFs were investigated, and thus these measurements are immediately relevant to those. Namely, the probed line-of-sight lies 25 mm above the axis of the magnet of the dipolar ECR module, and the plasma faces a surface entirely covered by Quartz. In addition, three different values of working gas pressure (0.8, 1.6 and 3.2 Pa) and transmitted microwave power (100, 150 and 200 W) were investigated.

**Fig. 4.14** displays the gas temperature that is derived by the process outlined in section 2.2.1 for several different operating conditions. The temperature is within several hundreds of Kelvin, with the mean values being between 400 K and 600 K. At the same time, increasing pressure or

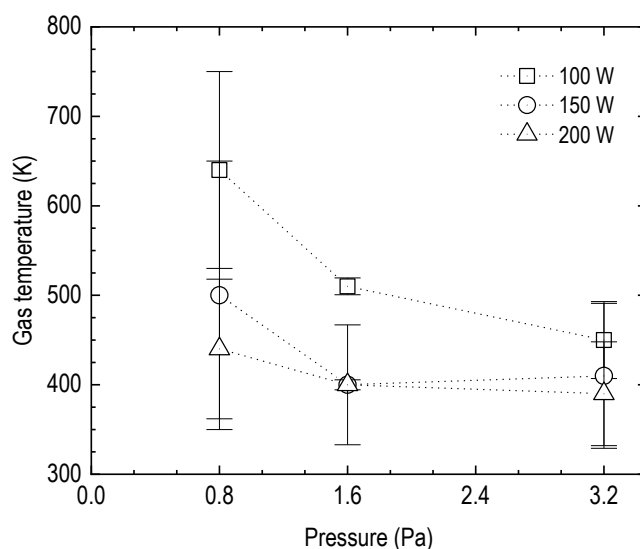


**Figure 4.14.** Estimated gas temperature in several characteristic plasma operating conditions.

power induces a decrease of the gas temperature. This is expected since both of these variations lead to a rise of collisions and subsequent energy loss for the atomic species.

The value of the gas temperature that is most relevant in this case is that for the 1.6 Pa/150 W pair of conditions that have been repeated throughout this chapter, i.e.  $400 \pm 5.6$  K. In fact, this result correlates well with a previous estimation of the gas temperature at  $465 \pm 30$  K [68], through the rotational temperature at that time, from experiments held at the same reactor also employing the VUV-FTS technique presented herein.

#### 4.4.2 Atom density and degree of dissociation

As it was briefly mentioned above, it is possible to infer the atomic density through the close inspection of the atomic Lyman transitions. Normally, from the processing of each of the observable Lyman lines the same result for the atom density should be obtained since the intensity of the absorption in principle is directly proportional to the population of the lower level, that is the  $n = 1$  state in this case. This is extremely useful since, often, the absorption line of the first or even second Lyman transition may appear to be saturated in the acquired spectra, which, upon processing would lead to erroneous calculations. The routine utilized to process the spectral lines of the Lyman transitions is a combination of the method used for the treatment of the VUV-FT spectra (section 4.1) and of that for the TDLAS signals (section 2.2.1). Briefly, first the inherent quasi-Gaussian baseline imposed by the synchrotron illumination is subtracted from the acquired spectra. This time, the evaluation of the baseline is based on a non-linear adjustment of four Gaussian profiles to the experimental spectrum using the “fminsearch” function of Matlab. This function utilizes the Nelder-Mead simplex algorithm as described in [177]. Afterwards, the spectral lines are identified, and potential blends with neighboring lines are also assessed. Deconvolution of the instrumental function from the line profile and subsequent calculation of the optical depth follow. The next step consists in fitting to the measured profile a pseudo-Voigt profile. In particular, for the Lyman lines in question, the fit returns a zero contribution of the Lorentzian component (it is reminded that the pseudo-Voigt profile is made from the sum of a Lorentzian and a Gaussian profile), thus the lines are characterized solely by a Gaussian profile. In the final step of the procedure, it is possible to calculate the atom density which is proportional to the integral of the spectral line, and from that also the degree of dissociation  $D$ :

$$D = \frac{n_D}{n_D + 2n_{D_2}} \quad (4.15)$$

where  $n_D$  and  $n_{D_2}$  denote the atom and molecule densities, respectively. It is noted that  $n_{D_2}$  is approximated via the ideal gas law.

**Table 4.12** shows the results for the atom density and the degree of dissociation for the two cases of materials investigated in the “SCHEME-II+” reactor, for additionally three characteristic values of the gas temperature, i.e. 294 K, 400 K, and 600 K.

**Table 4.12.** Atom density in the cases of coverage of the interior of the reactor with quartz and Tantalum, and degree of dissociation for three different values of the gas temperature. D<sub>2</sub> plasma; 1.6 Pa, 150 W.

	Quartz (Q)			Tantalum (Ta)		
	294 K	400 K	600 K	294 K	400 K	600 K
Molecule density (m <sup>-3</sup> )	3.9×10 <sup>20</sup>	2.9×10 <sup>20</sup>	1.9×10 <sup>20</sup>	3.9×10 <sup>20</sup>	2.9×10 <sup>20</sup>	1.9×10 <sup>20</sup>
Atom density (m <sup>-3</sup> )		4.2×10 <sup>19</sup>			1.6×10 <sup>19</sup>	
Uncertainty (m <sup>-3</sup> )		0.4×10 <sup>19</sup>			1.2×10 <sup>19</sup>	
Degree of dissociation (%)	5.1	6.8	9.5	2	2.7	4

For the experimental conditions considered in this chapter (D<sub>2</sub> plasma; 1.6 Pa, 150 W) and in taking into account the estimation of the gas temperature at 400 K in those (section 4.4.1), the degree of dissociation is found to be about 2.5 times higher in the case of quartz than in the case of tantalum. This also correlates well, qualitatively, with the results of **Table 4.10** when conducting a comparison of the values of  $\sum v^n$  between the quartz and the tantalum cases in Configuration A (**Fig. 4.11**), in which the probed region of the plasma is that of its creation (in the vicinity of the magnet of the dipolar ECR module). A higher degree of dissociation leads to a more pronounced decrease in the molecule density, therefore it appears logical to see a lower value of  $\sum v^n$  when quartz faces the plasma as opposed to tantalum. On the contrary, this is not observed in Configuration B (**Fig. 4.11**), which could be an indication that this effect is compensated by the synergy of other processes.

## 4.5 Discussion

By now it has been evidenced that gaining information on the EEDF is crucial for evaluating the dissociative electron attachment (DEA) reaction (R1 and R2; **Table 1.3**) in the volume production of negative H<sup>-</sup> and D<sup>-</sup> ions. However, it is important to keep in mind that knowledge on the VDF may reveal equally valuable insight onto the molecular constituents of the same reaction. Hence the focus, in this chapter, on the determination of the VDFs, and the presentation in the previous section of four such curves (**Fig. 4.13**) in characteristic plasma conditions. In this section, several key conclusions that can be drawn from the shape of these curves and through their comparison between each other are presented.

But before that, it is deemed necessary to provide an explanation regarding the choice of the two particular spatial configurations of the “SCHEME-II+” reactor that were chosen (**Fig. 4.11**). Given that the line-of-sight for the synchrotron radiation is constant, the displacement of the dipolar ECR module to two different positions results in ultimately probing two different regions in the produced plasma. One is the production region (25 mm above the axis of the magnet of the dipolar ECR module; Configuration A), and the other is the diffusion region (75 mm downstream of the mid-plane of the magnet of the dipolar ECR module; Configuration B) where negative ion production predominantly takes place, as it has been highlighted in the previous chapters. It is worth noting that, particularly Configuration B is similar to that of the “Prometheus I” reactor in

the experiments that have been presented in Chapter 3, where the probing area was 65 mm below the mid-plane of the magnet of the dipolar ECR module.

The variety of reactions balancing the population and de-excitation of the vibrational levels have been laid out in **Table 1.4**. All of these contribute to the final shape of the VDF which exhibits a markedly non-Boltzmann character with a plateau and an overpopulated tail [75]. With a first glance it is worth noting the similar shape of the VDFs of **Fig. 4.13** with the distribution of the cross section of the E-V process among the vibrational levels on **Fig. 1.7(c)**, indicating the crucial role of this reaction. Nevertheless, the results also unveil an influence of the recombinative processes on the VDF which will be evaluated.

With regard to **Fig. 4.13**, firstly, it can be seen that for the lower vibrational levels ( $v'' = 0-3$ ) the population density is the nearly the same regardless the material, or the probing position. This pattern suggests that the mechanism governing the population of these vibrational levels is common to all of the cases, and is most likely one that takes place in the plasma volume, i.e. the e-V and E-V processes. On the contrary, when the higher vibrational levels are considered ( $v'' > 3$ ) there is a noticeable increase of the population density in the case where Ta is used, independently of the configuration. This hints towards a positive contribution of the surface processes that could occur, thus leading to an enhancement of the creation of vibrationally excited molecules with respect to the Q case. In fact, an example reported in [93] that correlates well with this hypothesis, states that the average vibrational level of the H<sub>2</sub> molecule formed by recombination of atomic recombination on graphite ranges from  $v'' = 4$  to  $v'' = 6$ , depending on the surface temperature and the kinetic energies of the impinging atoms. Indicatively, from **Fig. 4.13**, for  $v'' = 6$  for example and Configuration B, the introduction of Ta in the reactor interior leads to the enhancement of the population in that level by a factor of around 3.4. If, additionally, one takes into account the significance of these intermediate and higher vibrational levels for the DEA reaction (the cross section increases dramatically with increasing vibrational level, cf. **Fig. 1.6**), this selective enhanced production of molecules in high-lying vibrational states should accordingly lead to a boost in the negative ion yield.

Furthermore, it is observed that in the case of where Q is the material exposed to the plasma, the population density in the tail of the VDF is lower in Configuration B than in Configuration A. This is expected since the probed area in Configuration B is downstream of the plasma production zone, where these molecules are predominantly created through volume mechanisms, whilst nearly no effect of surface processes is to be anticipated. On the other hand, in the case where Ta is investigated, the VDFs in both configurations almost coincide. A possible explanation can be derived if the surface-produced molecules have a long lifetime. If conversely a short lifetime were to be assumed, it would mean that these molecules would be destroyed via competing mechanisms shortly after their creation, and thus their detection further away from the surfaces

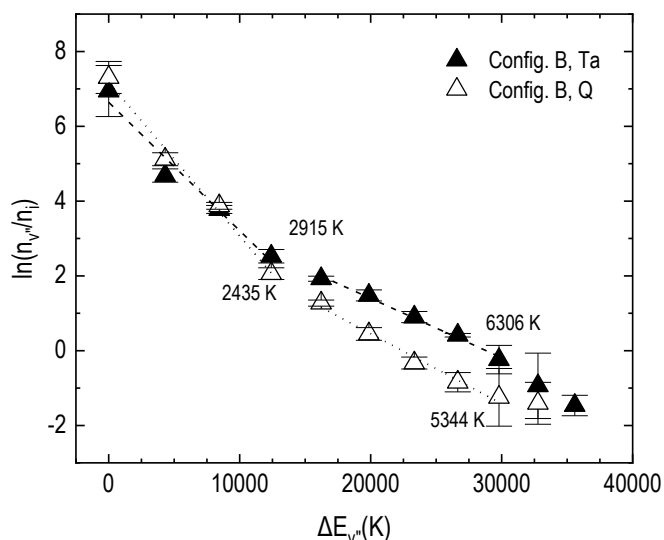


**Figure 4.15.** Boltzmann plot for the derivation of the vibrational temperature. For each configuration two quasi-linear regions are distinguished, and a fit is performed for each one. The resulting average temperatures are given next to the adjusted lines.

would not be feasible. But, since indeed close the VDFs for Ta between the two configurations are practically the same, it is safe to say that the produced molecules in fact have lifetimes comparable to those created through volume processes. Typical lifetimes of molecules excited in different vibrational levels have been reported by [130], ranging from around 400  $\mu\text{s}$  to 100  $\mu\text{s}$ , respectively, for  $v''$  from 0 up to 10.

Finally, another interesting parameter that can be deduced from these measurements is the vibrational temperature. This temperature can influence the rates of various vibrational-vibrational or vibrational-translational energy exchange processes [178], and at the same time may be a valuable input used in numerical models aiming to the exploration of the vibrational kinetics [179]. In **Fig. 4.15** the VDFs for two of the abovementioned studied configurations are re-drawn so that the abscissa is refers to the logarithm of the relative population density whereas the ordinate is expressed in terms of the energy difference,  $\Delta E$ , between the vibrational energy of each level with respect to that of the first vibrational level,  $v''=0$  [155]. This representation is equivalent to a Boltzmann plot. In that, two quasi-linear regions are identified, one comprising the first four vibrational levels ( $v''=0-3$ ) and the other including the next five ( $v''=4-8$ ). From each of these regions a different vibrational temperature can be determined, and according to theory, the reciprocal of the negative slope of these regions gives this value directly. The lines that are adjusted via a linear fit through the respective data points, in each of the two regions for both configurations are shown in the same figure. Alongside those, the resulting temperature is marked. The same procedure is repeated for all of the studied configurations and **Table 4.13** collects the vibrational temperatures for the two different regions. In Configuration A, regardless of the material the vibrational temperature is found to not differ significantly.

**Table 4.13.** Average vibrational temperatures derived from the head and tail of the VDFs in the four experimental conditions described in the text. The standard error given in the values for the temperature correspond to the fitting procedure rather than the uncertainty in the data itself.

<b>Experimental conditions</b>	$T_{\text{vib. (v}^{\text{''}} = 0\text{-}3)} \text{ (K)}$	$T_{\text{vib. (v}^{\text{''}} = 4\text{-}8)} \text{ (K)}$
Config. A, Ta	$2725 \pm 411$	$6492 \pm 431$
Config. A, Q	$2899 \pm 213$	$6768 \pm 454$
Config. B, Ta	$2915 \pm 468$	$6306 \pm 326$
Config. B, Q	$2435 \pm 173$	$5344 \pm 400$

On the other hand, a difference of about 1000 K is noted between the vibrational temperatures of the higher levels when comparing Ta and Q in Configuration B. Calculations in [179] of VDFs as a function of the recombination coefficient,  $\gamma$ , show that for increasing values of the latter the distribution warms up. For the materials under scrutiny, based on literature, it would be expected that Q has a recombination coefficient of around 0.003 at 300 K [101], while the value for Ta, under the assumption that it is similar to the one for W, it would be around 0.06 at 353 K [100]. Thus, indeed, the present experimental results correlate well with the aforementioned statement.

## CHAPTER 5

# INTERROGATION OF PLASMAS SUSTAINED IN THE PULSED MODE OF OPERATION

---

In this chapter an alternative, with respect to that followed in the previous two chapters, operation regime is studied, that of pulsed plasma operation, in order to explore the potentiality of enhancing the negative ion yield. The feasibility of deducing time-resolved measurements of the basic plasma parameters is demonstrated and these are consequently discussed. In particular, these preliminary experimental investigations refer to a D<sub>2</sub> plasma produced under typical operational conditions at the “SCHEME-II+” reactor.

## 5.1 Time-resolved D<sub>2</sub> plasma parameters

D<sub>2</sub> plasmas sustained in the pulsed mode of operation were subject to scrutiny in the “SCHEME-II+” reactor by means of Langmuir probe and single-beam laser-induced photodetachment measurements. The details on the installation of these two diagnostic techniques, and the necessary actions for the synchronization between the different instruments for their application have already been given in sections 2.2.3 and 2.2.4. The treatment of the current-voltage characteristics follows the same procedure that was outlined in section 3.1, while that of the signals obtained by the photodetachment technique is the standard one also described in section 2.1.2. Here, the time-resolved plasma parameters are presented in typical operating conditions.

Measurements have been conducted in D<sub>2</sub> plasmas in the characteristic configuration for the “SCHEME-II+” reactor that has been shown in **Fig. 2.18**, i.e. the probing region in the plasma is 75 mm downstream of the mid-plane of the magnet of the dipolar ECR module. Moreover, these experiments are effected for specific operating conditions, namely for a working gas pressure of 1.6 Pa and for injected microwave power of 150 W. It is recalled that the mentioned operating conditions are the ones that have been chosen throughout the experimentation in this reactor. The frequency of the plasma pulses is 2 kHz, with a duty cycle of 30%. It is noted that, the choice of these values were not made as a part of an extensive parametric study but arbitrarily. Lastly, while all of the aforementioned parameters remain constant, the surface which faces the plasma differs between quartz and tungsten (W). The tungsten comes in the form of a metallic foil, 0.1 mm thick, as in the case of tantalum which was used in the experiments described in the previous chapter. Tungsten, which has a similar positive effect in yielding ro-vibrationally excited molecules, was preferred instead of tantalum for these measurements particularly because of its higher resistance to becoming brittle when exposed to H<sub>2</sub>/D<sub>2</sub> plasmas.

**Fig. 5.1** shows the evolution, within a plasma pulse, of the floating and the plasma potentials. **Fig. 5.1(a)** corresponds to the case where a full Q surface faces the plasma, whereas **Fig. 5.1(b)** shows the same for a full W surface facing the plasma. In both cases, the two potentials quickly reach a constant value, within 50 μs after the beginning of the pulse, and diminish in about the same amount of time when the microwave power is no longer transmitted. However, it is observed that both potentials are higher when the plasma is enclosed in the Q surface. The average floating and plasma potential is around 11 V and 12 V, respectively, while for a W enclosure these are around 3 V and 6.5 V, accordingly. The higher values obtained for Q may be attributed to its dielectric nature. In practice, there remain some very few metallic surfaces exposed to the plasma (the magnet of the dipolar ECR module, the stainless steel supports of the two capillaries, and part of the inner copper cylinder of the reactor) to which electrons find a way to escape to. In the meantime, some equilibrium should be established for the sheath created at the boundaries with

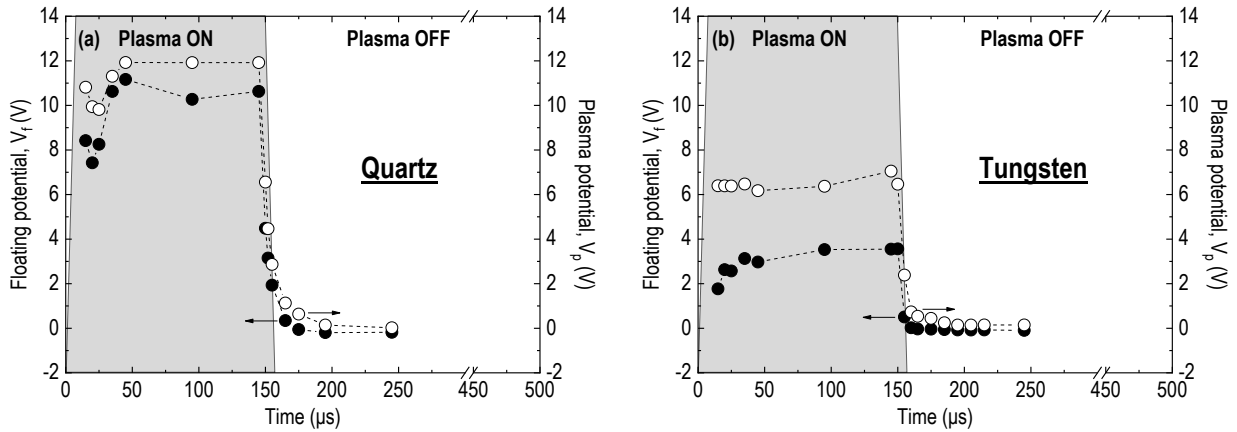


**Figure 5.1.** Time-resolved measurements of the floating and plasma potentials, with (a) a full quartz surface and (b) a full tungsten surface facing the plasma.  $D_2$  plasma probed 75 mm downstream of the midplane of the magnet of the dipolar ECR module on the reactor axis; 1.6 Pa, 150 W (2 kHz, 30% duty cycle).

either surface (quartz or metallic). Thus, the plasma potential increases naturally in order to enhance the ion mobility towards the small portion of metallic surfaces.

In the same manner **Fig. 5.2(a)** and **(b)** display the temperature and density of the cold electron population, for quartz and tungsten, respectively. The electron temperature appears to rise from the beginning of the pulse (more evident in the quartz condition) and finally attains a value of 0.85 eV and 1.3 eV towards the end of the pulse, in quartz and tungsten respectively. At the end of the pulse, the electron temperature decays rapidly. Indicatively, if an exponential function is used to describe this decaying behavior the following time constants may be derived in quartz and tungsten;  $15.37 \pm 9.11 \mu$ s and  $5.83 \pm 0.36 \mu$ s, respectively. Thus, a more rapid decay is observed when the entire interior surface of the “SCHEME-II+” reactor is covered by the tungsten foil. With regard to the cold electron density, a similar trend to that of the temperature

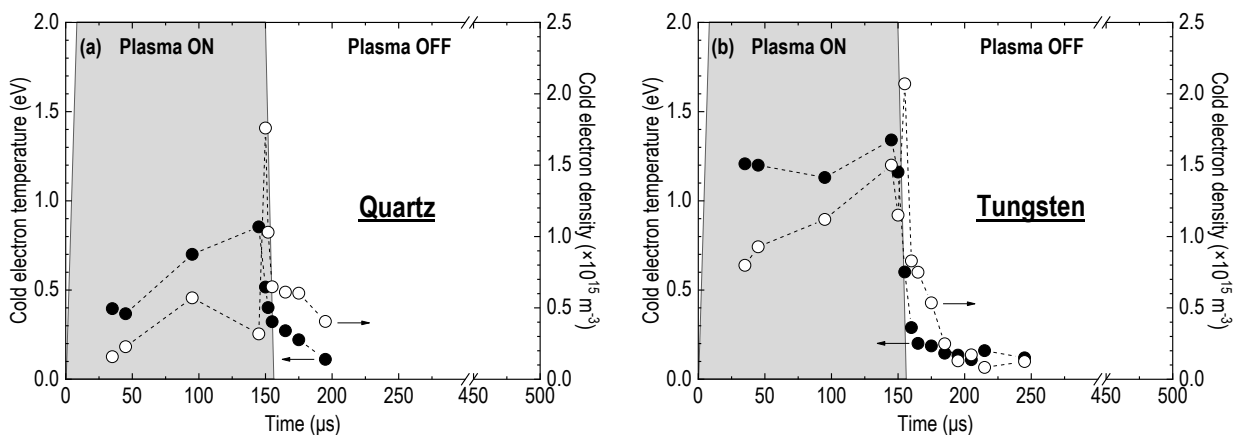


**Figure 5.2.** Time-resolved measurements of the cold electron temperature and cold electron density, with (a) a full quartz surface and (b) a full tungsten surface facing the plasma.  $D_2$  plasma probed 75 mm downstream of the midplane of the magnet of the dipolar ECR module on the reactor axis; 1.6 Pa, 150 W (2 kHz, 30% duty cycle).

is seen, with the only remarkable difference being the presence of a spike in the density at the very end of the plasma pulse. Following the end of the pulse, the density decays, however it remains important (nearly  $0.5 \times 10^{15} \text{ m}^{-3}$ ) even at  $175 \text{ }\mu\text{s}$ , i.e.  $20 \text{ }\mu\text{s}$  after the complete extinction of the plasma pulse at  $155 \text{ }\mu\text{s}$ . This value for the electron density is close to that obtained inside the plasma pulse for quartz, and nearly half of that when tungsten is used (compare the times  $100 \text{ }\mu\text{s}$  and  $175 \text{ }\mu\text{s}$  in the subplots of **Fig. 5.2**). These remarks will be proven interesting in the study of the evolution of the negative ion density in the corresponding conditions that is described in the next section.

## 5.2 Time-resolved measurements of the negative ion density

In this section and for the same conditions examined in the previous section, measurements of the negative ion density in different time points in the plasma pulse are given. Due to the fact that these measurements were carried out on different days than those presented before, potential discrepancies between the exact values of the plasma parameters may be observed. Factors such as the venting of the reactor between the measurements, and alternation of the working gases may affect the results. With this in mind and to ensure thus credibility, the results shown below correspond to measurements that have been effected on the same day.

### 5.2.1 The case of a full quartz surface facing the plasma

**Fig. 5.3** displays the current-voltage characteristic (Langmuir probe) curves ((**a1**)-(f1)) and current impulses obtained through the photodetachment technique ((**a2**)-(f2)) for six time points inside a plasma pulse (2 kHz, 30%). At the top of each subfigure the probed time point within the plasma pulse is marked, counting from  $t_0 + 5 \text{ }\mu\text{s}$  (see **Fig. 2.20**). That is,  $5 \text{ }\mu\text{s}$  after the command signal triggers the microwave output, compensating thus for the delay between those two.

Especially for the signals showing the current impulse induce by the photodetached electrons during the application of the technique, the figures display the raw signal recorded by the wideband current transformer (details in section 2.2.4) after the subtraction of a baseline. Superposed on the same plots are the smoothed signals. An FFT (Fast Fourier Transform) filter employing a 125-point window, resulting in a cutoff-frequency of 10 MHz. This way the noise seen on the raw signal is suppressed, all the while ensuring minimal distortion of the signal since the window is equal to only 2.5% of the total amount of data points of the signals.

A notable increase of the photodetached electron current appears in the post-discharge time of the plasma pulse. Specifically, these measurements show that the maximum amplitude of this current is obtained at  $165 \text{ }\mu\text{s}$ , i.e.  $10 \text{ }\mu\text{s}$  after the total extinction of the microwave power (it is reminded that the “Microwave output” has a falling time of  $5 \text{ }\mu\text{s}$ ). At this time, the amplitude is nearly 5 times larger than that observed inside the plasma pulse ( $11.15 \text{ }\mu\text{A}$  at  $165 \text{ }\mu\text{s}$  versus

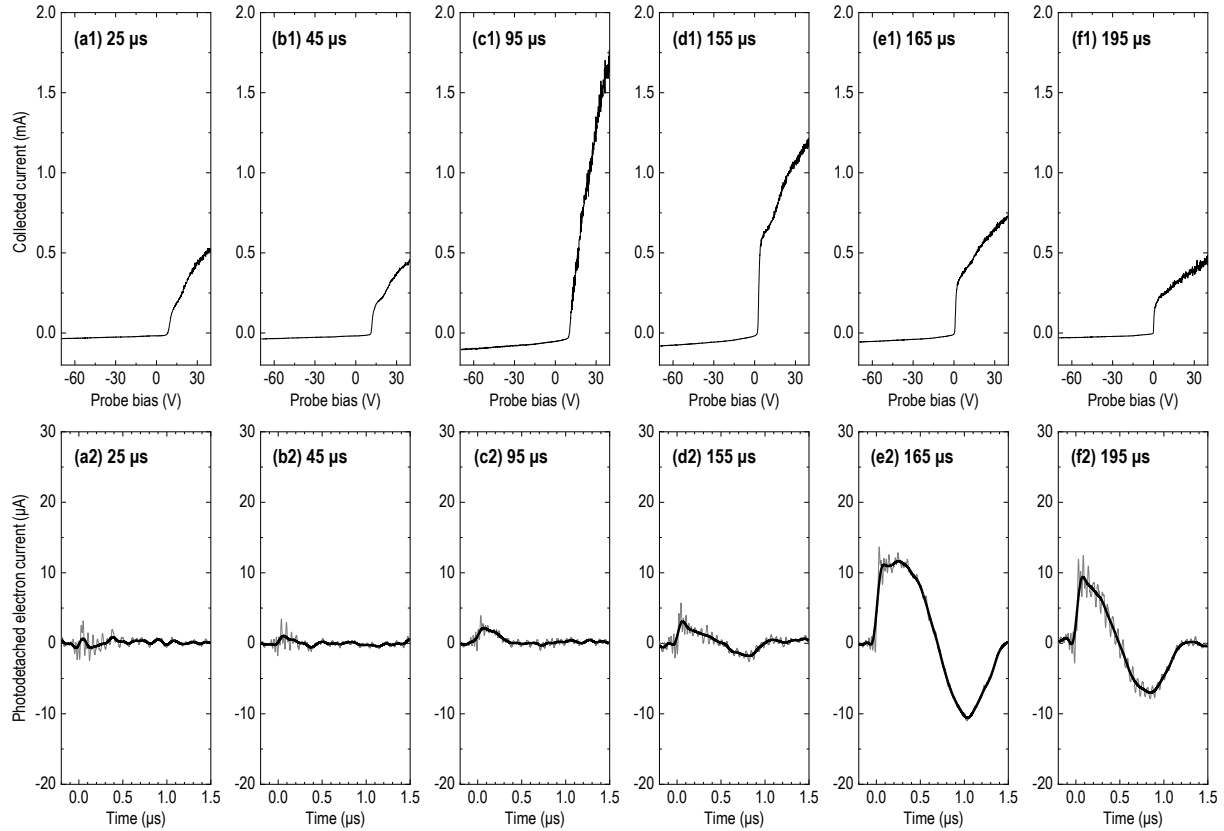


**Figure 5.3.** (a1)-(f1) I-V characteristics in specific time points within a 2 kHz (30% duty cycle) plasma pulse, and (a2)-(f2) the corresponding signals induced by photodetachment. Each subfigure of the bottom line displays both the raw signal from which only a baseline has been removed (grey solid line), and the smoothed signal (black solid line). D<sub>2</sub> plasma probed 75 mm downstream of the midplane of the magnet of the dipolar ECR module on the reactor axis; 1.6 Pa, 150 W (2 kHz, 30% duty cycle).

2.17  $\mu\text{A}$  at 95  $\mu\text{s}$ ). Noteworthy is the fact that even at more extended times (e.g. at 195  $\mu\text{s}$ ) the signal remains considerable. At the same time, the gradual increase of the collected current in the recorded I-V characteristics is distinguished at times in the pulse, and contrarily it decrease after the end of it.

For comparisons sake, **Fig. 5.4** depicts a I-V characteristic and the corresponding photodetachment signal obtained in an identical plasma, when it is sustained in the continuous mode of operation. This curve normally should be similar to the ones obtained during (and mostly towards the end of) the pulse. In the case presented here, this is not true as they differ in a way that the one in the continuous mode appears shifted towards higher bias potentials while the maximum collected current is lower. Empirically, this phenomenon has been observed in particular in the case where quartz is the material facing the plasma, and after several hours of plasma operation. Nevertheless, this mostly affects the value of the floating and plasma potentials, whereas the rest of the plasma parameters that are extracted will be seen to differ only slightly (**Fig. 5.5**). As for the, photodetachment signal, despite the presence of a small peak after the applied smoothing to suppress the noise in the signal, this is considered as a zero-signal because it does

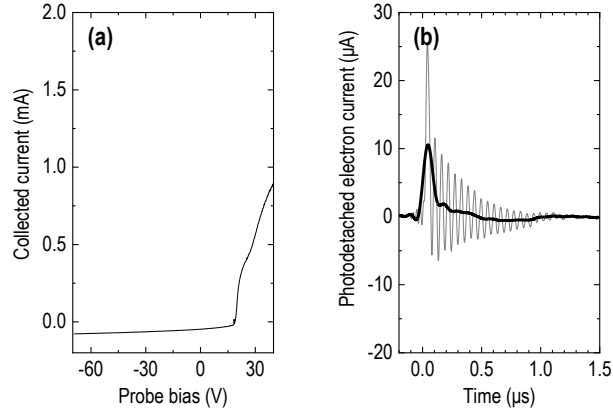


**Figure 5.4.** I-V characteristic (a) and photodetachment signal (b) for a plasma sustained in the continuous mode of operation. In (b), the bold black line corresponds to the smoothed signal which is superposed on the raw one from which a baseline is subtracted. D<sub>2</sub> plasma probed 75 mm downstream of the midplane of the magnet of the dipolar ECR module on the reactor axis; 1.6 Pa, 150 W enclosed by a full quartz surface. not resemble a typical photodetachment signal in any way. Thus, the negative ion density is deemed to be undetectable, represented by a data point set to zero (**Fig. 5.5**). Note that the same goes for the first two data points for 25  $\mu$ s and 45  $\mu$ s.

From the collection of these signals the basic plasma parameters are extracted, and the most important ones are displayed in **Fig. 5.5**. The cold electron density is of the order of  $10^{14} \text{ m}^{-3}$  and, as it was shown also in the previous section, displays an increasing tendency during the pulse but diminishes in the post-discharge. The cold electron temperature remains lower than 1 eV throughout, but as expected it decreases slowly even further in the post-discharge time. On the contrary, the negative ion yield reaches a maximum shortly after the end of the plasma pulse and then also starts to ware off. Simultaneously, since there is an increase in the negative ion

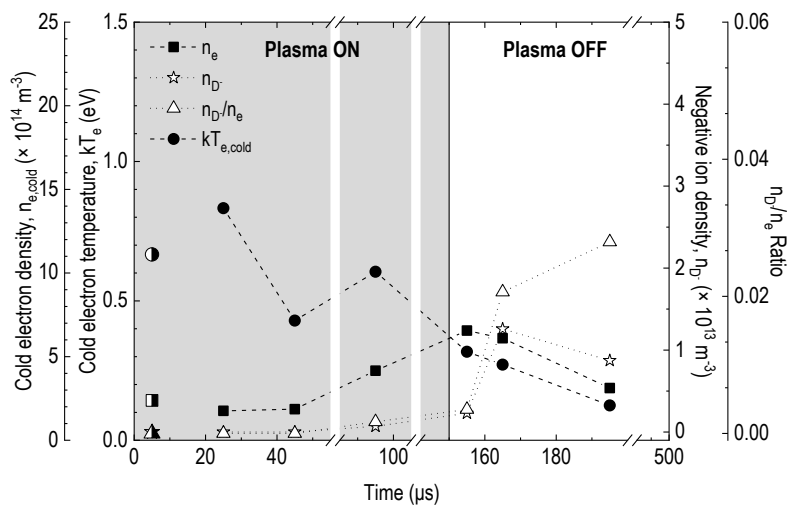


**Figure 5.5.** Cold electron density and temperature, and negative ion density and relative negative ion density for the case where the plasma faces a full quartz surface. The data points that correspond to the plasma parameters for a plasma sustained in the continuous mode of operation are represented by half-colored symbols (same shapes) and are set arbitrarily at the 5  $\mu$ s point for clarity.

production but a diminution of the electron density, the relative ratio of negative ions ( $n_{D^-}/n_e$ ) increases noticeably. However, still the negative ion yield is by an order of magnitude lower than the cold electron density, and the ratio is accordingly small (below 10%). Nonetheless, it is worth noting that a maximum absolute negative ion density of  $1.25 \times 10^{13} \text{ m}^{-3}$  is achieved at  $165 \mu\text{s}$ , which is about 17.8 times higher than the value obtained at  $95 \mu\text{s}$  ( $0.07 \times 10^{13} \text{ m}^{-3}$ ). Finally, on the same figure, the individual half-full symbols denote the respective values of the parameters in the continuous mode of operation.

### 5.2.2 The case of a full tungsten surface facing the plasma

Measurements identical to the ones featuring in the previous subsection have been also performed for the case where tungsten foils are set appropriately on the quartz surface, thus mimicking an entirely metallic surrounding. **Fig. 5.6** shows the corresponding to **Fig. 5.3** bundle of I-V characteristics and photodetachment signals for this second case. As in the case of quartz, there is a prominent increase of the recorded photodetached electron current in the post-discharge time, with respect to that occurring during the plasma pulse. In particular, an increase of a factor of 3 is apparent ( $31.01 \mu\text{A}$  at  $155 \mu\text{s}$  versus  $10.03 \mu\text{A}$  at  $95 \mu\text{s}$ ).

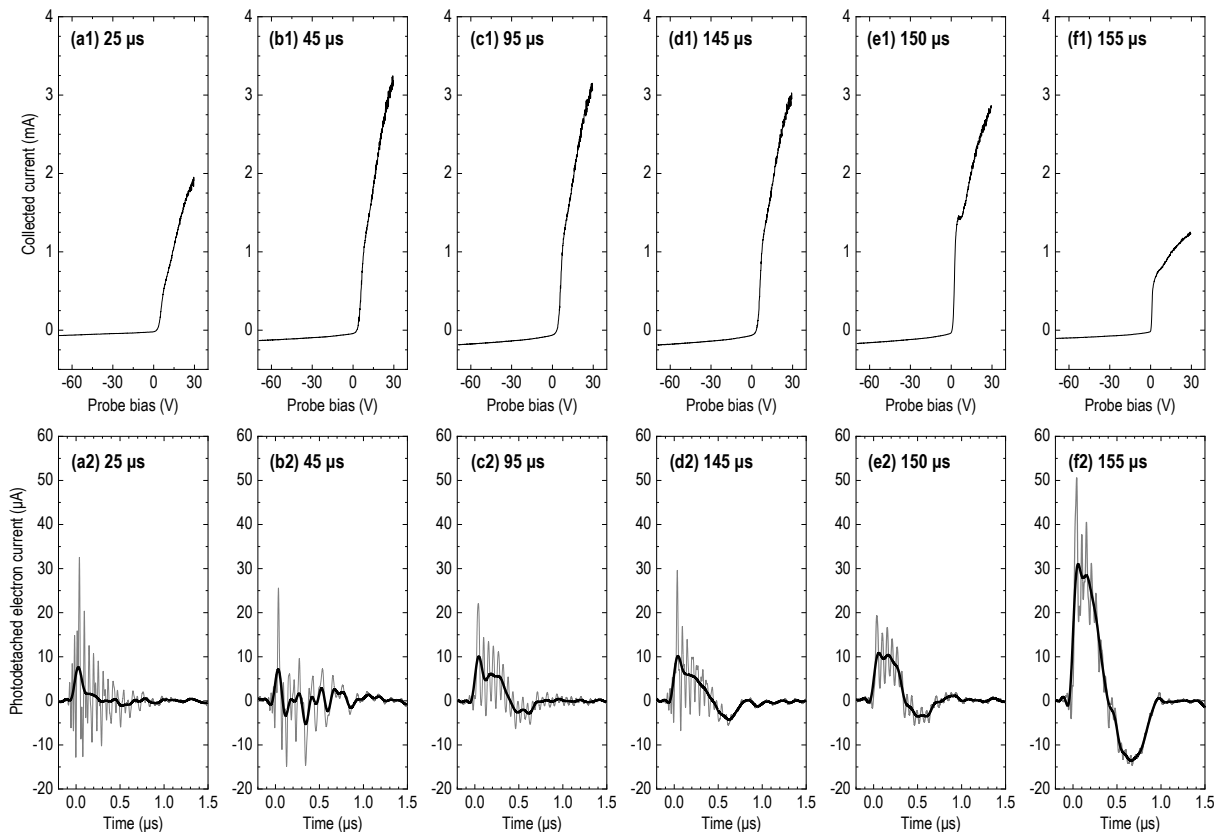


**Figure 5.6.** (a1)-(f1) I-V characteristics in specific time points within a 2 kHz (30% duty cycle) plasma pulse, and (a2)-(f2) the corresponding signals induced by photodetachment. Each subfigure displays both the raw signal from which only a baseline has been removed (grey solid line), and the smoothed signal (black solid line).

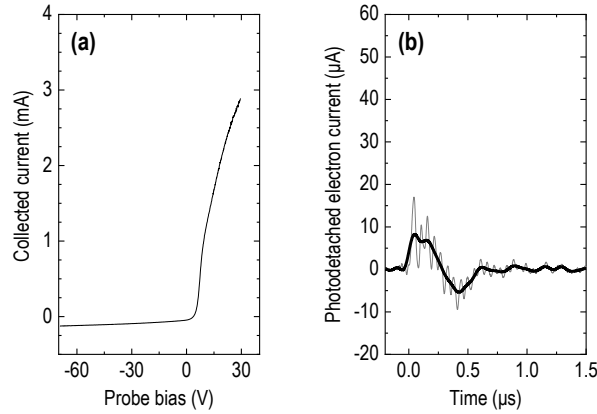


**Figure 5.7.** I-V characteristic (a) and photodetachment signal (b) for a plasma sustained in the continuous mode of operation. In (b), the bold black line corresponds to the smoothed signal which is superposed on the raw one from which a baseline is subtracted. D<sub>2</sub> plasma; 1.6 Pa, 150 W enclosed by a full tungsten surface.

Subsequently, with **Fig. 5.7**, a direct comparison can be carried out with corresponding measurements made when the plasma is sustained in the continuous mode of operation. In this case, both the I-V characteristic and the photodetachment signal is found to be in agreement with those obtained inside the plasma pulse. One should compare the signals with those obtained at a time equal to 95 μs. In fact, at least for the amplitude of the photodetachment signal, 8.23 μA in the continuous mode are compared with 10.03 μA at 95 μs.

Moreover, with the treatment of all the presented signals in **Fig. 5.6**, **Fig. 5.8** is derived, displaying the evolution of the cold electron density and temperature, and the negative ion density and relative negative ion density during a plasma pulse. On the same figure, the half-full symbols set arbitrarily for clarity at the 5 μs point correspond to the continuous mode of operation. The trends and the absolute values, overall, of the cold electron density and temperature are in good

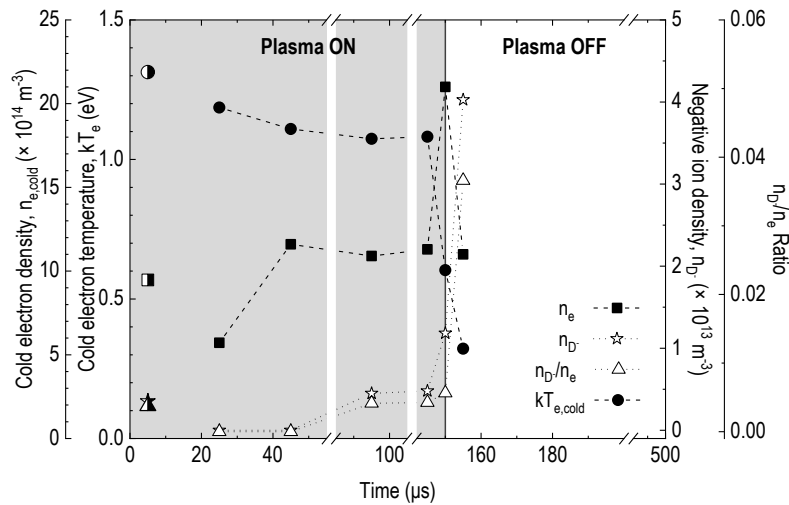


**Figure 5.8.** Cold electron density and temperature, and negative ion density and relative negative ion density for the case where the plasma faces a full tungsten surface. The data points that correspond to the plasma parameters for a plasma sustained in the continuous mode of operation are represented by half-colored symbols (same shapes) and are set arbitrarily at the 5 μs point for clarity.

agreement with those already presented in **Fig. 5.2**. The absolute negative ion density is found to be at  $4.03 \times 10^{13} \text{ m}^{-3}$  at  $155 \text{ }\mu\text{s}$ , higher by almost a factor of 8 than that measured at  $95 \text{ }\mu\text{s}$  ( $0.45 \times 10^{13} \text{ m}^{-3}$ ). This is also mirrored upon the negative ion to cold electron density ratio. This factor reaches nearly 11 when the comparison is made with the absolute negative ion density in the continuous mode of operation, i.e.  $0.35 \times 10^{13} \text{ m}^{-3}$ . Note that the negative ion density and negative ion to cold electron density ratio is set to zero in the cases for which the amplitude of the photodetachment signal cannot be defined.

### 5.3 Discussion

In the introductory chapter it was mentioned that by sustaining plasmas in the pulsed mode of operation a higher negative ion yield can be achieved. The results presented in this chapter demonstrate this potential, as a strong enhancement of the negative ion density at the end of the plasma pulse was evidenced.

It is reasonable to also conduct a comparison between the two investigated materials, quartz and tungsten, with respect to their efficiency of negative ion production. First of all, in the continuous mode of operation, the negative ion density in quartz was undetectable, contrary to the case of tungsten where it was found to be  $0.35 \times 10^{13} \text{ m}^{-3}$ . Secondly, with respect to the pulsed mode measurements, quartz yielded a maximum negative ion density of  $1.25 \times 10^{13} \text{ m}^{-3}$ , whereas tungsten  $4.03 \times 10^{13} \text{ m}^{-3}$ . In other words, the introduction of tungsten leads to a 3 times higher negative ion yield. Both maxima were found in the post-discharge period, at  $165 \text{ }\mu\text{s}$  and  $155 \text{ }\mu\text{s}$  for quartz and tungsten respectively.

A rather simplistic explanation of this phenomenon will be attempted herein as certainly more extensive measurements and modeling would be needed in order to arrive at a concrete conclusion. In returning to the statement that the dominant reaction for negative ion production is the DEA of low energy electron to highly ro-vibrationally excited molecules, the abovementioned higher negative ion density in the case where tungsten is used can be partially explained by the higher cold electron density measured. On average, the cold electron density indeed results in being about 3.4 times higher when tungsten is employed. At the same time, the positive influence of the metallic surface in creating ro-vibrationally excited molecules should be acknowledged since they are key components in the DEA reaction. This was justified through the measurements presented in Chapter 4. Despite the fact that the material studied in those measurements was tantalum, a similar effect should be expected for tungsten as well (this fact has been reported in [68]). On the other hand, the particular enhancement of the negative ion density in the post-discharge can be potentially traced back to three main contributing factors that could promote their creation: i) the lowering of the cold electron temperature which can coincide with the range of temperatures for which the cross section of the DEA reaction peaks. In fact, the electron temperature of below

1 eV obtained is ideal for DEA via the high-lying vibrationally excited molecules (**Fig. 1.6**). ii) the non-immediate decay of the cold electron population, and iii) the long lifetime of the ro-vibrationally excited molecules of several hundreds of microseconds that has been reported in [130]. At the same time, it is important to evaluate the destruction processes in the post discharge time. Given the substantial increase of the negative ion yield in the post-discharge, one can assume that the rates of reactions leading to their destruction through different direct or indirect processes (see Chapter 1), but the present results alone do not suffice to evaluate them. Nonetheless, collectively, it seems that the synergy all of the above factors is responsible for the observation of a large negative ion yield in the post-discharge time.

Overall, it should be mentioned that while this series of measurements provides initial insight into negative ion creation in D<sub>2</sub> plasmas driven by a dipolar ECR module sustained in the pulsed mode, this primary approach remains rather superficial. Additional parametric studies as a function for example of the frequency and the duty cycle of the imposed microwave pulses, and measurements of the properties of the molecular species (e.g. time-resolved measurements of the vibrational distribution function) in this mode of operation would be crucial. However, modeling efforts (0-D and species diffusion) would be essential in order to shed light onto the dynamics that take place so as to ultimately develop a solid understanding of the underlying physics.

# CHAPTER 6

## CONCLUSIONS

---

This thesis reports on experimental investigations of H<sub>2</sub> and D<sub>2</sub> plasmas driven by elementary ECR dipolar modules, aiming towards quantitative evaluation of the mechanisms that govern negative ion production in volume ion sources and to the optimization of the negative ion yield. This chapter summarizes the most important results.

In a reactor employing a two-dimensional network of five elementary ECR modules, having a volume of  $1.38 \times 10^4 \text{ cm}^3$  and a surface-to-volume ratio of 0.16, the comparative study of  $\text{H}_2$  and  $\text{D}_2$  plasmas within the pressure range of 0.26 - 2.6 Pa (corresponding gas flow rate ranges of 3.9 – 23.4 sccm for  $\text{H}_2$  and 4.8 – 29.2 sccm for  $\text{D}_2$ ) and for a delivered microwave power of up to 0.9 kW, resulted in the following main findings:

- Two quasi-Maxwellian electron populations are produced independently of the gas, the pressure and the microwave power. The populations are characterized as *cold* and *hot* on account of their different temperatures, i.e. one lies below 2 eV while the other attains values around 15 eV.
- For the extreme operating conditions (2.6 Pa and 0.9 kW), the density of the cold electron population achieves a value close to  $4.5 \times 10^{16} \text{ m}^{-3}$  and  $7 \times 10^{16} \text{ m}^{-3}$  for  $\text{H}_2$  and  $\text{D}_2$ , respectively. At the same time, the density of the hot electron population reaches nearly  $5.5 \times 10^{14} \text{ m}^{-3}$  for both  $\text{H}_2$  and  $\text{D}_2$ .
- The cold electron population is found consistently higher in the  $\text{D}_2$  plasma, and this is attributed to the higher confinement time of positive ions in the case of deuterium. The theoretical factor of  $\sqrt{2}$  is approached but not precisely met.
- The negative ion density at the extreme operating conditions reaches  $0.57 \times 10^{16} \text{ m}^{-3}$  and  $0.54 \times 10^{16} \text{ m}^{-3}$  for  $\text{H}_2$  and  $\text{D}_2$ , respectively.
- In general,  $\text{H}^-$  and  $\text{D}^-$  negative ion densities are not substantially different in the two plasmas under the same operating conditions, however the  $\text{H}^-$  density is higher at a given plasma density.
- The existence of two negative ion populations is proven in a study conducted for a pressure of 1.3 Pa and characteristic values for the microwave power. A *cold* population with energies below 0.05 eV dominates (65-70%) and is linked with the production of the negative ions through the dissociative electron attachment (DEA) reaction in the main volume of the plasma. The presence of a *hot*-er population attaining energies from just below 1 eV to 2.5 eV is explained by still considering DEA as the pathway for negative ion formation, in which however the participating molecules have resulted from recombinative desorption reactions occurring on the walls of the reactor.
- A strong isotope effect exists on the negative ion to electron density ratio, which may be up to 80% higher in a  $\text{H}_2$  plasma.
- Based on the negative ion to electron density ratio across the operational range, optimum operating windows are distinguished. For the pressure values of 0.53, 1.07 and 1.6 Pa and as the microwave power is varied, the optima are found at 1.07 Pa/0.4 kW (ratio of about 0.225) for  $\text{H}_2$ , and at 1.07 Pa/0.3 kW (ratio of about 0.125) for  $\text{D}_2$ . However, when the pressure is varied for the maximum power of 0.9 kW the optimum is observed at 1.3 Pa (the ratio is about 0.17 and 0.11 for  $\text{H}_2$  and  $\text{D}_2$ , respectively).

In a second reactor employing one ECR dipolar module having a volume of  $0.26 \times 10^4 \text{ cm}^3$  but a higher surface to volume ratio (0.32) compared to the former one, the experimental efforts were

centered on the detection of the molecular precursors of the negative ions taking part in the DEA reaction, i.e. the ro-vibrationally excited molecules in the molecular ground state ( $X^1\Sigma_g^+$ ). This was made possible with the application of VUV Fourier Transform absorption spectroscopy using synchrotron radiation. At the same time, the influence of either quartz or tantalum exposed to the plasma on their production was assessed. The following statements summarize the most important points in this study conducted for a  $D_2$  plasma at 1.6 Pa and 150 W:

- The introduction of tantalum into the reactor induces a notable increase (of about a factor of 3.4) of the molecule population in the high-lying vibrational levels ( $v'' = 4-8$ ) with respect to quartz, in the diffusion region (downstream of the ECR module).
- The population of the lower vibrational levels ( $v'' = 0-3$ ) is found to be similar regardless of the region of the plasma that is probed or if quartz or tantalum is considered.
- Absolute values of the molecule population in the lowest vibrational level of the ground state ( $v'' = 0$ ) and are found equal to  $3.0 \times 10^{20} \text{ m}^{-3}$  and  $2.1 \times 10^{20} \text{ m}^{-3}$  for quartz and tantalum, respectively, in the diffusion region.
- A precise determination of the absorption length is necessary in order to derive the absolute densities in the upper vibrational levels ( $v'' > 0$ ).
- The atomic density in the ground level ( $n=1$ ) is derived from the atomic Lyman transitions. For the cases of tantalum and quartz the atomic density is found to be equal to  $1.6 \times 10^{19} \text{ m}^{-3}$  and  $4.19 \times 10^{19} \text{ m}^{-3}$ , respectively.
- The gas temperature is experimentally derived complementarily through tunable diode laser absorption spectroscopy and found to be around 400 K in these operating conditions.
- The dissociation of the gas attains a value of 6.8% in the case of quartz as opposed to just 2.7% in the case of tantalum.

Finally, in the second reactor, a  $D_2$  plasma at a pressure of 1.6 Pa and a microwave power of 150 W was sustained in the pulsed mode of operation. Time-resolved measurements of the basic plasma parameters in pulses of a duration of 150  $\mu\text{s}$  (2 kHz repetition rate) reveal:

- A significant increase of the negative ion density is noted in the post-discharge period. In particular, there is an increase from  $0.45 \times 10^{13} \text{ m}^{-3}$  (at 95  $\mu\text{s}$ ) to  $4.03 \times 10^{13} \text{ m}^{-3}$  (at 155  $\mu\text{s}$ ) when tungsten faces the plasma. When quartz is considered, accordingly, the density increases from  $0.07 \times 10^{13} \text{ m}^{-3}$  (at 95  $\mu\text{s}$ ) to  $1.25 \times 10^{13} \text{ m}^{-3}$  (at 165  $\mu\text{s}$ ).
- A maximum of the electron density within 10  $\mu\text{s}$  after the end of the plasma pulse combined with a decreasing trend in the cold electron temperature in the post discharge imply that conditions are met for efficient DEA and thus efficient negative ion production.

Overall, the present thesis: a) demonstrates that ECR excitation efficiently triggers the mechanisms of volume production of negative ions, the principal of which is DEA, b) unveils the existence of dual populations of electrons and negative ions which are directly correlated to the DEA reaction, c) makes

evident that for the development of future negative ion sources for fusion applications the study of deuterium is crucial, d) established VUV Fourier transform absorption spectroscopy with the use of synchrotron radiation as a powerful tool having the capacity of providing direct and absolute measurements of the molecule population rotationally/vibrationally excited levels of the molecular ground state and also of the atomic population in the ground state, e) analytically presents the process of the determination of experimental VDFs, and finally f) implies that the use of specific wall materials and driving regimes of the plasma carries a potential for the optimization of negative ion sources.

# BIBLIOGRAPHY

---

- [1] G. I. Dimov, “Use of hydrogen negative ions in particle accelerators”, *Rev. Sci. Instrum.*, **67**(10), 3393–3404 (1996).
- [2] R. Welton *et al.*, “Negative hydrogen ion sources for particle accelerators: Sustainability issues and recent improvements in long-term operations”, *J. Phys.: Conf. Series*, **2244**(1), 012045 (2022).
- [3] D. Faircloth and S. Lawrie, “An overview of negative hydrogen ion sources for accelerators”, *New J. Phys.*, **20**(2), 025007 (2018).
- [4] D. P. Moehs, J. Peters, and J. Sherman, “Negative hydrogen ion sources for accelerators”, *IEEE Trans. Plasma Sci.*, **33**(6), 1786–1798 (2005).
- [5] M. Muramatsu *et al.*, “Application of compact electron cyclotron resonance ion source”, *Rev. Sci. Instrum.*, **79**(2), 02A328 (2008).
- [6] Culham Centre for Fusion and Energy, <https://ccfe.ukaea.uk>
- [7] J. Wesson, *Tokamaks, Third Edition*. Oxford University Press Inc, New York (2004).
- [8] J. Friedberg, *Plasma Physics and Fusion Energy*. Cambridge Univeristy Press, New York (2007).
- [9] International Atomic Energy Agency (IAEA), “IAEA Bulletin, Fusion Energy”, **62–2** (2021).
- [10] G. Federici *et al.*, “DEMO design activity in Europe: Progress and updates”, *Fusion Eng. Des.*, **136**, 729-741 (2018).
- [11] P. Agostinetti, T. Franke, U. Fantz, C. Hopf, N. Mantel, and M. Q. Tran, “RAMI evaluation of the beam source for the DEMO neutral beam injectors”, *Fusion Eng. Des.*, **159**, 111628 (2020).
- [12] R. S. Hemsworth and T. Inoue, “Positive and negative ion sources for magnetic fusion”, *IEEE Trans. Plasma Sci.*, **33**(6), 1799–1813 (2005).
- [13] R. Hemsworth *et al.*, “Status of the ITER heating neutral beam system”, *Nucl. Fusion*, **49**(4), 045006 (2009).
- [14] M. Bacal and M. Wada, “Negative hydrogen ion production mechanisms”, *App. Phys. Rev.*, **2**(2), 021305 (2015).
- [15] E. Nicopoulou, M. Bacal, and H. J. Doucet, “Equilibrium Density of H<sup>-</sup> in a Low Pressure Hydrogen Plasma.”, *J. Phys.*, **38**(11), 1399–1404, (1977).
- [16] M. Bacal and G. W. Hamilton, “H<sup>-</sup> and D<sup>-</sup> Production in Plasmas”, *Phys. Rev. Lett.*, **42**(23), 1538 (1979).
- [17] S. Aleiferis, “Experimental study of H<sup>-</sup> negative ion production by electron cyclotron resonance plasmas”, Doctoral thesis, University of Patras, University Grenoble Alpes, (2017).
- [18] B. Schunke *et al.*, “Overview of the negative ion based neutral beam injectors for ITER”, *Rev. Sci. Instrum.*, **87**(2), 02C101 (2016).
- [19] R. S. Hemsworth *et al.*, “Overview of the design of the ITER heating neutral beam

- injectors”, *New J. Phys.*, **19**(2), 025005 (2017).
- [20] U. Fantz *et al.*, “Low pressure and high power rf sources for negative hydrogen ions for fusion applications (ITER neutral beam injection) (invited)”, *Rev. Sci. Instrum.*, **79**(2), 02A511 (2008).
- [21] B. Heinemann *et al.*, “Towards large and powerful radio frequency driven negative ion sources for fusion”, *New J. Phys.*, **19**(1), 015001 (2017).
- [22] U. Fantz, L. Schiesko, and D. Wunderlich, “A comparison of hydrogen and deuterium plasmas in the IPP prototype ion source for fusion”, *AIP Conf. Proc.*, **1515**, 187–196 (2013).
- [23] D. Wunderlich *et al.*, “Formation of large negative deuterium ion beams at ELISE”, *Rev. Sci. Instrum.*, **90**(11), 113304 (2019).
- [24] W. Kraus, D. Wunderlich, U. Fantz, B. Heinemann, F. Bonomo, and R. Riedl, “Deuterium results at the negative ion source test facility ELISE”, *Rev. Sci. Instrum.*, **89**(5), 052102 (2018).
- [25] G. Serianni *et al.*, “SPIDER in the roadmap of the ITER neutral beams”, *Fusion Eng. Des.*, **146**, 2539–2546 (2019).
- [26] M. Barbisan *et al.*, “Negative ion density in the ion source SPIDER in Cs free conditions”, *Plasma Phys. Control. Fusion*, **64**, 065004 (2022).
- [27] G. Serianni *et al.*, “First operation in SPIDER and the path to complete MITICA”, *Rev. Sci. Instrum.*, **91**(2), 023510 (2020).
- [28] D. Marcuzzi *et al.*, “Lessons learned after three years of SPIDER operation and the first MITICA integrated tests”, *Fusion Eng. Des.*, **191**, 113590 (2023).
- [29] F. Taccogna *et al.*, “Latest experimental and theoretical advances in the production of negative ions in caesium-free plasmas” *Eur. Phys. J. D*, **75**(8), 227 (2021).
- [30] A. Simonin, C. Blondel, W. Chaibi, C. Dechelle, C. Drag, and E. Villedieu, “Towards a maintainable and high efficiency neutral beam system for future fusion,” *Nucl. Fus.*, **61**(4), 046003 (2021).
- [31] A. Simonin *et al.*, “Negative ion source development for a photoneutralization based neutral beam system for future fusion reactors”, *New J. Phys.*, **18**(12), 125005 (2016).
- [32] A. Simonin *et al.*, “R&D around a photoneutralizer-based NBI system (Siphore) in view of a DEMO Tokamak steady state fusion reactor”, *Nucl. Fusion*, **55**(12), 123020 (2015).
- [33] D. A. Skinner, A. M. Bruneteau, P. Berlemont, C. Courteille, R. Leroy, and M. Bacal, “Isotope effect and electron-temperature dependence in volume H and D ion sources,” *Phys. Rev. E*, **48**, 2122 (1993).
- [34] A. M. Bruneteau, C. Courteille, R. Leroy, and M. Bacal, “Investigation of two negative hydrogen and deuterium ion sources: Effect of the volume”, *Rev. Sci. Instrum.*, **67**(11), 3827–3830 (1996).
- [35] A. A. Mullan and W. G. Graham, “Plasma parameter characterization of a tandem multicusp ion source operating in H<sub>2</sub> and D<sub>2</sub>”, *Rev. Sci. Instrum.*, **61**(1), 451–453 (1990).
- [36] A. A. Mullan and W. G. Graham, “Study of the discharge of a multicusp ion source operating with H<sub>2</sub> and D<sub>2</sub>”, *J. Phys. D: Appl. Phys.*, **24**(9), 1533 (1991).

- 
- [37] R. Leroy, M. Bacal, P. Berlemont, C. Courteille, and R. A. Stern, “H<sup>-</sup> and D<sup>-</sup> temperature in volume sources,” *Rev. Sci. Instrum.*, **63**(4), 2686–2688 (1992).
- [38] O. Fukumasa and S. Mori, “Volume production of D<sup>-</sup> negative ions in low-pressure D<sub>2</sub> plasmas - Negative ion densities versus plasma parameters”, *Nucl. Fusion*, **46**(6), S287 (2006).
- [39] S. Mori and O. Fukumasa, “D<sup>-</sup>/H<sup>-</sup> negative ion production versus plasma parameters in a volume negative ion source”, *Rev. Sci. Instrum.*, **79**(2), 02A507 (2008).
- [40] T. Inoue *et al.*, “Comparison of H<sup>-</sup> and D<sup>-</sup> production in a magnetically filtered multicusp source”, *Rev. Sci. Instrum.*, **61**(1), 496–498 (1990).
- [41] R. McAdams, R. F. King, and A. F. Newman, “Hydrogen/deuterium negative ion scaling from a magnetic multipole ion source” *Rev. Sci. Instrum.*, **63**(2), 1777–1782 (1992).
- [42] M. Hamabe, Y. Oka, M. Osakabe, Y. Takeiri, K. Tsumori, and O. Kaneko, “Comparison of H<sup>-</sup>/D<sup>-</sup> measurement in the magnetically filtered region of the large negative ion source”, *Rev. Sci. Instrum.*, **71**(2), 1151–1153 (2000).
- [43] K. Ikeda *et al.*, “Exploring deuterium beam operation and the behavior of the co-extracted electron current in a negative-ion-based neutral beam injector”, *Nucl. Fusion*, **59**(7), 076009 (2019).
- [44] M. Bacal, C. Michaut, L. I. Elizarov, and F. el Balghiti, “Basic processes of negative hydrogen ion production and destruction in sources and beams (invited)”, *Rev. Sci. Instrum.*, **67**(3), 1138-1143 (1996).
- [45] C. Jacquot, J. Pamela, D. Riz, and Y. Belchenko, “Negative ion production in large volume source with small deposition of cesium”, *Rev. Sci. Instrum.*, **67**(3), 1036–1038 (1996).
- [46] R. McAdams, R. F. King, G. Proudfoot, and A. J. T. Holmes, “Pure and cesiated cw volume source performance at the Culham Ion Source Test Stand”, *AIP Conf. Proc.*, **287**, 353–367 (2008).
- [47] J. Komppula, O. Tarvainen, T. Kalvas, H. Koivisto, P. Myllyperkiö, and V. Toivanen, “A study of VUV emission and the extracted electron-ion ratio in hydrogen and deuterium plasmas of a filament-driven H<sup>-</sup>/D<sup>-</sup> ion source”, *Phys. Plasmas*, **26**(7), 076517 (2019).
- [48] D. Rauner, S. Briefi, and U. Fantz, “RF power transfer efficiency of inductively coupled low pressure H<sub>2</sub> and D<sub>2</sub> discharges”, *Plasma Sources Sci. Technol.*, **26**(9), 095004 (2017).
- [49] S. Cristofaro, R. Friedl, and U. Fantz, “Negative Hydrogen and Deuterium Ion Density in a Low Pressure Plasma in Front of a Converter Surface at Different Work Functions”, *Plasma*, **4**(1), 94–107 (2021).
- [50] L. Schiesko, M. Carrère, J.-M. Layet, and G. Cartry, “ A comparative study of H<sup>-</sup> and D<sup>-</sup> production on graphite surfaces in H<sub>2</sub> and D<sub>2</sub> plasmas”, *Plasma Sources Sci. Technol.*, **19**(4), 045016 (2010).
- [51] G. Cartry *et al.*, “Alternative solutions to caesium in negative-ion sources: A study of negative-ion surface production on diamond in H<sub>2</sub>/D<sub>2</sub> plasmas”, *New J. Phys.*, **19**(2), 025010 (2017).
- [52] S. Briefi and U. Fantz, “Investigation of Helicon discharges as RF coupling concept of

- negative hydrogen ion sources”, *AIP Conf. Proc.*, **1515**, 278-283 (2013).
- [53] C. Marini *et al.*, “Spectroscopic characterization of H<sub>2</sub> and D<sub>2</sub> helicon plasmas generated by a resonant antenna for neutral beam applications in fusion”, *Nucl. Fusion*, **57**(3), 036024 (2017).
- [54] R. Agnello *et al.*, “Negative ion characterization in a helicon plasma source for fusion neutral beams by cavity ring-down spectroscopy and Langmuir probe laser photodetachment”, *Nucl. Fusion*, **60**(2), 026007 (2020).
- [55] V. D. Dougar-Jabon, “Production of Hydrogen and Deuterium Negative Ions in an Electron Cyclotron Resonance Driven Plasma” *Phys. Scr.*, **63**(4), 322–325 (2001).
- [56] D. Rauner, U. Kurutz, and U. Fantz, “Comparison of measured and modelled negative hydrogen ion densities at the ECR-discharge HOMER”, *AIP Conf. Proc.*, **1655**, 020017 (2015).
- [57] R. Friedl, D. Rauner, A. Heiler, and U. Fantz, “Dissociative recombination and its impact on the line profile of the hydrogen Balmer series,” *Plasma Sources Sci. Technol.*, **29**(1), 015014 (2020).
- [58] R. Friedl, U. Kurutz, and U. Fantz, “Efficiency of Cs-free materials for negative ion production in H<sub>2</sub> and D<sub>2</sub> plasmas,” *AIP Conf. Proc.*, **1869**, 030022 (2017).
- [59] U. Kurutz, R. Friedl, and U. Fantz, “Investigations on Cs-free alternatives for negative ion formation in a low pressure hydrogen discharge at ion source relevant parameters”, *Plasma Phys. Control. Fusion*, **59**(7), 075008 (2017).
- [60] A. Lacoste, T. Lagarde, S. Béchu, Y. Arnal, and J. Pelletier, “Multi-dipolar plasmas for uniform processing: Physics, design and performance,” *Plasma Sources Sci. Technol.*, **11**(4), 407–412 (2002).
- [61] A. A. Ivanov, C. Rouillé, M. Bacal, Y. Arnal, S. Béchu, and J. Pelletier, “H<sup>-</sup> ion production in electron cyclotron resonance driven multicusp volume source”, *Rev. Sci. Instrum.*, **75**(5), 1750-1753 (2004).
- [62] P. Svarnas, J. Breton, M. Bacal, and T. Mosbach, “Pressure optimization for H<sup>-</sup> ion production in an electron cyclotron resonance-driven and a filamented source”, *Rev. Sci. Instrum.*, **77**(3), 03A532 (2006).
- [63] P. Svarnas, J. Breton, M. Bacal, and R. Faulkner, “Plasma electrode bias effect on the H<sup>-</sup> negative-ion density in an electron cyclotron resonance volume source”, *IEEE Trans. Plasma Sci.*, **35**(4), 1156–1162 (2007).
- [64] P. Svarnas, B. M. Annaratone, S. Béchu, J. Pelletier, and M. Bacal, “Study of hydrogen plasma in the negative-ion extraction region”, *Plasma Sources Sci. Technol.*, **18**(4), 045010 (2009).
- [65] S. Béchu *et al.*, “Multi-dipolar microwave plasmas and their application to negative ion production”, *Phys. Plasmas*, **20**(10), 101601 (2013).
- [66] J. Bentounes *et al.*, “Effects of the plasma-facing materials on the negative ion H<sup>-</sup> Density in an ECR (2.45 GHz) plasma”, *Plasma Sources Sci. Technol.*, **27**(5), 055015 (2018).
- [67] S. Béchu *et al.*, “Detection of rovibrationally excited molecular hydrogen in the electronic

- ground state via synchrotron radiation,” *Appl. Phys. Lett.*, **111**(7), 074103 (2017).
- [68] S. Béchu *et al.*, “Direct measurements of electronic ground state ro-vibrationally excited D<sub>2</sub> molecules produced on ECR plasma-facing materials by means of VUV-FT absorption spectroscopy,” *J. Quant. Spectrosc. Radiat. Transf.*, **257**, 107325 (2020).
- [69] S. Aleiferis, P. Svarnas, I. Tsiroidis, S. Bechu, M. Bacal, and A. Lacoste, “H<sup>-</sup> negative ion production from a 2D network of ECR dipolar plasma sources,” *IEEE Trans. Plasma Sci.*, **42**(10), 2828–2829 (2014).
- [70] S. Aleiferis, O. Tarvainen, P. Svarnas, M. Bacal, and S. Béchu, “Experimental investigation of the relation between H<sup>-</sup> negative ion density and Lyman- $\alpha$  emission intensity in a microwave discharge,” *J. Phys. D. Appl. Phys.*, **49**(9), 095203 (2016).
- [71] S. Aleiferis, P. Svarnas, S. Béchu, O. Tarvainen, and M. Bacal, “Production of hydrogen negative ions in an ECR volume source: Balance between vibrational excitation and ionization”, *Plasma Sources Sci. Technol.*, **27**(7), 075015 (2018).
- [72] V. D. Dougar Jabon, A. J. Chacon Velasco, and F. A. Vivas, “Hydrogen negative ion production in an electron cyclotron resonance driven plasma”, *Rev. Sci. Instrum.*, **69**(2), 950-952 (1998).
- [73] J. S. Yoon *et al.*, “Electron-impact cross sections for deuterated hydrogen and deuterium molecules”, *Reports Prog. Phys.*, **73**(11), 116401 (2010).
- [74] L. H. Scarlett, D. V Fursa, M. C. Zammit, I. Bray, and Y. Ralchenko, “Complete collision data set for electrons scattering on molecular hydrogen and its isotopologues: II . Fully vibrationally-resolved”, *At. Data Nucl. Data Tables*, **139**, 101403 (2021).
- [75] M. Bacal, Ed., *Physics and Applications of Hydrogen Negative Ion Sources*. Springer Series on Atomic, Optical, and Plasma Physics 124, (2023).
- [76] R. Friedl, S. Cristofaro, and U. Fantz, “Work function of Cs-free materials for enhanced H<sup>-</sup> surface production”, *AIP Conf. Proc.*, **2011**, 050009 (2018).
- [77] J. M. Wadehra, “Dissociative attachment and dissociation of molecular hydrogen and its heavier isotopes by electron impact”, *Contrib. to IAEA-CRP ("Atomic Plasma-Wall Interact. Data Fusion React. Divertor Model. 3rd IAEA Reasearch Co-ord. Meet. Vienna, (1999)*.
- [78] J. M. Wadehra and J. N. Bardsley, “Vibrational- and rotational-state dependence of dissociative attachment in e-H<sub>2</sub> collisions”, *Phys. Rev. Lett.*, **41**(26), 1795–1798 (1978).
- [79] J. N. Bardsley and J. M. Wadehra, “Dissociative attachment and vibrational excitation in low-energy collisions of electrons with H<sub>2</sub> and D<sub>2</sub>”, *Phys. Rev. A*, **20**(4), 1398–1405 (1979).
- [80] R. Celiberto, R. K. Janev, A. Laricchiuta, M. Capitelli, J. M. Wadehra, and D. E. Atems, “Cross section data for electron-impact inelastic processes of vibrationally excited molecules of hydrogen and its isotopes”, *At. Data Nucl. Data Tables*, **77**(2), 161–213 (2001).
- [81] M. Bacal and M. Wada, “Negative ion source operation with deuterium”, *Plasma Sources Sci. Technol.*, **29**(3), 033001 (2020).
- [82] B. Peart and K. T. Dolder, “Collisions between electrons and H<sub>2</sub><sup>+</sup> ions VI. Measurements of cross sections for the simultaneous production of H<sup>+</sup> and H<sup>-</sup>”, *J. Phys. B At. Mol. Phys.*,

- 8**(9), 1570–1574 (1975).
- [83] B. Peart and K. T. Dolder, “Measurements of cross sections for the dissociative recombination of  $D_2^+$  ions”, *J. Phys. B At. Mol. Phys.*, **6**, L359 (1973).
- [84] K. A. Miller *et al.*, “Isotope effect for associative detachment:  $H(D)^- + H(D) \rightarrow H_2(D_2) + e^-$ ”, *Phys. Rev. A - At. Mol. Opt. Phys.*, **86**(3), 032714 (2012).
- [85] W. G. Graham, “The kinetics of negative hydrogen ions in discharges”, *Plasma Sources Sci. Technol.*, **4**, 281 (1995).
- [86] R. K. Janev, D. Reiter, and U. Samm, “Collision Processes in Low-Temperature Hydrogen Plasmas”, *Forschungszentrum Jülich* (2003).
- [87] W. Yang *et al.*, “Benchmarking and validation of global model code for negative hydrogen ion sources”, *Phys. Plasmas*, **25**(11), 113509 (2018).
- [88] A. V Demyanov *et al.*, “Properties of a beam-driven discharge in an  $H_2$ -Ar mixture”, *Sov. J. Plasma Phys.*, **11**(3), 210 (1969).
- [89] M. S. Huq, L. D. Doverspike, and R. L. Champion, “Electron detachment for collisions of  $H^-$  and  $D^-$  with hydrogen molecules”, *Phys. Rev. A*, **27**(6), 2831 (1983).
- [90] M. J. J. Eerden, M. C. M. Van De Sanden, D. K. Otorbaev, and D. C. Schram, “Cross section for the mutual neutralization reaction  $H_2^+ + H^-$ , calculated in a multiple-crossing Landau-Zener approximation”, *Phys. Rev. A*, **51**(4), 3362–3365 (1995).
- [91] A. A. Matveyev and V. P. Silakov, “Kinetic processes in a highly-ionized non-equilibrium hydrogen plasma”, *Plasma Sources Sci. Technol.*, **4**(4), 606–617 (1995).
- [92] J. R. Hiskes, “Cross sections for the vibrational excitation of the  $H_2$   $X^1\Sigma_g^+(v)$  levels generated by electron collisional excitation of the higher singlet states”, *J. Appl. Phys.*, **70**(7), 3409–3417 (1991).
- [93] M. Capitelli *et al.*, “Vibrational kinetics, electron dynamics and elementary processes in  $H_2$  and  $D_2$  plasmas for negative ion production: Modelling aspects”, *Nucl. Fusion*, **46**(6), S260 (2006).
- [94] S. Morisset, F. Aguilon, M. Sizun, and V. Sidis, “Quantum dynamics of  $H_2$  formation on a graphite surface through the Langmuir-Hinshelwood mechanism”, *J. Chem. Phys.*, **121**(13), 6493–6501 (2004).
- [95] D. D. Eley and E. K. Rideal, “Parahydrogen conversion on tungsten”, *Nature*, **146**, 402 (1940).
- [96] J. Harris and B. Kasemo, “On precursor mechanisms for surface reactions”, *Surf. Sci. Lett.*, **105**, L281-287 (1981).
- [97] B. Gordiets, C. M. Ferreira, M. J. Pinheiro, and A. Ricard, “Self-consistent kinetic model of low-pressure  $N_2$ - $H_2$  flowing discharges: II. Surface processes and densities of N, H,  $NH_3$  species”, *Plasma Sources Sci. Technol.*, **7**(3), 379–388 (1998).
- [98] J. R. Hiskes and A. M. Karo, “Analysis of the  $H_2$  vibrational distribution in a hydrogen discharge”, *Appl. Phys. Lett.*, **54**(6), 508–510 (1989).
- [99] J. Ellis, J. Branson, K. Niemi, E. Wagenaars, and T. Gans, “Influence of surface materials on the volume production of negative ions in a radio-frequency driven hydrogen plasma”,

- J. Phys. D. Appl. Phys.*, **53**(48), 485202 (2020).
- [100] B. J. Wood and H. Wise, “Kinetics of hydrogen atom recombination on surfaces”, *J. Phys. Chem.*, **65**(11), 1976–1983 (1961).
- [101] B. J. Wood and H. Wise, “The kinetics of hydrogen atom recombination on pyrex glass and fused Quartz”, *J. Chem. Phys.*, **66**(6), 1049–1052 (1962).
- [102] T. Kammler and J. Küppers, “Interaction of H atoms with Cu(111) surfaces: Adsorption, absorption, and abstraction”, *J. Chem. Phys.*, **111**(17), 8115–8123 (1999).
- [103] T. Kammler, D. Kolovos-Vellianitis, and J. Küppers, “A hot-atom reaction kinetic model for H abstraction from solid surfaces”, *Surf. Sci.*, **460**(1–3), 91–100 (2000).
- [104] M. Rutigliano and M. Cacciatore, “Isotope and surface temperature effects for hydrogen recombination on a graphite surface”, *ChemPhysChem.*, **9**(1), 171–181 (2008).
- [105] B. Jackson and D. Lemoine, “Eley-Rideal reactions between H atoms on metal and graphite surfaces: The variation of reactivity with substrate”, *J. Chem. Phys.*, **114**(1), 474–482 (2001).
- [106] M. Cacciatore and M. Rutigliano, “The semiclassical and quantum-classical approaches to elementary surface processes: Dissociative chemisorption and atom recombination on surfaces”, *Phys. Scr.*, **78**(5), 058115 (2008).
- [107] R. I. Hall, I. Cadez, M. Landau, F. Pichou, and C. Schermann, “Vibrational excitation of hydrogen via recombinative desorption of atomic hydrogen gas on a metal surface”, *Phys. Rev. Lett.*, **60**(4), 337–340 (1988).
- [108] S. Markelj and I. Ade, “Production of vibrationally excited hydrogen molecules by atom recombination on Cu and W materials”, *J. Chem. Phys.*, **134**(12), 124707 (2011).
- [109] M. Rutigliano and M. Cacciatore, “Eley-Rideal recombination of hydrogen atoms on a tungsten surface”, *Phys. Chem. Chem. Phys.*, **13**(16), 7475–7484 (2011).
- [110] R. K. Janev, “Alternative mechanisms for divertor plasma recombination”, *Phys. Scr. T*, **96**, 94-101 (2002).
- [111] S. I. Krasheninnikov, “Molecule assisted recombination (MAR): Mechanisms and plasma conditions for effective operation”, *Phys. Scr. T*, **96**, 7-15 (2002).
- [112] K. Sawada and T. Fujimoto, “Effect of initial vibrational excitation of molecular hydrogen on molecule assisted recombination in divertor plasmas”, *Contrib. Plasma Phys.*, **42**(6-7), 603-607 (2002).
- [113] M. A. Lieberman and A. J. Lichtenberg, *Principles of plasma discharges and materials processing*, Second Ed. John Wiley & Sons, Inc., Hoboken, New Jersey, (2005).
- [114] F. F. Chen, *Introduction to Plasma Physics and Controlled Fusion*, Third Ed. Switzerland: Springer International Publishing, (2018).
- [115] J. R. Roth, *Industrial Plasma Engineering Volume 1: Principles*, IOP Publishing Ltd., (1995).
- [116] S. Béchu, O. Maulat, Y. Arnal, D. Vempaire, A. Lacoste, and J. Pelletier, “Multi-dipolar plasmas for plasma-based ion implantation and plasma-based ion implantation and deposition”, *Surf. Coatings Technol.*, **186**(1-2), 170–176 (2004).

- [117] I. Ilescu, N. Skryabina, D. Fruchart, A. Bes, and A. Lacoste, “Morphology and microstructure of Mg-Ti-H films deposited by microwave plasma-assisted co-sputtering”, *J. Alloys Compd.*, **708**, 489–499 (2017).
- [118] F. Zoubian, N. Renaut, and L. Latrasse, “Distributed elementary ECR microwave plasma sources supplied by solid state generators for production of large area plasmas without scale limitation: Plasma density measurements and comparison with simulation”, *Plasma Res. Express*, **3**(2), 025010 (2021).
- [119] L. Latrasse, M. Radoiu, T. Nelis, and O. Antonin, “Self-matching plasma sources using 2.45 GHz solid-state generators: microwave design and operating performance”, *J. Microw. Power Electromagn. Energy*, **51**(4), 237–258 (2017).
- [120] T. Lagarde, Y. Arnal, A. Lacoste, and J. Pelletier, “Determination of the EEDF by Langmuir probe diagnostics in a plasma excited at ECR above a multipolar magnetic field”, *Plasma Sources Sci. Technol.*, **10**(2), 181–190 (2001).
- [121] K. N. Mellon, B. P. Coonan, and M. B. Hopkins, “Spatially dependent photodetachment measurements in a low-pressure high-power modulated volume ion source”, *J. Phys. D. Appl. Phys.*, **28**(3), 473–478 (1995).
- [122] C. Gorse and M. Capitelli, “Enhanced production of negative ions in low-pressure hydrogen and deuterium pulsed discharges: Theoretical calculations”, *Phys. Rev. A*, **46**(4), 2176–2177 (1992).
- [123] M. B. Hopkins and W. G. Graham, “Time-resolved electron energy distribution function measurements in a pulsed magnetic multipole hydrogen discharge”, *J. Appl. Phys.*, **69**(6), 3461–3466 (1991).
- [124] M. B. Hopkins and K. N. Mellon, “Enhanced production of negative ions in low-pressure hydrogen and deuterium discharges”, *Phys. Rev. Lett.*, **67**(4), 449–452 (1991).
- [125] M. B. Hopkins, M. Bacal, and W. G. Graham, “Enhanced volume production of negative ions in the post discharge of a multicusp hydrogen discharge”, *J. Appl. Phys.*, **70**(4), 2009–2014 (1991).
- [126] K. N. Mellon, B. P. Coonan, and M. B. Hopkins, “Investigation of the temporal behaviour of the  $H^-$  density in a low-pressure pulsed discharge using laser photodetachment”, *J. Phys. D. Appl. Phys.*, **27**(12), 2480–2486 (1994).
- [127] A. Al-Jibouri and W. G. Graham, “Photodetachment measurements of the  $H^-$  and  $D^-$  density in a tandem multicusp ion source”, *AIP Conf. Proc.*, **287**, 595–603 (1992).
- [128] T. Mosbach, H. M. Katsch, and H. F. Döbele, “Temporal behaviour of the H-minus density in a pulsed multipole discharge investigated by the photodetachment technique”, *Plasma Sources Sci. Technol.*, **7**(1), 75–81 (1998).
- [129] M. Hamabe, Y. Oka, O. Tsumori, T. Kuroda, and M. Bacal, “Time-resolved study of the negative ion density in a volume  $H^-$  ion source by photodetachment”, *Rev. Sci. Instrum.*, **69**(3), 1298–1301 (1998).
- [130] T. Mosbach, H. M. Katsch, and H. F. Döbele, “In situ diagnostics in plasmas of electronic-ground-state hydrogen molecules in high vibrational and rotational states by laser-induced

- fluorescence with vacuum-ultraviolet radiation”, *Phys. Rev. Lett.*, **85**(16), 3420–3423 (2000).
- [131] A. Rousseau, L. Tomasini, G. Gousset, C. Boisse-Laporte, and P. Leprince, “Pulsed microwave discharge: a very efficient H atom source”, *J. Phys. D. Appl. Phys.*, **27**(11), 2439–2441 (1994).
- [132] A. Rousseau, G. Cartry, and X. Duten, “Surface recombination of hydrogen atoms studied by a pulsed plasma excitation technique”, *J. Appl. Phys.*, **89**(4), 2074–2078 (2001).
- [133] P. Svarnas, M. Bacal, P. Auvray, S. Béchu, and J. Pelletier, “H<sup>-</sup> extraction from electron-cyclotron-resonance-driven multicusp volume source operated in pulsed mode”, *Rev. Sci. Instrum.*, **77**(3), 111–114 (2006).
- [134] H. M. Katsch and E. Quandt, “Production of Negative Hydrogen ions in a Pulsed Low Pressure Volume Discharge”, *J. Phys. D. Appl. Phys.*, **25**(3), 430–435 (1992).
- [135] A. Rousseau, E. Teboul, and N. Sadeghi, “Time-resolved gas temperature measurements by laser absorption in a pulsed microwave hydrogen discharge”, *Plasma Sources Sci. Technol.*, **13**(1), 166–176 (2004).
- [136] M. Q. Tran *et al.*, “Status and future development of Heating and Current Drive for the EU DEMO”, *Fusion Eng. Des.*, **180**, 113159 (2022).
- [137] R. L. Merlino, “Understanding Langmuir probe current-voltage characteristics”, *Am. J. Phys.*, **75**(12), 1078–1085 (2007).
- [138] F. F. Chen and J. P. Chang, *Lecture Notes on Principles of Plasma Processing*. New York: Springer Science and Business Media, (2003).
- [139] V. A. Godyak and V. I. Demidov, “Probe measurements of electron-energy distributions in plasmas: What can we measure and how can we achieve reliable results?”, *J. Phys. D. Appl. Phys.*, **44**(26), 269501 (2011).
- [140] A. Aanesland, J. Bredin, P. Chabert, and V. Godyak, “Electron energy distribution function and plasma parameters across magnetic filters”, *Appl. Phys. Lett.*, **100**(4), 100–103 (2012).
- [141] S. Aleiferis and P. Svarnas, “Automated electrostatic probe device of high resolution and accuracy”, *Rev. Sci. Instrum.*, **85**(12), 10–18 (2014).
- [142] M. Bacal, “Photodetachment diagnostic techniques for measuring negative ion densities and temperatures in plasmas”, *Rev. Sci. Instrum.*, **71**(11), 3981–4006 (2000).
- [143] R. A. Stern, P. Devynck, M. Bacal, P. Berlemont, and F. Hillion, “Nonresonant optical tagging and monopolar transport in negative-ion plasmas”, *Phys. Rev. A*, **41**(6), 3307–3320 (1990).
- [144] L. Friedland, C. I. Ciubotariu, and M. Bacal, “Dynamic plasma response in laser-photodetachment experiments in hydrogen plasmas”, *Phys. Rev. E*, **49**(5), 4353–4361 (1994).
- [145] N. Oudini, F. Taccogna, A. Bendib, and A. Aanesland, “Numerical simulations used for a validity check on the laser induced photo-detachment diagnostic method in electronegative plasmas”, *Phys. Plasmas*, **21**(6), 063515 (2014).
- [146] J. Bredin, P. Chabert, and A. Aanesland, “Langmuir probe analysis of highly

- electronegative plasmas”, *Appl. Phys. Lett.*, **102**(15), 154107 (2013).
- [147] J. E. Allen, “A note on the Bohm criterion for electronegative gases”, *Plasma Sources Sci. Technol.*, **13**(1), 48–49 (2004).
- [148] M. Mitrou, P. Svarnas, and S. Béchu, “Corrigendum: Experimental study on dynamic effects of  $H^-$  and  $D^-$  negative ions in an ECR-plasma source”, *J. Phys. Conf. Ser.*, **2244**(1), 012110 (2022).
- [149] D. L. Hillis *et al.*, “Comparison of hydrogen and tritium uptake and retention in JET”, *J. Nucl. Mater.*, **290–293**, 418–422 (2001).
- [150] L. Buzi *et al.*, “Influence of particle flux density and temperature on surface modifications of tungsten and deuterium retention”, *J. Nucl. Mater.*, **455**(1–3), 316–319 (2014).
- [151] J. Guterl, R. D. Smirnov, S. I. Krasheninnikov, M. Zibrov, and A. A. Pisarev, “Theoretical analysis of deuterium retention in tungsten plasma-facing components induced by various traps via thermal desorption spectroscopy”, *Nucl. Fusion*, **55**(9), 093017 (2015).
- [152] T. Tanabe, “Review of hydrogen retention in tungsten”, *Phys. Scr.*, **T159**, 014044 (2014).
- [153] Y. Oya *et al.*, “Comparison of Hydrogen Isotope Retention in Divertor Tiles of JET with the ITER-Like Wall Following Campaigns in 2011–2012 and 2015–2016”, *Fusion Sci. Technol.*, **76**(4), 439–445 (2020).
- [154] C. H. Skinner *et al.*, “Recent advances on hydrogen retention in ITER’s plasma-facing materials: Beryllium, carbon and tungsten”, *Fusion Sci. Technol.*, **54**(4), 891–945 (2008).
- [155] F. Taccogna, R. Schneider, S. Longo, and M. Capitelli, “Modeling of a negative ion source. I. Gas kinetics and dynamics in the expansion region”, *Phys. Plasmas*, **14**(7), 073503 (2007).
- [156] L. Nahon *et al.*, “DESIRS: A state-of-the-art VUV beamline featuring high resolution and variable polarization for spectroscopy and dichroism at SOLEIL”, *J. Synchrotron Radiat.*, **19**(4), 508–520 (2012).
- [157] L. Nahon *et al.*, “DESIRS: A state-of-the-art VUV beamline featuring high resolution and variable polarization for spectroscopy and dichroism at SOLEIL”, *J. Phys.: Conf. Ser.*, **425**, 122004 (2013).
- [158] O. Marcouille *et al.*, “Design, construction and magnetic measurements of the HU640 (OPHELIE2) undulator dedicated to the DESIRS VUV beamline at SOLEIL”, *AIP Conf. Proc.*, **879**, 311–314 (2007).
- [159] B. Mercier *et al.*, “Experimental and theoretical study of a differentially pumped absorption gas cell used as a low energy-pass filter in the vacuum ultraviolet photon energy range”, *J. Vac. Sci. Technol. A Vacuum, Surfaces, Film.*, **18**(5), 2533–2541 (2000).
- [160] N. De Oliveira, M. Roudjane, D. Joyeux, D. Phalippou, J. C. Rodier, and L. Nahon, “High-resolution broad-bandwidth Fourier-transform absorption spectroscopy in the VUV range down to 40 nm”, *Nat. Photonics*, **5**(3), 149–153 (2011).
- [161] N. De Oliveira *et al.*, “A Fourier transform spectrometer without a beam splitter for the vacuum ultraviolet range: From the optical design to the first UV spectrum”, *Rev. Sci. Instrum.*, **80**(4), 043101 (2009).
- [162] S. Briefi and U. Fantz, “A revised comprehensive approach for determining the  $H_2$  and  $D_2$

- rovibrational population from the Fulcher- $\alpha$  emission in low temperature plasmas”, *Plasma Sources Sci. Technol.*, **29**(12), 125019 (2020).
- [163] N. Hershkowitz, “How Langmuir Probes Work,” in *Plasma Diagnostics*, Academic Press, Inc., 113-183 (1989).
- [164] L. H. Scarlett, D. V. Fursa, J. Knol, M. C. Zammit, and I. Bray, “Isotopic and vibrational-level dependence of H<sub>2</sub> dissociation by electron impact”, *Phys. Rev. A*, **103**(2), 1–7 (2021).
- [165] X. Yang *et al.*, “TALIF measurements of hydrogen and deuterium surface loss probabilities on quartz in low pressure high density plasmas”, *Plasma Sources Sci. Technol.*, **30**(1), 015013 (2021).
- [166] A. A. Ivanov, “Two negative ion groups in volume H<sup>-</sup> sources”, *Rev. Sci. Instrum.*, **75**(5), 1754–1756 (2004).
- [167] “MOLAT Atomic and Molecular Data.”, <https://molat.obspm.fr/>
- [168] J.-Y. Roncin and F. Launay, “Atlas of the Vacuum Ultraviolet Emission Spectrum of Molecular Hydrogen”, *J. Phys. Chem. Ref. Data*, (1994).
- [169] H. Abgrall, E. Roueff, X. Liu, D. E. Shemansky, and G. K. James, “High-resolution far ultraviolet emission spectra of electron-excited molecular deuterium”, *J. Phys. B At. Mol. Opt. Phys.*, **32**(15), 3813–3838 (1999).
- [170] “Sesam, Spectroscopy of Atoms and Molecules.”, <https://sesam.obspm.fr/>
- [171] N. Sadeghi, “Molecular Spectroscopy Techniques Applied for Processing Plasma Diagnostics” *J. Plasma Fusion Res.*, **80**(9), 767–776 (2004).
- [172] R. K. Hanson, R. M. Spearrin, and C. S. Goldenstein, *Spectroscopy and Optical Diagnostics for Gases.*, (2016).
- [173] G. Herzberg, *Molecular spectra and molecular structure, Vol. 1: Spectra of diatomic molecules*, Second Ed. D. Van Nostrand Company, Inc., (1950).
- [174] J. M. Hollas, *Modern spectroscopy*, Fourth Ed. John Wiley and Sons, Ltd., (2004).
- [175] U. Fantz and D. Wunderlich, “Franck-Condon factors, transition probabilities, and radiative lifetimes for hydrogen molecules and their isotopomers”, *At. Data Nucl. Data Tables*, **92**(6), 853–973 (2006).
- [176] M. Larsson, “Conversion formulas between radiative lifetimes and other dynamical variables for spin-allowed electronic transitions in diatomic molecules”, *Astron. Astrophys.*, **128**, 291–298 (1983).
- [177] J. C. Lagarias, J. A. Reeds, M. H. Wright, and P. E. Wright, “Convergence Properties of the Nelder-Mead Simplex Method in Low Dimensions”, *SIAM J. Optim.*, 9(1), 112–147 (1998).
- [178] C. Biloiu, X. Sun, Z. Harvey, and E. Scime, “Determination of rotational and vibrational temperatures of a nitrogen helicon plasma”, *Rev. Sci. Instrum.*, **77**(10), 10F117 (2006).
- [179] M. Capitelli, G. Colonna, G. D’Ammando, K. Hassouni, A. Laricchiuta, and L. D. Pietanza, “Coupling of Plasma Chemistry, Vibrational Kinetics, Collisional-Radiative Models and Electron Energy Distribution Function Under Non-Equilibrium Conditions”, *Plasma Process. Polym.*, **14**(1–2), 1–11 (2017).

- [180] “COMSOL Multiphysics, Molecular flow module.”, <https://www.comsol.com/molecular-flow-module>

# LIST OF PUBLICATIONS

---

## 1. JOURNAL PUBLICATIONS

- [J4] Isotope effect in plasmas driven by ECR modules towards  $H^-$  and  $D^-$  production  
*Plasma Sources Science and Technology* 32, 105001 (2023) (doi: 10.1088/1361-6595/acfbf5)  
M. Mitrou, P. Svarnas, S. Béchu, S. Aleiferis
- [J3]  $H^-$  and  $D^-$  production efficiency in a multi-dipole ECR-plasma source  
*Journal of Physics: Conference Series* 2244, 012007 (2022) (doi:10.1088/1742-6596/2244/1/012007)  
M. Mitrou, P. Svarnas, S. Béchu
- [J2] Experimental study on dynamic effects of  $H^-$  and  $D^-$  negative ions in an ECR-plasma source  
*Journal of Physics: Conference Series* 2244, 012006 (2022) (doi:10.1088/1742-6596/2244/1/012006)  
M. Mitrou, P. Svarnas, S. Béchu
- [J1] Last experimental and theoretical advances in the production of negative ions in Cesium-free plasmas  
*The European Physical Journal D* 75, 227 (2021) (doi:10.1140/epjd/s10053-021-00228-y)  
F. Taccogna et al.

## 2. BOOK CHAPTERS

- [B1] ECR-driven negative ion sources operating with hydrogen and deuterium  
*Chapter 12 in "Physics and applications of hydrogen negative ion sources", Edited by M. Bacal, Springer series on atomic, optical, and plasma physics vol. 124 Springer, Cham., (2023) (doi:10.1007/978-3-031-21476-9\_12)*  
P. Svarnas, M. Mitrou, J.L. Lemaire, L. Gavilan, N. de Oliveira, S. Béchu

## 3. CONFERENCES

- [C3] Laser-induced photodetachment diagnostic for interrogating pulsed ECR-driven plasmas: Application to  $H^-$  and  $D^-$  negative ions  
*Poster presentation, International Conference on Ionized Gases (ICPIG XXXV<sup>th</sup> Edition), Egmond aan Zee, The Netherlands, 9-14 July 2023*  
M. Mitrou, S. Béchu, P. Svarnas
- [C2] Cylindrical SDBD of well-defined expansion area for standardized studies  
*Poster presentation, International Conference on Ionized Gases (ICPIG XXXV<sup>th</sup> Edition), Egmond aan Zee, The Netherlands, 9-14 July 2023*  
K. Giotis, P. Svarnas, M. Mitrou, K. Gazeli, G. Lombardi, S. Béchu

[C1] Two-laser photo-detachment for negative ion diagnostic: Installation and preliminary results in the  $H^-$  source “Prometheus I”

*XXXIV International Conference on Phenomena in Ionized Gases (XXXIV ICPIG) & 10<sup>th</sup> International Conference on Reactive Plasmas (ICRP-10), Sapporo, Hokkaido Japan 14-19.7.2019*

**M. Mitrou**, P. Svarnas, S. Aleiferis, S. Béchu, A. Lacoste

# Appendix A: Gas flow modeling in COMSOL

The COMSOL Multiphysics<sup>®</sup> software is used in view of modeling the gas flow through the structure of the “SCHEME-II+” reactor. In particular, it was performed for the amelioration of the differential pumping system, described in section 2.2, which is crucial for the experiments held at the SOLEIL synchrotron facility. To this end, the Molecular Flow Module is employed.

In general, the gas flows that occur inside vacuum systems are described by different physics than conventional fluid flow problems. At low pressures, as the ones considered herein, the mean free path of the gas molecules becomes comparable to the size of the system and gas rarefaction becomes important. The degree of rarefaction is expressed through the Knudsen number,  $K_n = \lambda/l$ , where  $\lambda$  is the mean free path of the molecules and  $l$  the characteristic length scale of the system [180]. Depending on the value of the Knudsen number several types of gas flow regimes can be distinguished, namely the molecular ( $K_n > 10$ ), transitional ( $0.1 < K_n < 10$ ), slip ( $0.01 < K_n < 0.1$ ) and continuum flow ( $K_n < 0.01$ ). In the present case, for the most representative pressure studied in the “SCHEME-II+” reactor, i.e. 1.6 Pa, and assuming a typical gas temperature of 400 K (see section 4.3.1), a value for  $\lambda$  of about 9.3 mm is calculated. The issue encountered in the “SCHEME-II+” reactor is that different parts of the structure have different characteristic dimensions and thus different flow regimes may occur. For instance, within the main body of the reactor the continuum flow regime may apply, whereas within the capillaries and the differential pumping unit since the dimensions are really small (in the order of a few mm) then the molecular flow regime takes over. However, presently, the Molecular Flow Module of the COMSOL software does not support modeling with the simultaneous definition of two different flow regimes in the

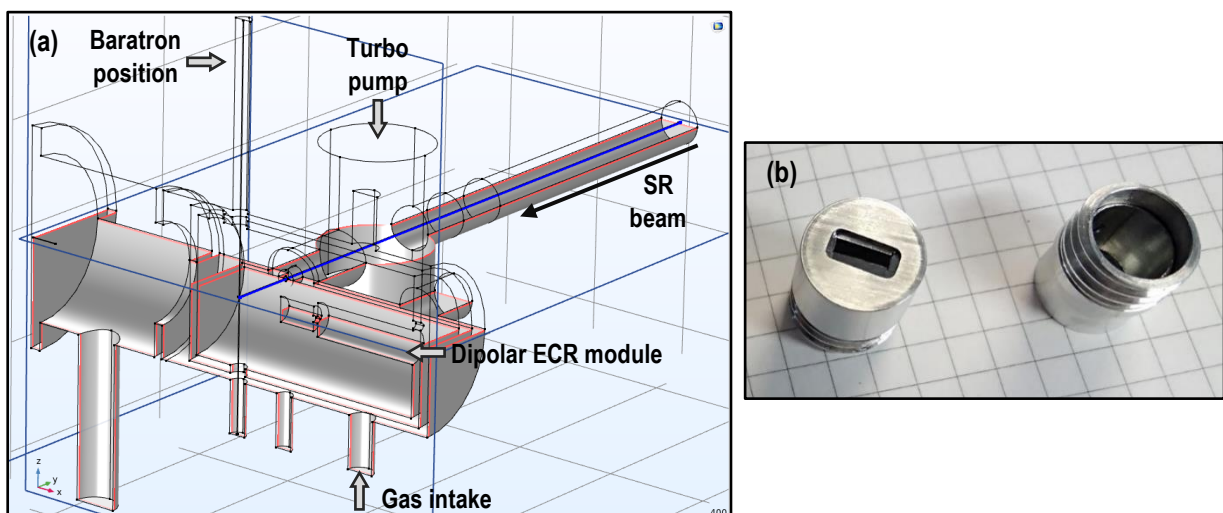


**Figure A.1.** (a) Illustration of the “SCHEME-II+” reactor geometry reproduced in the interface of the COMSOL Multiphysics software. The main parts of the reactor are marked on the illustration. The blue line that traverses the reactor in the direction of the SR beam denotes the virtual surface upon the particle density is calculated as described in text. (b) Photo of the capillaries (0.1 mm thick) and their supports used in the case of the measurements at the SOLEIL synchrotron facility described in Chapter 4.

same geometry. Thus, since the interest in the “SCHEME-II+” reactor consists in deriving the gas flow through the capillaries of the differential pumping unit, it was chosen to model the entire geometry in the molecular flow regime.

**Fig. A.1(a)** shows first of all a cross-sectional view of the geometry of the “SCHEME-II+” as it is re-produced in the software interface. As it was briefly already mentioned in section 2.2, in the molecular flow regime the gas molecules are considered to interact only with the surfaces of the flow domain and there is no scattering between the molecules themselves [180]. In the Free Molecular Flow interface that is used to model this regime, the pressure and the particle number density can be calculated on any surface of the model. In order thus to derive the particle number density along the same line that is traced by the synchrotron radiation beam, a virtual two-dimensional surface (0.2 mm wide) is created along the same trajectory (blue line in **Fig. A.1(a)**) on which the calculations are performed. **Fig. A.1(b)** shows a picture of the capillaries made out of a thin metallic foil (0.1 mm thick) which are used in the experiments whose analysis was detailed in Chapter 4. **Fig. A.2** presents the calculated  $D_2$  molecule number density along the two-dimensional virtual surface. The position of the capillaries (bold black line on the same figure; 62 mm from the center of the reactor) corresponds to the limit for the consideration of the passive gas. It is found that the particle density diminishes by 90% (or, by one magnitude) at a distance of 6.5 mm away from the capillaries. Finally, the passive gas (as illustrated on **Fig. A.2**) is evaluated at 13% of the total particle density.

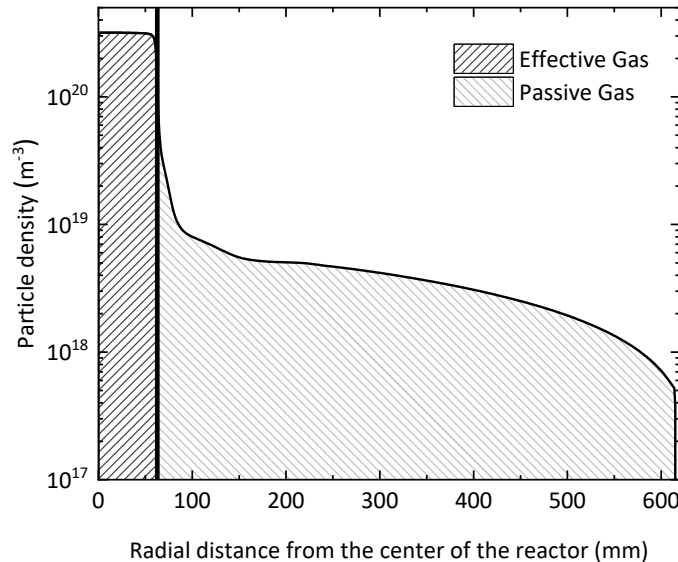


**Figure A.2.** Calculated  $D_2$  molecule number density along the virtual two-dimensional surface representing the path of the SR beam. Since the model is symmetric, the graph presents the calculations as a function of the radial distance from the center of the reactor. The vertical bold black line on the figure denotes the position of the capillaries, at a distance of 62 mm from the center. This also sets the boundary for the consideration as effective or passive.

## Appendix B: Validating the Langmuir probe design

---

In order to validate the use of the coil serving as a reference around the probe so that correct I-V characteristic curves are recorded, a series of measurements were effected with and without it and the results were compared. More specifically, measurements were effected in the “SCHEME-II+” reactor configured as shown on the left of **Fig. 4.11** (Configuration A), i.e. the dipolar ECR module is positioned “off-axis” and the Langmuir probe is displaced vertically at a distance of 35 mm away from the axis of the magnet of the dipolar ECR module. Moreover, the plasma faces an entirely tungsten surface which shares the same ground as the entire structure, thus in a way mimicking a fully metallic reactor. The working gas is D<sub>2</sub> at a pressure of 1.6 Pa and the transmitted microwave power is set at 150 W.

**Fig. B.1** presents the EEDFs derived from the measured I-V characteristics for the two cases studied. A Bi-Maxwellian shape is evident, similarly to the EEDFs presented in Chapter 3 acquired in the “Prometheus I” reactor. Thus, in the same figure, additionally an example of the derived EEDFs for the two different electron populations (a low- and high-energy component) that exist is shown. At the same time, **Table B.1** gives the values for the basic plasma parameters that are obtained through the processing of the said characteristic curves for a more detailed observation for potential discrepancies.

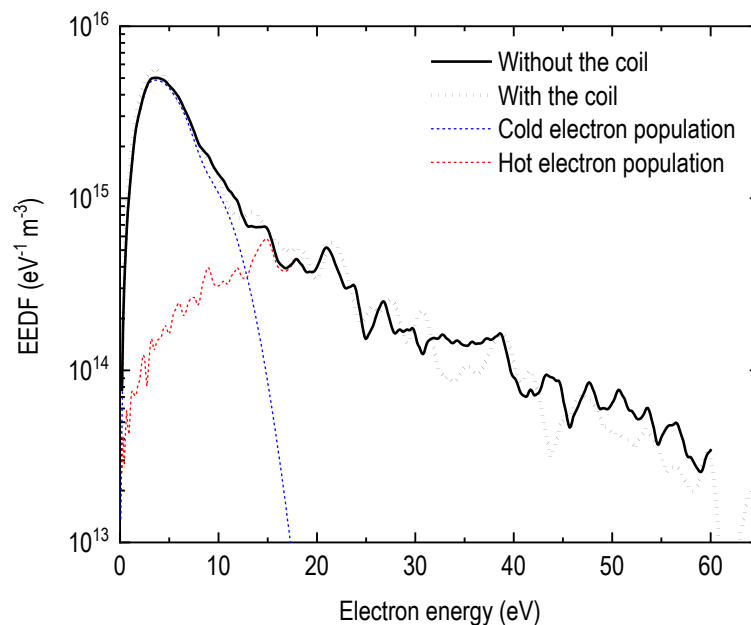


**Figure B.1.** Bi-Maxwellian EEDFs obtained with the two different probes, with (black dotted line) and without (black solid line) the use of the coil reference. At the same time, the blue and the red dashed lines indicate the EEDFs for the two electron populations, the low- and high-energy populations, respectively. D<sub>2</sub>; 1.6 Pa, 150 W.

**Table B.1.** Values of the basic plasma parameters derived from the treatment of the measured I-V characteristics. D<sub>2</sub>; 1.6 Pa, 150 W.

	Without the coil	With the coil
$V_p$ (V)	11.32	11.16
$n_{e,cold}$ (m <sup>-3</sup> )	$3.2 \times 10^{16}$	$2.5 \times 10^{16}$
$n_{e,hot}$ (m <sup>-3</sup> )	$1.1 \times 10^{16}$	$1.7 \times 10^{16}$
$T_{e,cold}$ (eV)	3.64	2.9
$T_{e,hot}$ (eV)	12.7	11.2

At a first glance, **Fig. B.1** attests to a good agreement of the EEDFs with and without the use of the coil reference electrode which is placed near the tip of the probe. The data for the plasma potential and the electron densities and temperatures also match within a 20% margin which is considered acceptable given that between the measurements venting the reactor to atmospheric pressure is inevitable and no special conditioning was performed. The latter by default can induce changes to the overall conditions that present in the reactor which can ultimately be responsible for this error.